DESIGN AND SYNTHESIS OF SEMICONDUCTOR NANOMATERIALS FOR PLASTIC REMEDIATION AND APPLICATION OF RECYCLED PLASTIC FOR REMOVAL OF ORGANIC CONTAMINANTS

Thesis Submitted for the Award of the Degree of

DOCTOR OF PHILOSOPHY

in

CHEMISTRY

By

Kuljit Kaur

42000034

Supervised By

Dr. Harpreet Kaur

Professor

Department of Chemistry,

Lovely Professional University,

Jalandhar, (Punjab), India



LOVELY PROFESSIONAL UNIVERSITY, PUNJAB

2026

DECLARATION

I, **Kuljit Kaur**, bearing Registration No. **42000034**, hereby declare that the research work embodied in the Ph.D. thesis titled "**Design and Synthesis of Semiconductor Nanomaterials for Plastic Remediation and Application of Recycled Plastic for Removal of Organic Contaminants**" submitted to Lovely Professional University, Punjab, India is the original and bonafide work carried out by me under the supervision of **Dr. Harpreet Kaur**, Professor, Department of Chemistry of Lovely Professional University, Punjab, India

I further declare that:

a) The work presented in this thesis is a genuine contribution to the field of research and is a result of investigations carried out by me during the period of my doctoral study.

b) The research work has been conducted in accordance with the academic and ethical standards prescribed by the university.

c) Due acknowledgements and references have been duly given wherever the work of others has been cited or used.

d) The thesis has not been submitted either partly or fully to any other university or institution for the award of any degree or diploma.

I understand that any violation of the above declarations may lead to the cancellation of my degree by the university at any stage.



Signature of Scholar
Kuljit Kaur
Registration No: 42000034
Date:

CERTIFICATE

This is to certify that the work reported in the Ph. D. thesis entitled "**Design and synthesis of semiconductor nanomaterials for plastic remediation and application of recycled plastic for removal of organic contaminants**" submitted in fulfillment of the requirement for the award of degree of **Doctor of Philosophy (Ph.D.)** in the **Department of Chemistry**, is a research work carried out by **Kuljit Kaur, 42000034**, is bonafide record of his/her original work carried out under my supervision and that no part of thesis has been submitted for any other degree, diploma or equivalent course.



Signature of Supervisor

Dr. Harpreet Kaur

UID: 11724

Date:

ABSTRACT

Plastics are extremely useful, but their inability to biodegrade has resulted in a significant amount of plastic waste accumulating in the environment. Plastic waste has emerged as a significant source of pollution in the environment around the world. Plastic contamination in the environment and water is a serious global issue. Micro(nano)plastic contamination has impacted aquatic ecosystems and contaminated drinking water, forcing the development of effective remediation solutions. To address the issue of plastic waste, it is important to remove it from the environment. Recent research is focused on using nanoparticles for environmental remediation, particularly water purification. Providing clean water and a healthy environment for a growing global population is a challenging task. This thesis explores the application of nanomaterials in environmental remediation, including water purification via sorption and photocatalysis of hazardous plastic pollutants and organic dyes.

In this study, three nitrogen doped metal oxides such as N-TiO_2, N-SnO_2 and N-ZrO_2 were synthesized via sol-gel method. Moreover, two carbonaceous materials such as graphene oxide and corncob based activated carbon were used to synthesize and nitrogen doped metal oxides-based nanocomposite materials in varying weight ratios of carbonaceous materials: metal oxide (1:3, 1:1, 3:1) such as GO/N-TiO_2 (GT13, GT11, GT31), CCAC/N-TiO_2 (CT13, CT11, CT31), GO/SnO_2 (GNSO13, GNSO11, GNSO31) were synthesized by one-step colloidal blending process and facile wet impregnation methods. The obtained nanoparticles, carbonaceous materials, and nanomaterials were characterized by XRD, FTIR, FESEM, EDX, XPS, TGA, PL, and UV-VIS analytical techniques and were used as adsorbents and photocatalysts for removal of PVC and PS plastics from aqueous solutions. The aqueous solutions PVC and PS encapsulated with fluorescent PTE dye were prepared by using nanoprecipitation method and characterized by FTIR, DLS, FESEM, Fluorescent microscopy, UV-visible spectroscopy. It was found that addition of GO and CCAC to N-TiO_2 improved the adsorption and photocatalytic activity for PVC-NPs removal, and among all the nanocomposites GT13 and CT13 composite yielded a remarkable degradation efficiency after 180 minutes of exposure under tungsten light. The major photodegradation by-products were identified using gas chromatography-mass

spectrometry (GC-MS) and after the reaction the left-over nanoparticles and nanocomposite materials were further characterized which confirmed the presence of PVC and PS nanoparticles on surface ultimately confirmed the removal of PVC and PS nanoparticles from water. Furthermore, polyethylene (PE)- and polyvinylchloride (PVC)-based nanocomposites such as PE/GO, PE/N-TiO_2, PE/GO/N-TiO_2, PVC/GO, PVC/N-TiO_2 and PVC/GO/N-TiO_2 were synthesized using graphene oxide (GO) and N-TiO_2. The synthesized nanocomposites were characterized by XRD, FTIR, FESEM, EDX, TGA, PL, and UV-VIS analytical techniques and used for the adsorptive removal and photocatalytic degradation of organic cationic dyes methylene blue (MB), and rhodamine B (RB). PE/GO, PE/GO/N-TiO_2, PVC/GO, and PVC/GO/N-TiO_2 exhibited excellent results for removal of MB and RB dyes. The proposed research work achieved good removal response of synthesized materials for removal of aforementioned toxic pollutants. This study sheds light on the use of various materials for water purification, providing a long-term solution to pollution.

ACKNOWLEDGEMENTS

I begin by expressing my heartfelt gratitude to Almighty for bestowing his blessings upon my research endeavors, enabling the successful completion of this academic journey. Special appreciation is extended to my esteemed research supervisor, Dr. Harpreet Kaur, Department of Chemistry, Lovely Professional University, Punjab. Her invaluable guidance, unwavering support, and patience played a pivotal role in the successful culmination of my Ph.D. research. I am deeply indebted to her for sharing his immense knowledge and vast experience, which greatly inspired my academic pursuits.

I would also like to express my sincere gratitude to Dr. Kailash Chandra Juglan, Head of School of Chemical Engineering and Physical Sciences and Dr. Harmanjit Singh Dosanjh, Head of the Department of Chemistry, for the supportive academic environment he fosters within the department, which was instrumental in my research endeavors. I extend my thanks to the Centre Instrumentation Facility of Lovely Professional University for helping in characterization of samples. A special acknowledgment goes to the administrative staff at Lovely Professional University for their punctual and outstanding services, which significantly contributed to the success of my research.

My love and gratitude to my parents, Mr. Harjinder Singh and Mrs. Nirmaljit Kaur, for their prayers, caring and sacrifices for educating and preparing me for my future. I am very thankful to my sister Ms. Ramandeep Kaur, her family and my brother Mr. Gursharan Singh and my partner Mr. Manavjot Singh for their love, understanding, prayers and continuing support to complete this research work. Without their tremendous understanding, sacrifices, and encouragement in the past few years, it would not have been possible to complete my research work.

(Ms. Kuljit Kaur)

Research Scholar

TABLE OF CONTENT

DECLARATION I

CERTIFICATE II

ABSTRACT III

ACKNOWLEGDEMENTS V

TABLE OF CONTENT VI

LIST OF FIGURES XV

LIST OF SCHEMES XXII

LIST OF TABLES XXIII

LIST OF APPENDICS XXV

ABBREVIATIONS XXVI

NOTATIONS XXVIII

CHAPTER 1 INTRODUCTION 1

CHAPTER 2 LITERATURE REVIEW 7

2.1 Plastic Removal Techniques 7

2.1.1 Adsorption 8

2.1.2 Photocatalysis 10

2.2 Modified Metal Oxides with Doped metals/non-metals/ions 16

2.3 Photocatalytic degradation of plastics 21

2.4 Carbon Material based Metal Oxides Nanocomposites for Photocatalytic Degradation 21

2.5 Photocatalytic Degradation Mechanism of Doped-Metal Oxides 23

2.6 Recycling of Plastics 24

2.7 Research Gap 26

2.8 Objectives of the Research work 27

CHAPTER 3 MATERIALS AND METHODS 28

3.1 Chemicals 28

3.2 Material Synthesis 28

3.2.1 Synthesis of Graphene Oxide (GO) 29

3.2.2 Synthesis of Corncob Activated Carbon (CCAC) 30

3.2.3 Synthesis of N-TiO_2 Nanoparticles 30

3.2.4 Synthesis of Graphene oxide/Nitrogen-doped TiO_2 Nanocomposite 31

3.2.5 Synthesis of Corncob Activated Carbon-based Metal Oxide nanocomposites 31

3.2.6 Synthesis of N-SnO_2 Nanoparticles 32

3.2.7 Synthesis of N-ZrO_2 Nanoparticles 33

3.2.8 Synthesis of PTE Dye 33

3.2.9 Preparation of Fluorescent Polyvinyl chloride and Polystyrene Solution 34

3.2.10 Photocatalytic and Adsorption Experiment 35

3.2.11 Quenching Test 35

3.2.12 Synthesis of PE/GO, PE/N-TiO_2 and PE/GO/N-TiO_2 Nanocomposites 35

3.2.13 Synthesis of PVC/GO, PVC/N-TiO_2 and PVC/GO/N-TiO_2 Nanocomposite 36

3.2.14 Removal Experiment 37

3.3 Material Characterization 37

CHAPTER 4 RESULTS AND DISCUSSION 39

4.1 GRAPHENE OXIDE/NITROGEN-DOPED TiO_2 NANOCOMPOSITES FOR REMOVAL OF POLYVINYL CHLORIDE (PVC) AND POLYSTYRENE (PS) FROM WATER 39

4.1.1 Characterization of Graphene oxide/N-TiO_2 (GT13, GT11 and GT31) Composites 39

4.1.1.1 X-ray Diffraction Analysis 39

4.1.1.2 Functional group Analysis 40

4.1.1.3 Scanning Electron Microscopy and Energy-Dispersive X-ray Spectroscopy Analysis 42

4.1.1.4 Optical Bandgap Analysis 45

4.1.1.5 Thermogravimetric Analysis 46

4.1.1.6 Photoluminescence Analysis 47

4.1.1.7 X-Ray Photoelectron Spectroscopy Analysis 48

4.1.2 Characterization of Perylene-3,4,9,10-tetracarboxytetrabutylester, Polyvinylchloride Nanoparticles (PVC-NPs) and Polystyrene Nanoparticles (PS-NPs) 52

4.1.2.1 Nuclear Magnetic Resonance Analysis of PTE 52

4.1.2.2 Optical Analysis of PVC-NPs 52

4.1.2.3 Scanning Electron Microscopy and Energy-Dispersive X-ray Spectroscopy Analysis of PVC-NPs 52

4.1.2.4 Dynamic Light Scattering Analysis of PVC-NPs 53

4.1.2.5 Functional group Analysis of PVC-NPs 54

4.1.2.6 Field Emission Scanning Electron Microscopy Analysis of PS-NPs 55

4.1.2.7 Energy Dispersive X-ray Analysis of PS-NPs 55

4.1.2.8 Dynamic light scattering Analysis of PS-NPs *56*

4.1.2.9 Functional group Analysis of PS-NPs 56

4.1.3 Photocatalytic Degradation and Adsorption Study of GO/N-TiO_2 Composites under different Conditions 57

4.1.3.1 Removal Study of PVC-NPs using GO/N-TiO_2 Nanocomposites 57

4.1.3.2 Effect of pH on the Removal of PVC-NPs 58

4.1.3.3 Effect of Light Intensity on the Removal of PVC-NPs 60

4.1.3.4 Effect of Scavengers 61

4.1.3.5 Effect of Time on the Removal of PVC-NPs 62

4.1.3.6 Effect of Catalyst dose on the Removal of PVC-NPs 63

4.1.3.7 Analysis of GT13 Composite and PVC Solution after Removal Experiment *64*

4.1.3.8 Mechanism of Removal of PVC-NPs 68

4.1.4 Removal study of PS-NPs using N-TiO_2 and GO/N-TiO_2 Composites 71

4.1.4.1 Effect of pH on the Removal of PS-NPs 72

4.1.4.2 Effect of Time on the Removal of PS-NPs 73

4.1.4.3 Analysis of N-TiO_2 after Removal of PS-NPs 74

4.2 CORN COB ACTIVATED CARBON (CCAC)/NITROGEN-DOPED TiO_2 NANOCOMPOSITES FOR REMOVAL OF POLYVINYL CHLORIDE (PVC) AND POLYSTYRENE (PS) FROM WATER 77

4.2.1 Characterization of CCAC/N-TiO_2 (CT13, CT11 and CT31) composites 77

4.2.1.1 Scanning Electron Microscopy and Energy-Dispersive X-ray Spectroscopy Analysis 77

4.2.1.2 Functional group Analysis 81

4.2.1.3 X-ray Diffraction Analysis 83

4.2.1.4 Optical Bandgap Analysis 85

4.2.1.5 Photoluminescence Analysis 86

4.2.1.6 Thermogravimetric Analysis 88

4.2.1.7 X-Ray Photoelectron Spectroscopy Analysis 90

4.2.2 Removal of PVC-NPs by using Synthesized Composites under different Conditions 92

4.2.2.1 Effect of pH on the Removal of PVC-NPs 94

4.2.2.2 Effect of Light Source on the Removal of PVC-NPs 94

4.2.2.3 Effect of Scavengers 95

4.2.2.4 Effect of Time on the Removal of PVC-NPs 96

4.2.2.5 Analysis of Composite Material and PVC-NP Solution after Removal Experiment 98

4.2.2.6 Mechanism of Removal of PVC-NPs 103

4.2.3 Removal Study of PS-NPs using CCAC/N-TiO_2 Nanocomposites 106

4.2.3.1 Effect of pH on the Removal of PS-NPs 106

4.2.3.2 Effect of Time on the Removal of PS-NPs 107

4.3 NITROGEN-DOPED SnO_2 AND GO/N-SnO_2 NANOCOMPOSITES FOR REMOVAL OF POLYVINYL CHLORIDE (PVC) AND POLYSTYRENE (PS) FROM WATER 109

4.3.1 Characterization of N-SnO_2, N-ZrO_2 and GO/N-SnO_2 109

4.3.1.1 Scanning Electron Microscope Analysis of Nanocomposite 109

4.3.1.2 Energy-Dispersive X-ray Spectroscopy Analysis 110

4.3.1.3 Functional group Analysis 111

4.3.1.4 X-ray Diffraction Analysis 112

4.3.1.5 Optical Bandgap Analysis 113

4.3.1.6 Photoluminescence Analysis 114

4.3.1.7 Thermogravimetric Analysis 114

4.3.2 Removal of PVC-NPs by using Synthesized Materials under different Conditions 115

4.3.2.1 Effect of pH on the Removal of PVC-NPs 116

4.3.2.2 Effect of Time on the Removal of PVC-NPs 117

4.3.2.3 Analysis of N-SnO_2 after PVC-NPs Removal Experiment 118

4.3.3 Removal Study of PS-NPs using Synthesized Materials under different Conditions 120

4.3.3.1 Effect of pH on the Removal of PS-NPs 121

4.3.3.2 Effect of Time on the Removal of PS-NPs 122

4.3.3.3 Analysis of N-SnO_2 after PS-NPs Removal Experiment 123

4.4 NITROGEN-DOPED ZrO_2 NANOPARTICLES FOR REMOVAL OF POLYVINYL CHLORIDE (PVC) AND POLYSTYRENE (PS) FROM WATER 126

4.4.1 Characterization of N-ZrO_2 126

4.4.1.1 Scanning Electron Microscope Analysis 126

4.4.1.2 Energy-Dispersive X-ray Spectroscopy Analysis 126

4.4.1.3 Functional group Analysis 127

4.4.1.4 X-ray diffraction Analysis 128

4.4.1.5 Optical Bandgap Analysis 128

4.4.1.6 Photoluminescence Analysis 129

4.4.1.7 Thermogravimetric Analysis 130

4.4.2 Removal Study of PVC-NPs using Synthesized Materials under different conditions 130

4.4.2.1 Effect of pH on the Removal of PVC-NPs 131

4.4.2.2 Effect of Time on the Removal of PVC-NPs 132

4.4.2.3 Analysis of N-ZrO_2 and PVC Solution after Removal Experiment 132

4.4.3 Removal study of PS-NPs using Synthesized Materials under different 134

Conditions
4.4.3.1 Effect of pH on the Removal of PS-NPs 134
4.4.3.2 Effect of Time on the Removal of PS-NPs 135
4.4.3.3 Analysis of N-ZrO_2 and PS Solution after Removal Experiment 136
4.5 POLYETHYLENE BASED NANOCOMPOSITES FOR REMOVAL OF METHYLENE BLUE AND RHODAMINE B FROM WATER 139
4.5.1 Characterization of PE/GO (PEGO), PE/N-TiO_2 (PENT) and PE/GO/N-TiO_2 (PEGNT) 139
4.5.1.1 X-Ray diffraction Analysis 139
4.5.1.2 Functional group Analysis 140
4.5.1.3 Scanning Electron Microscope Analysis 141
4.5.1.4 Energy Dispersive X-ray Spectroscopy analysis 142
4.5.1.5 Brunauer-Emmett-Teller Analysis 144
4.5.1.6 Thermogravimetric Analysis 144
4.5.1.7 Photoluminescence Analysis 145
4.5.1.8 Optical Bandgap Analysis 146
4.5.2 Removal study of MB using Synthesized materials under different Conditions 147
4.5.2.1 Effect of pH on the Removal of MB 148
4.5.2.2 Effect of Time on the Removal of MB 149
4.5.2.3 Effect of Scavengers 151
4.5.2.4 Analysis of PE-based Nanocomposite after Removal of MB 151
4.5.3 Removal study of RB using Synthesized Materials under different Conditions 152

4.5.3.1 Effect of pH on the Removal of RB 153

4.5.3.2 Effect of Time on the Removal of RB 155

4.5.3.3 Effect of Scavengers 156

4.5.3.4 Analysis of PE-based Nanocomposite after Removal of RB 156

4.5.3.5 Mechanism of MB and RB Removal using synthesized PE-based nanocomposite 157

4.6 POLYVINYL CHLORIDE BASED NANOCOMPOSITES FOR REMOVAL OF METHYLENE BLUE AND RHODAMINE B FROM WATER 160

4.6.1 Characterization of PVC/GO (PVG), PVC/ N-TiO_2 (PVNT) and PVC/GO/N-TiO_2 (PVGNT) 160

4.6.1.1 X-Ray diffraction Analysis 160

4.6.1.2 Functional group Analysis 161

4.6.1.3 Scanning Electron Microscope Analysis 162

4.6.1.4 Energy-Dispersive X-ray Spectroscopy Analysis 163

4.6.1.5 Thermogravimetric Analysis 165

4.6.1.6 Photoluminescence Analysis 167

4.6.1.7 Optical Bandgap Analysis 167

4.6.2 Removal study of MB using Synthesized Materials under different Conditions 168

4.6.2.1 Effect of pH on the Removal of MB 169

4.6.2.2 Effect of time on the Removal of MB 170

4.6.2.3 Effect of Scavengers 172

4.6.2.4 Analysis of PVC-based Nanocomposite after Removal of MB 172

4.6.3 Removal Study of RB using Synthesized Materials under different 173

Conditions

4.6.3.1 Effect of pH on the Removal of RB 174

4.6.3.2 Effect of Time on the Removal of RB 176

4.6.3.3 Effect of Scavengers 177

4.6.3.4 Analysis of PVC-based Nanocomposite after Removal of RB 177

4.6.3.5 Mechanism of MB and RB Removal using Synthesized PVC-based Nanocomposite 178

CHAPTER 5 CONCLUSION AND FUTURE PERSPECTIVE 179

5.1 Summary and Conclusion 179

5.2 Future perspectives 181

BIBLIOGRAPHY 183

LIST OF FIGURES

Figure No.	Figure Title	Page
1.1	Various techniques used in the characterization of nanomaterials	5
3.1	Schematic representation of the synthesized nitrogen doped metal oxides and the corresponding nanocomposites for objective 1	28
3.2	Schematic representation of the synthesized plastic-based nanocomposites for objective 3	29
3.3	Schematic representation of the synthesis of graphene oxide (GO)	30
3.4	Schematic representation of the synthesis of corncob activated carbon (CCAC)	30
3.5	Schematic representation of the synthesis of N-TiO_2 nanoparticles	31
3.6	Schematic representation of the synthesis of GO/N-TiO_2 nanocomposites	31
3.7	Schematic representation of the synthesis of CCAC/N-TiO_2 nanocomposites	32
3.8	Schematic representation of the synthesis of N-SnO_2	32
3.9	Schematic representation of the synthesis of N-SnO_2	33
3.10	Schematic representation of the synthesis of PTE dye	34
3.11	Schematic representation of the preparation of PVC-NPs and PS-NPs	34
3.12	Schematic representation of the synthesis of PE/GO, PE/N-TiO_2 and PE/GO/N-TiO_2	36
3.13	Schematic representation of the synthesis of PVC/GO, PVC/N-TiO_2 and PVC/GO/N-TiO_2	37
4.1	XRD analysis of GO, N-TiO_2, GT13, GT11, GT31	40
4.2	FTIR spectra of GO, N-TiO_2, GT13, GT11, and GT31	41
4.3	Scanning electron microscope (SEM) images of (a) GO (b) N-TiO_2 (c) GT13 (d) GT11 and (e) GT31 composite	42
4.4	EDS mapping of (a) GO (b) N-TiO_2 (c) GT13 (d) GT11 and (e) GT31 composite	43
4.5	Optical bandgap of (a) GO (b) N-TiO_2 (c) GT13 (d) GT11 and (e) GT31 using Tauc's plot	46
4.6	TGA of GO, N-TiO_2, GT13, GT11, and GT31 composites	47
4.7	Photoluminescence emission spectra of N-TiO_2, GT13, GT11 and GT31	48
4.8	(a) Fully scanned XPS of GT13, GT11 and GT31; XPS spectra of Ti 2p states for (b) GT13, (c) GT11 and (d) GT31; O 1s states for (e) GT13, (f) GT11 and (g) GT31; C 1s states for (h) GT13, (i)	49

	GT11 and (j) GT31; N 1s states for (k) GT13, (l) GT11 and (m) GT31.	
4.9	(a) Absorption (b) emission spectra of PVC-NPs nanoparticles dispersed in water	52
4.10	(a) SEM images depicting morphology of PVC-NPs and the inset represents the size distribution curve of PVC-NPs obtained from SEM image at scale bar 100nm; (b) EDS mapping and elemental atomic% and weight% of PVC-NPs	53
4.11	FTIR spectra of (a) PTE and (b) PVC-NPs	54
4.12	(a) SEM images depicting morphology of PS-NPs and the inset represents the size distribution curve of PS-NPs obtained from SEM image at scale bar 100nm; (b) EDS mapping and elemental atomic% and weight% of PS-NPs	55
4.13	FTIR spectra of PTE and PS-NPs	56
4.14	Comparison of % removal PVC-NPs with GT13, GT11, and GT31 under (a) tungsten bulb (b) room light (c) without light (d) comparison of % removal PVC particles under tungsten bulb light using GT13+quenchers isopropyl alcohol, sodium oxalate, and parabenzoquinone	61
4.15	(a) Absorbance spectra of removal of PVC-NPs in the time interval of 30-180 minutes with 0.08 g of GT13. The inset shows the image of removal of PVC-NPs from water in the time interval of 30-180 minutes; Removal of PVC-NPs from water treated by GT13, GT11 and GT31 photocatalysts at pH 4, 7, and 10 in time interval of 30-180 minutes under (b) tungsten bulb light, (c) room light (d) dark	62
4.16	Degradation results of PVC-NPs treated with addition of different amounts of GT13 composite under TL at pH 4	64
4.17	SEM, EDS and elemental mapping images of GT13 after reaction (a) with light (b) without light	65
4.18	Optical micrographs of (a) PVC-NPs solution (b) GT13 composite after the remediation with light (c) GT13 composite after the remediation without light showing the PVC nanoparticles dyed with PTE dye	66
4.19	FTIR spectra of (a) PVC-NPs solution before and after the remediation (b) GT13 composite before and after photocatalytic activity under tungsten bulb light	68
4.20	Comparison of % removal PS-NPs with N-TiO_2, GT13, GT11, and GT31 at pH 4, pH 7 and pH 10 under (a) tungsten bulb light (b) dark	73

4.21	(a) UV absorption spectra of PS-NP removal with N-TiO_2 at pH4 (b) real-life image of PS-NP solution in the time interval of 30–180min at pH 4; PS-NP removal from water treated with N-TiO_2, GT13, GT11, and GT31 over a 30- to 180-minute time period under (c) tungsten bulb light at pH 4 (d) tungsten bulb light at pH 7 (e) tungsten bulb light at pH 10 (f) dark at pH 4 (g) dark at pH 7, and (h) dark at pH 10	73
4.22	Real-life image of N-TiO_2 before and after reaction showing adsorbed PS-NPs after the reaction at pH 4, pH 7 and pH 10	75
4.23	SEM, EDS and elemental mapping of N-TiO_2 after PS-NPs removal under dark at pH 4	75
4.24	FTIR spectra of bare PS-NPs and N-TiO_2 before and after reaction with and without light at pH 4	76
4.25	Scanning electron microscope (SEM) images including pore size and particles size of (a) $ZnCl_2$-impregnated corncob activated carbon (CCAC) (b) CT13 (c) CT11 and (d) CT31 composites	78
4.26	EDS mapping of (a) CCAC (b) CT13 (c) CT11 and (d) CT31 composite	80
4.27	FTIR spectra of N-TiO_2, CCAC, CT13, CT11, and CT31	83
4.28	XRD analysis of N-TiO_2, CCAC, CT13, CT11, and CT31	84
4.29	Optical bandgap of (a) N-TiO_2 (b) CT13 (c) CT11 and (d) CT31	85
4.30	Photoluminescence emission spectra of N-TiO_2, CT13, CT11 and CT31	87
4.31	TGA of CT13, CT11, and CT31 composites. Inset TGA of bare N-TiO_2 and CCAC	89
4.32	(a) Fully scanned XPS of CT13, CT11 and CT31; Ti 2p states the composites (b) CT13, (c) CT11 and (d) CT31; O 1s states the composites (e) CT13, (f) CT11 and (g) CT31; C 1s states the composites (h) CT13, (i) CT11 and (j) CT31; N 1s states the composites (a) CT13, (b) CT11 and (c) CT31	91
4.33	Comparison of % removal PVC-NPs with CCAV, N-TiO_2, CT13, CT11, and CT31 under (a) without light (b) room light (c) tungsten bulb light (d) comparison of % removal PVC-NPs under tungsten bulb light using CT13 +quenchers isopropyl alcohol, sodium oxalate, and parabenzoquinone at pH 4	96
4.34	(a) UV absorption spectra of PVC-NP removal with CT13 at pH4 (b) real-life image of PVC-NP solution in the time interval of 30–180min at pH 4; PVC-NP removal from water treated with CCAC, N-TiO_2, CT13, CT11, and CT31 over a 30- to 180-minute time period under (c) dark at pH 4 (d) dark at pH 7 (e) dark at pH 10 (f) room light at pH 4 (g) room light at pH 7 (h) room light at pH 10	97

	(i) tungsten bulb light at pH 4 (j) tungsten bulb light at pH 7, and (k) tungsten bulb light at pH 10.	
4.35	Real-life image of CT13 composite before and after reaction showing PVC-NPs adsorbed on composite at pH 4, pH 7 and pH 10, and PVC-NPs solution before and after reaction	98
4.36	SEM, EDS and elemental mapping images after reaction using (a) CT13 with light (b) CT13 without light (c) N-TiO_2 with light	99
4.37	Optical micrographs of (a) PVC-NPs; CT13 after the remediation experiment (b) with light (c) without light; CT11 composite after the remediation experiment (d) with light (e) without light	100
4.38	FTIR spectra of (a) CT13 and CT11 before and after reaction with and without light (b) pure PVC-NPs solution and PVC solution after the remediation experiment (c) N-TiO_2 before and after reaction with and without light	101
4.39	Comparison of % removal PS-NPs at pH 4, pH 7 and pH 10 with CCAC, CT13, CT11, and CT31 under (a) tungsten bulb light (b) dark	107
4.40	PS-NPs removal from water treated with CCAC, N-TiO_2, CT13, CT11, and CT31 over a 30- to 180-minute time period under (a) tungsten bulb light at pH 4 (b) tungsten bulb light at pH 7 (c) tungsten bulb light at pH 10 (d) dark at pH 4 (e) dark at pH 7, and (f) dark at pH 10	108
4.41	Scanning electron microscope (SEM) images of (a) N-SnO_2 and (b) GNSO13 composite	109
4.42	EDS mapping of (a) N-SnO_2 (b) GNSO13 composite	110
4.43	FTIR spectra of GO, N-SnO_2, GNSO13, GNSO11, and GNSO31	112
4.44	XRD of N-SnO_2, GO, GNSO13, GNSO11, and GNSO31	113
4.45	Optical bandgap of (a) SnO_2, (b) N-SnO_2, (c) GNSO13 (d) GNSO11, and (e) GNSO31	113
4.46	Photoluminescence emission spectrum of SnO_2 and N-SnO_2	114
4.47	TGA of GO, SnO_2, N-SnO_2, and GNSO13	115
4.48	Comparison of % removal PVC-NPs at pH 4, pH 7 and pH 10 with N-SnO_2, GNSO13, GNSO11, and GNSO31 under (a) tungsten bulb light (b) room light (c) dark	117
4.49	(a) UV absorption spectra of PVC-NP removal with N-SnO_2 at pH4; PVC-NP removal from water treated with N-SnO_2, GNSO13, GNSO11, and GNSO31 over a 30- to 180-minute time interval at pH 4, pH7, and pH 10under (b) tungsten bulb light (c) room light (d) dark	118
4.50	Real-life image of N-SnO_2 before and after reaction showing PVC-NPs adsorbed on N-SnO_2 at pH 4, pH 7 and pH 10	119

4.51	SEM, EDS and elemental mapping images after reaction with PVC-NPs using N-SnO_2 with light	119
4.52	FTIR spectra of (a) N-SnO_2 composite before and after removal of PVC-NPs under tungsten bulb light, room light and dark (b) pure PVC-NPs solution and PVC solution after the remediation under tungsten bulb light, room light and dark	120
4.53	Comparison of % removal PS-NPs at pH 4, pH 7 and pH 10 with N-SnO_2, GNSO13, GNSO11, and GNSO31 under tungsten bulb light, room light, and dark	122
4.54	(a) UV absorption spectra of PS-NP removal with N-SnO_2 at pH4; PVC-NP removal from water treated with N-SnO_2, GNSO13, GNSO11, and GNSO31 over a 30- to 180-minute time interval at pH 4, pH7, and pH 10 under (b) tungsten bulb light (c) room light (d) dark	122
4.55	Real-life image of N-SnO_2 before and after reaction showing PS-NPs adsorbed on N-SnO_2 at pH 4, pH 7 and pH 10	123
4.56	SEM, EDS and elemental mapping images after reaction with PS-NPs using N-SnO_2 under dark at pH4.	124
4.57	FTIR spectra of N-SnO_2 before and after removal of PS-NPs	125
4.58	Scanning electron microscope (SEM) images of N-ZrO_2	126
4.59	EDS mapping of N-ZrO_2	127
4.60	FTIR spectra of N-ZrO_2	128
4.61	XRD of ZrO_2 and N-ZrO_2	128
4.62	Optical bandgap of ZrO_2 and N-ZrO_2	129
4.63	Photoluminescence emission spectra of ZrO_2 and N-ZrO_2	129
4.64	TGA of ZrO_2 and N-ZrO_2	130
4.65	% Removal PVC-NPs with N-ZrO_2, under tungsten bulb light, room light, and dark at pH 4, pH 7 and, pH 10	131
4.66	(a) UV absorption spectra of PVC-NP removal with N-ZrO_2 at pH4; PVC-NP removal from water treated with N-ZrO_2 over a 30- to 180-minute time period under (b) dark at pH 4, pH 7, and pH 10 (c) room light at pH 4, pH 7, and pH 10 (d) tungsten bulb light at pH 4, pH 7, and pH 10	132
4.67	SEM, EDS and elemental mapping images after reaction with PVC-NPs using N-ZrO_2 with light	133
4.68	FTIR spectra of N-ZrO_2 before and after reaction with PVC-NPs	134
4.69	% Removal PVC-NPs with N-ZrO_2, under tungsten bulb light, room light, and dark at pH 4, pH 7 and, pH 10	135
4.70	(a) UV absorption spectra of PS-NP removal with N-ZrO_2 at pH4; PS-NP removal from water treated with N-ZrO_2 over a 30- to 180-minute time period under (b) dark at pH 4, pH 7, and pH 10 (c)	135

	room light at pH 4, pH 7, and pH 10 (d) tungsten bulb light at pH 4, pH 7, and pH 10	
4.71	SEM, EDS and elemental mapping images after reaction with PS-NPs using N-ZrO_2 with light	136
4.72	FTIR spectra of N-ZrO_2 before and after reaction with PS-NPs	137
4.73	X-ray diffraction pattern of GO, LDPE, PEGO, N-TiO_2, PENT and PEGNT	139
4.74	FTIR spectra of GO, LDPE, PEGO, N-TiO_2, PENT and PEGNT	141
4.75	FESEM images of (a) PEGO (b) PENT and (c) PEGNT	142
4.76	EDS mapping of (a) PVGO (b) PVNT (c) PVGNT	143
4.77	TGA of GO, PE, PEGO, N-TiO_2, PENT, and PEGNT	145
4.78	Photoluminescence emission spectra of N-TiO_2, PEGO, PENT, and PEGNT	146
4.79	Comparison of % removal MB with PEGO, PENT, and PEGNT under (a) tungsten bulb light (b) dark; comparison of % removal MB under tungsten bulb light at pH 4 using (c) PEGO + quenchers isopropyl alcohol, sodium oxalate, and parabenzoquinone (d) PEGNT + quenchers isopropyl alcohol, sodium oxalate, and parabenzoquinone.	149
4.80	(a) UV absorption spectra of MB removal with PEGNT at pH 10 (b) real-life image of MB solution in the time interval of 30–180min at pH 10; MB removal from water treated over a 30- to 180-minute time period under TL and dark with (c) PEGO (d) PENT (e) PEGNT	150
4.81	FTIR spectra of removal of MB before and after reaction (a) PEGO (b) PEGNT	152
4.82	Comparison of % removal RB with PEGO, PENT, and PEGNT under (a) tungsten bulb light (b) dark; comparison of % removal RB under tungsten bulb light at pH 4 using (c) PEGO + quenchers isopropyl alcohol, sodium oxalate, and parabenzoquinone (d) PEGNT + quenchers isopropyl alcohol, sodium oxalate, and parabenzoquinone	154
4.83	(a) UV absorption spectra of RB removal with PEGNT at pH 4 (b) real-life image of RB solution in the time interval of 30–180 min at pH 4; RB removal from water treated over a 30- to 180-minute time period under TL and dark with (c) PEGO (d) PENT (e) PEGNT	155
4.84	FTIR spectra of removal of RB before and after reaction (a) PEGO (b) PEGNT	157
4.85	X-ray diffraction pattern of PVC, GO, PVGO, N-TiO_2, PVNT and PVGNT	160

4.86	FTIR spectra of GO, PVC, PVGO, N-TiO_2, PVNT, and PVGNT	162
4.87	FESEM images of (a) PVGO, (b) PVNT, and (c) PVGNT	162
4.88	EDS mapping of (a) PVGO (b) PVNT (c) PVGT	164
4.89	TGA of GO, PVC, PVGO, N-TiO_2, PVNT, and PVGNT	166
4.90	Photoluminescence emission spectra of N-TiO_2, PVGO, PVNT, and PVGNT	167
4.91	Comparison of % removal MB with PVGO, PVNT, and PVGNT under (a) tungsten bulb light (b) dark; comparison of % removal MB under tungsten bulb light at pH 4 using (c) PVGO + quenchers isopropyl alcohol, sodium oxalate, and parabenzoquinone (d) PVGNT + quenchers isopropyl alcohol, sodium oxalate, and parabenzoquinone	170
4.92	(a) UV absorption spectra of MB removal with PVGNT at pH 10 (b) real-life image of MB solution in the time interval of 30–180 min at pH 10; MB removal from water treated over a 30 to 180-minute time period under TL and dark with (c) PVGO (d) PVNT (e) PVGNT	171
4.93	FTIR spectra of removal of MB before and after reaction with and without light with (a) PVGO (b) PVNT (c) PVGNT	172
4.94	Comparison of % removal RB with PVGO, PVNT, and PVGNT under (a) tungsten bulb light (b) dark; comparison of % removal RB under tungsten bulb light at pH 4 using (c) PVGO + quenchers isopropyl alcohol, sodium oxalate, and parabenzoquinone (d) PVGNT + quenchers isopropyl alcohol, sodium oxalate, and parabenzoquinone	175
4.95	(a) UV absorption spectra of RB removal with PVGNT at pH 4 (b) real-life image of RB solution in the time interval of 30–180min at pH 4; RB removal from water treated over a 30- to 180-minute time period under TL and dark with (c) PVGO (d) PVNT (e) PVGNT	176
4.96	FTIR spectra of removal of RB before and after reaction with and without light with (a) PVGO (b) PVNT (c) PVGNT	178

LIST OF SCHEMES

Scheme No.	Scheme Title	Page
4.1	GC–MS analysis of PVC degradation using GT13	67
4.2	Proposed mechanism of PVC degradation under visible light illumination using GT13 photocatalyst	70
4.3	GC–MS analysis of PVC degradation using CT13	103
4.4	Proposed mechanism of PVC degradation under visible light illumination using CT13 photocatalyst	106

LIST OF TABLES

Table No.	Table Title	Page
2.1	Various techniques for the removal of plastic pollutants	7
2.2	Various types of photocatalysts used to remove contaminants from water	11
2.3	Energy bandgaps and wavelengths of some traditional photocatalysts	12
2.4	Photocatalytic degradation of various pollutants using doped metal-oxide nanoparticles	18
2.5	Various doping agents and preparation methods used for TiO_2 photocatalyst	19
2.6	Metal oxide and modified metal oxides for photocatalytic degradation of various plastics	21
4.1	The average crystallite sizes of GO, N-TiO_2, GT13, GT11, and GT31	40
4.2	Content of elements in atomic% and weight % of GO, N-TiO_2, GT13, GT11 and GT31	44
4.3	Optical band gap values of GO, N-TiO_2, GT13, GT11 and GT31	45
4.4	Comparison of % weight loss of composites in three different stages and total weight loss	47
4.5	Surface elemental composition of composites GT13, GT11 and GT31	51
4.6	Comparison of % Removal with GT13, GT11 and GT31 with light and without light	60
4.7	% Removal pf PVC-NPs using various catalytic doses of GT13 under tungsten bulb light at pH 4	63
4.8	Content of elements in atomic% and weight % of CCAC, CT13, CT11 and CT31	81
4.9	The average crystallite sizes of CCAC, N-TiO_2, CT13, CT11, and CT31	85
4.10	Optical band gap values of N-TiO_2, CT13, CT11 and CT31	86
4.11	Comparison of % removal of N-TiO_2, CCAC, CT13, CT11 and CT31 with light and without light	96
4.12	Content of elements in atomic% and weight % of N-SnO_2 and GNSO13	111
4.13	Content of elements in atomic% and weight % of N-ZrO_2	127

4.14	A comparison of the efficiency of synthesized materials with other catalysts for plastic remediation	138
4.15	Content of elements in atomic% and weight % of PVGO, PVNT, and PVGNT	144
4.16	BET surface area, pore volume and pore diameter of all materials	144
4.17	Optical band gap values of GO, N-TiO_2, PEGO, PENT, and PGNT	147
4.18	Content of elements in atomic% and weight % of PVGO, PVNT, and PVGT	165
4.19	Optical band gap values of GO, N-TiO_2, PVGO, PVNT, and PVGNT	168

LIST OF APPENDICES

Appendix	Title	Page
1.	List of Publications	223
2.	List of Patents	224
3.	List of Conferences Attended	224
4.	List of Trainings attended	225

ABBREVIATIONS

XRD	:	X-ray Diffraction
FTIR	:	Fourier-Transform Infrared Spectroscopy
FESEM	:	Field Emission Scanning Electron Microscopy
EDX/EDS	:	Energy Dispersive X-ray
XPS	:	X-ray Photoelectron Spectroscopy
TGA	:	Thermogravimetric Analysis
PL	:	Photoluminescence
UV-VIS	:	Ultraviolet–Visible Spectroscopy
NMR	:	Nuclear Magnetic Resonance
GCMS	:	Gas Chromatography–Mass Spectrometry
BET	:	Brunauer-Emmett-Teller
DLS	:	Dynamic light scattering
PVC	:	Polyvinylchloride
PS	:	Polystyrene
PE	:	Polyethylene
GO	:	Graphene oxide
RGO	:	Reduced graphene oxide
AC	:	Activated carbon
CCAC	:	Corncob activated carbon
N	:	Nitrogen
MB	:	Methylene blue
RB	:	Rhodamine B
MPs	:	Microplastics
NPs	:	Nanoplastics/ nanoparticles
PET	:	Polyethylene terephthalate
LDPE	:	low-density polyethylene
UV	:	Ultraviolet
VB	:	Valance band
CB	:	Conduction band
THF	:	Tetrahydrofuran

PTE	:	Perylene-3,4,9,10-tetracarboxylic acid (Perylenetetraester)
DBU	:	1,8-Diazabicyclo (5.4.0) undec-7-ene
DMF	:	N, N-dimethylformamide
PDI	:	Polydispersity index
PZC	:	Point zero charge

NOTATIONS

V	:	Volt
eV	:	Electronvolt
mL	:	Milliliter
M	:	Molar
W	:	Watt
mM	:	Millimolar
nm	:	Nanometer
cm	:	Centimetre
°C	:	degree Celsius
MHz	:	Megahertz
ppm	:	parts per million
mg	:	Milligram
θ	:	Bragg angle
Min	:	Minute
mV	:	Millivolt

Chapter - 1 Introduction

Plastics have emerged as the industry's preferred material because of its numerous appealing qualities, including their extensive use in all aspects of our life. The consumption of plastic has grown rapidly by around 180 times between 1950 and 2018. In 2022, the global plastic production reached 400.3 million tons [*Pilapitiya et al., 2024*]. Widespread use and increased manufacturing of plastics led to major waste generation and disposal challenges. Plastic garbage is either landfilled (79%), burned (12%), or discarded in the environment, with barely 9% of used plastics being recycled, showing plastic trash recycling was a massive failure. There is now a significant amount of plastic in the environment because of improper disposal and the slow decomposition of plastic garbage. [*Kumar et al., 2021*]. Numerous habitats, including freshwater lakes, rivers, marine habitats, and rural areas, have been found to be contaminated by plastics. Under environmental conditions, these plastic waste materials slowly degrade from macro- and mesoplastics (> 5 mm) [*Mariano et al., 2021*], releasing smaller particles known as micro- (< 5 mm) or nanoplastics (<1 μm or <100 nm) particles. Tiny plastic particles are ingested by a wide range of marine organisms, such as plankton, fish, and even humans [*Kumar et al., 2025*]. Smaller plastic particles are more hazardous than bigger macroparticles and can go from the digestive tract to other parts of the body of the organisms [*Kurniawan et al., 2021*]. Furthermore, the hydrophilicity, rough surface morphologies, negatively charged surface characteristics, and many functional groups of various MPs/NPs facilitate the adsorption of harmful pollutants such as polychlorinated biphenyls (PCBs), heavy metals, and polycyclic aromatic hydrocarbons (PAHs) [*Pal et al., 2025*]. Therefore, plastic waste has become a major global pollution issue that has gained global attention.

Several physical, chemical, and biological techniques have been developed to remove microplastics and nanoplastics from water, including coagulation, flocculation [*Zhang et al., 2021, Zhou et al., 2021*], membrane technology, filtration [*Ma et al., 2019, Talvitie et al., 2017*], ozonation [*Zafar et al., 2021]*, chlorination [*Li et al., 2022*], hydrolysis [*Sarno et al., 2021*], Adsorption on Green Microalgae [*Lagarde et al., 2016]*, magnetic removal [*Wang et al., 2021*], chemical oxidation [*Miao et al., 2020, Nabi et al., 2020*], advanced membrane bioreactor [*Lares et al., 2018*], biodegradation [*Muhonja et al., 2018, Peng et al., 2021*], biological ingestion [*Arossa et al., 2019*], and

microorganism aggregation [*Begum et al., 2025*]. However, every technique has its own set of drawbacks and limitations, such as energy requirements, efficiency, applicability constraints to specific types of micro-/nanoplastics, and environmental impact [*Puteri et al., 2025*].

Lately, photocatalytic technology has become a potential solution for environmental issues because of its high rate of pollutant degradation including plastic pollution. It is user-friendly and affordable method and becoming more popular because of its sustainability and low environmental impact [*Shi et al., 2021, Lee et al., 2021*, *Wu et al., 2025*]. Using nanomaterials as a photocatalyst in heterogeneous photocatalysis is a promising advanced oxidation method (AOP) for treatment of toxic wastewater and non-biodegradable organics [*Bethi et al., 2016*].

Semiconductor nanoparticles including metal oxides, ceramics, and composites are best suitable for photocatalytic application due to their high surface area, unique electronic structures, and ability to enhance charge separation and transport, leading to higher efficiency in light-activated chemical reactions [*Malik et al., 2023*, *Yaqoob et al., 2020*, *Mazari et al., 2021*, Babuji *et al., 2023*]. Metal oxide such as TiO_2, ZnO, CuO, WO_3, CeO_2, AgO, ZrO_2, and SnO_2 nanoparticles have received a lot of attention over the last two decades because of their improved physical and chemical properties at the nanoscale, which has led to applications in sensors, catalysis, and environmental remediation [*Pascariu et al., 2023, Pattnaik et al., 2023*].

The use of metal oxides for photocatalysis is limited as due to their wide band gap they show absorption in UV region, but in recent years, researchers have focused on increasing the light absorption of metal oxides under visible light. This is achieved through various strategies such as metallic or non-metallic doping, and loading with co-catalysts such as noble metal particles or dye molecules [*Pérez-Molina et al., 2020, Chiesa et al., 2020*]. Nonmetal elements such as N, F, S, B, C, and P doped metal oxides have been extensively researched for their visible-light photocatalytic properties. Nitrogen doping is the most effective and extensively studied because oxygen and nitrogen have similar chemical, structural, and electrical properties such as polarizability, electronegativity, coordination numbers, and ionic radii. When other elements, such as N 2p, with atomic orbitals with higher potential energy than O 2p

atomic orbitals are introduced, a new valance band (VB) can form instead of O 2p atomic orbitals, resulting in a smaller band gap without affecting the conduction band (CB) level, resulting in a visible-light-driven photocatalyst with band edge potentials suitable for the water splitting reaction [*Wang et al., 2018*].

Recently, enhancements of the photocatalytic activity of metal oxides by visible light have been also demonstrated by the modification of metal oxides with carbonaceous substances such as fullerenes, carbon nanotubes, and graphene to form carbon-metal oxide composites, [*Giovannetti et al., 2017*] that aid in the degradation of organic pollutants like polycyclic aromatic hydrocarbons, dyes, pesticides, and drugs [*Ansari et al., 2025*]. Graphene is an exceptional material with a two-dimensional carbon sheet structure and its derivatives, such as graphene oxide (GO) and reduced graphene oxide (rGO), can improve photocatalytic efficiency by creating a synergistic effect with metal oxides. The delocalized conjugated system of π- bonds in graphene materials can accept photogenerated electrons, preventing electron-hole recombination. Oxygenated functionalities on GO (and to a lesser extent on rGO) may provide reactive sites for semiconductor and graphene construction [*Pérez-Molina et al., 2020, Yue et al., 2024*]. Furthermore, Ginkgo leaves, rose, fallen leaves, argy wormwood, coconut shells, bamboo, banana peel, and other biomass wastes can be used to create porous carbon. Corncob waste is a relatively pure precursor when compared to other types of biomasses, so it can be used to synthesize products with low impurities and high yield. The production of bio-derived carbon compounds from diverse biomaterials with and without chemical activation has received a lot of interest [*Sandeep et al., 2024*]. Activating agents like H_3PO_4, KOH, and $ZnCl_2$ etc. are indeed used during biomass activation to increase the number of surface oxygen-containing functional groups. These agents play a crucial role in creating a porous structure and enhancing the surface chemistry of the resulting activated carbon [*Neme et al., 2020*]. However, the best activating agent ultimately depends on the specific application and desired properties of the activated carbon. Activation with an adequate proportion of $ZnCl_2$, provides a cheap, abundant, and very promising precursor material for the synthesis of activated carbon with high carbon content and good adsorption characteristics [*Suhdi et al., 2021*].

While carbonaceous materials are effective in removing some pollutants, it has limitations such as producing harmful byproducts and not fully degrading persistent pollutants. To address these shortcomings and improve pollutant removal, carbonaceous materials are being combined with metal oxide semiconductors to create nanocomposites. This combination of carbon-based metal oxide nanocomposites offers enhanced pollutant degradation through photocatalysis and adsorption, leading to efficient removal of various pollutants [*Yue et al., 2024*].

Although plastic remediation is being done exhaustively but the plastic accumulation remains a major problem, and there is a need of mitigation of waste plastic pollution [*Huang et al., 2022, Rajmohan et al., 2019*]. Reuse, recycle and energy recovery are three important reclamation strategies by which plastic waste could be converted into different products with different applications thereby increasing the lifespan of plastic. Plastic waste has been reused in catalytic support technologies that can treat toxic water, simultaneously addressing plastic pollution and water contamination. This innovative strategy turns plastic waste, a persistent pollutant, into useful resources, creating a circular economy where the materials from discarded plastics can be repurposed for water treatment, leading to more sustainable environmental systems. The immobilized catalysts enable easier recovery and reuse, reducing economic and environmental concerns and improving process scalability and efficiency [*De Assis et al., 2018, Valadez-Renteria et al., 2021, de Assis et al., 2021*].

Several methods have been used to synthesize metal oxide nanoparticles, such as sol–gel, precipitation, hydrothermal, and microemulsion techniques, as well as physical methods like ball milling and laser ablation [*Rani et al., 2024*]. Among these, the sol–gel method, a wet chemical process, is widely used because it allows better control over the size and shape of the particles. It also produces high-purity materials and works at relatively low temperatures compared to other methods [*Deshmukh et al., 2020*].

The techniques used for characterisation of nanomaterials have been summarized in **Figure 1**. Electrochemical Impedance Spectroscopy can be used to characterize nanomaterials and their synthesized composites to study their physical, chemical, morphological, and electrochemical properties [*Wang et al., 2008, Liu et al., 2014, Zhou et al., 2013*]. TEM, HRTEM, SEM, and FESEM are electron microscopy tools used to determine morphological characteristics of materials. Electron microscopes use

powerful electrons as a source and focus on electromagnetic lenses [*Bozzola et al., 1999*]. UV-vis is used to characterize the optical transparency of nanomaterials by measuring their transmittance properties [*Quevedo et al., 2021*]. XRD measures atomic arrangement, crystallinity, defects, crystallite size, and material structure among other factors [*Lee et al., 2017*]. FTIR validates the connections and functions of various materials. Thermogravimetric Analysis (TGA) is used to investigate thermal properties of nanomaterials. Cyclic voltammetry and EIS study the electrochemical or conductive properties of materials [*Adamopoulos et al., 2023*]. Raman spectroscopy serves as a non-destructive instrument. The technology assesses the quality of produced materials by analyzing structural traces and identifying compounds [*Kneipp et al., 1999*].

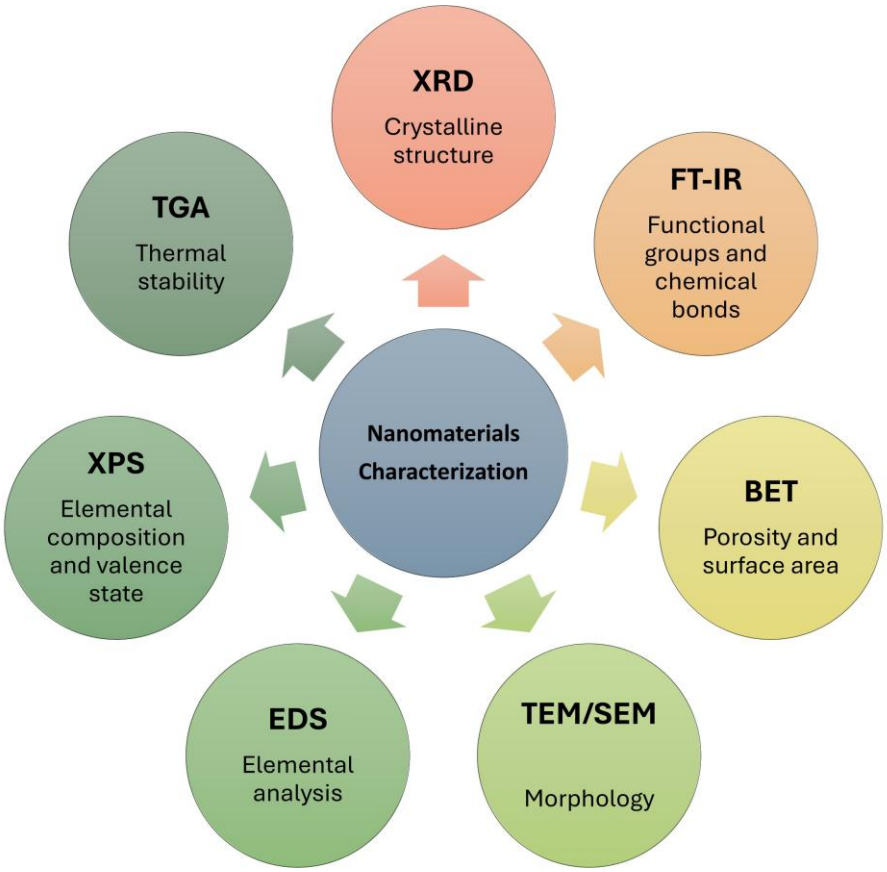


Figure 1. Various techniques used in the characterization of nanomaterials.

Based on the context, plastic contamination has posed a serious threat to the survival of aquatic ecosystems. To reduce their environmental impact, removal of plastic pollutants with metal oxide, and modified metal oxide composites are emerging as highly effective solutions and evolved as a successful photocatalytic approach. Although a lot of

research has taken place to eradicate the problem, but a systematic and cost-effective approach is required. In the current study three metal oxides, as TiO_2, SnO_2, and ZrO_2 were synthesized by the sol-gel method, followed by nitrogen doping. Graphene oxide and corncob-based activated carbon (chemically activated with $ZnCl_2$) were used to synthesize carbonaceous materials/metal oxide nanocomposites. These materials were developed to enhance their performance in removing plastics such as polyvinyl chloride (PVC) and polystyrene from water through both adsorption and photocatalytic degradation. Furthermore, waste plastics, including polyethylene (PE) and polyvinyl chloride (PVC), were recycled to fabricate nanocomposites, which were subsequently employed for the removal of organic dyes like methylene blue and rhodamine B from aqueous solutions.

The extensive use of widely produced plastics such as PE, PET, PS, PVC, and PP has created significant challenges in waste management, leading to serious environmental concerns. These durable, degradation-resistant polymers accumulate in the environment, breaking down into harmful macroplastics, microplastics, and nanoplastics and can contaminate the environment, make their way into the food chain, and endanger the health of animals and humans. Poor waste management systems, especially in low-income countries, worsen this issue, emphasizing the urgent need to reduce waste, enhance disposal methods, and create sustainable alternatives [*Schade et al., 2024, Zhi et al., 2025, Miino et al., 2024*]. To reduce the possible ecological hazards, it is critical to create technology for the removal and recycling of plastic pollution.

2.1 Plastic Removal Techniques

Different physical, chemical, and biological approaches have been designed to remove microplastics from water, and these methods are presented in **Table 2.1**.

Table 2.1 Various techniques for the removal of plastic pollutants.

Method	Type of MP/NPs	MPs/NPs Size	Efficiency (%)	References
Ultrafiltration	PE	< 5000 µm	100%	*Ma et al., 2019*
Discfilter	All type	> 20 µm	97%	*Talvitie et al., 2017*
Adsorption on Green Microalgae	PP	>400 µm	recovery rate of 94.5	*Lagarde et al., 2016*
Magnetic removal	PS	1 µm	94.8%	*Wang et al., 2021*
Coagulation	PET PS PE	<500 µm <5000 µm	91.45 77.83%, 29.70%	*Zhang et al., 2021* *Zhou et al., 2021*
Hydrolysis	Partially degraded polyester MP fibers	20–25 µm	Complete degradation	*Sarno et al., 2021*
Chemical oxidation	PVC PS	100−200 µm 400 nm	> 30% 98.4%	*Miao et al., 2020* *Nabi et al., 2020*

Advanced Membrane Bioreactor	fibers (82%) and particles (18%)	mostly < 1 mm	Usually > 98%	*Lares et al., 2018*
Chlorination	nano-sized PS	<1 μm–5 mm	7.1	*Li et al., 2022*
Ozonation	PE	Different sizes	44%	*Zafar et al., 2021*
Biodegradation	LDPE	3 cm × 3cm	35.7%, 20.4%	*Muhonja et al., 2018*
	PLA	<100 μm	90.9%	*Peng et al., 2021*
Biological Ingestion	PE	53–500 μm	66.03	*Arossa et al., 2019*

All the aforesaid methods are effective in plastic removal but there are some demerits and merits related to each method. There is a need for more appropriate and sustainable methods. In this regard, A study of Dayal *et al.* explained that adsorption and photocatalysis are promising approaches for various pollutants including plastic pollutants. Adsorption offers high removal efficiency, low cost, and reusability, while photocatalysis breaks down plastic pollutants through chemical reactions and can totally mineralize polymers and transform MPs into simple, harmless substances. Combining these techniques could offer a more effective solution, though improvements are needed in adsorbent targeting and the scalability of photocatalytic processes [*Dayal et al., 2024*].

2.1.1 Adsorption

Adsorption is often employed to remove inorganic and organic pollutants including microplastics from water and wastewater. Conventional adsorbents are often limited by surface area, selectivity, and adsorption kinetics. Nanoadsorbents are becoming a popular alternative to traditional adsorbents. Metal oxide nanoadsorbents are extensively researched due to their distinct qualities compared to bulk materials. Metal oxide nano-adsorbents offer significant improvements in adsorption due to their ultrafine size, large surface area, associated sorption sites, short intra-particle diffusion, high density of corner or edge surface sites, tunable pore size, chemical stability, and non-toxicity [*El-Sayed 2020, Heo et al., 2022*]. Adsorption removal depends on the adsorption action between MPs and adsorbents and has a comparatively high efficacy

in removing MPs and nanoplastics (NPs). The adsorption mechanism involves π-π interactions, hydrogen bonding, and electrostatic interactions [Pan et al., 2023]. Researchers used various adsorbents to remove MPs.

Yuan *et al.* found that three-dimensional reduced graphene oxide (3D RGO) effectively adsorbs polystyrene (PS) microplastics from water, achieving a maximum capacity of 617.28 mg/g. The adsorption process is primarily driven by strong π–π interactions between the graphene and PS, enhanced by electrostatic attraction and physical retention. Key factors like pH, ion concentration, adsorption time, and temperature influence the adsorption efficiency, with optimal conditions yielding high removal rates, making 3D RGO promising for microplastic removal due to its high adsorption capacity, fast kinetics, and potential for use in real-world water treatment [*Yuan et al., 2020*].

Wang *et al.* proposed efficient Mg/Zn-modified magnetic biochar adsorbents, which effectively adsorb and simultaneously thermally degrade polystyrene microspheres, even after multiple adsorption-pyrolysis cycles. Mg/Zn-modified magnetic biochars (Mg-MBC and Zn-MBC) and unmodified magnetic biochar (MBC) achieved removal efficiencies of 98.8%, 99.5%, and 94.8%, respectively, for polystyrene microspheres. Adsorption occurs through electrostatic interactions and chemical bonding between the biochar and the microplastic particles. The adsorbed MPs are degraded through a simultaneous thermal process, which also regenerates the biochar adsorbent for reuse. The catalytic active sites of Mg and zinc Zn promote MP degradation and release adsorption sites for reuse. The use of biochar and the simultaneous regeneration process make it a low-cost and eco-friendly approach for microplastic removal with retained adsorption capabilities and potential for large-scale applications [*Wang et al., 2021]*.

Wang *et al.* developed a fatigue-resistant, biodegradable plant-protein-based sponge (OPS) that rapidly adsorbs microplastics from water through hydrophobic interactions and intra-particle diffusion, demonstrating high removal efficiency and good reusability (maintaining about 60% removal after four cycles). The sponge's high porosity allows for rapid adsorption, with 38% microplastics removed in under 10 seconds. It also exhibits significant biodegradability, offering a sustainable and eco-friendly solution for microplastic pollution.

Zhu et al. synthesized a contaminated corncob-derived biochar effectively removed polystyrene nanoplastics (PSNPs) from water by adsorbing them and then degrading them through hydrothermal treatment, regenerating the biochar in the process. The adsorption had a maximum capacity of 56.02 mg/g [*Wang et al., 2021]*.

Ganie et al. found that efficiency of sugarcane bagasse-derived biochar in removing nanoplastics from water is highly dependent on its pyrolysis temperature. The study showed that the biochar pyrolyzed at 750°C achieved over 99% nanoplastic removal within 5 minutes. In contrast, biochar pyrolyzed at 550°C and 350°C showed significantly lower removal rates (<39% and <24%). This enhanced performance at high temperatures is attributed to increased surface area and pore abundance, which facilitate physical trapping within pores, alongside increased aromaticity and reduced carbonyl functional groups that enable mechanisms like pore-retention and electrostatic attraction. Conversely, biochar produced at lower temperatures show lower removal efficiency, with removal dependent on oxygen-containing functional groups and less developed pore structures [Ganie *et al., 2021]*.

Sun *et al.* have fabricated robust, compressive chitin-graphene oxide (ChGO) sponges to efficiently remove various microplastics (MPs) through electrostatic interactions, hydrogen bonding, and π-π interactions. The sponges achieved high removal efficiencies, with one study reporting 89.8% for polystyrene (PS) and 72.4-88.9% for functionalized polystyrene (PS-COOH, PS-NH_2) even after three adsorption-desorption cycles. These composite sponges offer excellent mechanical strength, good reusability, high adsorption capacities, and demonstrate promising biocompatibility and biodegradability, offering a sustainable method for mitigating microplastic pollution [Sun *et al., 2020]*.

These studies highlight the great potential of various adsorbents for the removal of microplastics from wastewater due to their low cost, environmental compatibility, renewability, and the ability to interact with diverse types of microplastics through mechanisms including electrostatic attraction, hydrophobic interactions, pore-filling, and π–π stacking.

2.1.2 Photocatalysis

Photocatalysis began with the "Honda-Fujishima effect," which involved splitting water into hydrogen and oxygen. This effect showed that a semiconductor material can

split H_2O into hydrogen and oxygen under light exposure, opening up a new era of photocatalysis [*Hassaan et al., 2023*]. The photocatalytic oxidation method employs light and a photocatalyst to break down organic molecules and plastic pollutants via redox reactions occurring on the surface of the catalyst. Light activates the photocatalyst, which then generates highly reactive species, like hydroxyl radicals ($^{\bullet}OH$) and superoxide radicals ($^{\bullet}O_2^-$), that break down pollutants into benign end-products such as CO_2 and H_2O. Degrading organic contaminants in wastewater has become a key focus of heterogeneous photocatalysis research in recent years [*Xiao et al., 2024, Rajaitha et al., 2022, Pandis et al., 2022*] because it eliminates the need for supplementary disposal methods, making it a significant benefit over traditional approaches. This technique has an advantage over sophisticated oxidation technologies since it uses ambient oxygen as an oxidant, eliminating the need for expensive oxidizing chemicals like hydrogen peroxide and ozone [*Kumari et al., 2023*]. Photocatalysts are self-regenerating, reusable, and recyclable, making the process more sustainable and cost-effective [*Afridi et al., 2025*].

Many semiconducting materials, such as metal oxides, metal nitrides, metal sulphides, alkali metal bases, Z-scheme systems, oxy sulphides, oxy nitrides and metal-organic frameworks (MOFs) and organic materials (carbon, graphene, etc.), have been employed as photocatalysts recently [*Tahir et al., 2020, Krishnan et al., 2024*]. **Table 2.2** provides a compilation of different semiconductor materials used for photocatalytic wastewater treatment.

Table 2.2 Various types of photocatalysts used to remove contaminants from water [reproduced with permission from *Bedia et al., 2019*].

Type of photocatalyst	Examples
Metal oxides	TiO_2, ZnO, WO_3, CeO_2, SnO_2, Fe_2O_3, In_2O_3 or Bi_2O_3
Metal sulfides	ZnS, CdS, MoS_2, Bi_2S_3 or CuS/ZnS
Ternary compounds	Titanates ($BaTiO_3$, $SrTiO_3$ or $La_2Ti_2O_7$) Tungstates (Bi_2WO_6 or $ZnWO_4$) Metalates [$A_xB_yO_z$] (such as $BiVO_4$)
Non-metal semiconductors	g-C_3N_4, graphene

Multicomponent materials	$Bi_2S_3/Bi_2O_3/Bi_2O_2CO_3$ $Bi_2O_2CO_3/Bi_2O_4$ $BiVO_4/Bi_2O_2CO_3$ g-C_3N_4-heterojunctions Graphene-heterojunctions

A suitable photocatalyst should possess characteristics such as low cost, tunable morphology, high photoactivity, non-toxicity, thermal stability, and efficient absorption of visible light [*Chakravorty et al., 2024*]. A band gap that permits the production of reactive species is essential for the degradation of contaminants, specifically that the redox potential of the $H_2O/^{\bullet}OH$ pair, which is -2.8V, falls within the band gap region of the photocatalyst to generate the hydroxyl radicals. ($^{\bullet}OH$) required for the degradation of contaminants [*Chang et al., 2024*]. The bandgap energy of several photocatalysts and the corresponding wavelengths are displayed in **Table 2.3.**

Table 2.3 Energy bandgaps and wavelengths of some traditional photocatalysts [reproduced with permission from *Molinari et al., 2017*].

Semiconductor	Bandgap (eV)	Bandgap wavelength (nm)
TiO_2 (anatase)	3.2	387
TiO_2 (rutile)	3.0	380
Fe_2O_3	2.2	560
SnO_2	3.8	318
ZnS	3.7	335–336
ZnO	3.2	387–390
ZrO_2	5.0	460
WO_3	2.8	443
CdS	2.5	496–497
GaP	2.3	539–540
V_2O_5	2.0	600
CdSe	1.7	729–730
GaAs	1.4	886–887

Severe photocorrosion and fast recombination of photogenerated charge carriers limit the use of metal sulphides in photocatalysis. The main constraint of metal-organic frameworks (MOFs) -based systems is their lower stability, which results from poor coordinate bonding between organic ligands and metal nodes. They have a low reduction capacity and high electron-hole recombination rate. Oxynitrides and oxy sulphides are more active but less stable than metal oxides. Metal oxides (MOs) offer several advantages over other photocatalysts, including high stability, low cost, favorable electronic structure, efficient light absorption, resistance to photo-corrosion, and effective charge transport properties [*Krishnan et al., 2024]*. Research has shown the potential of TiO_2, SnO_2 and ZrO_2 for removal of various organic pollutants as discussed below:

TiO_2 is a widely studied photocatalyst with advantages like low cost, high stability, and non-toxicity, making it suitable for environmental remediation. TiO_2 exists as one of three mineral phases: anatase, brookite, and rutile. The anatase phase of titania has the highest photocatalytic degradation tendency. Being an ideal photocatalyst by itself, researchers have used this photocatalyst in different environmental applications. Its wide bandgap limits its activity to UV light and results in low quantum efficiency, is one of its primary drawbacks. Additionally, its efficiency also reduces by the quick recombination of photogenerated charge carriers (holes and electrons) [*Liao et al., 2020*].

According to Estrada-Flores *et al*. anatase TiO_2 with a spherical and porous shape enhanced the photocatalytic degradation process by boosting visible light absorption through better light scattering within the pores [*Estrada-Flores et al., 2020*].

Ko *et al*. used a template-free sol-gel technique to create spherically shaped TiO_2 nanoparticles. The resultant nanoparticles showed extremely strong and consistent photocatalytic activity for the degradation of toluene [*Ko et al., 2023*].

Kaewkam *et al.* showed that UV-C light (254 nm) in conjunction with TiO_2 resulted in significantly higher degradation of LDPE films compared to UV-A light (365 nm), which showed negligible degradation. The study demonstrated that TiO_2 treated at 900°C (TiO_2-900°C) exhibited the highest photocatalytic activity for LDPE

degradation under UV-C illumination. This superior performance of the high-temperature treated TiO_2 suggests that its specific crystal structure, likely rutile, is more effective for photodegradation of LDPE compared to other phases or lower-temperature preparations (such as TiO_2-450°C). The UV-activated TiO_2 produces reactive oxygen species (ROS), which starts the degradation process. These ROS then break down the polymer chains of the LDPE into smaller byproducts. This suggests that the crystal structure formed by high-temperature treatment enhances the photocatalyst's effectiveness in breaking down LDPE [*Kaewkam et al., 2022*].

A study of Nabi *et al.* showed TiO_2 nanoparticle films achieved almost complete photocatalytic mineralization of PS microplastics, converting 98.40% of 400-nm PS into CO_2 within 12 hours, while PE also showed high degradation rates. This method uses UV light to activate the TiO_2 catalyst, generating reactive oxygen species that break down the microplastics into harmless substances like CO_2, demonstrating a promising, low-cost approach for microplastic remediation [*Nabi et al., 2020*].

SnO_2 is an n-type semiconductor characterized by a wide bandgap of 3.6 eV, making it responsive only to ultraviolet (UV) light. SnO_2 has unique physicochemical characteristics and exceptional catalytic properties. It is an affordable, non-toxic, chemically stable material used by researchers for degradation of various pollutants. [*Rajput et al., 2021*].

According to Letifi *et al*., SnO_2 is a promising candidate with remarkable and adaptable properties, such as high mechanical and chemical stability, high electron mobility, strong thermal stability in the air, high transparency in the visible region, and strong chemical and physical interaction with absorbed species [*Letifi et al., 2019*].

Begam *et al.* reported a simple and eco-friendly method for synthesizing SnO_2 nanoparticles using L-lysine monohydrate. The nanoparticles exhibited spherical tetragonal rutile structures with sizes varying from 4 to 17 nm, depending on the reaction temperature. These nanoparticles were effective photocatalysts for the photodegradation of humic acid, achieving complete degradation within 180 minutes under solar irradiation, indicating a promising application for treating aromatic pollutants [*Begam et al.2016*].

Wu et al. used the amino acid-assisted hydrothermal synthesis method to create highly crystalline, ultra-small SnO_2 nanocrystals with enhanced photocatalytic activity. Because of their small size and increased surface area, they were able to completely degrade (100%) Rhodamine B (RhB) under UV light irradiation in 150 minutes [*Wu et al. 2009]*.

Sangami *et al.* demonstrated high degradation percentage of 94.48% for RhB in 60 minutes using tin(IV) oxide nanoparticles under UV irradiation. The degradation mechanism involves N-deethylation, where ethyl groups are removed from the RhB molecule, and also structural disruption, which leads to a gradual decrease in absorption peak over time [Sangami *et al.*, 2012].

ZrO_2 is a promising substance for use as a photocatalyst. It possesses great thermal and chemical stability, outstanding mechanical strength, high photocorrosion stability, and a high negative conduction band potential, which can generate holes with very strong oxidation power [*Zheng et al., 2009*]. Furthermore, its large band gap [*Qi et al., 2000*] and appropriate redox potentials in bands are extremely favorable for the degradation of a wide range of organic contaminants [*Kralik et al., 1998*].

Sreethawong *et al.* found that ZrO_2 exhibits strong photocatalytic performance in degrading methyl orange under UV irradiation. They also suggested that doping ZrO_2 with metals is an effective strategy to enhance its photocatalytic efficiency, especially under visible light exposure [*Sreethawong et al., 2013].*

Basahel *et al.* reported that the monoclinic (m-ZrO_2) phase of nanosized ZrO_2 exhibited the highest photocatalytic degradation of methyl orange, achieving 99% degradation in 110 minutes, compared to 90% for the tetragonal (t-ZrO_2) phase and 80% for the cubic (c-ZrO_2) phase within the same timeframe. This enhanced performance of m-ZrO_2 is linked to several contributing factors, such as its high crystallinity, wide pore size distribution, and abundant surface hydroxyl groups. In addition, the presence of a small amount of oxygen-deficient zirconium oxide phase helps promote charge separation, thereby enhancing its overall photocatalytic efficiency [*Basahel et al., 2015*].

Hanafi *et al.* demonstrate that ZrO_2 catalysts can achieve 80% degradation of mixed dye and phenol solutions within an hour under fluorescent light irradiation at pH 9 [*Hanafi et al., 2019*].

Alkhalifa *et al.* reported a green synthesis approach for preparing ZrO_2 nanoparticles using Asphodelus fistulosus plant extract as both a reducing and capping agent. Characterization by XRD, XPS, and FTIR confirmed that the produced nanoparticles were crystalline and spherical in shape. Under UV irradiation at pH 7, the green-synthesized ZrO_2 nanoparticles were able to degrade 92% of Congo Red dye within 75 minutes [Alkhalifa *et al., 2025*].

Although research has shown the potential of TiO_2, SnO_2, and ZrO_2 for removal of organic pollutants, several research gaps limit their effectiveness in removing plastic pollution from water. These gaps include improving catalyst efficiency under visible light, optimizing degradation of persistent polymers, and managing toxic byproducts [*Silva et al., 2025*]

The practical application of pure metal oxides is restricted by their high activation energy and the rapid recombination of photogenerated electron–hole pairs. Therefore, enhancing photocatalytic performance requires minimizing the recombination rate of these charge carriers. Coupling of metal oxides with other materials is a viable strategy that could result in varied band gap energies for the metal oxide. Doped materials are anticipated to exhibit enhanced photocatalytic activity because they can lower the activation energy and suppress the recombination of electron–hole (e^-–h^+) pairs [*Shabna et al., 2023*]. Introducing structural defects like Ti^{+3} or doping metal oxides with certain metal or non-metal ions can significantly lower its band gap and cause a red shift in its absorption spectrum. This strategy is commonly used to improve the photocatalytic performance of titania, especially under visible light, by incorporating metal or non-metal ions or by combining it with carbon-based materials [*Aïnoucheet al., 2016, Liao et al., 2020*]

The next **Section 2.2 and 2.3** addresses methods of enhancing the properties of the metal oxide in order to boost catalytic activity.

2.2 Modified Metal Oxides with Doped metals/non-metals/ions

However, these metal oxides can perform photocatalysis only under UV irradiation, which accounts for approximately 4% of the total electromagnetic spectrum. Reducing the bandgaps of photocatalysts has been the main goal of photocatalysis over the years in order to replace UV light with visible light. Nevertheless, the process of lowering the bandgap is expensive. Furthermore, one issue that must be resolved during photocatalysis is the recombination of electron-hole pairs [*Tahir et al., 2020*].

According to Ambasta *et al.,* introducing transition metals like Zn, Fe, Cu, Co, Ni, Zr, and Mn into metal oxides can significantly enhance their photocatalytic activity. Modified metal oxides are increasingly being used in wastewater treatment because inorganic dopants such as N, B, P, O, S, and F have been shown to increase the photolytic activity of metal oxides [*Ambasta et al., 2025*].

Sen *et al.* reported that transition metals like iron, manganese, copper, and nickel, along with their oxides, are commonly used as dopants to enhance the performance of photocatalysts such as TiO_2. This approach has been shown to effectively enhance photocatalytic performance under visible light by reducing the bandgap of the catalysts. While single-doping of TiO_2 nanocatalysts has shown promise in improving photocatalytic efficiency, co-doping with multiple transition metals can sometimes produce unfavorable results due to the intricate interplay between electron-hole recombination and nanoparticle shielding. In recent years, the use of nonmetal dopants such as nitrogen, carbon, fluorine, sulphur, and iodine has gained popularity as an alternate doping method. The use of these nonmetals offers several benefits, such as improved thermal stability of the resulting catalysts and enhanced activity under visible light. These improvements are mainly due to a notable narrowing of the bandgap and a reduction in the recombination of electron–hole pairs [*Sen et al., 2023*].

Du *et al.* reported that doping ZrO_2 with rare earth metals such as Sm and Eu markedly enhanced its photocatalytic performance for degrading rhodamine B and methylene blue under visible light [*Du et al., 2013*]. The outstanding photocatalytic performance is attributed to the increased specific surface area and the favourable electronic structure of the material. Nevertheless, doping ZrO_2 with transition metals such as Cu, Pt, and Au reduced its ability to photodegrade aqueous carbonate [*Sayama and Arakawa, 1993*]. Using metal dopants brings up serious concerns about their potential toxicity,

suggesting that nonmetal dopants may be a safer and more effective option for improving the photocatalytic activity of pristine ZrO_2 [*Liu et al., 2010*].

A study of Zhang *et al.* reported that carbon doping of ZnO nanoparticles reduced their bandgap, enhanced the separation of electron–hole pairs, and significantly increases their photocatalytic activity under visible light [*Zhang et al., 2015*].

Liu et al. suggested that nitrogen, having lower electronegativity than oxygen, is an effective nonmetal dopant for enhancing the photocatalytic activity of wide bandgap metal oxides such as ZrO_2 [*Liu et al., 2010*]. The uniform distribution of the entire doped matrix may also result from its similar radius to that of O [*Charanpahari et al., 2013*]. A summary of various doped metal-oxide nanoparticles used by different researchers for photocatalytic degradation of pollutants is given in **Table 2.4**.

Table 2.4 Photocatalytic degradation of different pollutants using doped metal-oxide nanoparticles.

Dopant	**Metal oxide**	**Light Source**	**Pollutant**	**% Removal**	**References**
Fe	TiO_2	Visible light UV light	Malachite green Dichloromethane	78% 88%	*Asiltürk et al., 2009* *Hung et al., 2007*
B	TiO_2	Visible light	4-chlorophenol	78%	*Xu et al., 2009*
N	SnO_2	Visible light	Methylene blue	98.4%	*Pan et al., 2009*
S	SnO_2	Visible light	RhB Cr (IV)	93% 87%	*Ma et al., 2016*
Pd Pt	ZrO_2	UV light	Indigo disulfonate	96% 94%	*Saeed et al., 2018*

Nanoparticles can be synthesized using two main strategies: (i) the bottom-up approach and (ii) the top-down approach. In the top-down method, bulk materials are broken down into nanoparticles (NPs) through size reduction techniques. In contrast, the bottom-up approach involves assembling nanoparticles using chemical, physical, or biological processes.

Top-down synthesis employs a destructive strategy in which the macroscopic material is reduced to smaller units by physical or chemical processes before being turned into appropriate nanoparticles. Thermal decomposition, mechanical grinding/ball milling,

physical vapor deposition, chemical etching, laser ablation, electro-explosion, sputtering and lithography are some examples of this approach [*Devesa et al., 2025, Abid et al., 2022*]. The top-down method is generally seen as simple, yet it often involves expensive equipment. Its main limitation is the synthesis of nanoparticles with surface imperfections, which can significantly influence their physical characteristics and surface chemistry due to their high aspect ratio [*Khan et al., 2019*].

The bottom-up synthesis, also known as the constructive method, is the opposite of the top-down approach. This approach is based on the self-assembly of individual atoms into bigger clusters, which then aggregate into final nanoparticles. Bottom-up processes include chemical vapor deposition, sol-gel, spinning, pyrolysis, and biological synthesis. Bottom-up synthesis, often known as the constructive method, is the inverse of the top-down approach. This approach is based on the self-assembly of individual atoms into bigger clusters and their subsequent aggregation into final nanoparticles. Chemical vapor deposition, sol-gel, spinning, pyrolysis, hydrothermal, co-precipitation and biological synthesis are all examples of bottom-up methods. This technique has a specific advantage in that it increases the potential of producing metallic nanoparticles with fewer defects and a more homogenous chemical composition; nonetheless, it requires suitable surfaces and molecules [*Devesa et al., 2025, Abid et al., 2022*]. Sreethawong *et al.* reported that ZrO_2 exhibited outstanding photocatalytic activity in degrading methyl orange under UV light. The nanoparticles were easily synthesized using a surfactant-assisted sol-gel method [*Sreethawong et al*., *2013*].

A summary of various synthesis methods used to prepare doped metal oxide by various researchers is given in **Table 2.5**.

Table 2.5 Various doping agents and preparation methods used for metal oxide photocatalyst.

Type of dopant	**Example of dopant**	**Preparation method of doped TiO_2**	**Reference**
	Fe	Hydrothermal	*Zhu et al., 2004*
		Sol gel	*Hung et al., 2007*
		Sol gel/microemulsion	*Adán et al., 2009*
	Pt	Impregnation	*Sakthivel et al., 2004*
		Impregnation/Photodeposition	*Kozlova et al., 2007*

Metal dopant		Photochemical deposition	*Sun et al., 2008*
		Photochemical reduction	*Huang et al., 2008*
	Ce	Sol gel	*Ishibai et al., 2008*
		Hydrothermal	*Xiao et al., 2006*
		Reflux	*Wang et al., 2010*
	V	Sol gel	*Bettinelli et al., 2007*
Non-Metal dopant	P	Hydrothermal	*Jin et al., 2009*
		Sol gel	*Raj et al., 2009*
	N	Hydrothermal	*Peng et al., 2008*
		Hydrothermal	*Senthilnathan et al., 2010*
	S	Hydrothermal	*Tian et al., 2009*
		Hydrothermal	*Ho et al., 2006*
	F	Hydrothermal	*Yu et al., 2009*
		Sol gel	*Todorova et al., 2008*
		Spray pyrolysis	*Li et al., 2005*
	I	Hydrothermal	*Zhang et al., 2011*
		Sol gel	*Ma et al., 2011*
Metalloid dopant	B	Sol gel	*Xu et al., 2009*
		Sol gel	*Zaleska et al., 2008*
	Si	Destabilization	*Estruga et al., 2010*
		Hydrothermal	*Jin et al., 2009*
		Templating	*He et al., 2010*
Co-dopant	F, N	Sol gel	*Livraghi et al., 2009*
	Sm, N	Coprecipitation	*Ma et al., 2010*
	Fe, Nb	Sol gel	*Estrellan et al., 2010*
	W, N	Hydrolysis	*Li et al., 2008*
	B, Fe	Sol gel	*Khan et al., 2008*
	N, S	Hydrolysis	*Yu et al., 2006*
	S, I	Sol gel	*Yu et al., 2010*
	N, S	Hydrothermal	*Wei et al., 2008*
	Cu, S	Sol gel	*Hamadanian et al., 2010*
	F, N	Sol gel	*Xie et al., 2008*
	Pt, Cu	Impregnation	*Li et al., 2010*
	Fe, C	Sol gel/Solvothermal	*Wu et al., 2010*
	Pt, N	Sol gel	*Sreethawong et al., 2009*
	Cr, W	Pyrolysis	*Biswas et al., 2008*

2.3 Photocatalytic degradation of plastics

Researchers used various metal oxides and modified metal oxides for the photocatalytic degradation of various plastics, summarised in **Table 2.6.**

Table 2.6 Metal oxide and modified metal oxides for photocatalytic degradation of various plastics.

Photocatalytic Material	Target Microplastic	Light Source	Time	Efficiency	Reference
ZnO nanorods	Polypropylene	Visible	456 h	65% reduction in particle volume	*Uheida et al., 2021*
C, N-TiO_2 Powders	High-Density Polyethylene	Visible	50h	71.77 ± 1.88%	*Vital-Grappin et al., 2021*
TiO_2/ β-SiC alveolar foams	Polymethyl methacrylate	UV-A	7 h	50%	*Allé et al., 2021*
TiO_2/ZnO	Polyethylene	UV-365nm	480 h	100% Mass loss (with $Na_2S_2O_8$)	*He et al., 2023*
Silver-doped titanium dioxide	Polyamide 66	UV-A	4 h	58.9 % mass loss	*Wang et al., 2025*
Cu-doped TiO_2 nanoparticles	Polyethylene	UV	48 h	96.7 % degradation	*Ejeta et al., 2026*

2.4 Carbon Material based Metal Oxides Nanocomposites for Photocatalytic Degradation

According to the available literature, over the past few years, numerous studies on developments in carbon-based photocatalysts for water remediation have been published. The carbonaceous materials explored by various researchers for photocatalytic performance include carbon dots [*Sendão et al., 2022*], graphitic carbon nitride (g-C_3N_4) [*Pham et al., 2023, Biswas et al., 2023*], activated carbon [*Abdullah et al., 2023, Liu et al., 2021*], graphene oxide [*Khan et al., 2019*], reduced graphene oxide [*Ramesh et al., 2021*] and carbon nanotubes (CNTs) [*Ansari et al., 2025*]. Introducing highly conductive carbon materials into the photocatalyst helps prevent the recombination of electron–hole pairs, improving its overall efficiency.

Hu *et al.* (2012) found that graphene oxide/TiO_2 (GOT) hybrids demonstrated remarkable adsorption and photocatalytic efficiency under visible light, successfully degrading MB dye during solar exposure. This enhanced activity was attributed to

ability of GOT to act as an electron sink, boosting its photocatalytic performance [*Hu et al., 2012*].

Nguyen-Phan *et al.* reported an environmentally friendly, one-step colloidal blending technique that retains properties of TiO_2 while integrating the benefits of graphene oxide. The resulting composites showed high adsorption and strong photocatalytic performance under both UV and visible light. Photodegradation experiments using methylene blue (MB) under simulated sunlight revealed that graphene oxide functioned as an adsorbent, electron acceptor, and photosensitizer, boosting the efficiency of the photocatalytic process [*Nguyen-Phan et al., 2011*].

The TiO_2/GO (8%) nanocomposite had the highest and fastest rate of methylene blue photocatalytic degradation, according to Khan *et al*. The thin two-dimensional sheet support, greater surface area, narrow band gap, stronger adsorption capacity, and good electron acceptance of GO were associated with their exceptional photocatalytic activity against synthetic dye and ciprofloxacin under the visible region spectrum. Therefore, synthesized nanocomponents may prove to be an effective photocatalytic system to protect our ecosystems from the harmful waste products released by various industries [*Khan et al., 2019*].

Kamalam *et al.* report that the SnO_2-GO nanocomposite degraded the RB dye in 120 minutes, which is much shorter time than the degradation performances of SnO_2 and GO alone. The combination of GO and SnO_2 produces a synergistic effect, where integrating GO into SnO_2 enhances carrier oxidation, slows down electron–hole recombination, and promotes more efficient separation of charge carriers. As a result, a relatively inexpensive graphene oxide-supported SnO_2 nanocomposite can be used as an effective actual wastewater treatment technique at an industrial scale [*Kamalam et al., 2019*].

Posa *et al.* synthesized GO/ZnO nanocomposites using a straightforward wet chemical method, demonstrating their effective photocatalytic mineralization under sunlight. The exceptional photocatalytic activity of nanocomposites is related to the formation of GO/ZnO, which enhanced the lifespan of transporters, and the excitation of dyes as a

visible light sensitizer. It was because the load separation of electric-hole carriers was effective [*Posa et al., 2016*].

Farghaly *et al.* conducted a comprehensive investigation on the removal of methylene blue (MB) from aqueous solutions using solar-driven photocatalysis with nano-sized TiO_2 and composites containing activated carbon (AC) and reduced graphene oxide. Instead of doing traditional batch tests to investigate the design configuration of a solar reactor, this study uses a continuous system. TiO_2 has a 93.13% MB removal efficiency. The study also demonstrated that combining TiO_2 with AC and RGO considerably improved MB photocatalytic degradation. The TiO_2/AC composite degraded 98.3% of the MB in 138 minutes of sun exposure. Similarly, the TiO_2/RGO composite achieved 97% removal, which is much higher than nano-TiO_2 [*Farghaly et al., 2004*].

Fadli *et al*. synthesized Ag/TiO_2/RGO composite catalyst that showed a high degradation percentage of 76% for polyethylene microplastics within 4 hours of UV irradiation, outperforming pure TiO_2 (56%) and Ag/TiO_2 (68%). This demonstrates that the presence of silver and reduced graphene oxide (RGO) boosts the catalytic oxidation efficiency for microplastic degradation. When exposed to UV light, the TiO_2 catalyst generates electron–hole pairs (e^-/h^+), which react with water and oxygen to form powerful oxidizing species such as hydroxyl radicals ($^{\bullet}OH$). These radicals subsequently target the chemical bonds within the microplastic polymers, causing them to break down and degrade. The addition of metal dopants (like Ag) and 2D materials (like RGO) improves the photocatalyst's light absorption and charge separation, preventing the rapid recombination of electrons and holes. Better charge separation leads to a higher rate of reactive oxygen species generation, enhancing the degradation efficiency. Studies have monitored the physical and chemical changes in microplastics, such as an increase in the carbonyl index and surface cracks, which signify the breakdown of the polymer structure. [*Fadli et al., 2021*]

2.5 Photocatalytic Degradation Mechanism of Doped-Metal Oxides

The basic mechanism of a metal oxide photocatalyst begins when it absorbs a photon with energy equal to its band gap. This excites an electron from the VB to the CB, generating a positive hole in the VB. They can also react with the species acceptor or

donor of electrons that are adsorbed on its surface. Consequently, the high oxidation potential of the ˙OH generated has a significant impact in photocatalysis [*Zhou et al., 2004*].

In contrast, interstitial metal doping introduces new energy levels within the band gap of the metal oxide by dispersing metal nanoparticles throughout the matrix. This doping enhances electron trapping, which reduces electron–hole recombination during photoactivation. As a result, the lower rate of charge-carrier recombination leads to improved photocatalytic activity [*Zaleska 2008*].

The modification of metal oxide by nonmetal ion doping modifies the nature mechanism of photocatalyst by bandgap narrowing, introduction of impurity energy level, oxygen vacancies, shallowing the acceptor states as detailed below. These modifications to the system will help to improve and sustain the treatment of organic contaminants.

Band gap narrowing: Asahi *et al.* reported that during visible light absorption, the energy levels of the CB and VB are quite narrow. In nitrogen-doped anatase TiO_2, the N 2p states hybridize with the O 2p states, resulting in a reduced band gap for N-TiO_2 [*Asahi et al., 2001*].

Impurity energy level: Irie *et al.* showed that introducing nitrogen ions into TiO_2 forms an isolated impurity energy level above the valence band. This newly created level enables electrons to be excited by visible light, thereby enhancing the photocatalyst's activity under visible-light irradiation [*Irie et al., 2003*].

Oxygen vacancies: Ihara *et al*. highlighted the role of oxygen-deficient sites, which act as barriers to reoxidation. These sites, located at grain boundaries, are crucial for enabling visible-light-driven photocatalytic activity.

Shallowing the acceptor states: Zhao and Liu studied the bandgap narrowing effect caused by substitutional nitrogen doping in TiO_2 [*Liu et al., 2008*].

2.6 Recycling of Plastics

The fabrication of polymeric supports for efficient, long-lasting, and low-cost heterogeneous catalysts for the treatment of organic/inorganic pollutants is highly

desirable but remains a significant challenge. Common commercial polymers, such as polystyrene (PS), polypropylene (PP), Polyethylene terephthalate (PET), polyethylene (PE), and polyvinyl chloride (PVC), are targeted for this work based on their primary physicochemical qualities, such as molecular mass, degree of crystallinity, and others [*de Assis et al., 2021*].

In studies published by Linda et al. (2016), the authors assessed the development of a composite (cellulose/PVC) to immobilize nanostructured ZnO, which was to be used in the UV light-assisted photodegradation of Congo red and crystal violet dyes. Polyvinyl chloride (PVC) is a significant polymer in both industry and society. After 120 minutes, about 90% of the dyes were broken down, based on response observations. When compared to PVC/ZnO, the results showed that the addition of cellulose enhanced the composite's surface and structural characteristics, raised its affinity for the reaction medium, and enhanced its photocatalytic efficiency. In light of the aforementioned, the ZnO photocatalyst based on the polymer composite shows promise for organic dye photodegradation [*Linda et al., 2016*].

Effective photocatalytic denitrification systems were studied by Sandhu et al. This was accomplished by examining the production of TiO_2 nanoparticles immobilized on polystyrene (PS-TiO_2). After five cycles of denitrification studies, the authors claim that the catalysts' fluctuating nature made recovery simple, with 98% catalyst recovery rates. The concept of immobilizing the photocatalyst on a floating support can allow more flexibility in using the supported photocatalyst for scale-up constructions by reducing issues with powder filtration and photocatalyst recovery [*Sandhu et al., 2020*].

In order to develop films for the immobilization of TiO_2 impregnated with copper and iron for use in photocatalytic systems in the breakdown of the medications ketoprofen, tenoxicam, and meloxicam, Moura et al. utilized polystyrene scraps from post-consumer yogurt packaging. The findings demonstrated that after 180 minutes of reaction, the photodegradation kinetic rates had increased to levels over 92%. The scientists also assessed toxicity before and after treatment, and no toxicity was found for watercress or lettuce seeds; nevertheless, the results revealed a slight sensitivity for thyme seeds to the chemicals generated during treatment. Furthermore, the photocatalyst's reuse efficiency was assessed, and even after the fifth treatment cycle,

the supported photocatalyst showed degradation more than 82%. These findings suggest that this photocatalytic system is appropriate for treating effluents containing medicinal chemicals [*Moura et al. 2021*].

Assis et al. converted polystyrene waste into value-added composites, demonstrating that combining two emerging concerns (exploring polystyrene reuse and water contamination by toxic dyes) is an important line of research in the development of multifunctional materials. The study resulted in the creation of polystyrene-based nanofoams to support nanostructured SnO_2, which were then tested for use in photodegradation of rhodamine B for environmental remediation and water purification purposes. All of the composite materials under investigation had rates above 96% of photocatalytic efficiency in 70-minute reactions and the authors showed that the composite's surface area was larger than that of individual SnO_2. This increase in surface area also contributed to the increase in the photodegradation rate. The authors assessed the production of less harmful byproducts in addition to dye discolouration. Consequently, the synergy between polystyrene and SnO_2 produced the desired outcome [*De Assis et al., 2018*].

Such catalysts made from plastic waste have several noteworthy benefits, including the ability to be converted, reused, and inexpensive, as well as the potential to be used in critical processes that affect the quality of environmental systems [*Bartáček et al., 2019*]. Reusing catalysts is just as crucial for the application of hazardous species degradation as catalytic activity.

2.7 Research Gap

A literature review on the role of adsorption and photocatalysts in removal of plastic pollutants and the significance of metal oxide nanoparticles and modified metal oxide nanocomposites in removal of organic pollutants including plastic pollutants and recycling of plastic for the application of environmental remediation revealed the following observations.

Metal oxide nanoparticles synthesized using diverse ways are effective in photocatalytic activity against a variety of pollutants under ultraviolet (UV) light. To substitute UV radiation with visible light, metal oxide nanoparticles can be synthesized

using a simple technique that involves doping and coupling with a significant host material, such as graphene oxide or activated carbon derived from biomass. Furthermore, composites can only exhibit photocatalytic activity at an optimum weight of carbon material, hence the current research was focused on this direction.

In general, adsorption provides a versatile and adaptable solution for removal of various pollutants including plastic pollutants whereas photocatalysis would have the ability to degrade various pollutants. Coupling these two methods can provide an effective removal pathway for the simultaneous capture and degradation of plastic pollutants in water. Graphene-oxide/metal-oxide and activated-carbon/metal-oxide composites are expected to be promising to remove the plastic pollutants because they exhibit the properties such as excellent adsorption capacity with enhanced charge separation and visible-light activity.

Furthermore, the development of catalytic support technologies has the potential to improve the quality of sustainable environmental systems by recovering environmentally damaging plastic waste and using it to develop new materials for wastewater treatment. This primarily focuses on plastic waste to obtain catalytic supports, which are then used for water purification.

Taken together, these findings indicate a research gap: the design and synthesis of doped metal-oxide nanocomposites that operate under visible light, combine adsorption and photocatalytic degradation mechanisms, and can efficiently target diverse plastic pollutants. The following chapters present the methodologies and results addressing this gap.

2.8 Objectives of the Research Work

- Synthesis and characterization of some metal oxides-based semiconductor nanomaterials.
- Remediation of macro/microplastics using synthesized materials.
- Synthesis and characterization of recycled plastic-based composite for the removal of organic contaminants.

3.1 Chemicals

Graphite flakes (99%), $KMnO_4$ (Potassium permanganate), $NaNO_3$ (Sodium nitrate), H_2O_2 (hydrogen peroxide) (30%), H_2SO_4 (concentrated sulfuric acid) (98%), Titanium butoxide, ethanol, ammonium nitrate (NH_4NO_3), acetone, and tetrahydrofuran (THF), sodium dodecyl sulfate (SDS), methylene blue, and rhodamine B were purchased from Sigma Aldrich. Floury corn cobs were purchased from local market of Apra (Punjab). The commercially available chemicals and solvents employed in the synthesis of perylenetetraester (PTE) such as perylene-3,4,9,10-tetracarboxylic dianhydride (PTCDA), 1-iodobutane, 1,8-Diazabicyclo (5.4.0) undec-7-ene (DBU), 1-butanol, N, N-dimethylformamide (DMF), hexane, chloroform, dichloromethane (DCM) and silica gel (60–120 mesh) were purchased from either Merck or Sigma-Aldrich. Polyvinyl chloride (PVC, Mw ~ 120,000), low density polyethylene (LDPE, Mw ~ 50,000) and polystyrene (PS, Mw ~ 150,000) pellets were taken from an industry named Hi-Tech Polymer Products Ludhiana (Punjab) in the form of pellets and used as received. Deionized water was used to make stock solutions for all experiments.

3.2 Material Synthesis

Three nitrogen-doped metal oxide nanoparticles, TiO_2, SnO_2, and ZrO_2, were synthesized using the sol-gel method. Different carbon-based materials, such as graphene oxide and corncob activated carbon, are used to synthesize the composite with N-TiO_2 and N-SnO_2. These composites were then subjected to various characterizations and utilized for plastic remediation.

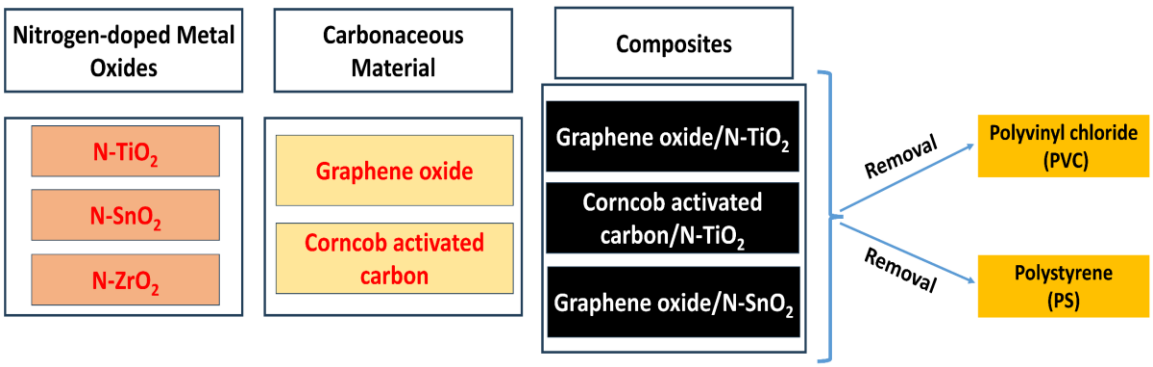


Figure 3.1 Schematic representation of the synthesized nitrogen doped metal oxides and the corresponding nanocomposites for removal of PVC-NPs and PS-NPs.

Additionally, low density polyethylene (PE) and polyvinyl chloride (PVC) were incorporated with various as-synthesized materials such as graphene oxide (GO) and N-TiO_2, for the synthesis of plastic-based nanocomposites and applied to photocatalytic degradation of cationic dyes.

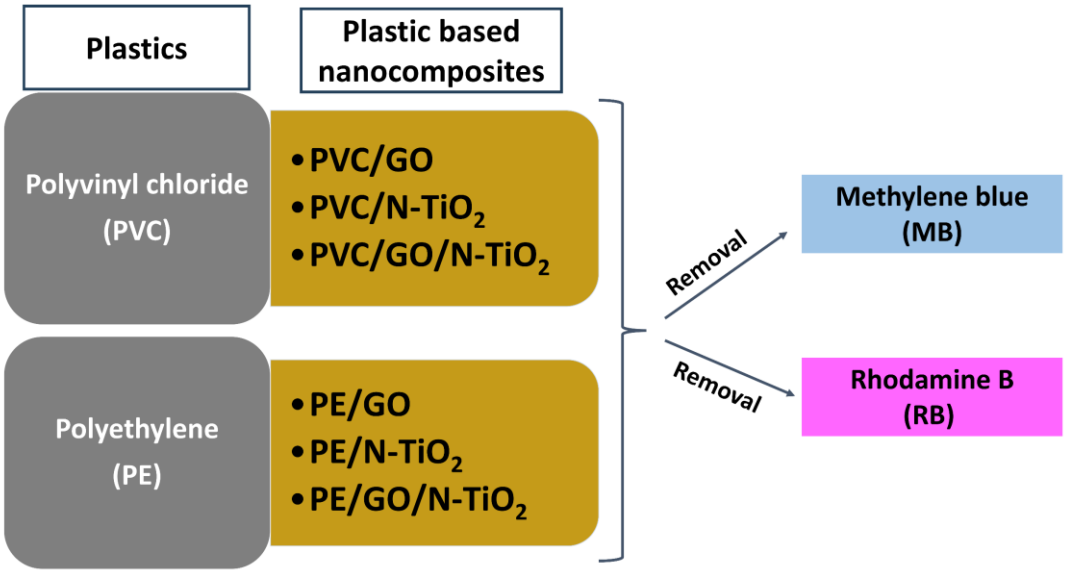


Figure 3.2 Schematic representation of the synthesized plastic-based nanocomposites for removal of organic pollutants.

3.2.1 Synthesis of Graphene Oxide (GO)

*G*raphene oxide sample was synthesized using Hummer's method by oxidizing graphite [*Hou et al., 2020; Hummers et al., 1958*]. In this reaction, 46 mL of H_2SO_4 (98%) and 1.0 g $NaNO_3$ were placed in a 250 mL flask with mechanical stirring in an ice bath, then 2.0 g graphite powder and 6.0 g $KMnO_4$ were slowly added. The suspension was held at a temperature of around 4°C for 2 hours. The ice water bath was then replaced by a warm water bath. The reaction was carried out at 35°C for 30 minutes. After the 30-minute reaction time, 46 mL deionized water was added dropwise to the reaction solution, and the temperature was kept at 95 °C for at least 15 minutes. 5 mL of 30% H_2O_2 slowly and the color of the solution changed from dark brown to yellow. The solution was allowed to stand until no more visible bubbles appeared. To remove metal ions, the solution was centrifuged and washed with 5% HCl aqueous solution, then washed with distilled water to remove the acid. It was then vacuum dried to get solid GO.

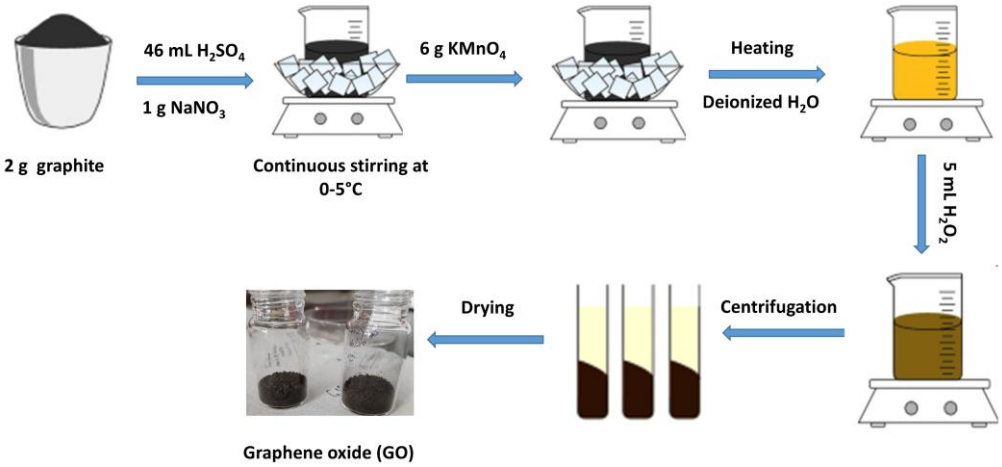


Figure 3.3 Schematic representation of the synthesis of graphene oxide (GO).

3.2.2 Synthesis of Corncob Activated Carbon (CCAC)

For the synthesis of activated carbon, corncob was washed with deionized water and dried for 60 minutes at 120°C in the oven and then was cut into small sizes. 15 g of corncob was added with 60 mL of 25% (w/v) $ZnCl_2$ solution (impregnation ratio 1: 1, i.e., 15 g corncob biomass and 15 g $ZnCl_2$ in 60 mL water) and mixed thoroughly. The resulting mixture was left for 22 h and then dried at 100°C for 2 h, and pyrolyzed at 850°C for 2 hours with an average heating rate of 10 °C min^{-1} under inert atmosphere using N_2. The activated carbon produced was poured into deionized water, and pH adjusted to 7 using 1N HCl with vigorous stirring and recovered after filtration and drying at 105°C. The produced activated carbon was named as 'CCAC'.



Figure 3.4 Schematic representation of the synthesis of corncob activated carbon (CCAC).

3.2.3 Synthesis of N-TiO_2 Nanoparticles

The N-doped TiO_2 samples were prepared using the sol-gel method [*Fiorenza et al., 2020*]. 0.0096g of ammonium nitrate was dissolved in 1:1 mixture of water and ethanol. The above prepared mixture and titanium butoxide were added drop wise in a beaker containing 70 ml of ethanol to get the nitrogen doped titanium oxide. The resultant

slurry was stirred for 3 hours and aged for 24 hours. Further it was dried at 100°C for 12 hours and then calcined at 500 ° C for 6 hours. The resultant solution was labelled as 'N-TiO_2'.

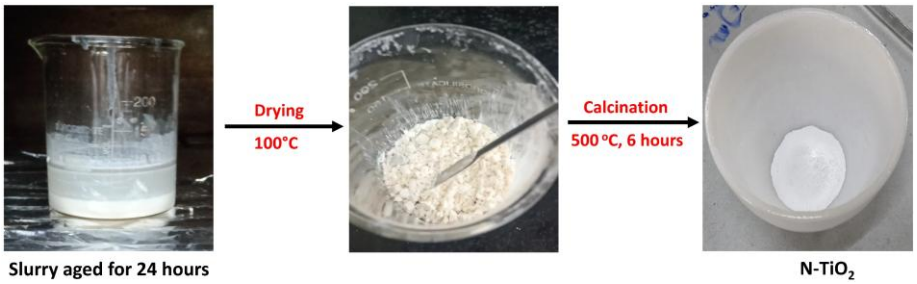


Figure 3.5 Schematic representation of the synthesis of N-TiO_2 nanoparticles.

3.2.4 Synthesis of Graphene Oxide/Nitrogen-doped TiO_2 Nanocomposite

Graphene oxide/N-TiO_2 composites were prepared with three different ratios (w/w) of GO: N-TiO_2 as 1:3, 1:1, and 3:1 by separately dispersing GO (0.2, 0.4, and 0.6 g) relative to N-TiO_2 (0.6, 0.4, and 0.2 g) in an appropriate amount of deionized water by a one-step colloidal blending process using the ultrasonication technique. The prepared samples were labelled "GT13, GT11, and GT31" for GO: N-TiO_2 1:3, 1:1, and 3:1, respectively.

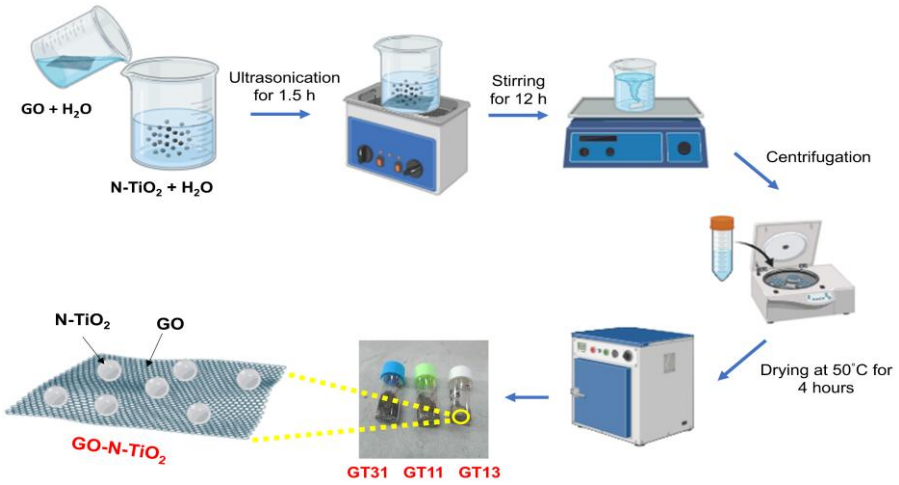


Figure 3.6 Schematic representation of the synthesis of GO/N-TiO_2 nanocomposites.

3.2.5 Synthesis of Corncob Activated Carbon-based Metal Oxide Nanocomposites

CCAC/N-TiO_2 composites were synthesized through a facile wet impregnation. First, N-TiO_2/water and CCAC/water suspensions were prepared. These suspensions were

mixed together and sonicated for 20 min. The resulting suspension was stirred for 4 hours, centrifuged and dried at 80°C. The dried material was calcinated at 500 °C for 3 hours in the presence of an inert atmosphere. CCAC/N-TiO_2 was allowed to cool and collected for further use. The above process was performed to synthesize CCAC/N-TiO_2 composites for different weight ratios of CCAC:N-TiO_2 as 1:3, 1:1, and 3:1 and are named as 'CT13, CT11, and CT31, respectively.



Figure 3.7 Schematic representation of the synthesis of CCAC/N-TiO_2 nanocomposites.

3.2.6 Synthesis of N-SnO_2 Nanoparticles

Aqueous solutions of 0.5 M tin (II) chloride ($SnCl_2$. $2H_2O$) and 0.75 M oxalic acid dihydrate ($C_2H_2O_4.2H_2O$) were prepared separately in 50 mL of deionized water and mixed together to obtain the white precipitates. Then, 1.0 N NaOH (a precipitation agent) was added dropwise to the solution until the pH was maintained at 8.0, stirred for 30 minutes, and left overnight for obtaining a white precipitate of SnC_2O_4. The transparent supernatant of the SnC_2O_4 solution was decanted. 0.0144 g of urea was added as a nitrogen precursor to wet precipitate and stirrer for 1 hour. The precipitate was filtered and washed 6-7 times using distilled water for complete removal of chloride ions and then with ethanol and dried at 70°C-80°C. Finally, it obtained material was calcined at 500°C for 2 hours to obtain nitrogen-doped SnO_2.

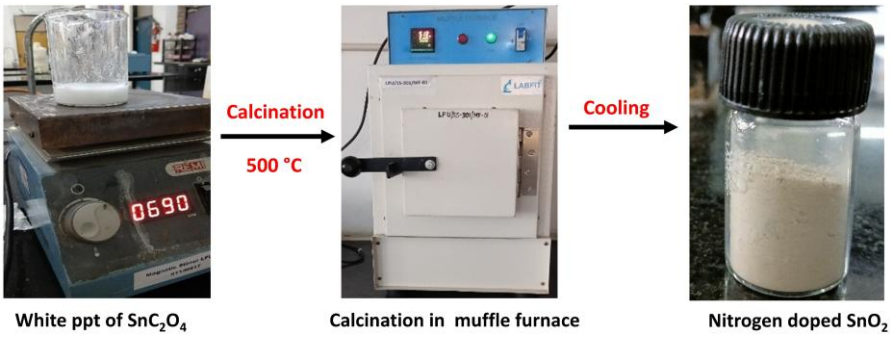


Figure 3.8 Schematic representation of the synthesis of N-SnO_2.

3.2.7 Synthesis of N-ZrO_2 Nanoparticles

The N-ZrO_2 was synthesized by thermal decomposition of zirconium hydroxide-urea complex. 12.89 g of zirconium oxychloride was dissolved in 40 mL of water. NaOH was slowly added to the solution under continuous stirring. The obtained precipitate of zirconium hydroxide [$Zr(OH)_4$)] was collected by centrifugation, repeatedly washed with water, and ground with 0.021 g of urea in an agate mortar for 30 min. The ground mixture was dried in an oven at 100 °C for 24 h and calcined at 500 °C for 3 h in a muffle furnace to form crystalline N-ZrO_2. The as-synthesized N-ZrO_2 was washed with water followed by ethanol prior to drying at 100 °C for 24 h. Furthermore, pristine ZrO_2 was synthesized by the same method without adding urea.

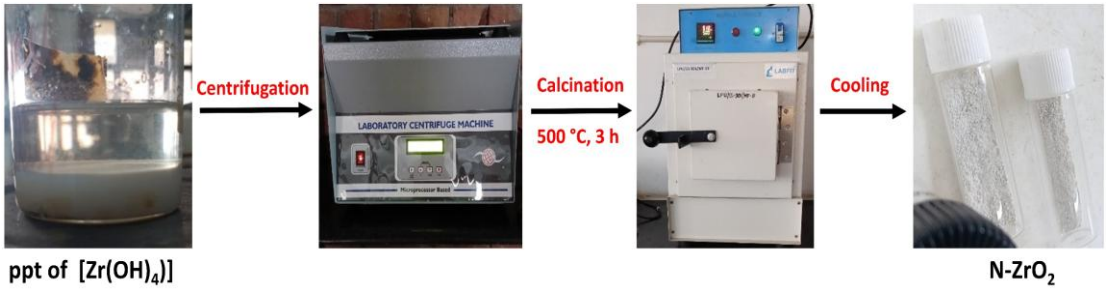


Figure 3.9 Schematic representation of the synthesis of N-SnO_2.

3.2.8 Synthesis of PTE Dye

It is difficult to identify the plastic nanoparticles in water using existing spectroscopic or microscopic methods since they are optically transparent. So, Perylene tetrabutylester (PTE) was chosen to be encapsulated inside the PVC particles [*Bhargava et al., 2018*].

Perylenetetraester (PTE) was prepared in the lab using a reported procedure [*Aksoy et al., 2018*]. 2.54 m mol perylene-3,4,9,10-tetracarboxylic dianhydride was placed in a 50 ml two-neck round bottom flask , 1.52 ml of DBU, 1.86 ml of n-butanol and 13 ml DMF were added to the reaction flask and they were stirred at 60 °C for 30 min. then 1.84g of 1-iodobutane mixed with 10 ml of DMF was added. The mixture was stirred at 60 °C for further 3 hours and cooled to room temperature. The reaction mixture was slowly added into distilled water (100 ml) and stirred for 15 minutes, and the solid was filtered. The solid material was dried at 80 °C and purified by column chromatography

on silica gel, eluting with dichloromethane (CH_2Cl_2) to give compound a golden-orange solid named as 'PTE'.

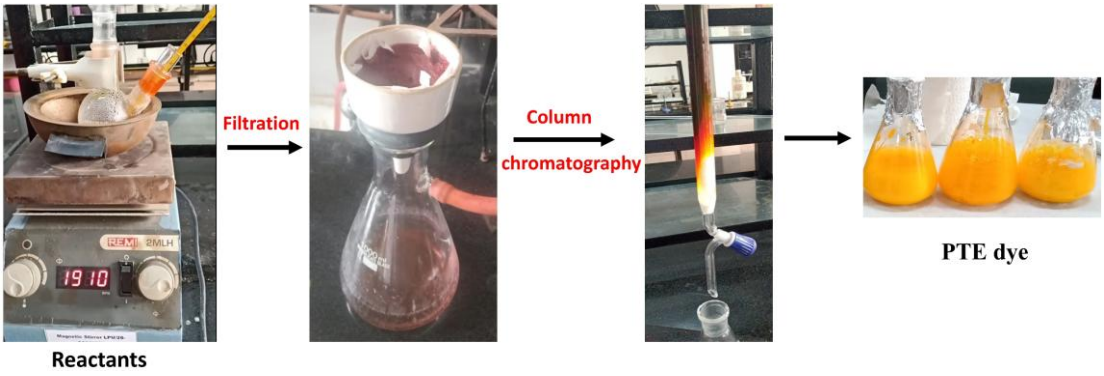


Figure 3.10 Schematic representation of the synthesis of PTE dye.

3.2.9 Preparation of Fluorescent Polyvinyl chloride and Polystyrene Solution

PVC and PS nanoparticles encapsulated with the fluorescent dye perylene-3,4,9,10 tetracarboxytetrabutylester (PTE) were prepared using a previously described nanoprecipitation process [*Batool et al., 2020*]. Typically, 50 mL of organic solvent, tetrahydrofuran (THF) was used to dissolve 4 mg (4 wt% w.r.t. PVC/PS) of PTE, 4 mg (4 wt% w.r.t. PVC/PS) of stabilizer sodium dodecylsulfate (SDS), 100 mg (2 mg/mL) of PVC, and 50 mg (1 mg/mL) of PS. The mixture was then sonicated for 30 minutes. 10 mL of PVC/PS stock solution was mixed with 50 mL of water and continuously stirred to allow the solvent to evaporate at room temperature. The resulting solutions containing fluorescent polymer nanoparticles were uniformly dispersed in water were referred to as "PVC-NPs and PS-NPs."

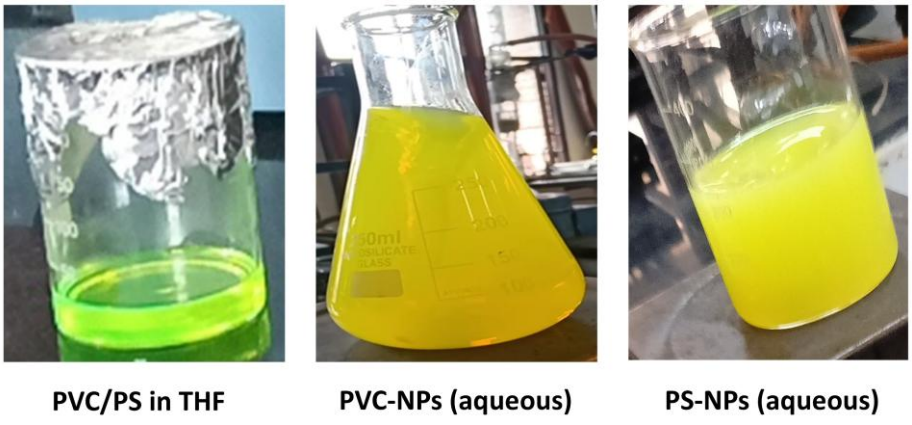


Figure 3.11 Schematic representation of the preparation of PVC-NPs and PS-NPs.

3.2.10 Photocatalytic and Adsorption Experiment

The removal efficiency of the synthesized materials was studied using aqueous solutions of PVC and PS under different conditions. Tungsten bulbs, room light, and three different pH values (4, 7, and 10) were used to test the material's photocatalytic activity in a 20 ml PVC and PS (2 mg/ml) solution using the catalyst dosage of 80 mg per 20 ml of pollutants. The adsorption-desorption equilibrium is obtained by keeping the solution in the dark for 30 minutes. A 400 W tungsten light/room light was then used to expose the solutions for 3 hours. The 3 ml aliquots were taken at regular intervals (30, 60, 90, 120, 150, and 180 minutes) and centrifuged to remove the catalyst. These samples were evaluated using a UV-Vis spectrophotometer to determine the PVC and PS removal.

To examine the adsorption mechanism in this system, the aforementioned experiments were carried out using the synthesized materials and an aqueous solution of PVC and PS at room temperature under dark.

The following formula was used to determine the removal efficiency in photocatalytic and adsorption experiments:

$$\text{Removal } \% = \frac{C_0 - C_f}{C_0} \times 100 \qquad (3.1)$$

Where, C_0 and C_f were the initial and final concentrations of an aqueous solution of PVC and PS solution, respectively.

3.2.11 Quenching Test

Various scavengers, such as sodium oxalate, isopropyl alcohol, and para-benzoquinone as quenchers of hydroxyl radical ($\cdot OH$), hole (h^+), and superoxide ($\cdot O_2^-$), respectively, were used to investigate the reactive species involved in the photocatalytic reaction. 2 mM of each scavenger was added to the mixture of the synthesized material and the aqueous solution of PVC, PS, and dyes in a setup similar to that employed for photocatalytic activity to assess the removal efficiencies after the addition of scavengers.

3.2.12 Synthesis of PE/GO, PE/N-TiO_2 and PE/GO/N-TiO_2 Nanocomposites

A thermally induced phase separation (TIPS) and lyophilization techniques were used to synthesize PE/GO nanocomposite [*De Assis et al., 2018; Jayanthi et al., 2016*]. 0.25g of PE was dissolved in cyclohexane under vigorous stirring using magnetic stirrer for 3 hours. 0.125 g of GO was added to 10 ml of PE solution to make the suspension for PE/GO sheets, which was then kept in an ultrasonic bath for 2 hours. The dispersion was frozen at −10°C in a freeze dryer, which is below the freezing point of cyclohexane (−6°C). Following a 24-hour freezing period, the sample underwent a 4-hour lyophilization process using a vacuum pump to sublimate the cyclohexane solvent. This sublimation effectively removed the solvent, resulting in a solid nanocomposite referred to as 'PEGO'.

To prepare PE/GO/N-TiO_2 nanocomposite, 0.25 g of PE was dissolved in 10 ml of cyclohexane. Then 0.125 g of GO and 0.54 g of N-TiO_2 was added in the solution. By following the aforementioned procedure, a solid nanocomposite was left behind labelled as 'PEGNT'. Similarly, PE/N-TiO_2 was synthesized using the same method without addition of GO and the synthesized nanocomposite was named as 'PENT'.

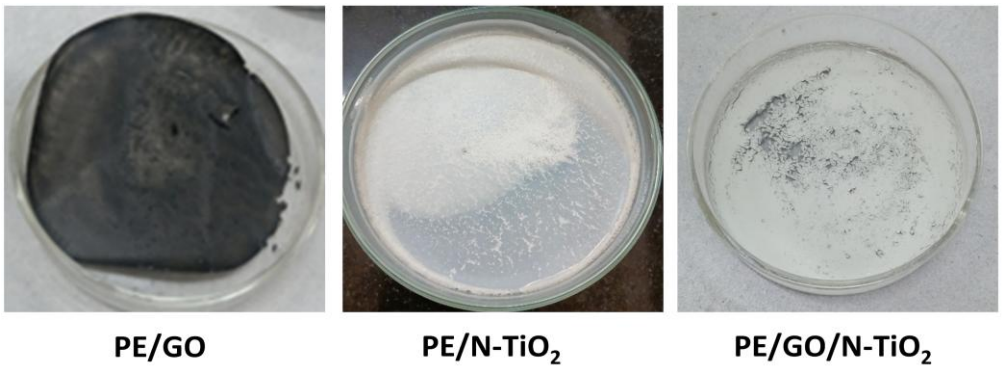


Figure 3.12 Schematic representation of the synthesis of PE/GO, PE/N-TiO_2 and PE/GO/N-TiO_2.

3.2.13 Synthesis of PVC/GO, PVC/N-TiO_2 and PVC/GO/N-TiO_2 Nanocomposite

0.25 g PVC was dissolved in 10 ml tetrahydrofuran (THF) at room temperature for 1 hour. Then, 0.125 g of GO was added to solution and ultrasonicated for 2 hours. The evenly dispersed solution was poured into petri dish. Finally, the nanocomposite was obtained after 12 hours drying at room temperature and labelled as 'PVGO'

For the synthesis of PVC/GO/N-TiO_2 nanocomposite sheets, 0.25 g PVC was dissolved in 10 ml tetrahydrofuran (THF) at room temperature for 1 hour**.** Then, 0.125 g of GO

and 0.375 g of N-TiO_2 was added to solution and ultrasonicated for 2 hours. The evenly dispersed solution was poured into petri dish. Finally, the nanocomposite was obtained after 12 hours drying at room temperature and labelled as 'PVGNT'. Similarly, PVC/N-TiO_2 was synthesized using the same method without addition of GO and the synthesized nanocomposite was named as 'PVNT'.



Figure 3.13 Schematic representation of the synthesis of PVC/GO, PVC/N-TiO_2 and PVC/GO/N-TiO_2.

3.2.14 Removal Experiment

To assess the removal efficiencies of synthesized plastic-based nanocomposites, the procedures in **Sections (3.2.10)** and **(3.2.11)** were then used for the removal of methylene blue and rhodamine B dyes of concentration 1×10^{-4} M using the synthesized plastic-based nanocomposites.

3.3 Material Characterization

Nanomaterials and nanocomposites were analyzed using a variety of characterisation techniques, which are described in detail in the as follows:

X-ray diffraction experiments were performed at room temperature to assess the powders' crystal phase composition and crystallite size. The X-ray diffraction (XRD) patterns were examined using a Bruker D-8 Advance X-ray diffractometer at room temperature with a scan range of 2θ = 10–80° to determine their purity, size, and crystallinity. The average crystallite sizes of the powders were determined using Scherrer's equation (shown below) based on the XRD results.

$$D = \frac{K\lambda}{\beta \cos\theta} \qquad (3.2)$$

Where, K is a dimensionless factor with a value close to unity, λ is the wavelength, β is the width at half height of the respective XRD peak, θ is Bragg's angle and D is the mean particle diameter. Images from Field Emission Scanning Electron Microscopy (FE-SEM) were obtained using JEOL JSM-7610F Plus. The Oxford EDS LN2 free, Au Coater; JEOL Smart Coater was used to study the energy dispersive spectrometry (EDS) analysis. XPS patterns have been recorded using Thermoscientific's NEXA Surface analyzer. Using a Perkin Elmer Spectrum 2 spectrophotometer, the materials' Fourier transform infrared spectroscopy (FT-IR) spectra were observed between the range of 4000 and 400 cm^{-1}. PVC-NPs in water were quantitatively analyzed using UV–vis spectroscopy both before and after removal at room temperature using a UV 1800S spectrophotometer. The band gap energies (Eg) of the samples were calculated using Tauc's approach, which uses the equation (2)

$$\alpha h\nu = A(h\nu - E_g) \tag{3.3}$$

Where, h - Planck constant, ν - frequency of irradiation light, α - absorption coefficient, Eg -bandgap, A – Proportionality constant.

For both indirect and direct transitions, the intercept of the straight line of the plot of $(\alpha h\nu)^{1/2}$ or $(\alpha h\nu)^2$ against hν was found. The LS6500 fluorescence spectrophotometer from Perkin Elmer was used to measure the photoluminescence (PL) spectra. A thermogravimetric analyzer (Perkin Elmer TGA 4000) was used to test the thermal stability of the produced materials. An instrument named the Malvern Zeta sizer Nano-ZS90 was used to measure the size and surface charges of the produced PVC-NPs. Using a confocal microscope (NIKON, model: A1R), fluorescent images were taken. After treatment, the PVC-NPs solution was characterized using Shimadzu QP 2010 Ultra GC MS Gas Chromatography and Mass Spectrometer. Total organic content was analysed by Walkley Black method .

4.1 GRAPHENE OXIDE/NITROGEN-DOPED TiO_2 NANOCOMPOSITES FOR REMOVAL OF POLYVINYL CHLORIDE (PVC) AND POLYSTYRENE (PS) FROM WATER

In this section, characterization of bare GO, N-TiO_2, and GO/N-TiO_2 composites (GT13, GT11, and GT31), PTE dye, PVC-NPs, and PS-NPs, is discussed. The removal studies on PVC-NPs and PS-NPs using the synthesized materials are also being explained.

4.1.1 Characterization of graphene oxide/N-TiO_2 (GT13, GT11 and GT31) Composites

4.1.1.1 X-ray Diffraction Analysis

The XRD patterns of GO, N-TiO_2 nanoparticles and a series of GO/N-TiO_2 nanocomposites with varying weight ratios (GT13, GT11, and GT31) are shown in **Figure 4.1**. The XRD pattern of bare GO shows reflections from the (001) and (100) planes of GO, respectively, with a notable diffraction peak at 11.14° and a smaller peak at 42.27° that is quite similar to that reported in literature (*Siburian et al. (2018)*). Pure N-TiO_2 exhibits characteristic peaks at 2θ values of 25.3°, 37.8°, 48.0°, 53.9°, 55.0°, 62.7°, 70.2°, and 75.2°. These peaks correspond to reflections from the (101), (004), (200), (105), (211), (204), (220), and (215) planes of the pure anatase phase [*Hodae et al., 2018*]. The XRD patterns of GT13, GT11, and GT31 nanocomposite demonstrate a two-phase composition of GO and N-TiO_2, with a tetragonal anatase phase that varies in intensity depending on the weight ratio. The figure clearly shows that when the amount of GO in nanocomposites (from GT31 to GT13) decreases, the intensity of the primary characteristic peak of GO at 11.14° in nanocomposites also decreases, indicating that the N-TiO_2 nanoparticle intercalation has disrupted the stacked planes of GO. Furthermore, N-TiO_2 nanoparticles interacting with GO break the stacking layer in (100) planes, resulting in a small shift in the peak at 42.27°. The peaks of the GT31 and GT11 composites are wider and more intense than those of the N-TiO_2 and GT13 composite. The increased intensities and broadening of the N-TiO_2 anatase diffraction planes in the GT31 and GT11 composites may be explained by weak intercalation between N-TiO_2 and GO, indicating N-TiO_2 on GO has a less developed crystalline structure, unlike those exhibited for the GT13 composite. Broadening and a minor

shifting of the N-TiO_2 (101) diffraction peak were found to indicate a decrease in crystallite size as the amount of GO in composites increased [*John et al., 2020*]. **Table 4.1** shows average crystallite sizes of GO, N-TiO_2, GT13, GT11, and GT31. It is evident that composites have smaller crystallites than N-TiO_2. This is most likely due to the inclusion of graphene oxide (GO), which suppresses the N-TiO_2 crystals and forms a coating on the surface of N-TiO_2 [*Natarajan et al., 2021*].

Table 4.1 The average crystallite sizes of GO, N-TiO_2, GT13, GT11, and GT31.

S. No.	Material	Average crystallite sizes (in nm)
1.	GO	5.69
2.	N-TiO_2	13.69
3.	GT13	6.13
4.	GT11	4.35
5.	GT31	3.13

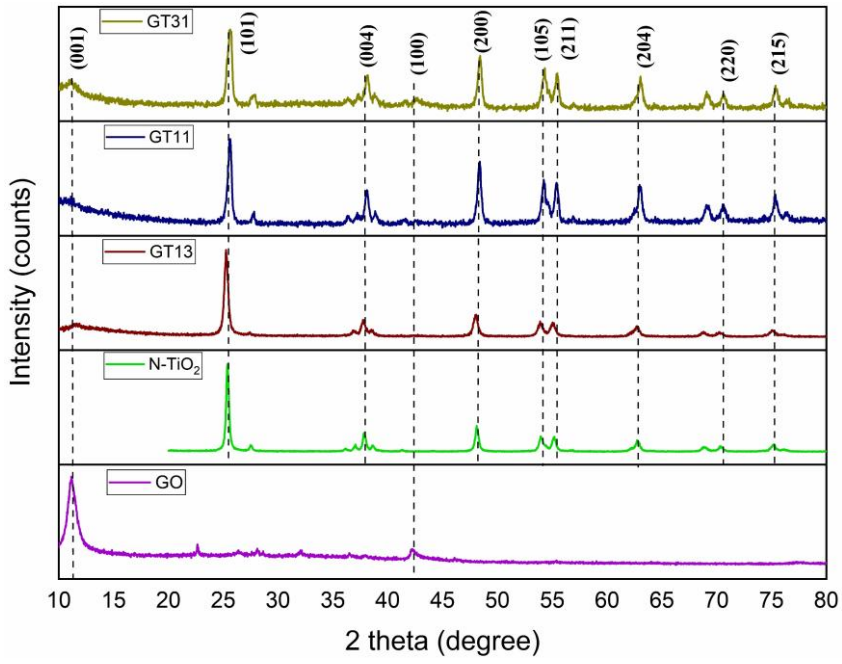


Figure 4.1 XRD analysis of GO, N-TiO_2, GT13, GT11, GT31.

4.1.1.2 Functional group Analysis

Fourier Transform Infrared (FT-IR) spectra of graphene oxide (GO), N-TiO_2, composites GT13, GT11, and GT31 are shown in Figure 4.2. GO showed distinct regions of absorption bands for oxygen-containing groups. The FT-IR spectra of GO show characteristic peaks, including stretching vibrations corresponding to C-O of

epoxy, ether, or peroxide groups (1047 cm^{-1}), bending vibrations of C-O-C to epoxy groups (1223 cm^{-1}), bending vibrations of C-OH hydroxyl groups (1384 cm^{-1}), stretching vibrations of aromatic sp^2 C=C bond (1619 cm^{-1}), and stretching of carboxylic groups C=O (1722 cm^{-1}) [*Nazri et al., 2018, Ruidíaz-Martínez et al., 2020*]. The stretching vibrations of absorbed water molecules and surface O-H groups were confirmed by a broad band at about 3229 cm^{-1}, while the stretching vibrations of symmetrical and asymmetrical CH_2 groups in GO are attributed to very minor peaks at 2918 cm^{-1} and 2846 cm^{-1}, respectively. The FTIR spectra of N-TiO_2 show a peak at 1604 cm-1 due to bending vibrations of O-H or N-H, and another peak at 1478 cm^{-1} due to Ti-N bond vibrations. The peaks in the 750–400 cm^{-1} range represent the vibration of the Ti–O and Ti–O–Ti groups [*Yang et al., 2010*]. The FTIR spectra of GT13, GT11, and GT31 nanocomposites showed additional peaks at 655 cm^{-1} and 435 cm^{-1} for Ti-O-C and Ti-O-Ti vibrations, respectively [*Ida et al., 2020*], indicating the chemical interaction between N-TiO_2 and graphene oxide [*Nguyen-Phan et al., 2011*]. The FTIR spectra of GT13 do not show the significant absorption at 1720 cm^{-1} for GO, indicating the disappearance of the C=O group. This can enhance electron mobility by reducing the number of oxygen-containing functional groups, such as hydroxyl, carboxyl, and epoxide groups, and by rebuilding a portion of the conjugated structure within graphene oxide [*Pei et al., 2013*].

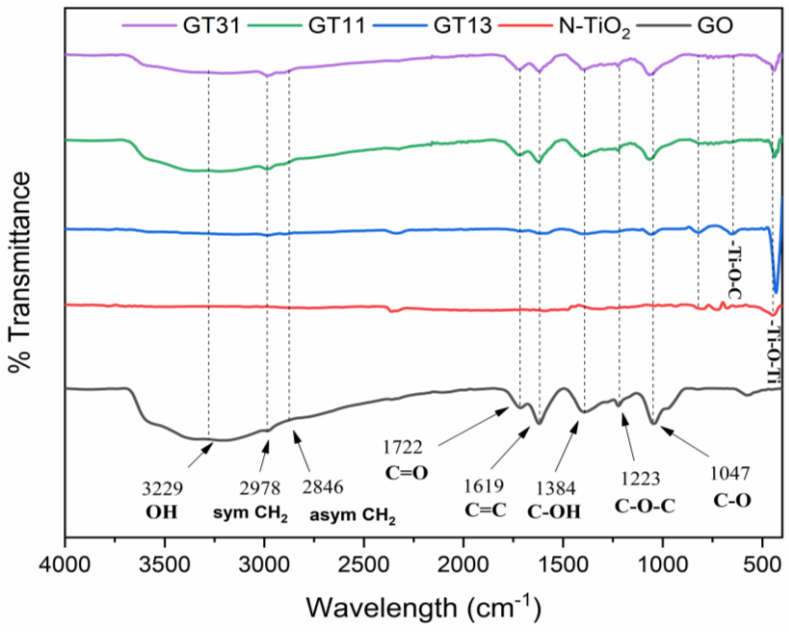


Figure 4.2 FTIR spectra of GO, N-TiO_2, GT13, GT11, and GT31.

4.1.1.3 Scanning Electron Microscopy and Energy-Dispersive X-ray Spectroscopy Analysis

The FESEM pictures of the GT13, GT11, and GT31 composites are shown in **Figure 4.3**. N-TiO_2 nanoparticles were found to be spherical, and some particles largely agglomerated together into clusters. The graphene oxide showed a crumpled structure with folded sheets. The composites showed cross-linking of N-TiO_2 nanoparticles on the GO sheet, leading to network structures [*Patil et al., 2021*]. It seems that adding GO to the composites did not significantly alter the morphological characteristics of N-TiO_2. Additionally, there were no notable variations in the SEM images of the composites.

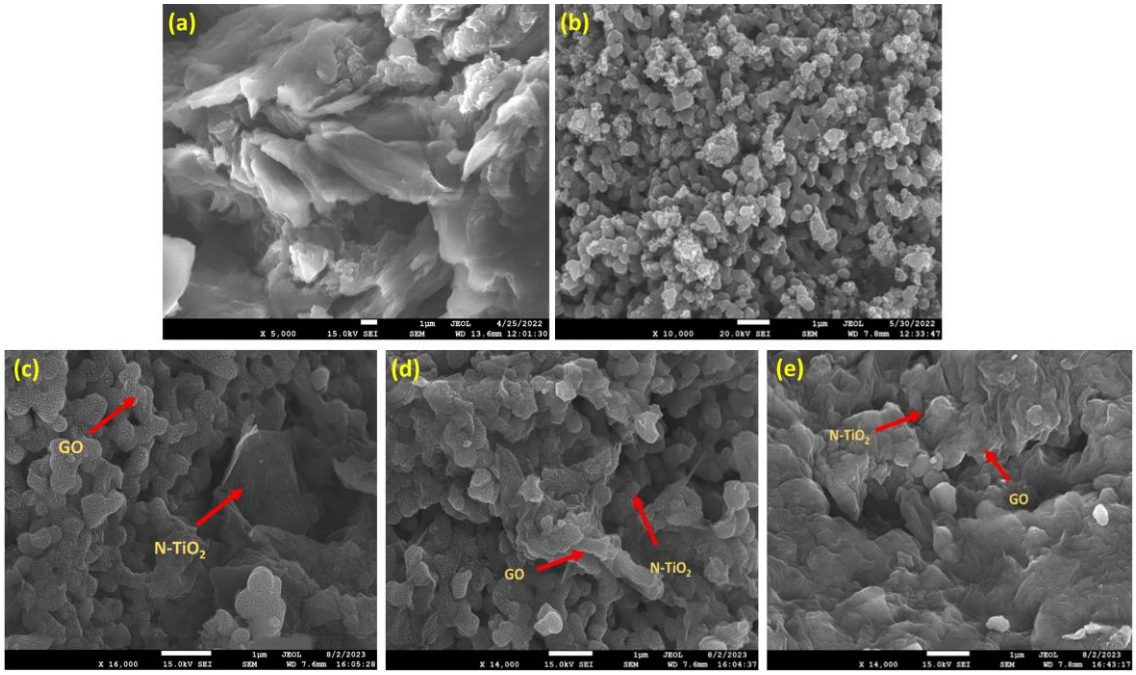
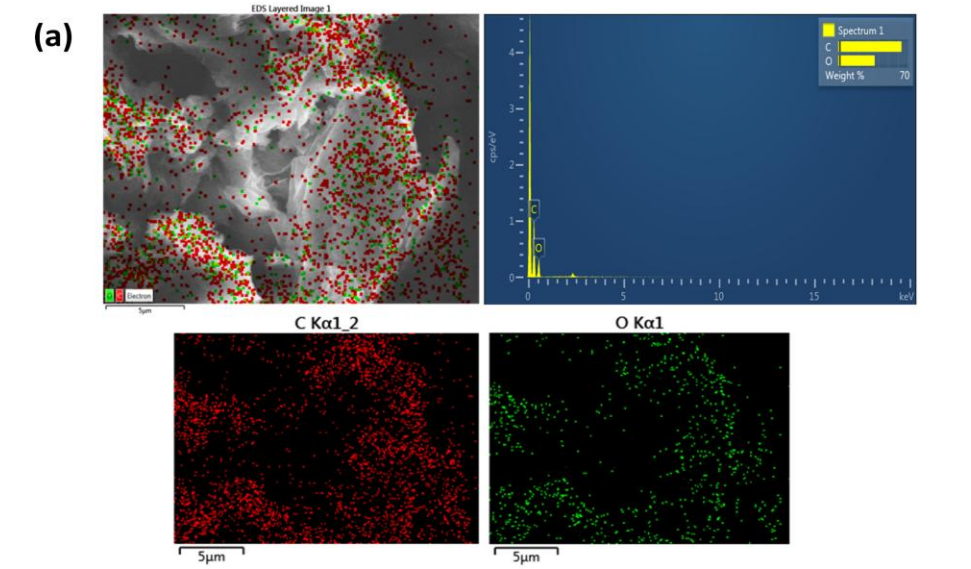
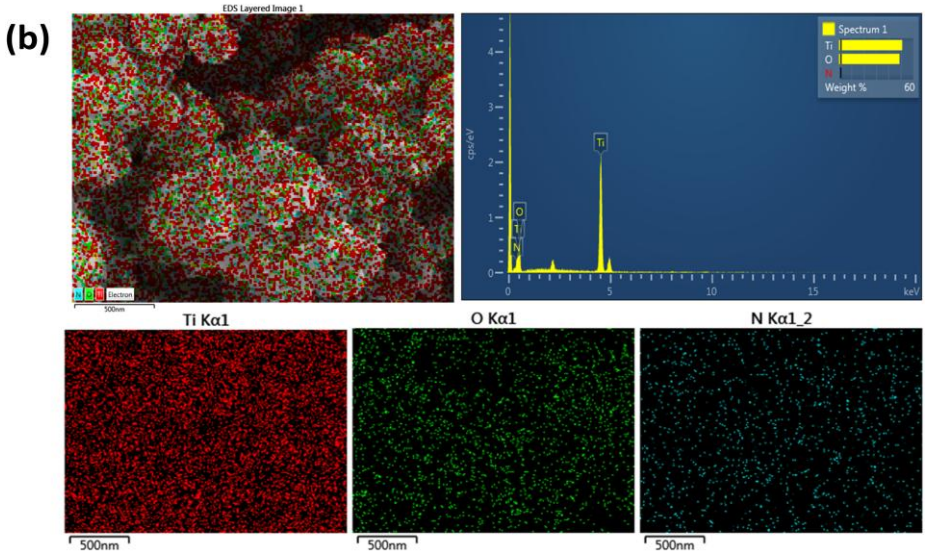
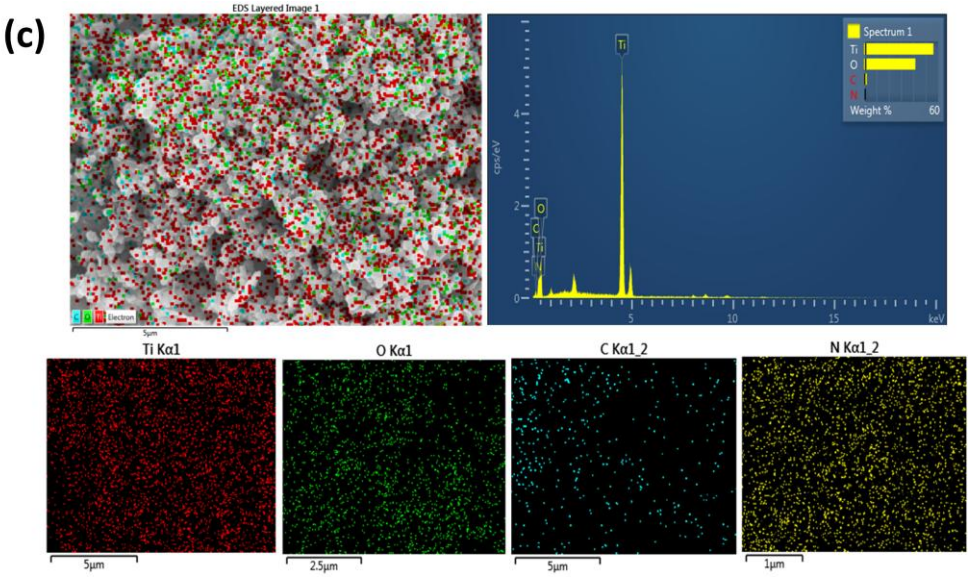


Figure 4.3 Scanning electron microscope (SEM) images of (a) GO (b) N-TiO_2 (c) GT13 (d) GT11 and (e) GT31 composite.

The elemental composition of all produced composites was determined by energy dispersive X-ray analysis (EDX). The EDX spectrum is shown in **Figure 4.4**, and the quantitative elemental composition is shown in **Table 4.2**. The maps indicate a distinct distribution of each element, indicating that N-TiO_2 nanoparticles were well spread or embedded between the GO layers. The presence of C, O, Ti, and N peaks indicated that the GT13, GT11, and GT31 composites were successfully formed without impurities. Carbon weight ratios often increased as the GO to N-TiO_2 ratio increased.


(a)
EDS Layered Image 1
Spectrum 1
C
O
Weight %
70
cps/eV
keV
C Kα1_2
O Kα1
5µm
5µm


(b)
EDS Layered Image 1
Spectrum 1
Ti
O
N
Weight %
60
cps/eV
keV
Ti Kα1
O Kα1
N Kα1_2
500nm
500nm
500nm


(c)
EDS Layered Image 1
Spectrum 1
Ti
O
C
N
Weight %
60
cps/eV
keV
Ti Kα1
O Kα1
C Kα1_2
N Kα1_2
5µm
2.5µm
5µm
1µm

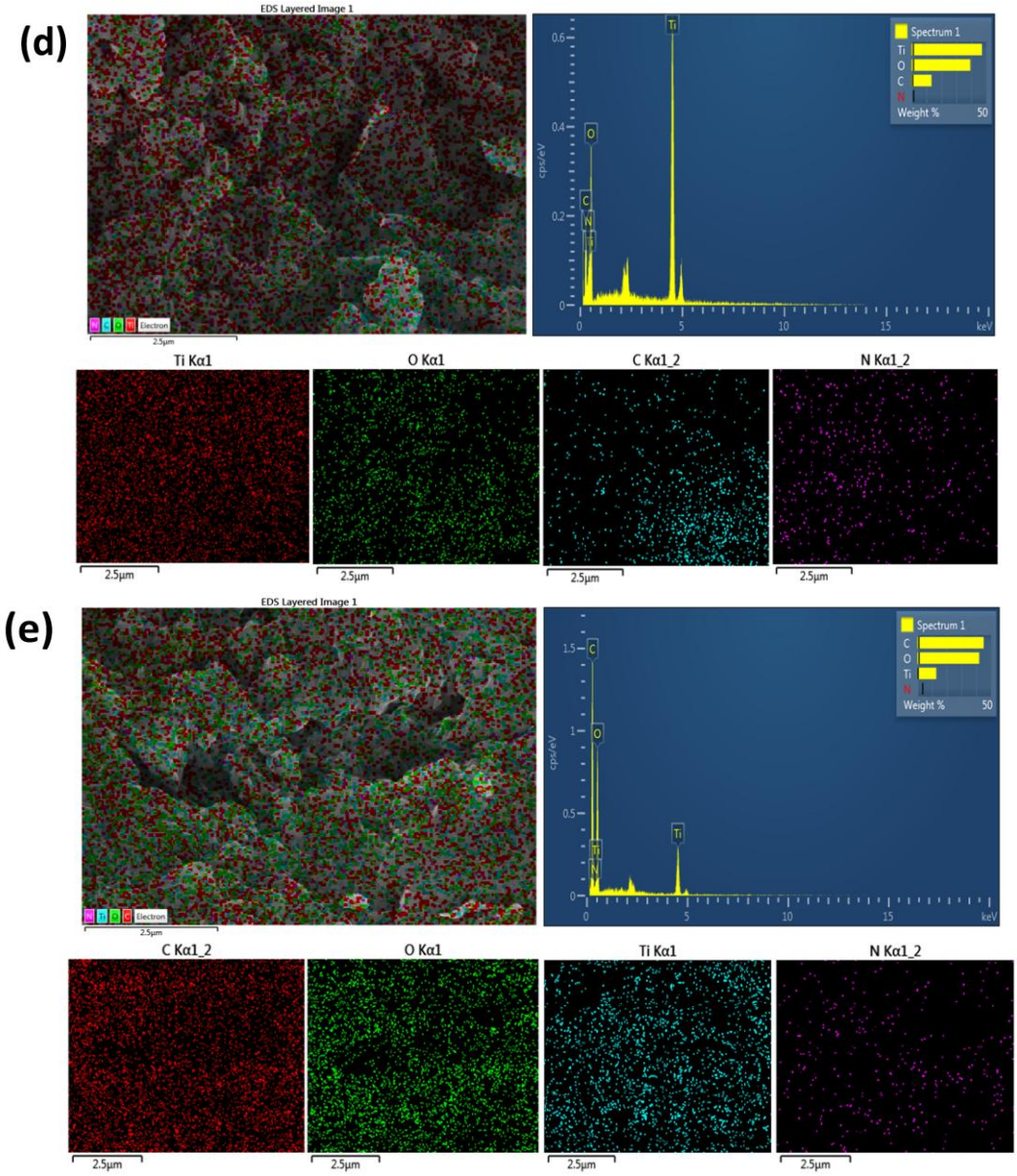


Figure 4.4 EDS mapping of (a) GO (b) N-TiO_2 (c) GT13 (d) GT11 and (e) GT31 composite

Table 4.2 Content of elements in atomic% and weight % of GO, N-TiO_2, GT13, GT11 and GT31.

Composite →	**GO**		**N-TiO_2**		**GT13**		**GT11**		**GT31**	
Elements ↓	Atomic %	Weight %	Atomic %	Weight %	Atomic %	Weight %	Atomic %	Weight %	Atomic %	Weight %
C	69.83	63.47	-	-	24.71	13.31	24.38	13.36	56.44	45.10
O	30.17	36.53	74.11	48.87	52.47	37.66	54.00	39.41	39.53	42.06
N	-	-	0.00	0.00	0.00	0.00	0.00	0.00	0.00	0.00
Ti	-	-	25.89	51.13	22.82	49.03	21.62	47.23	4.03	12.84
Total	100.00	100.00	100.00	100.00	100.00	100.00	100.00	100.00	100.00	100.00

4.1.1.4 Optical Bandgap Analysis

Optical band gap of GO and N-TiO_2, GT13, GT11, and GT31 are shown in **Figure 4.5**, and the values are given in **Table 4.3**. There were two band gap values discovered for the GT13 and GT11 composites. The individual transition of N-TiO_2 was responsible for the band gaps seen at 2.8 and 2.9 eV for GT13 and GT11, respectively, while the band gaps reported at 2.1 eV and 2.4 eV, respectively, were caused by the synergistic action of N-TiO_2 and GO in composites [*Bansal et al., 2015*]. The individual transition of N-TiO_2 disappeared due to the high concentration of GO in GT31. The band gap narrowing in the composites GT13, GT11, and GT31 may be attributed to the improved chemical bonding between N-TiO_2 and GO by the formation of Ti-O-C bonds at the interface between N-TiO_2 and GO [*Juárez et al., 2019*], as further supported by FT-IR and XRD studies. The bonding of free electrons on the surface of N-TiO_2 with unpaired π- electrons is the cause of formation of Ti–O–C bonds. Furthermore, when crystallite size increased, the composite's band gap reduced due to severe quantum confinement in nanoscale crystals, as confirmed by XRD results [*Khammar et al., 2020*].

Table 4.3 Optical band gap values of GO, N-TiO_2, GT13, GT11 and GT31.

S. No.	Material	Optical band gap (E_g) (eV)
1.	GO	2.2
2.	N-TiO_2	2.9
3.	GT13	2.1–2.8
4.	GT11	2.4–2.9
5.	GT31	2.6

The valence band (VB) and conduction band (CB) of a semiconductor originate from the highest occupied molecular orbitals (HOMO) and lowest unoccupied molecular orbitals (LUMO), respectively [*Al-Madanat et al., 2021*]**.** In N-doped TiO_2, nitrogen introduces N 2p states above the O 2p-derived valence band maximum. These N 2p states raise the HOMO energy, reducing the excitation energy required for electron transition. The LUMO is mainly composed of Ti 3d states. Although N-doping primarily modifies the VB, it can also create oxygen vacancies that introduce mid-gap states, which may serve as lower-energy LUMO levels or coexist with the Ti 3d CB.

The reduced energy gap between the N 2p-derived VB (or mid-gap states) and the Ti 3d conduction band narrows the bandgap, shifting TiO_2 absorption into the visible region [*Saini et al., 2020*].

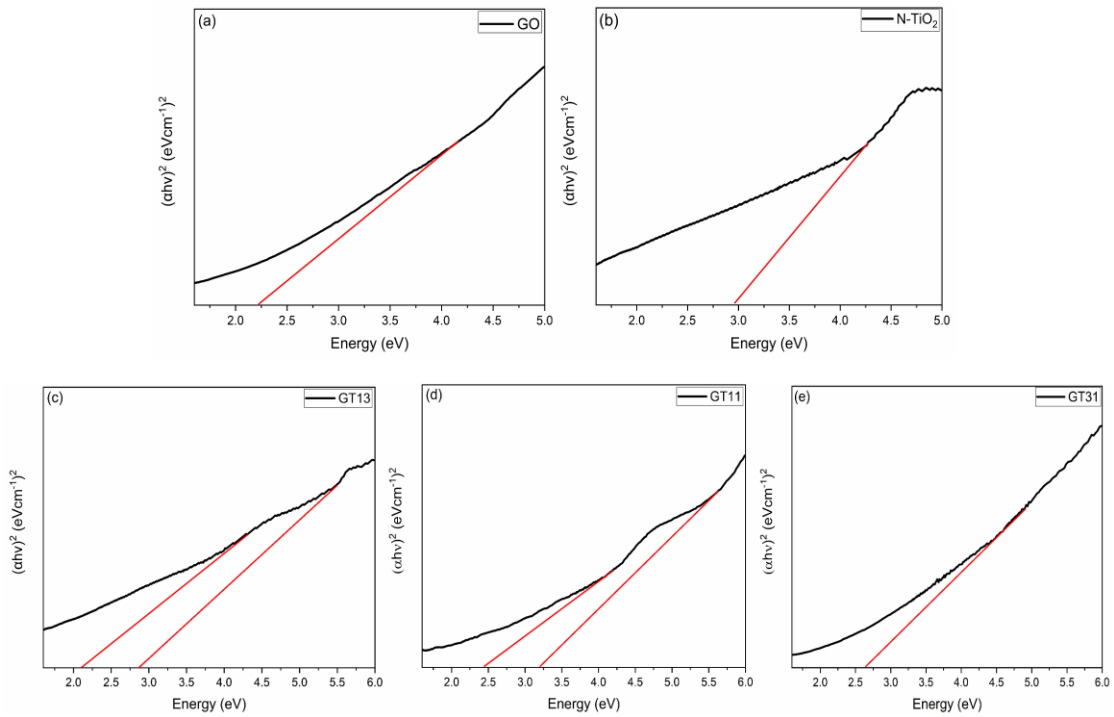


Figure 4.5 Optical bandgap of (a) GO (b) N-TiO_2 (c) GT13 (d) GT11 and (e) GT31 using Tauc's plot.

4.1.1.5 Thermogravimetric Analysis

Thermogravimetric analysis (TGA) was used to investigate the thermal stability of the materials at a heating rate of 10°C/min under an N_2 environment. **Figure 4.5** displays the TGA curves for the bare GO, N-TiO_2, and the composite materials GT13, GT11, and GT31, which include three stages of weight loss up to 600°C. In the first stage, water molecules and adsorbed solvents desorb below 180°C. In the second step, which takes place between 200 and 270°C, oxygen atoms are lost along with the release of CO_x species from the labile functional groups (such epoxy, hydroxyl, and carboxyl) in the GO structure. The final stage involves the destruction of the GO carbon backbone at temperatures above 350°C and GO lose more stable oxygenated groups, including carbonyls, at this point [*Ganguly et al., 2011*].

The percentage weight loss of GO, N-TiO_2, GT13, GT11, and GT31 at different steps, along with the overall weight reduction percentage is shown in **Table 4.4**.

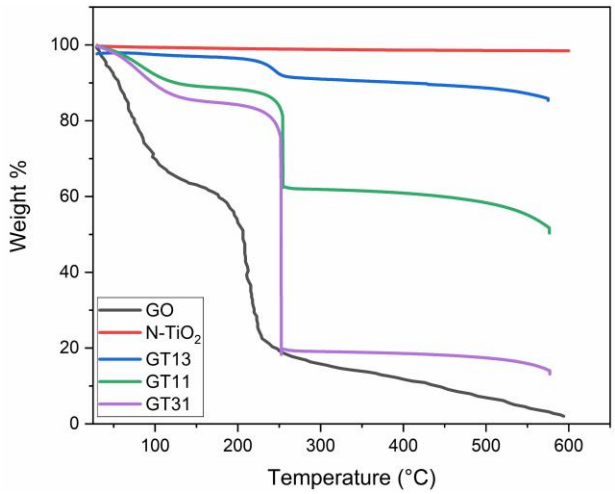


Figure 4.6 TGA of GO, N-TiO_2, GT13, GT11, and GT31 composites.

In comparison to GT11 and GT31, the composite GT13 showed a comparatively lower overall weight loss. This suggests that the GT13 composite has greater thermal stability compared to GT11 and GT31, and thermal stability of synthesized composites increases in the following order: GT13 > GT11 > GT31. The latter two may have seen more mass losses in their second and third stages because to the increased concentration of GO, which has a higher proportion of labile oxygen functional groups connected to the surface in its hexagonal structure [*Chang et al., 2012*].

Table 4.4 Comparison of % weight loss of composites in three different stages and total weight loss

Material	First stage	Second stage	Third stage	Total weight loss (%)
GO	35.1%	44.8%	16.9%	96.8%
N-TiO_2	0.24%	0.29%	0.94%	1.47%
GT13	1.13%	5.56%	6.12%	12.8%
GT11	11.1%	26.8%	11.3%	49.2%
GT31	15.1%	65.28%	5.1%	85.5%

4.1.1.6 Photoluminescence Analysis

The recombination process in GO/N-TiO_2 composites was investigated using PL experiments. The PL spectra for N-TiO_2 and all the composite samples are shown in **Figure 4.7**. An excitation wavelength of 230 nm was used to record the spectra of powdered materials. The PL spectra show that when the concentration GO increases in composites, peak intensity decreases and reaches a minimum for GT31. A decrease in

the peak intensity of the PL spectrum indicates that the addition of GO reduces N-TiO_2 recombination due to an immediate electron transfer from N-TiO_2 to GO via a Ti-O-C bond [*Yadav et al., 2019*]. The intensity decrease is caused by the quick transfer of photogenerated electrons by GO, which inhibits electron-hole pair recombination [*Shi et al., 2014, Ni et al., 2014*]. In **Figure 4.7**, the emission peaks in the 400–600 nm wavelength region may be due to oxygen vacancy defects, dopants, or defects in the lattice of GO/N-TiO_2 composites. Previous research indicates that surface defects such as oxygen vacancy states and Ti^{3+} species occur at energy levels between the conduction band (CB) and the valence band (VB), increasing the photo-response to visible light [*Tho et al., 2019*].

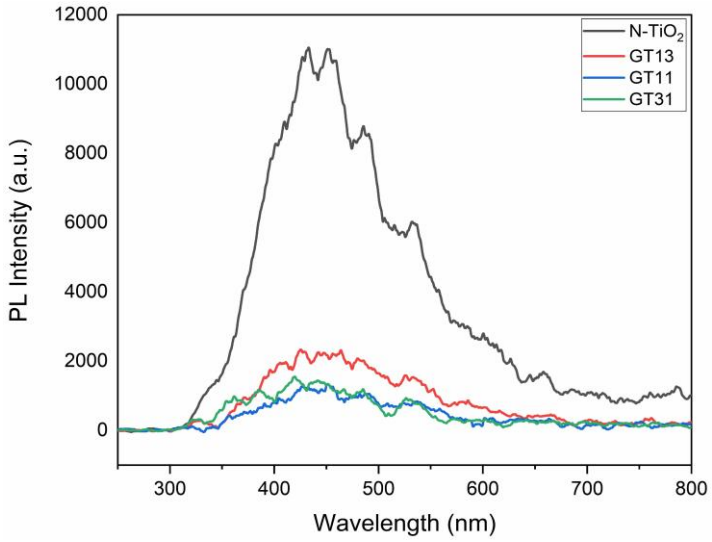


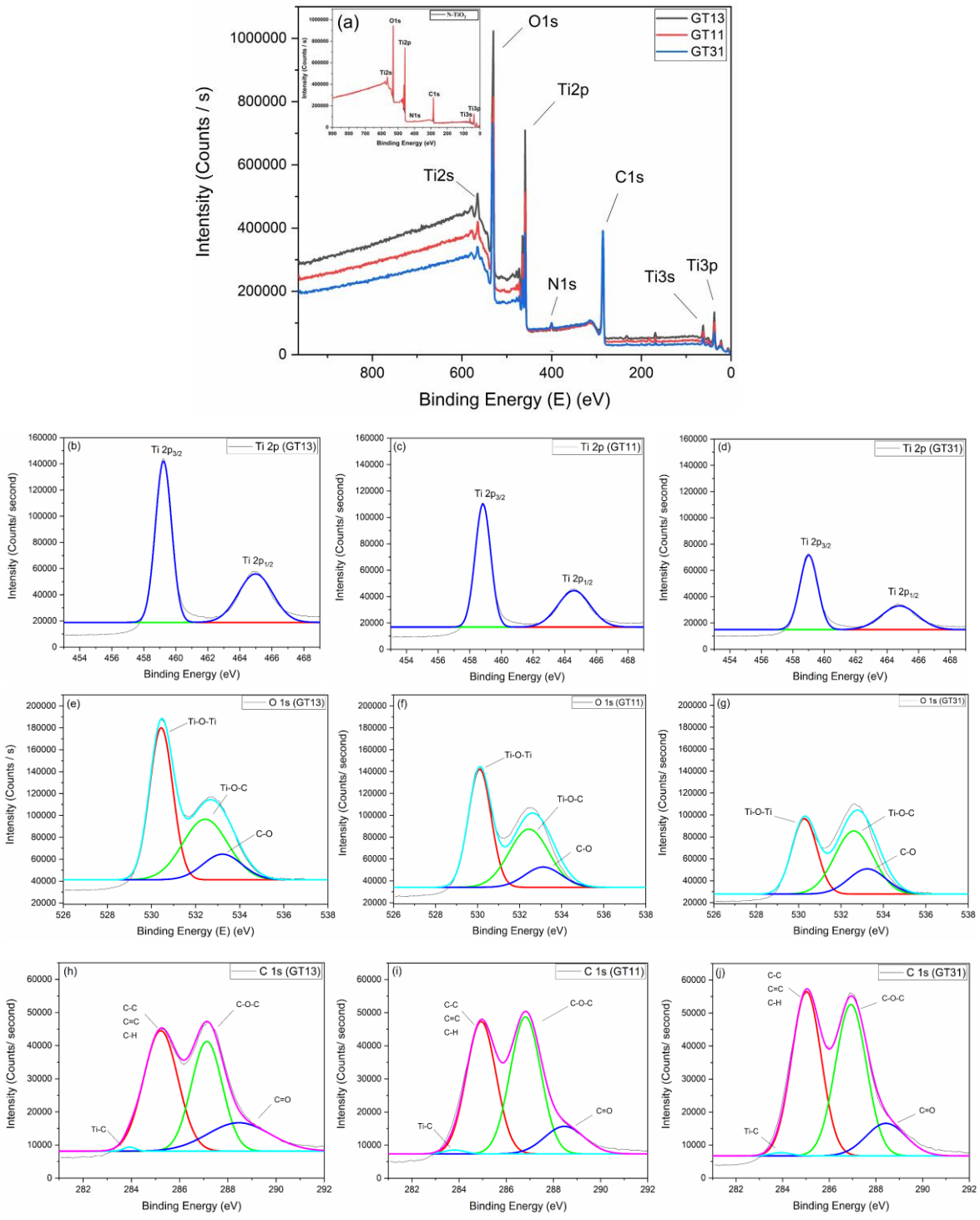
Figure 4.7 Photoluminescence emission spectra of N-TiO_2, GT13, GT11 and GT31.

4.1.1.7 X-Ray Photoelectron Spectroscopy Analysis

The composite materials were analyzed using XPS to determine the chemical bonding and interactions between GO and N-TiO_2. The fully scanned XPS of GT13, GT11, and GT31 shown in **Figure 4.8(a)** indicates the presence of carbon, titanium, nitrogen, and oxygen in the composite.

The Ti 2p spectrum spectra of composite materials in the 450–470 eV range consist of two centered peaks at 458.8 eV and 464.5 eV, respectively, which are ascribed to Ti $2p_{3/2}$ and Ti $2p_{1/2}$, according the XPS Wagner Handbook [*Wagner, 1979*]. The separation energy of 5.7 eV is equivalent to Ti^{4+} binding energies in pure anatase [*Sheydaei et al., 2018*]. According to the results, all three composites include TiO_2, and

the Ti 2p position remains constant. The deconvoluted components generated for Ti $2p_{3/2}$ for the GT13, GT11, and G31 composites show that anatase titanium, or Ti^{4+}, is present in the Ti-O bonds. A peak at 458.3 eV revealed the presence of Ti^{4+} in the composite. As can be seen from the intensity of Ti $2p_{3/2}$, the Ti^{4+} level in GT13 is substantially greater than in GT11 and GT31 [**Figure 4.8(b), 4.8(c), 4.8(d)**].



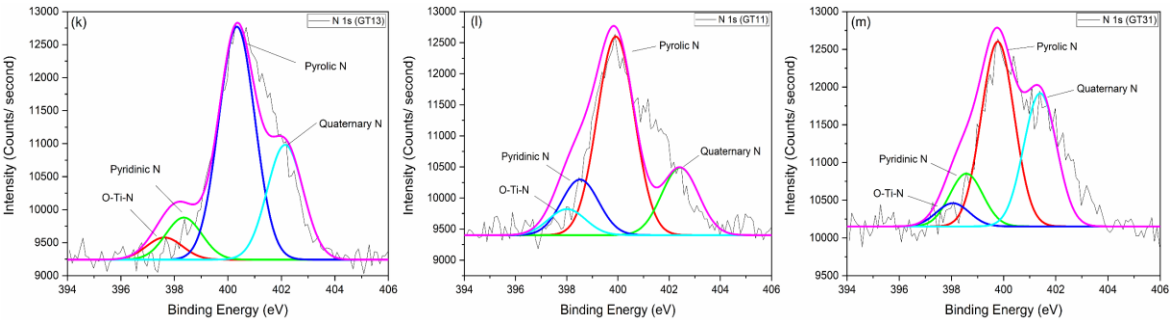


Figure 4.8 (a) Fully scanned XPS of GT13, GT11 and GT31; XPS spectra of Ti 2p states for (b) GT13, (c) GT11 and (d) GT31; O 1s states for (e) GT13, (f) GT11 and (g) GT31; C 1s states for (h) GT13, (i) GT11 and (j) GT31; N 1s states for (k) GT13, (l) GT11 and (m) GT31.

Figures 4.8(e), 4.8(f), and 4.8(g) show the O 1s spectra at the core level for each composite. O1s in the O–Ti bond of TiO_2 is represented by the signal at 532.3 eV [*Shi et al., 2012*]. According to earlier research, the main peak of O 1s in pure N-TiO_2 nanoparticles can be deconvoluted into two peaks. The Ti-OH bond exhibits the first peak, which is centered at approximately 529.7 eV, while the Ti-O-Ti bond exhibits the second peak, which has a higher binding energy of 531.4 eV [*Xing et al., 2009*]. However, a single peak in the composites at 532.4 eV is caused by the presence of epoxy and hydroxyl groups found on the surface of the GO layer [*Yu et al., 2014*]. In **Figure 4.8(e), 4.8(f), and 4.8(g)**, the intensity of this peak is considerably lower for GT13 composites than for GT11 and GT31 composites. This indicates that all oxygen-containing groups on the surface of GO are reduced upon the addition of N-TiO_2. The two peaks in the O 1s level for the sample with less GO (GT13) are nearly identical to those observed for pure N-TiO_2. On the other hand, the peak at 529.7 eV and 531.4 eV that is ascribed to O in N-TiO_2 shows a positive shift of 0.37 eV and 1.1 eV for the composite GT11, which has peak values of 530.07 eV and 532.5 eV, respectively. Additionally, GT31 showed a positive shift of 0.52 eV and 1.17 eV, with peak values of 532.67 eV and 530.22 eV, respectively. It shows that GO and N-TiO_2 have a strong bond generated by electron transfer from the latter to the former. The N-TiO_2 peak in the O 1s level decreases in composite GT31 with a higher GO content (**Figure 4.8g**), indicating that GO coverage leads to less N-TiO_2 on the surface. At maximal loading, XPS results show that GO sheets predominantly surround N-TiO_2. After deconvolution, the peak 533.2 eV is ascribed to the Ti-O-C bond that develops at the interface between GO and N-TiO_2 [*Umrao et al., 2014*].

The presence of sp^2 hybridized carbon atoms of GO, indicated by C-C, C=C, and C-H bonds, is typically associated with a peak in the C 1s spectrum at approximately 284.7-285.0 eV. This peak is often referred to as the "graphitic" or "aromatic" carbon peak [*Bhunia et al., 2014*]. The XPS spectra of the C 1s level of the GT13, GT11, and GT31 composites are primarily deconvoluted into various peaks as shown in **Figure 4.8(h), 4.8(i), and 4.8(j)**, respectively. For GT13, GT11, and GT31, the peaks with binding energy values in the range of 285.9-288.4 eV correspond to C-O-C and C=O bonds [*Kusiak-Nejman et al., 2018, Tho et al., 2019*]. As seen in **Figures 4.8(h), 4.8(i), and 4.8(j)**, a weak signal was found by resolution analysis of the C1s binding energies of the XPS spectra at 283.5 eV for GT13 as compared to GT11 and GT31 because of the low concentration of GO. N-TiO_2 and graphene oxide form a Ti-C bond, which is another important component in expanding the photo-responsive wavelength of the composites [*Tho et al., 2019*].

The presence of nitrogen and its efficient doping into Ti (TiO_2), as shown by the peak at 399.8 eV in Figure **4.8 (k-m)**. By replacing oxygen atoms in the TiO_2 lattice, the peak verifies the formation of an O-Ti-N bond [*Shi et al., 2012*].

The results presented above provide confirmation of the formation of the GT13, GT11, and GT31 nanocomposites. **Table 4.5** displays the surface elements composition of the GT13, GT11, and GT31 composites.

Table 4.5 Surface elemental composition of composites GT13, GT11 and GT31

Element	Composite	Peak/eV	Composition/at. %
C 1s	GT13	286.04	42.68
	GT11	285.67	48.88
	GT31	285.63	56.89
O 1s	GT13	531.01	43.4
	GT11	530.68	39.8
	GT31	531.59	34.51
N 1s	GT13	400.72	1.72
	GT11	400.18	1.6
	GT31	400.28	2.02
Ti 2p	GT13	459	12.2
	GT11	458.37	9.72
	GT31	458.92	6.58

4.1.2 Characterization of Pollutants Polyvinylchloride Nanoparticles (PVC-NPs) and Polystyrene Nanoparticles (PS-NPs)

Perylene-3,4,9,10-tetracarboxytetrabutylester (PTE), PVC-NPs and PS-NPs were thoroughly characterized as follows before investigating the removal of PVC-NPs and PS-NPs with synthesized materials.

4.1.2.1 Nuclear Magnetic Resonance Analysis of PTE

^{1}H NMR ($CDCl_3$, 500MHz): 0.95 (t, 12H), 1.46 (m, 8H), 1.77 (m, 8H), 4.26 (t, 8H), 7.72 ppm (m, 8H).

^{13}C NMR ($CDCl_3$, 100 MHz): 13.8, 19.3, 30.7, 65.3, 121.1, 128.3, 128.5, 130.1, 132.4, 168.5 ppm [*Ozser et al., 2017*].

4.1.2.2 Optical Analysis of *PVC-NPs*

Figure 4.8 shows the optical properties of the PVC that has been encapsulated with PTE dye. Two distinctive peaks were visible in the UV-vis spectra of the PTE dye enclosed within the PVC nanoparticles at 446 and 470 nm (Figure 4.8(a)), and a distinctive peak was visible in the emission spectra at 550 nm (**Figure 4.8(b)**).

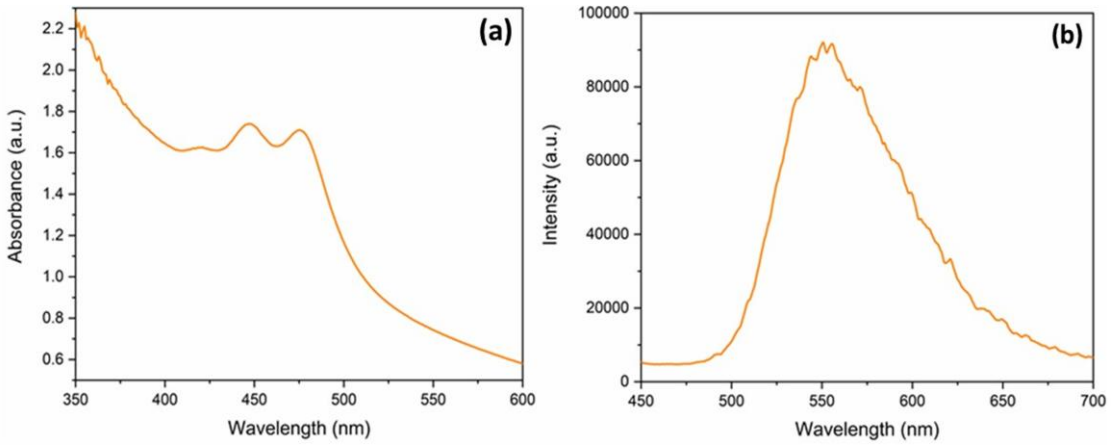
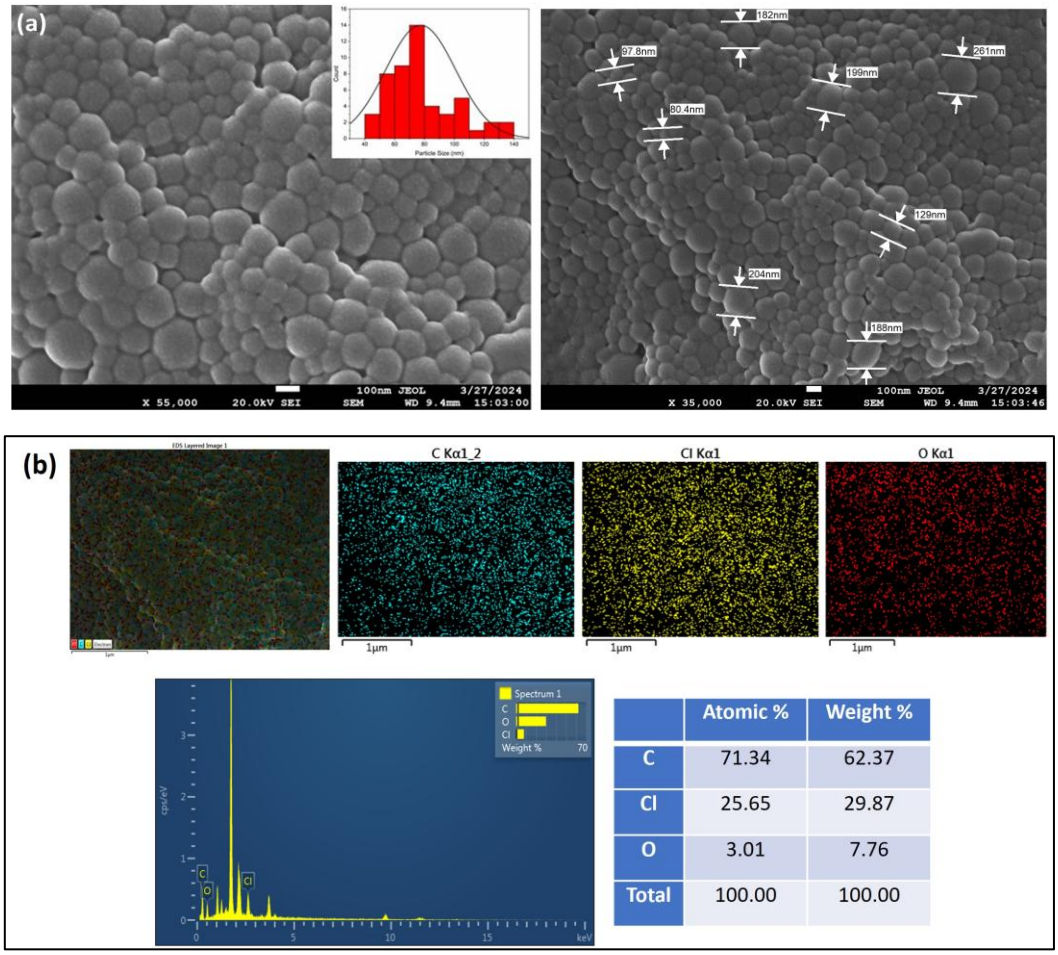


Figure 4.9 (a) Absorption (b) emission spectra of PVC-NPs nanoparticles dispersed in water.

4.1.2.3 Scanning Electron Microscopy and Energy-Dispersive X-ray Spectroscopy Analysis of PVC-NPs

The size distribution and shape of the nanoparticles were examined using scanning electron microscopy (SEM), and the SEM micrographs of PVC-NPs revealed a

spherical morphology, as seen in **Figure 4.9(a)**. The inset of **Figure 4.9(a)** depicts the size analysis of all PVC nanoparticles collected from SEM micrographs, with an estimated average particle size of 69.9 nm.



	Atomic %	Weight %
C	71.34	62.37
Cl	25.65	29.87
O	3.01	7.76
Total	100.00	100.00

Figure 4.10 (a) SEM images depicting morphology of PVC-NPs and the inset represents the size distribution curve of PVC-NPs obtained from SEM image at scale bar 100nm; (b) EDS mapping and elemental atomic% and weight% of PVC-NPs.

4.1.2.4 Dynamic Light Scattering Analysis of *PVC-NPs*

Furthermore, dynamic light scattering (DLS) studies of PVC-NPs in water were used to evaluate their hydrated size and zeta potential. The average hydrodynamic size of the PVC-NPs ranged from 120.9 to 123.7 nm, and their zeta potential at neutral pH (7.0) and room temperature was found to be negative, ranging from -21.5 to -30.3 mV. The polydispersity index (PDI) is another essential parameter that describes the width or spread of the particle size distribution. The PDI value of PVC-NPs was determined to

be 0.132, indicating mid-range polydisperse particle size distributions [*Raval et al., 2019*].

DLS readings represent particle size when hydrated, whereas SEM micrographs normally measure particle diameters under dry conditions. DLS exhibited a wider size distribution for PVC polymer particles compared to SEM micrographs. This was due to a discrepancy in measuring conditions, as DLS data showed hydrated size, whereas SEM determined dry size of particles.

4.1.2.5 Functional group Analysis of PVC-NPs

Figure 4.11(a) displays the FT-IR spectra of pure perylene-3,4,9,10-tetracarboxytetrabutylester (PTE). Peaks associated with 2962 cm^{-1}: (C_{Ar}-H), 2874 cm^{-1}: (C_{Alkyl}-H), 1722 cm^{-1}: (C=O), and 1276–1172 cm^{-1} (C-O) are found in the pure PTE spectrum. Following the addition of PTE to PVC, PVC-NPs displayed comparable peaks (**Figure 4.11(b)**), along with additional characteristic peaks of PVC. The new peaks at 616, 692, and 831 cm^{-1} are ascribed to the stretching of C-Cl groups [*Mallakpour et al., 2017*], CH_2-Cl angular deformation at 1425 cm^{-1}, -CH-Cl out of plane angular deformation at 1279 cm^{-1}, C-H out of plane trans deformation at 960 cm^{-1}, and cis -CH wagging 2912 cm^{-1}. Furthermore, the stretching vibrations of CH_2 and C-C are correlated with the peaks at 2971 cm^{-1} and 1097 cm^{-1}, respectively. These characteristic peaks of PVC matched with reported data [*Coltro et al., 2013*].

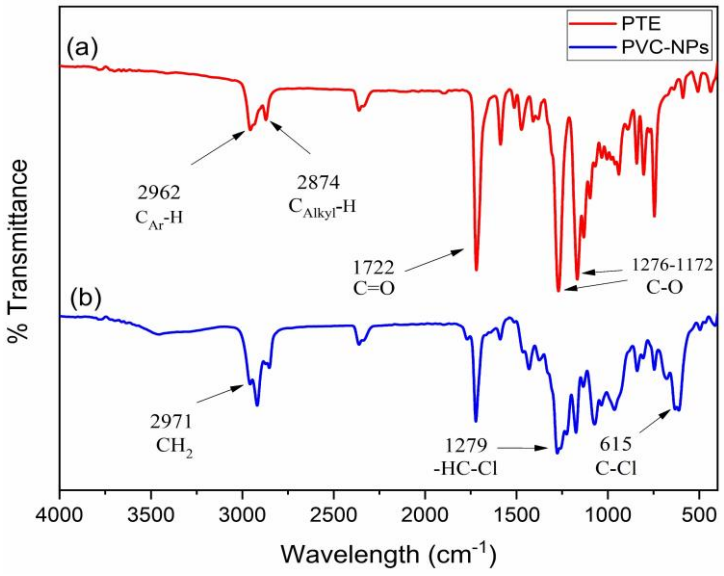


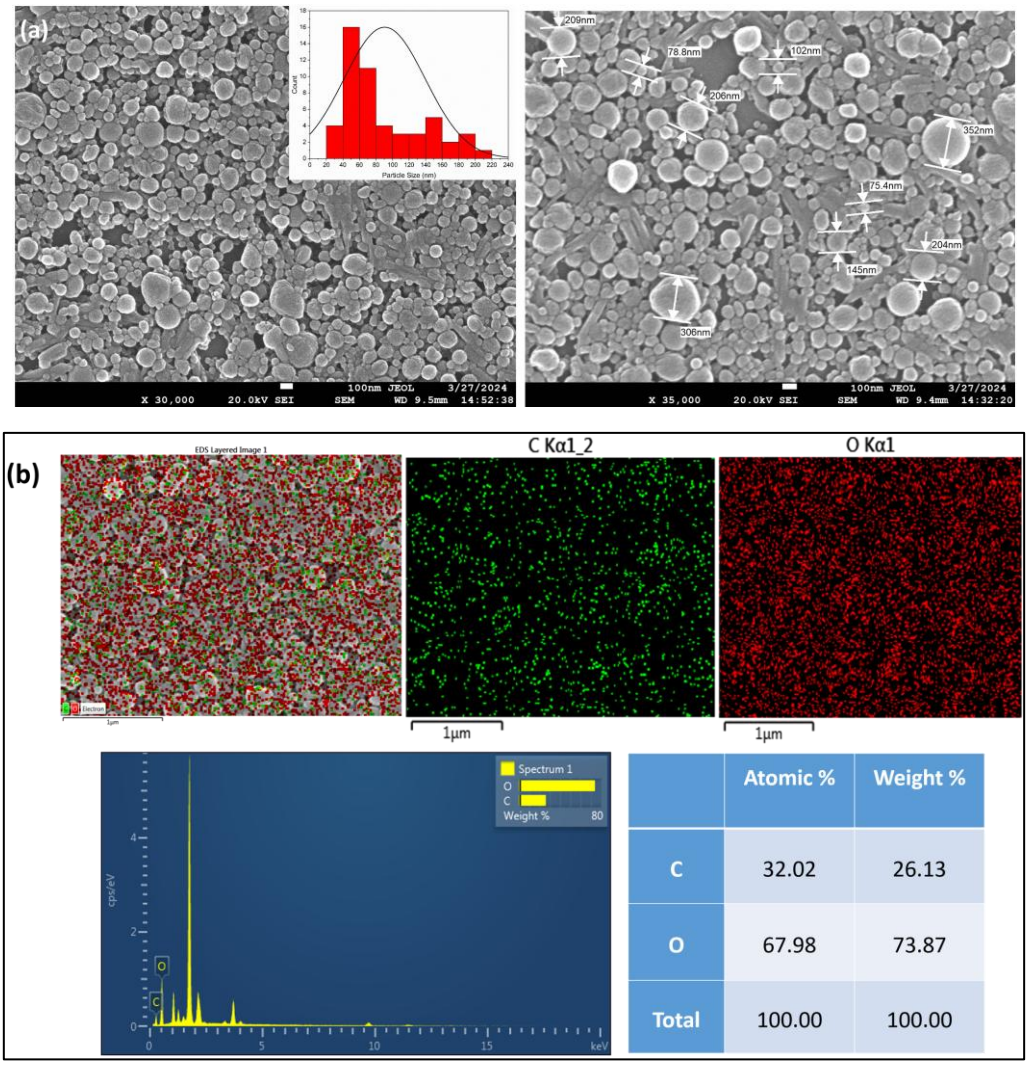
Figure 4.11 FTIR spectra of (a) PTE and (b) PVC-NPs.

4.1.2.6 Field Emission Scanning Electron Microscopy Analysis of PS-NPs

Scanning Electron Microscopy (SEM) was used to investigate the shape and size distribution of the nanoparticles, and a spherical morphology has been observed in the SEM micrographs of PS-NPs, as shown in **Figure 4.12**. The inset of **Figure 4.12(a)** depicts the size analysis of all PS nanoparticles collected from SEM micrographs, with an estimated average particle size of 90.4 nm.

4.1.2.7 Energy Dispersive X-ray Analysis of PS-NPs

EDX analysis was used to examine the elemental composition of the adsorbents; the profiles that were produced are displayed in **Figure 4.12**, and Table displays the percentage of each element. Results indicated that C and O are present in high percentage.



	Atomic %	Weight %
C	32.02	26.13
O	67.98	73.87
Total	100.00	100.00

Figure 4.12 (a) SEM images depicting morphology of PS-NPs and the inset represents the size distribution curve of PS-NPs obtained from SEM image at scale bar 100nm; (b) EDS mapping and elemental atomic% and weight% of PS-NPs.

4.1.2.8 Dynamic Light Scattering Analysis of *PS-NPs*

Zeta potential of the prepared PS-NPs was measured in water at neutral pH (7.0) and room temperature. PS-NPs exhibited negative charge of value -34.8 mV. The hydrated size and zeta potential of PS-NPs was measured using dynamic light scattering. The size distribution of all PS polymer particles obtained from dynamic light scattering (DLS) was 253.2 nm. The size distribution of PS polymer particles obtained from DLS was larger than the values obtained from SEM micrographs owing to the different conditions (i.e., hydrated in DLS and dry in SEM) of measurements. The polydispersity index (PDI) is another important parameter that describes the width or spread of the particle size distribution. The PDI value is 0.194, implies polydisperse particle size distributions [*Raval et al., 2019*].

4.1.2.9 Functional group Analysis of PS-NPs

Figure 4.13 displays the FT-IR spectra of pure perylene-3,4,9,10-tetracarboxytetrabutylester (PTE) (already discussed in **Section *4.1.2.5)***.

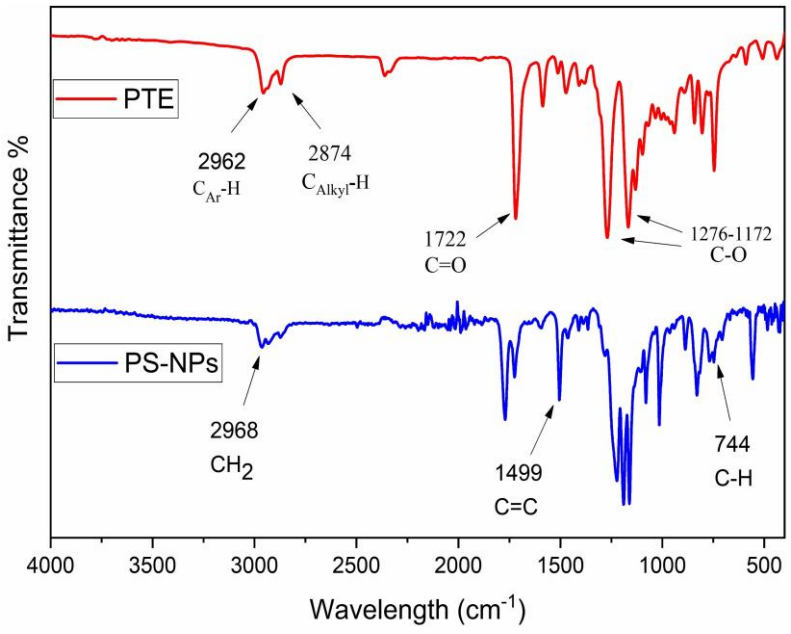


Figure 4.13 FTIR spectra of PTE and PS-NPs.

Following the addition of PTE to PS, PS-NPs displayed comparable peaks (**Figure 4.19**), along with a few more distinctive PS peaks. The band at 2919 cm^{-1} represents the vibration of the CH_2 group. Additionally, the transmission bands at 1499 cm^{-1} were attributed to the aromatic C=C stretching vibration of the benzene ring, as expected in the PS structure. Strong vibrational modes at 744 cm^{-1} indicate out-of-plane bending vibration of C-H, which is characteristic for polystyrene [*Budlayan et al., 2021*].

4.1.3 Photocatalytic Degradation and Adsorption Study of GO/N-TiO_2 Composites under different Conditions

4.1.3.1 Removal Study of PVC-NPs using GO/N-TiO_2 Nanocomposites

Synthesized composites with varying weight ratios of GO: N-TiO_2 (1:3, 1:1, and 3:1) were used to remove PVC-NPs when exposed to visible light sources (a tungsten bulb and room light) at pH values of 4, 7, and 10, with varying catalyst doses and irradiation times (30, 60, 90, 120, 150, and 180 minutes) within 3 hours. The similar experiments were conducted in the dark as well. The concentration change in PVC-NPs was measured at λ_{max} 446nm.

In order to evaluate the effect of adsorption on the degrading efficiency of PVC-NPs, an adsorption experiment was conducted using all three synthesized composites, namely GT13, GT11, and GT31 under dark. Under these experimental conditions, PVC-NP removal efficiency for GT13, GT11, and GT31 at pH 4 were determined to be 51.42%, 23.17%, and 17.6%.

Moreover, similar experimental conditions were used for photocatalytic study under tungsten bulb light and room light sources. The photocatalytic degradation results showed that the GT13, GT11, and GT31 composites had greater catalytic activity than bare N-TiO_2 (**Table 4.11**). The percentage removal of PVC-NPs was 59.98% for N-TiO_2 and 99.2% for GT13 after 180 minutes at pH 4. These results validate that the inclusion of GO sheets in N-TiO_2 has a positive impact on the photodegradation of PVC-NPs. This increased photocatalytic activity of GO/N-TiO_2 composites is due to following reasons. In GO/N-TiO_2 composites, the two-dimensional π framework of graphene oxide (GO) acts as an electron acceptor, facilitating the transfer of excited electrons from N-TiO_2's conduction band to the GO. This electron transfer suppresses

the recombination of photo-generated charge carriers, leading to enhanced photocatalytic degradation, as evidenced by the photoluminescence data in **Figure 4.7**. Furthermore, Ti-O-C bonding facilitates electron movement from the valence to the conduction band, enhancing free radical formation. This process is significant for photocatalysis, allowing for visible light activation and improved efficiency [*Jiang et al., 2011, Awfa et al., 2018*].

The photocatalytic activity of GO/N-TiO_2 composite materials is influenced by their GO concentration. According to the results, the photocatalytic degradation of PVC-NPs decreases in the following order: GT13 > GT11 > GT31 (**Table 4.6)**. These results indicate that the weight ratio of GO to N-TiO_2 affects photodegradation process performance. The optimal weight ratio of GO to N-TiO_2 maximizes the synergistic effects of enhanced pollutant adsorption by GO and improved photocatalytic activity of N-TiO_2 due to reduced electron-hole recombination and broader light absorption, leading to higher photodegradation efficiency. The ideal GO to N-TiO_2 ratio for maximum pollutant degradation varies depending on the type of composite due to the uniformity of titanium dioxide anchoring. Excess GO particles can hinder light penetration to the N-TiO_2 active sites and lead to agglomeration of N-TiO_2 nanoparticles, reducing the number of catalytic sites and serve as recombination centers [*Awfa et al., 2018, Min et al., 2014, Petala et al., 2019*, *Long et al., 2013].* Therefore, an optimal ratio is crucial to maximize the beneficial effects of both components. According to the aforementioned results, the ideal GO to N-TiO_2 weight ratio in the current system is 1:3, which corresponds to the GT13 composite. After the removal of luminous PVC-NPs, the yellow PVC-NP solution turns colorless (as seen in the inset of **Figure 4.13a**), leaving yellow dots on the composite materials. The vapours produced from the photocatalytic reaction flask was passed through lime water, which turned milky and indicated that vapours might be containing CO_2. Furthermore, the mineralization efficiency of PVC-NPs solution with GT13 at pH 4 was investigated using **Total Organic Carbon (TOC)** analysis. The reduction of 96.9% in TOC indicated the transformation of PVC-NPs into mineralized products.

4.1.3.2 Effect of pH on the Removal of PVC-NPs

The effects of pH on PVC-NPs removal were investigated at pH levels 4, 7, and 10 as shown in **Figures 4.14(a)**, **4.14(b)**, and **4.14(c)** showing that as pH increases from 4 to 10, the removal percentage of PVC-NPs decreases. According to the results, all of the composites degraded at very high rates at pH 4 and 7, but at relatively low rates at pH 10. A maximum of 99.2% PVC-NP removal was achieved at pH 4.

The pH has a considerable impact on photocatalysis degradation processes because it influences adsorption, catalyst surface charge, valence band oxidation potential, free radical generation, and other physicochemical properties [*Tayeb et al., 2015, Kansal et al., 2007*].

The positive charge on the surface of N-TiO_2 decreases with increasing pH until they reach zero at the charge (PZC), which was previously known to be around 5-6.3 [*Nguyen et al., 2020, Jaffrezic-Renault et al., 1986*]. $TiOH_2^+$, the predominant species, produces a positive surface charge for pH values below the PZC, while TiO^- produces a negative surface charge for pH values above the PZC [*Kamble et al., 2003, Sun et al., 2008*].

The surfaces of GT13, GT11, and GT31 are positively charged at initial pH values of 4.0 and 7.0, whereas the PVC-NPs solution is negatively charged (**Section 4.1.2.4*)***. Electrostatic attraction forces are therefore expected at pH 4 and pH 7. The photodegradation rates of all materials decreased with higher pH values (10.0) due to the electrostatic repulsion of negatively charged surfaces of GO/N-TiO_2 composites and PVC-NPs. The decrease in removal percentage in alkaline conditions, as mentioned, is indeed likely due to the high concentration of hydroxyl ions (OH^-). These ions compete with the PVC-NPs (negatively charged) for adsorption sites on the composite materials. This competition reduces the efficiency of the adsorption process, leading to a lower removal percentage. In acidic conditions, the perhydroxyl radical ($HO_2^\bullet$), which is formed from superoxide ($^\bullet O_2^-$), can react with hydrogen ions (H^+) to produce hydrogen peroxide (H_2O_2), which can lead to increased levels of hydrogen peroxide (H_2O_2), and subsequently, hydroxyl radicals ($^\bullet OH$). This increase in $^\bullet OH$ radicals enhance oxidizing capability, causing degradation reactions to occur faster in acidic environments. The

rate of these reactions is further accelerated by the higher concentration of H^+ ions at lower pH [*Umar et al., 2013, Nagaraja et al., 2012*].

The difference in removal rates in alkaline and acidic media also increases with increasing GO levels in GT11 and GT31 compared to GT13 with lower GO content. This is because the GO surface was negatively charged in the pH range of 5.0-12.0, probably due to deprotonation of oxygen-containing functional groups, including carboxylic acid and phenolic hydroxyl groups on GO [*Peng et al., 2016, Li et al., 2015*]. Highly negatively charged GO sheets in suspension could disperse uniformly, considerably reducing the removal rate of negatively charged PVC-NPs due to electrostatic repulsions [*Vo et al., 2020*].

4.1.3.3 Effect of Light Intensity on the Removal of PVC-NPs

The intensity of the light also has a significant effect on photodegradation. Room light and tungsten bulb light have been used in a number of experiments. The degradation rate under room light conditions was lower than that under tungsten bulb light, according to the experimental results, since the room light was a light source with the visible light spectrum range from approximately 400 nm to 780 nm [*Duncan et al., 2012*], while tungsten bulb light was within a wavelength range of 350-1000 nm [*Thoms et al., 2013*], the experimental results demonstrated that the degradation rate under room light conditions was lower than that under tungsten bulb light. This is because, the wavelength of the light source significantly impacts a photocatalyst's ability to absorb light and subsequently drive a reaction. Shorter wavelengths (higher energy) range are generally more effective for exciting electrons across the band gap of photocatalysts, leading to higher photocatalytic activity. UV-A radiation, which usually has a wavelength range of 315–400 nm, is included in tungsten bulb light. In theory, higher light intensity enhances the excitation of electrons from the valence band to the conduction band and increase the rate at which electron–hole pairs are generated by increasing the number of incident photons on the photocatalyst surface per unit time [Paiu et al., 2025].

Table 4.6 Comparison of % removal with GT13, GT11 and GT31 with light and without light

	% Removal with GT13				% Removal with GT11			% Removal with GT31		
	TL	RL	CFL	Dark	TL	RL	Dark	TL	RL	Dark
pH 4	99.2	98.2	78.7	51.42	88.7	41.1	23.17	37.2	20.9	17.6
pH 7	98.3	83.7	55.9	44.4	78.9	38.4	21.8	33.5	18.09	10.7
pH 10	95.3	75.2	42.2	26.1	57.4	37.7	20.7	32.3	13.49	8.8

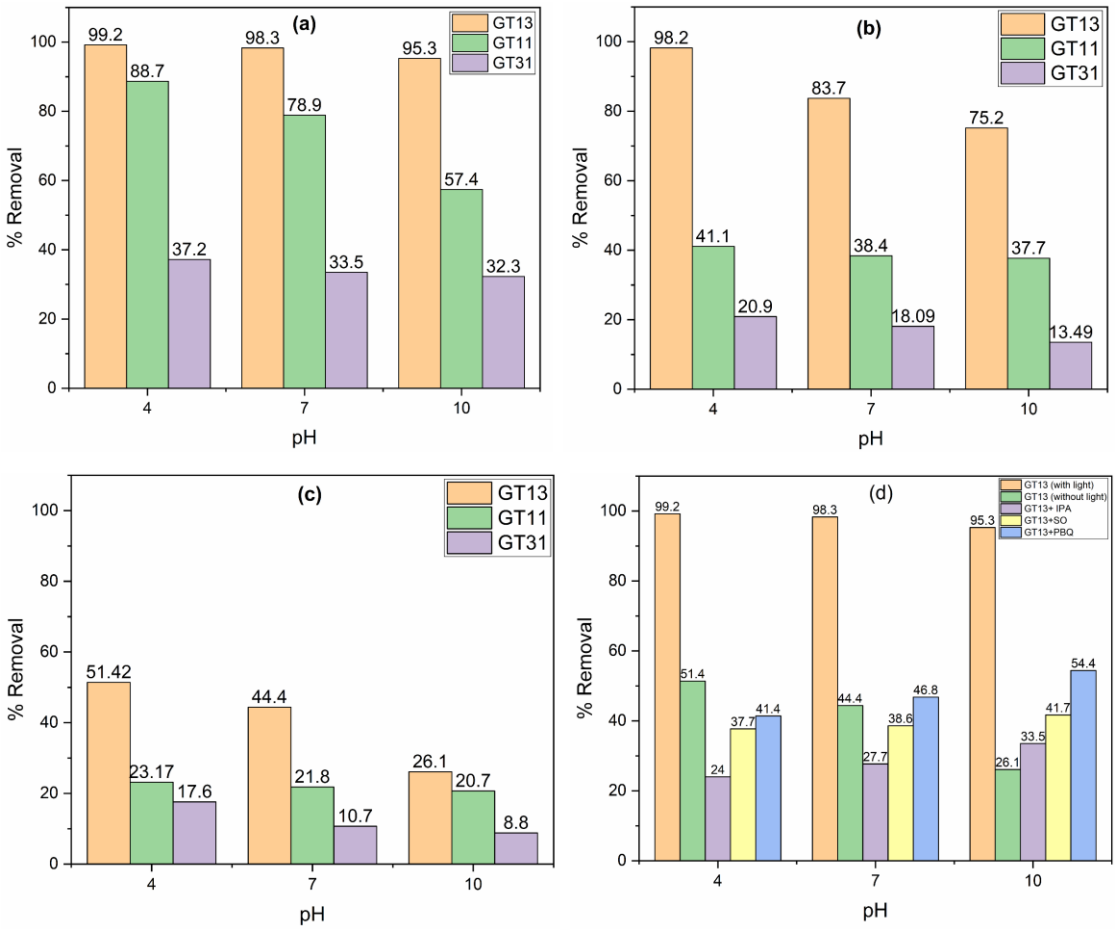


Figure 4.14 Comparison of % removal PVC-NPs with GT13, GT11, and GT31 under (a) tungsten bulb (b) room light (c) without light (d) comparison of % removal PVC particles under tungsten bulb light using GT13+quenchers isopropyl alcohol, sodium oxalate, and parabenzoquinone.

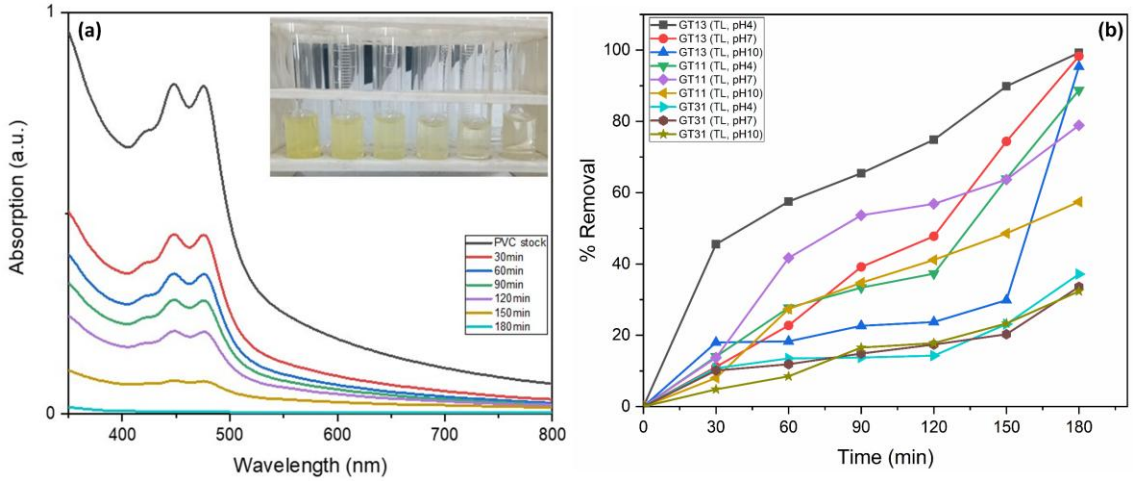
4.1.3.4 Effect of Scavengers

To study the mechanism of the photocatalytic reaction, isopropyl alcohol (IPA), sodium oxalate (SO), and parabenzoquinone (PBQ) were chosen as scavengers of $^{\bullet}OH$, h^{+}, and $^{\bullet}O_2^{-}$, respectively. **Figure 4.14(d)** illustrates that the degradation rates of PVC-NPs decrease significantly upon the addition of IPA, PBQ, and SO, and the results indicate

that reactive radical species (RRS) $^{\bullet}OH$ and h^{+} play important roles in the photocatalytic reaction of PVC-NPs. The degradation rate of PVC-NPs for GT13 photocatalysts is reduced in the presence of any scavenger, indicating the involvement of photogenerated holes h^{+}, $^{\bullet}OH$, and $^{\bullet}O_2^{-}$ radical species in the PVC-NPs degradation pathway. Photogenerated carriers (electrons and holes) form on the surface of N-TiO_2 photocatalysts when exposed to sufficient light. Photogenerated electrons (e^{-}) are produced when light energy excites electrons from the valence band to the conduction band. In the meantime, photogenerated holes (h^{+}) with oxidative characteristics were created in the valence band. By storing and transmitting electrons, GO can enhance the migration and separation of electrons produced by N-TiO_2, prevent carrier combination, and boost photocatalytic activity. When H_2O and O_2 are adsorbed on N-TiO_2 and GO surfaces during photocatalysis, $^{\bullet}OH$ and $^{\bullet}O_2^{-}$ are produced [*Linsebigler et al., 1995, Zan et al., 2006*]. The PVC molecular chain was attacked by $^{\bullet}O_2^{-}$ and $^{\bullet}OH$, resulting in a free radical chain centered on carbon atoms. An oxygen-containing group was formed after the contact with O_2 under tungsten bulb illumination, and this group was then broken down into small molecules [*Yousif et al., 2015, Cho et al., 2001*].

4.1.3.5 Effect of Time on the Removal of PVC-NPs

The effect of removal time on removal efficacy of PVC-NPs was evaluated by agitating them with composites at time interval of 30-180 minutes. To assess the PVC-NP removal rate, an optimal quantity of the synthesized composites (80 mg) was used.



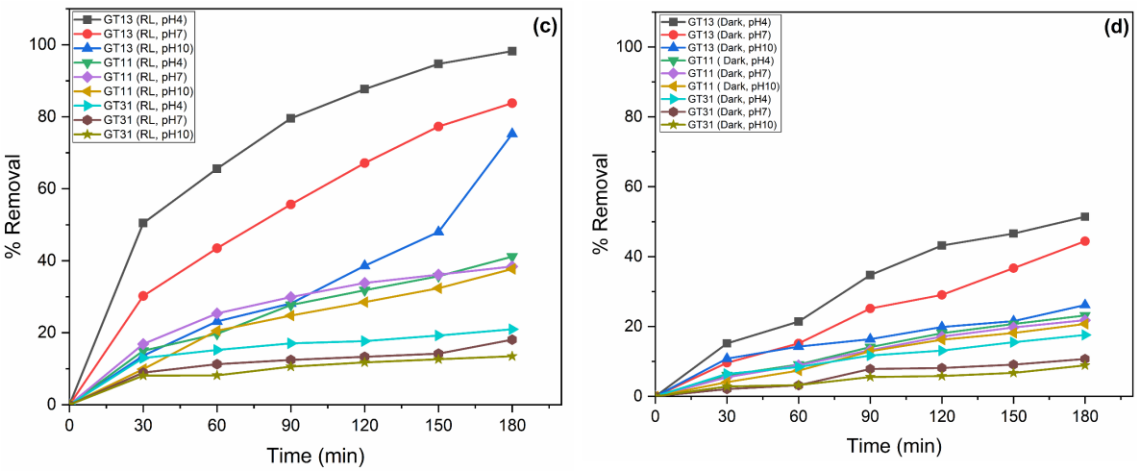


Figure 4.15 (a) Absorbance spectra of removal of PVC-NPs in the time interval of 30-180 minutes with 0.08 g of GT13. The inset shows the image of removal of PVC-NPs from water in the time interval of 30-180 minutes; Removal of PVC-NPs from water treated by GT13, GT11 and GT31 photocatalysts at pH 4, 7, and 10 in time interval of 30-180 minutes under (b) tungsten bulb light, (c) room light (d) dark.

As the time span increased from 30 to 180 minutes, the removal rate (%) of PVC-NPs for GT13, GT11, and GT31 at pH 4 under tungsten bulb light increased from 45.54% to 99.2%, 14.03% to 88.7%, and 10.76% to 37.2%, respectively (**Figure 4.15(b)**, **4.15(c)**, and **4.15(d)**). The catalyst's surface receives more light energy over time, which causes photoexcited species to develop and increases photocatalytic activity.

4.1.3.6 Effect of Catalyst dose on the Removal of PVC-NPs

Various doses of the GT13, ranging from 10 to 80 mg (10, 20, 30, 40, 60, and 80 mg were used in the experiments to examine the effect of photocatalyst concentration on the rates of photocatalytic degradation. After three hours of photocatalytic treatment with various doses of composite photocatalyst under tungsten light at pH 4 for 20 mL of PVC-NP solution at an initial concentration of 0.4 mg/mL, the results are shown in **Figure 4.16**, which demonstrates that the degradation rate increased to 99.2% as the amount of composite photocatalyst increased to 80 mg. The % removal values of PVC-NPs using various catalytic doses of GT13 under tungsten bulb light at pH 4 are shown in **Table 4.7**.

Table 4.7 % Removal pf PVC-NPs using various catalytic doses of GT13 under tungsten bulb light at pH 4

	GT13 doses (mg)	PVC-NPs: GT13 ratio	% Removal
1.	10	2:1	17.28
2.	20	1:1	17.69
3.	30	1:1.5	31.48
4.	40	1:2	56.48
5.	60	1:3	95.62
6.	80	1:4	99.27

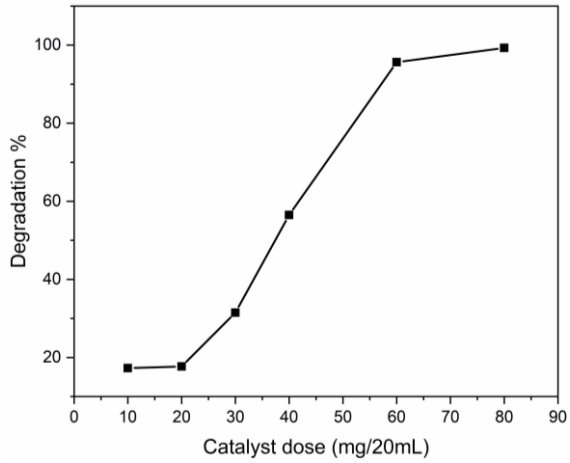


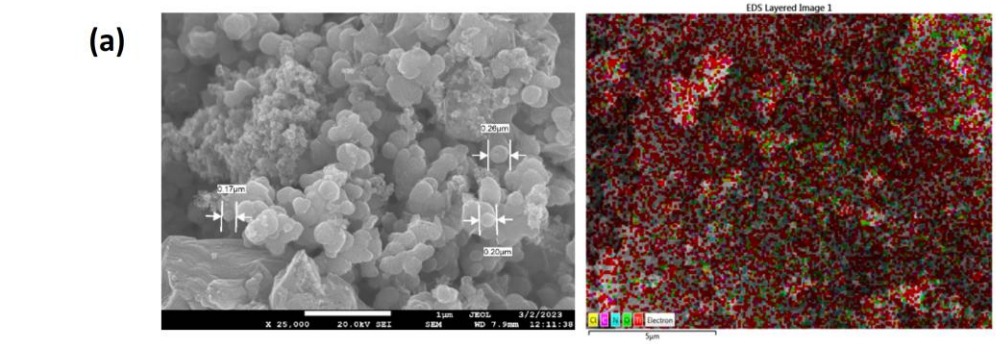
Figure 4.16 Degradation results of PVC-NPs treated with addition of different amounts of GT13 composite under TL at pH 4.

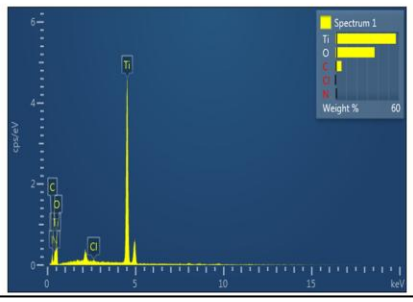
4.1.3.7 Analysis of GT13 Composite Material and PVC Solution after Removal Experiment

To understand the mechanism involved in the remediation process, further study of SEM, EDS, fluorescence microscopy, zeta potential FTIR spectroscopy and GCMS studies were conducted on GT13 and the solution left behind after the remediation experiment.

Figures 4.17(a) and **4.17(b)** show **SEM micrographs** of the surface morphology of GT13 composite following the removal experiment of PVC-NPs, with and without light. There was no discernible difference in the surface morphology of GT13 before and after the removal of spherical PVC-NPs; however, **EDS analysis** and elemental mapping revealed the presence of chlorine, as shown in **Figures 4.17(a)**, and **4.17(b)**, indicating the interaction between PVC-NPs and GT13 composite after the removal process.

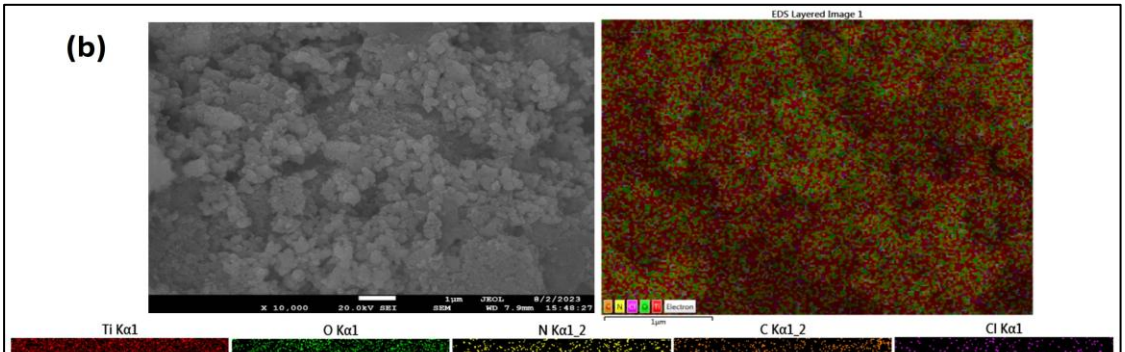
(a)

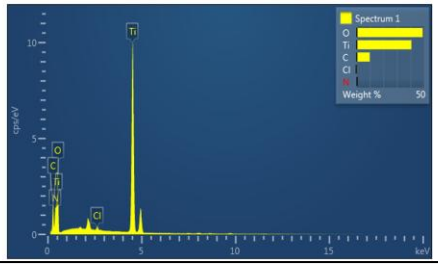




	Atomic %	Weight %
C	11.81	5.65
N	0.00	0.00
O	58.06	36.98
Cl	0.17	0.24
Ti	29.96	57.13
Total	100.00	100.0

(b)





	Atomic %	Weight %
C	17.37	9.91
N	0.00	0.00
O	64.50	48.99
Cl	0.23	0.39
Ti	17.90	40.71
Total	100.00	100.00

Figure 4.17 SEM, EDS and elemental mapping images of GT13 after reaction (a) with light (b) without light.

After the removal experiment, GT13 composite was visulized by **fluorescence microscope** and it revealed the presence of yellow stained PVC nanoparticles on it. The fluorescence microscopic images of pure PVC-NPs and GT13 composite (after the remediation experiment) are shown in **Figure 4.18**. These images clearly show that the GT13 surface was covered with green fluorescent PVC nanoparticles upon interaction with PVC-NPs. This suggested the existence of significant interactions between the surface functionalities of composites and PVC-NPs.

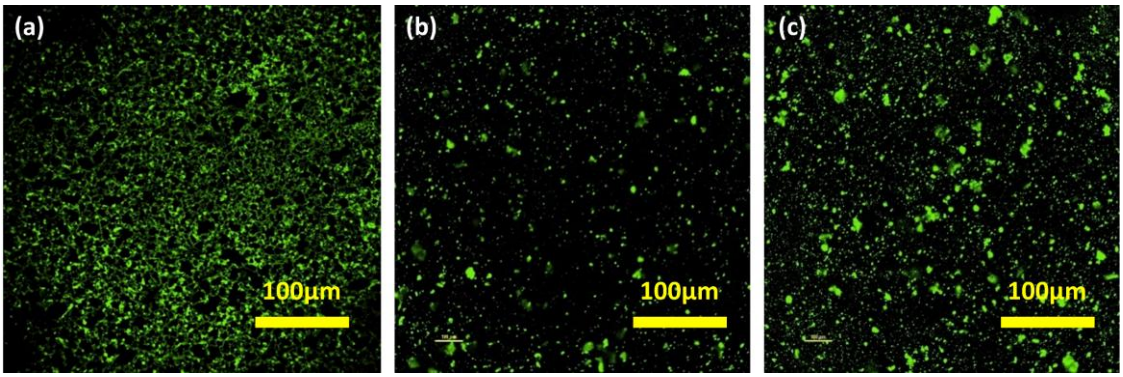
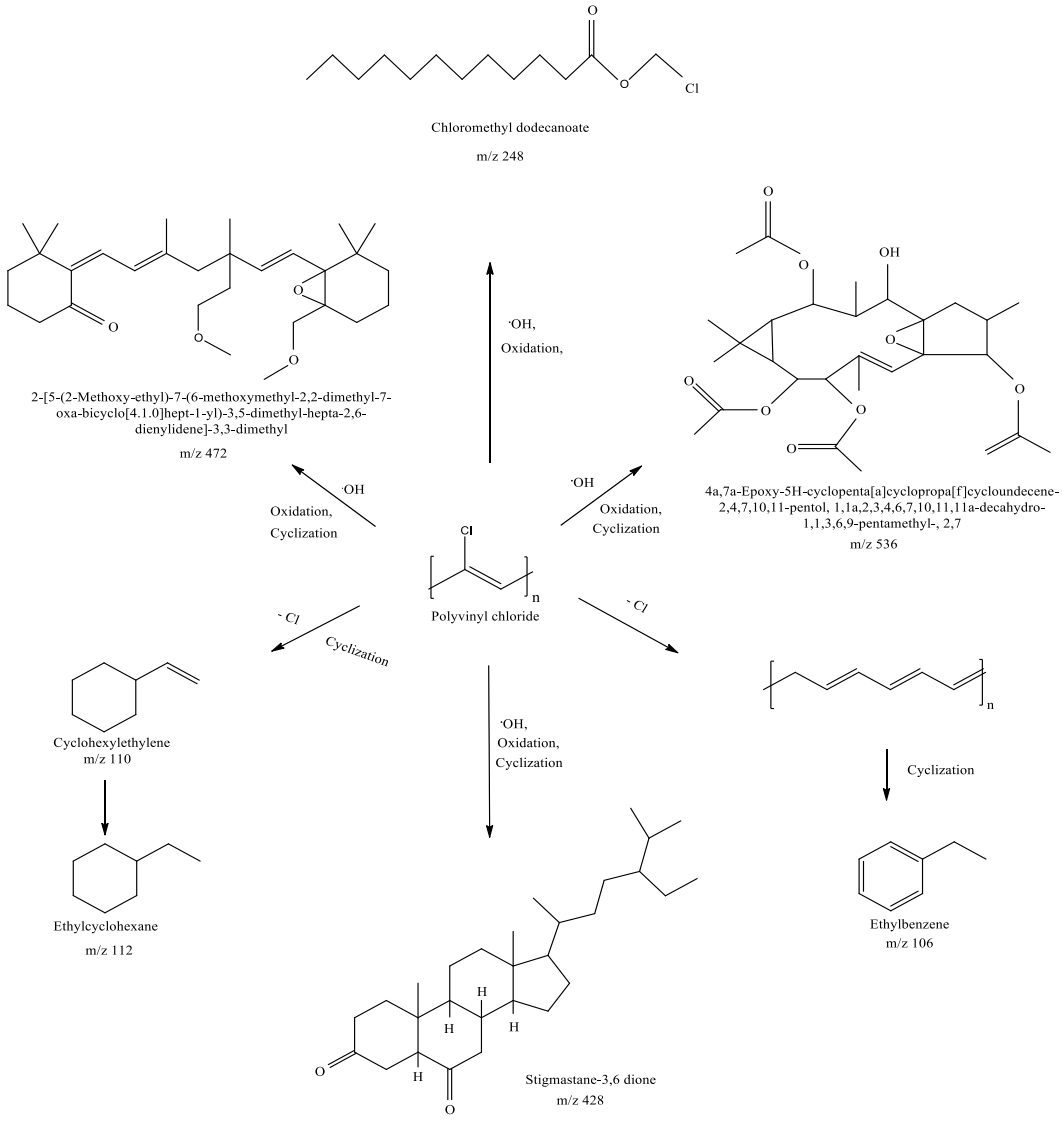


Figure 4.18 Optical micrographs of (a) PVC-NPs solution (b) GT13 composite after the remediation with light (c) GT13 composite after the remediation without light showing the PVC nanoparticles dyed with PTE dye.

Zeta potential changes were evaluated by doing DLS measurements on the solution that was collected right after the removal experiment. The zeta potential of the solution obtained after removing the PVC-NPs was -0.792 mV. The values are lower than that of pure PVC-NPs (-21.5 to -30.3), possibly due to charge neutralisation by the GT13 composite [*Batool et al., 2020*].

After the photocatalytic process, the degradation products of PVC in the PVC-NP solution were evaluated using **GCMS.** The degradation of PVC can be depicted schematically in **Scheme 4.1**. The mass fragments of degraded products were correlated with the reported literature and structure determination was carried out [*Miao et al., 2020*].



Scheme 4.1 GC–MS analysis of PVC degradation using GT13.

The composition of the GT13 composite and pure PVC solution was examined using **FTIR spectroscopy** both before and after the PVC-NPs were removed, as seen in **Figure 4.19(a)**. Because there are only trace amounts of PVC particles adsorbed on the surface of GT13, the spectra of GT13 before and after appears to be similar. As mentioned earlier the FTIR peaks at 655 cm^{-1} and 435 cm^{-1} correspond to Ti-O-C and Ti-O-Ti vibrations, respectively. As shown in **Figure 4.19(b)**, the strength of these peaks decreased significantly, possibly due to the electrostatic attraction of PVC with Ti-O-C and Ti-O-Ti, indicating the interactions of PVC nanoparticles with GT13 composite [*Wang et al., 2018*]. Furthermore, after the removal of PVC, the GT13

composite peaks at 435 cm^{-1} and 655 cm^{-1} shifted to higher frequencies of 443 cm^{-1} and 668 cm^{-1}, respectively. This type of frequency shifting suggests that there are interactions between PVC and GT13 composite [*Mohanta et al., 2020*].

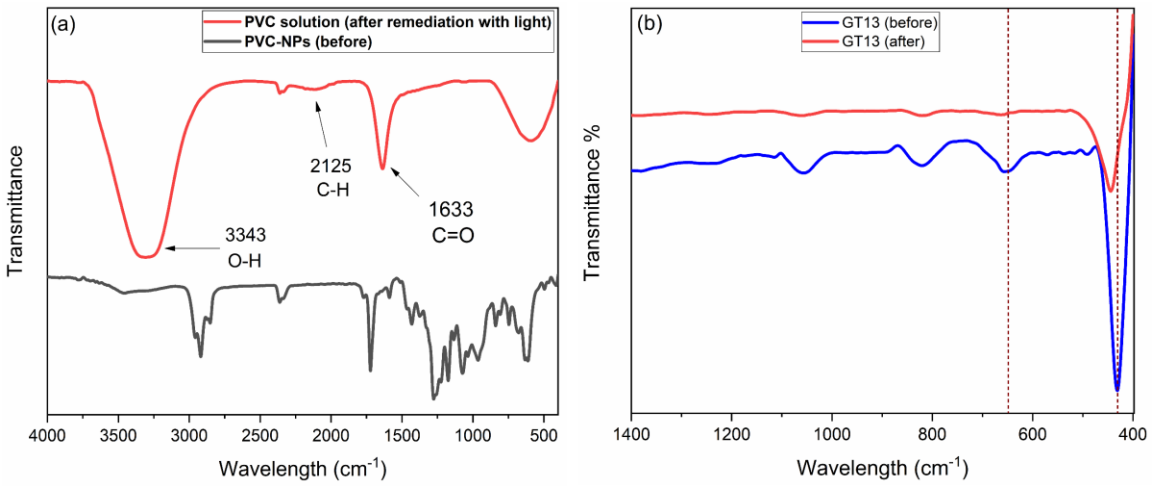


Figure 4.19 FTIR spectra of (a) PVC-NPs solution before and after the remediation experiment (b) GT13 composite before and after photocatalytic activity under tungsten bulb light.

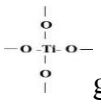
4.1.3.8 Mechanism of Removal of PVC-NPs

The mechanism of the photocatalytic reaction of GO/N-TiO_2 composites is schematically represented in **Scheme 4.2**, showing the effect of doping. The conduction band (CB) of graphene oxide (GO) and the d orbital of Ti atoms in N-TiO_2 are close in energy, allowing the interaction and the formation of a hybrid electron orbital. When N-TiO_2 absorbs visible light, its electrons are excited to the CB, creating holes in the valence band (VB). The nitrogen doping introduces new energy levels within the band gap, allowing electrons to be excited by visible light. These photoexcited electrons in the CB of N-TiO_2 can then transfer to the CB of graphene oxide, which then facilitates the reduction of O_2, and H_2O deposited on the graphene surface [*Jiang et al., 2011*]. The holes in VB oxidize the hydroxyl anions, generating hydroxyl radicals that degrade the PVC-NPs adsorbed on the surface [*Tomkiewicz, 2000*]. This process, where electrons are transferred from N-TiO_2 to GO, is key to the enhanced photocatalytic activity of the GO/N-TiO_2 composite, as it promotes charge separation and reduces electron-hole recombination. Also, the formation of Ti-O-C bonds due to the interaction between N-TiO_2 and graphene oxide can also contribute to visible light absorption. These bonds can cause an upward shift in the valence band edge, reducing

the bandgap of the composites and further enhancing its ability to absorb visible light [*Umrao et al., 2014*].

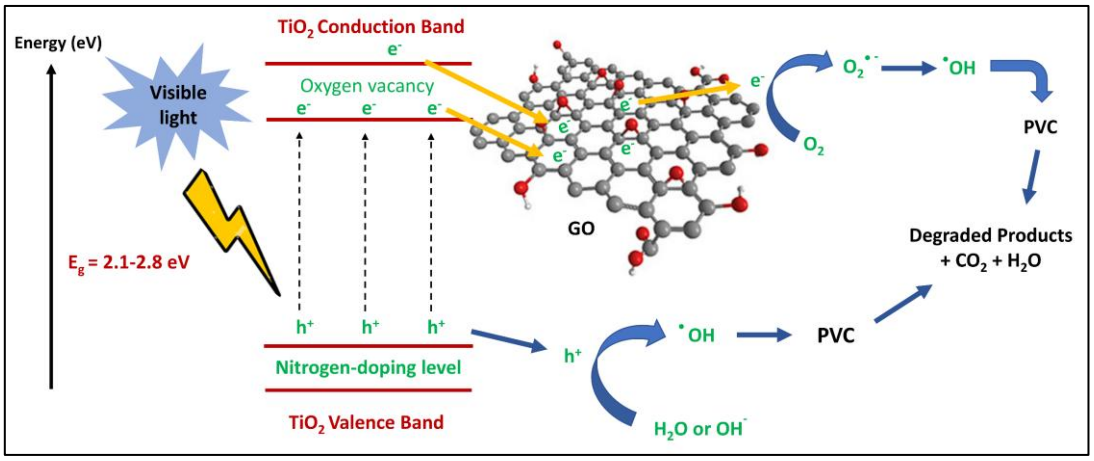
Furthermore, greater photoactivity of GT13 in comparison to GT11 and GT31 can be explained by the PL (**Section 4.1.1.6**) and XPS (**Section 4.1.1.7**) data. In PL spectra, a decrease in intensity with increasing GO concentration in a GT31 composite caused by the rapid transfer of photogenerated electrons by GO, which reduces electron-hole recombination. This is because GO acts as an electron acceptor, facilitating the separation of photogenerated electron-hole pairs and preventing them from recombining [*Shi et al., 2014, Ni et al., 2014*]. This indicates that the variation in electron-hole recombination rates may be primarily, but not only, responsible for the variation in photocatalytic efficiency between the samples. Other factors like the formation of new energy states within the bandgap due to oxygen vacancies and a reduced bandgap caused by impurity bands also play a role [*Manju et al., 2020*]. There is a direct correlation between structural oxygen vacancies and the PL spectra. A stronger photoluminescence (PL) signal indicates a higher concentration of these defects [*Chuang et al., 2012*]. Oxygen vacancies and defects in materials can enhance photocatalysis by facilitating exciton formation and reducing electron-hole recombination. Additionally, oxygen vacancies can facilitate the adsorption of O_2, and a strong interaction exists between the adsorbed O_2, and the photo-induced electrons bound by oxygen vacancies. This suggests that oxygen vacancies could facilitate the adsorbed O_2 to pick up photo-induced electrons and form O_2 radical at the same time, which enhance the oxidation of organic pollutants. Increased photocatalytic activity of GT13 results from the presence of more oxygen vacancies or defects, which are indicated by a higher excitonic PL spectrum [*Liqiang et al., 2006*].

Structural defects, such as oxygen vacancies, exist on the surface of N-TiO_2 reduce nearby Ti^{4+} ions to Ti^{3+} ions. The interaction between surface oxygen vacancies and Ti^{3+} defects promotes the separation of photogenerated electron-hole pairs, reducing recombination and enhancing photocatalytic performance. The presence of these Ti^{3+} defects also aids in electron transfer to oxygen, generating superoxide radicals and contributing to higher activity. According to XPS data, which reveal that the amount of Ti^{4+} on the surface of the GT13 particle is 1.2 and 1.8 times greater, respectively. The

presence of  groups (Ti^{4+}), contributes directly to the photocatalytic process and increases GT13's conductivity in comparison to GT11 and GT31. As a result, high Ti^{4+} levels are associated with strong electrical conductivity and high photoactivity [*Alshoaibi et al., 2023, Li et al., 2008*].

Additionally, the size of the crystallite is a significant factor in the photocatalytic process, and an increase in crystallite size directly affects the improvement of catalytic performance. The redox reaction that converts H_2O, OH^-, and O_2 on the catalyst surface is accelerated by the bigger crystallite size of GT13 composite, which makes it easier to transport light-generated carriers to the particle surface and absorb more energy [*Bellardita et al., 2018*, *Wang et al., 2014, Nandiyanto, et al., 2020*, *Jung et al., 2002*].

As a result of a complex multifunctional process that involves reactive species including h^+, $^{\bullet}OH$, and $^{\bullet}O_2^-$, GO/N-TiO_2 composites enhance the photocatalytic degradation of PVC-NPs [*Zhao et al., 2012*].



Scheme 4.2 Proposed mechanism of PVC degradation under visible light illumination using GT13 photocatalyst.

Equations presenting the proposed photocatalytic process are as follows:

$$N\text{-}TiO_2 + h\nu \rightarrow N\text{-}TiO_2\ (e^- + h^+)$$

$$N\text{-}TiO_2\ (e^-) + GO \rightarrow N\text{-}TiO_2 + GO\ (e^-)$$

$$h^+ + H_2O \rightarrow \cdot OH + H^+$$

$$e^- + O_2 \rightarrow {}^{\bullet}O_2^-$$

$$h^+ + \text{Pollutants} \rightarrow \text{Degradation products}$$

$$^{\bullet}OH + \text{Pollutants} \rightarrow \text{Degradation products}$$

$$^{\bullet}O_2^- + \text{Pollutants} \rightarrow \text{Degradation products}$$

4.1.4 Removal Study of PS-NPs using N-TiO_2 and GO/N-TiO_2 Composites

A series of experiments were conducted to determine the removal efficiency of N-TiO_2 and GO/N-TiO_2 composites under tungsten light and dark conditions at pH values of 4, 7, and 10, within 3 hours. The concentration change in PS-NPs was measured at λ_{max} of 446nm.

In order to evaluate the role of adsorption on removal of PS-NPs, an adsorption experiment was conducted using N-TiO_2 and GO/N-TiO_2 composites under dark. Under these experimental conditions, pure N-TiO_2 achieved the highest PS-NPs removal of 99.6% followed by the GO/N-TiO_2 composites (15.9%, 14.2% and 17.2% for GT13, GT11 and GT31 respectively) as shown in **Figure 4.20(b)**. The highest PS-NPs removal achieved by pure N-TiO_2 showing excellent adsorption performance. The decreased adsorption of GO/N-TiO_2 composites is due to excessive doping of GO which can reduce the specific active surface area of N-TiO_2. This reduction can result from the formation of larger aggregates due to increased van der Waals forces between the GO sheets and the N-TiO_2 nanoparticles, hindering the material's ability to efficiently interact with light and reactants. The resulting smaller surface area and increased agglomeration can reduce the number of active sites available for photocatalysis, ultimately leading to poorer photocatalytic efficacy [*Mohtar et al., 2021, Liao et al., 2022*].

Moreover, similar experimental conditions were used for photocatalytic study of removal of PS-NPs under tungsten bulb light (**Figure 4.20(a)**). Under these conditions, GT13, GT11, and GT31 demonstrated greater removal of PS-NPs than under dark conditions; GT13 reached the highest percentage removal of 32.2% in tungsten light at pH 4. It could be said that photocatalytic degradation would also concurrently occur with adsorption as light interacts with the material. Additionally, the percentage

removal of PS-NPs by pure N-TiO_2 under light condition was found to be 98.7%. These results are almost similar percentage removal of PS-NPs as that under dark conditions, suggests that the material is likely acting as an adsorbent rather than a photocatalyst in this specific pollutant. Photocatalysis relies on light to drive chemical reactions, while adsorption is a process that can occur both in the presence and absence of light. PS is extremely resistant to degradation since it cannot be broken down through hydrolysis [*Silva et al., 2025*]. Polystyrene (PS) is inherently resistant to degradation due to its chemical structure, which primarily features a carbon-carbon backbone and aromatic rings. These rings are relatively stable and do not readily participate in chemical reactions that would lead to breakdown [*Zhang et al., 2022*]

4.1.4.1 Effect of pH on the Removal of PS-NPs

The effects of pH on PS-NPs removal were investigated at pH levels 4, 7, and 10 as shown in **Figures 4.20(a)**, and **4.20(b)** showing that as pH increases from 4 to 10, the removal percentage of PS-NPs for N-TiO_2 decreases. A maximum of 99.6% PS-NP removal was achieved at pH 4 by N-TiO_2 under dark.

The pH has a considerable impact on removal process**.** The positive charge on the surface of N-TiO_2 decreases with increasing pH until they reach zero at the charge (PZC), which was previously known to be around 5-6.3 as discussed in **Section 4.1.3.2.** The surface of N-TiO_2 is positively charged at initial pH values of 4.0 and 7.0, whereas the PS-NPs solution is negatively charged (**Section 4.1.2.8*)***. Electrostatic attraction forces are therefore expected at pH 4 and pH 7. The photodegradation rates of N-TiO_2 decreased with higher pH values (10.0) due to the electrostatic repulsion of negatively charged surfaces of N-TiO_2 and PS-NPs. The decrease in removal percentage in alkaline conditions, as mentioned, is indeed likely due to the high concentration of hydroxyl ions (OH^-). These ions compete with the PS-NPs (negatively charged) for adsorption sites on the composite materials. This competition reduces the efficiency of the adsorption process, leading to a lower removal percentage**.**

Similarly, the surfaces of GT13, GT11, and GT31 are positively charged at pH values of 4.0 and 7.0 (**Section 4.1.3.2)**, which show maximum % removal for negatively charged PS-NPs at pH4 (**Figure 4.20**).

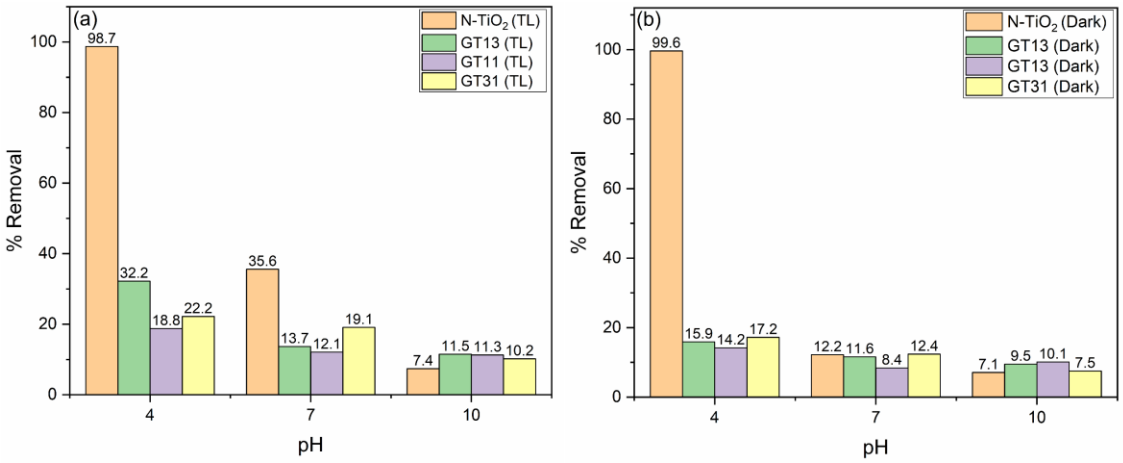
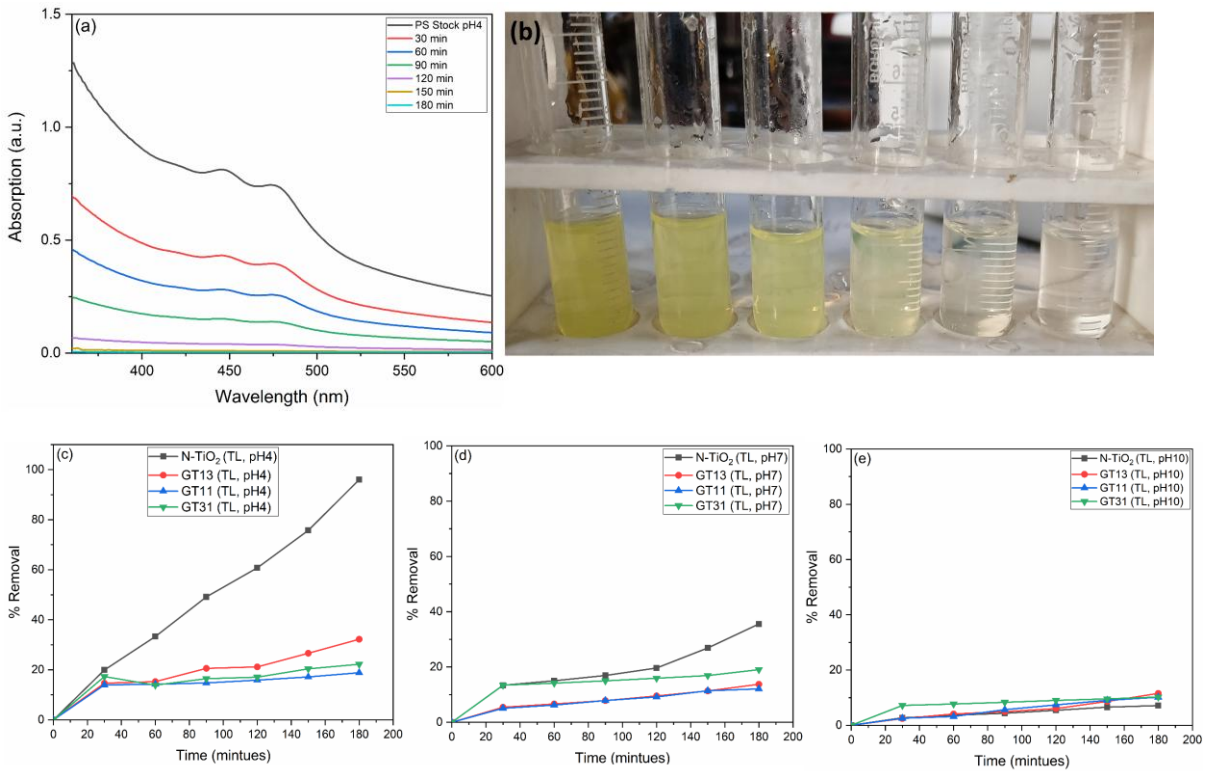


Figure 4.20 Comparison of % removal PS-NPs with N-TiO_2, GT13, GT11, and GT31 at pH 4, pH 7 and pH 10 under (a) tungsten bulb light (b) dark.

4.1.4.2 Effect of Time on the Removal of PS-NPs

The effect of removal time on removal efficacy of PS-NPs was evaluated by agitating them with composites at time interval of 30-180 minutes. To assess the PS-NP removal rate, an optimal quantity of the synthesized N-TiO_2 and GO/N-TiO_2 composites (80 mg) was used.



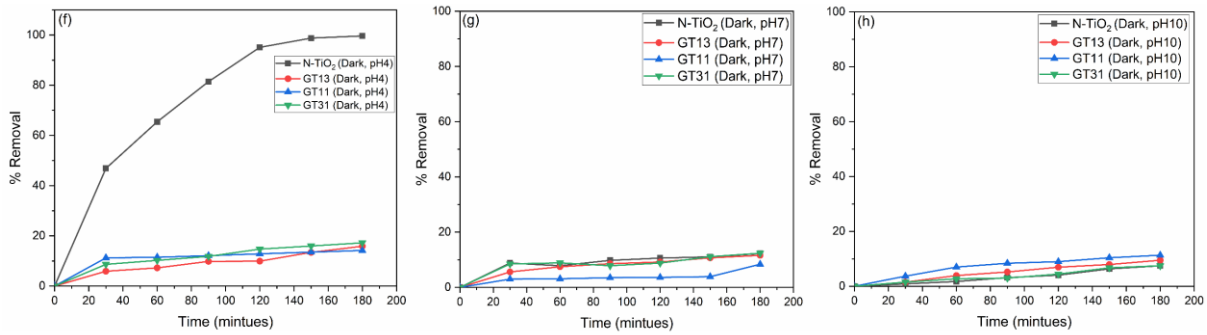


Figure 4.21 (a) UV absorption spectra of PS-NP removal with N-TiO_2 at pH4 (b) real-life image of PS-NP solution in the time interval of 30–180min at pH 4; PS-NP removal from water treated with N-TiO_2, GT13, GT11, and GT31 over a 30- to 180-minute time period under (c) tungsten bulb light at pH 4 (d) tungsten bulb light at pH 7 (e) tungsten bulb light at pH 10 (f) dark at pH 4 (g) dark at pH 7, and (h) dark at pH 10.

As the time span increased from 30 to 180 minutes, the % removal of PS-NPs for N-TiO_2, GT13, GT11, and GT31 at pH 4, pH 7, pH 10 under tungsten bulb light are shown in **Figure 4.21(c)**, **4.21(d)**, and **4.21(e)** and under dark are shown in **Figure 4.21(f)**, **4.21(g)**, and **4.21(h)** showing that % removal increases with increase in reaction time. The catalyst's surface receives more contact time, which increases removal activity. After the removal of luminous PS-NPs, the yellow PS-NP solution turns colourless (as seen in the inset of **Figure 4.21(a)**), leaving yellow dots on the left-out N-TiO_2. Real-life image of PS-NP solution in the time interval of 30–180 min at pH 4 is shown in **Figure 4.21(b)**.

4.1.2.3 Analysis of N-TiO_2 after Removal of PS-NPs

To understand the mechanism involved in the remediation process, further study of SEM, EDS, and FTIR spectroscopy studies were conducted on GT13 and the solution left behind after the remediation.

To understand the mechanism involved in the remediation process, more studies were conducted on N-TiO_2 and the solution left behind after the remediation. After the process, a real-life image of PS-NPs adsorbed on N-TiO_2 at pH 4 was clearly visible and decreases at pH 7 and pH 10. A visible colour changes as well as swelling of N-TiO_2 at pH 4 was observed after the reaction, as shown in **Figure 4.22**. The swelling of N-TiO_2 nanoparticles could be attributed to adsorption-induced swelling, which refers

to the expansion or deformation of a porous material when it adsorbs a pollutant [Bakhshian et al., 2017].

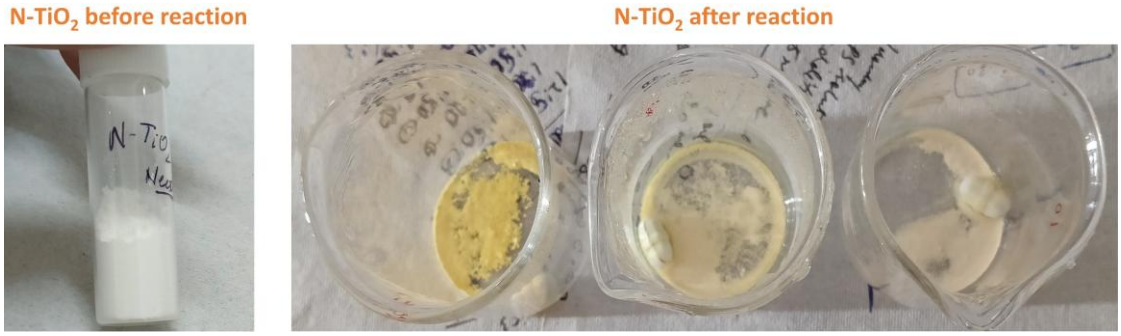


Figure 4.22 Real-life image of N-TiO_2 before and after reaction showing adsorbed PS-NPs after the reaction at pH 4, pH 7 and pH 10.

SEM micrographs of the surface morphology of N-TiO_2 nanoparticles after the removal of PS-NPs are shown in **Figure 4.23**, under dark at pH4.

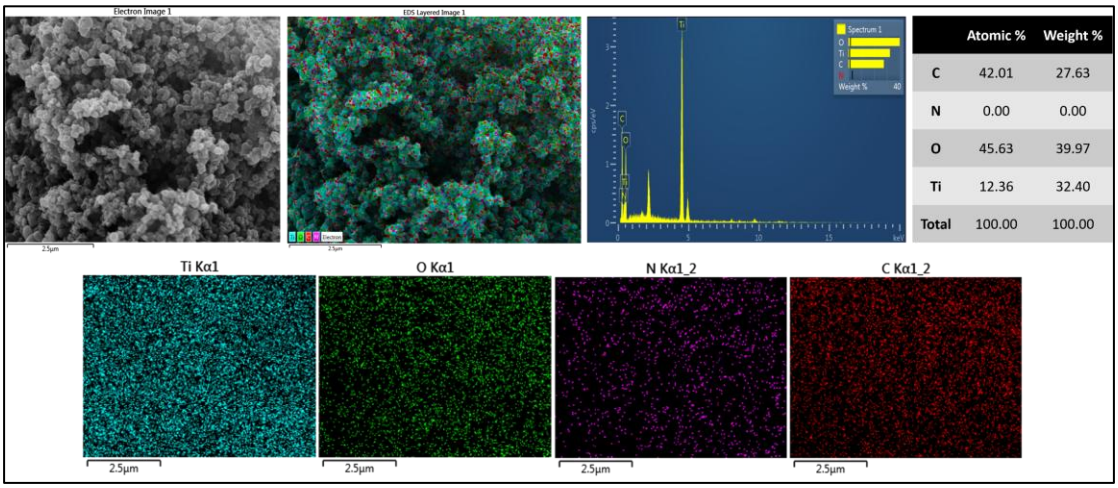


Figure 4.23 SEM, EDS and elemental mapping of N-TiO_2 after PS-NPs removal under dark at pH 4.

It was discovered that there are some distinct spherical particles of PS-NPs on the surface of N-TiO_2 nanoparticles, but the distinction is difficult because both N-TiO_2 and PS-NPs exhibit spherical surface morphology. **EDS analysis** and elemental mapping confirmed the presence of carbon of PS-NPs, as depicted in **Figure 4.23**, demonstrating the interaction between PS-NPs and N-TiO_2 nanoparticles after the removal reaction.

FTIR spectroscopy was used to analyze the composition of N-TiO_2 nanoparticles and pure PS-NPs before and after the removal of PS nanoparticles as shown in **Figure 4.24**.

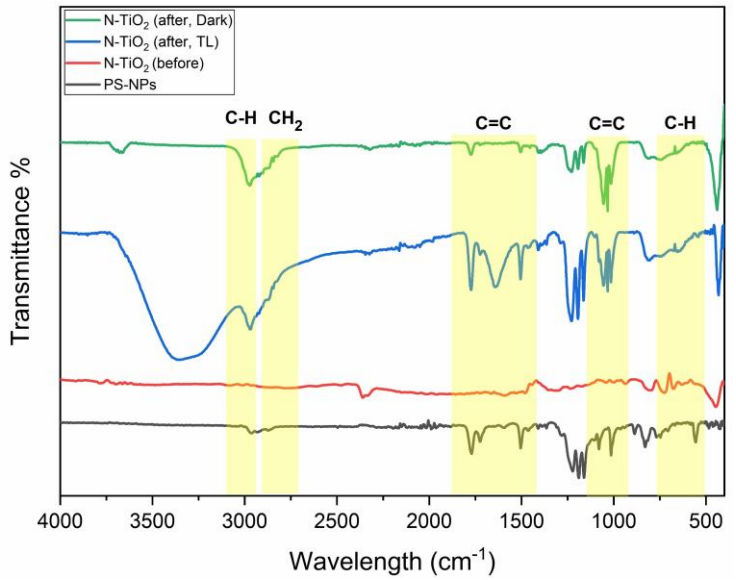


Figure 4.24 FTIR spectra of bare PS-NPs and N-TiO_2 before and after reaction with and without light at pH 4.

After removal experiment, FTIR spectra of N-TiO_2 displays the additional peaks corresponding to polystyrene, which point towards the existence of PS-NPs adsorbed on N-TiO_2 surface. The absorption peak at the wave numbers of 3060.8 cm^{-1} corresponds to aromatic C-H stretching vibration absorption. The peak at 2919 cm^{-1} represents the vibration of the CH_2 group. Additionally, the transmission bands at 1600.8, 1492.7, and 1452.2 cm^{-1} were attributed to the aromatic C=C stretching vibration of the benzene ring, as expected in the PS structure. Strong vibrational modes at 744 and 698.2 cm^{-1} indicate out-of-plane bending vibration of C-H, which is characteristic for polystyrene [*Fang et al., 2010*]. In addition, the absorption peak at the wave number of 3446.5 cm^{-1} is for the stretching vibration absorption of O-H.

4.2 CORN COB ACTIVATED CARBON (CCAC)/NITROGEN-DOPED TiO_2 NANOCOMPOSITES FOR REMOVAL OF POLYVINYL CHLORIDE (PVC) AND POLYSTYRENE (PS) FROM WATER

In this section, characterization of bare CCAC and CCAC/N-TiO_2 composites (CT13, CT11, and CT31) and the removal study of PVC-NPs and PS-NPs using the synthesized materials are explained. Furthermore, analysis of composite material after the PVC-NPs and PS-NPs removal experiment is discussed.

4.2.1 Characterization of CCAC/N-TiO_2 (CT13, CT11 and CT31) Composites

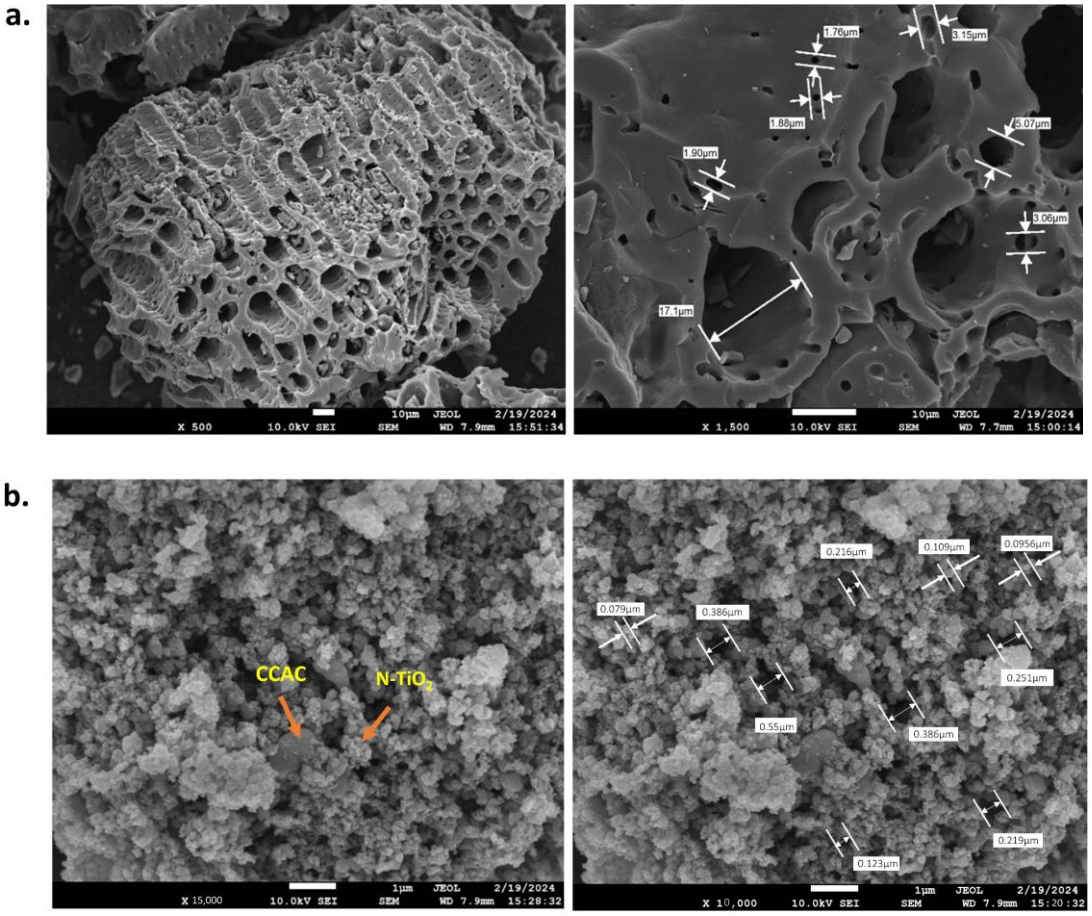
Characterization of base materials such as corncob activated carbon (CCAC) and N-TiO_2 is discussed with the composites.

4.2.1.1 Scanning Electron Microscopy and Energy-Dispersive X-ray Spectroscopy Analysis

The morphology of synthesized composite materials was examined using field emission scanning electron microscope (FESEM). The well-organized and regular arrangement of the honeycomb-shaped surface pores on $ZnCl_2$-impregnated corncob activated carbon results in a porous structure with a huge surface area [*Thongkrua et al., 2022*]. The SEM images of CCAC revealed a highly porous morphology with evenly distributed spherical hollows, as well as a large number of wide varieties of pores. A pore-forming effect resulted from the evaporation of $ZnCl_2$ and the decomposition of water and other organic substances during carbonization process caused by the $ZnCl_2$ breakdown enhanced the biochar's surface area. The porous and rougher surface of CCAC might have contributed to the enhanced adsorption capacity [*Yan et al. 2020, Areti et al., 2024*]. The porous structure of the corncob activated carbon (CCAC) can be clearly seen from the SEM images in **Figure 4.25(a)**.

The FESEM images of the CT13, CT11 and CT31 composites are shown in **Figure 4.25(b-d)**. As demonstrated in our earlier study, the pure N-TiO_2 nanoparticles have a spherical crystalline shape as discussed in **Section 4.1.3**. In CCAC/N-TiO_2 composites, spherically shaped N-TiO_2 agglomerates on CCAC show uniform distribution of spherical N-TiO_2 nanoparticles on the CCAC surface. The images in **Figure 4.25(b-d)**

showed that tiny N-TiO_2 granules are well dispersed on the CCAC and increasing the amount of N-TiO_2 loading in composites also resulted in better coverage of the CCAC. The addition of CCAC to the composites does not seem to have significantly altered the morphological characteristics of N-TiO_2. As the weight ratio of N-TiO_2 in CCAC/N-TiO_2 composites increased, N-TiO_2 particles progressively collected on the CCAC's exterior, causing pore blockage. The composite also contained some bigger N-TiO_2 particles. According to these results, the N-TiO_2 particles' increased free energy in the nanosystem caused a decrease in relative stability, which in turn caused particle aggregation because of intrinsic instability [*Zhang et al., 2009*]. As a result, the SEM image showed comparatively some large N-TiO_2 particles. Additionally, the amount of N-TiO_2 scattered on the CCAC surface increased as the weight ratio of N-TiO_2 increased, potentially producing an adequate number of photocatalytic radicals. A sufficient amount of photocatalytic radicals may also be produced by an increase in the amount of N-TiO_2 distributed over the CCAC surface.



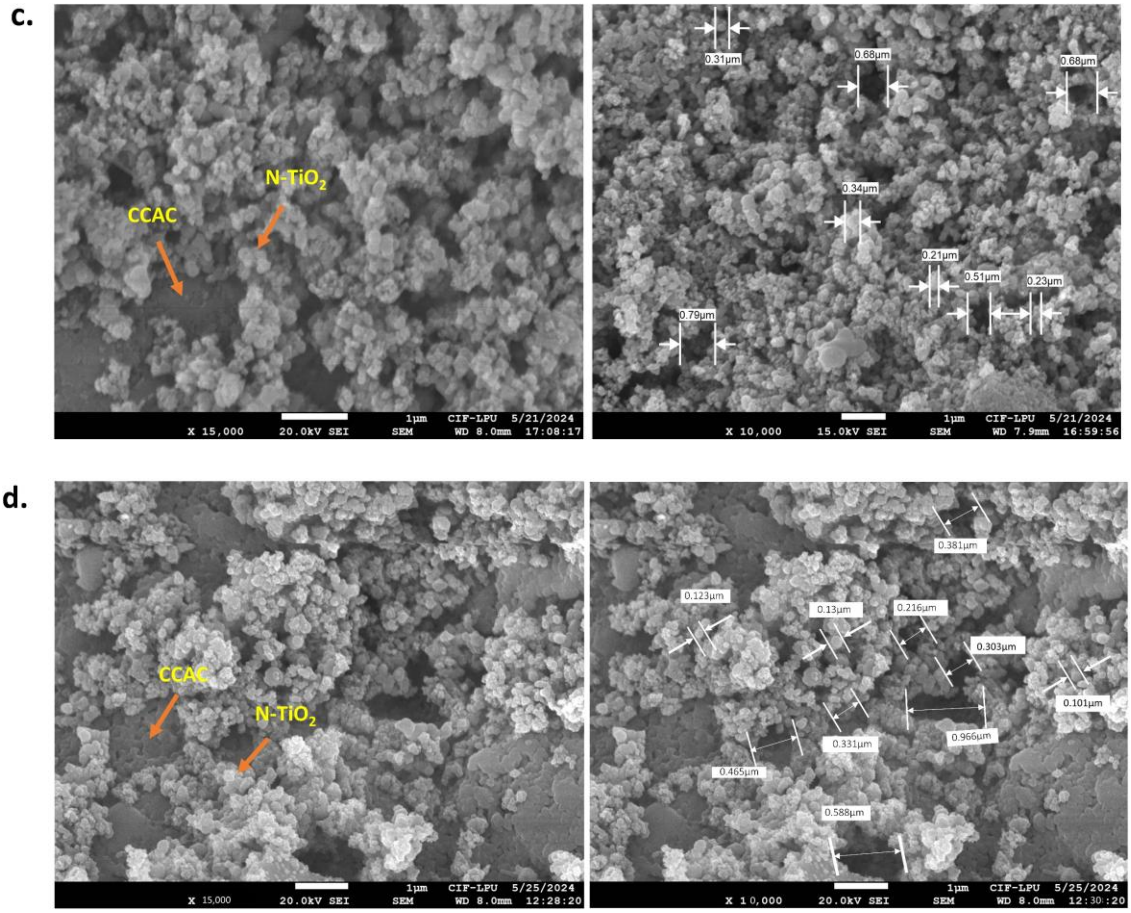
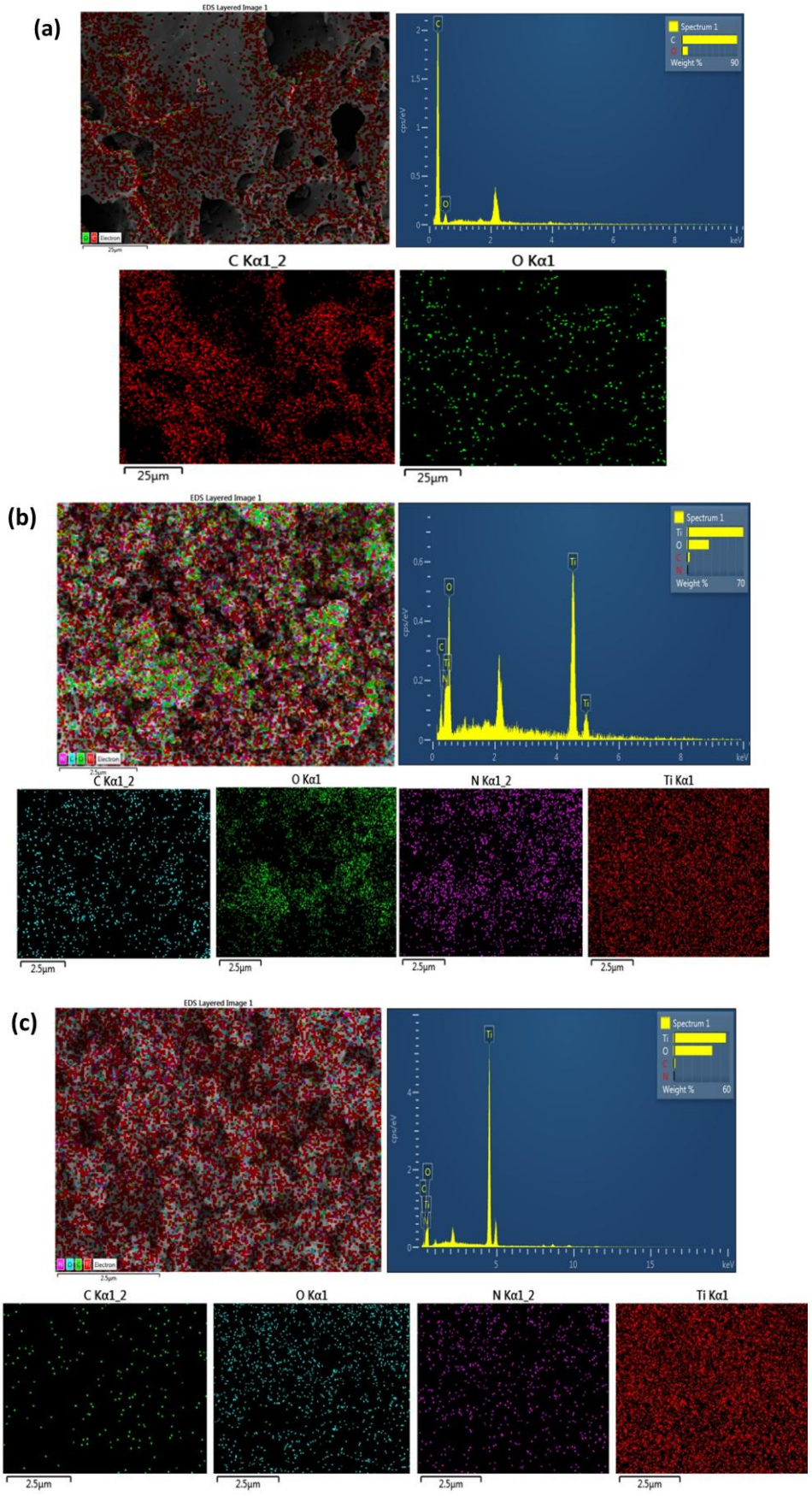


Figure 4.25 Scanning electron microscope (SEM) images including pore size and particles size of (a) $ZnCl_2$-impregnated corncob activated carbon (CCAC) (b) CT13 (c) CT11 and (d) CT31 composites.

Energy dispersive X-ray (EDX) analysis was used to examine the elemental composition of all synthesized composites. The EDX spectrum and quantitative elemental composition of CCAC, CT13, CT11, and CT31 are shown in **Figures 4.26**. Results indicated that C and O are present in high percentage while no accumulation of Zn over the surface of CCAC was shown. In CCAC/N-TiO_2 composites, the elemental mapping confirmed the existence of C, O, N and Ti, suggesting that N-TiO_2 nanoparticles have been adequately dispersed or embedded on the honeycomb-shaped surface of CCAC. The existence of C, O, Ti, and N peaks proved the successful formation of the CT13, CT11, and CT31 composites without impurities. The weight ratio of carbon normally increased as the ratio of CCAC to N-TiO_2 increased. The EDX profiles also indicated the absence of any other elements. The content of elements in atomic% and weight % of CCAC, CT13, CT11 and CT31. Is shown in **Table 4.8**.


(a)
EDS Layered Image 1
Spectrum 1
Weight % 90
C Kα1_2
O Kα1
25µm
(b)
EDS Layered Image 1
Spectrum 1
Weight % 70
C Kα1_2
O Kα1
N Kα1_2
Ti Kα1
2.5µm
(c)
EDS Layered Image 1
Spectrum 1
Weight % 60
C Kα1_2
O Kα1
N Kα1_2
Ti Kα1
2.5µm

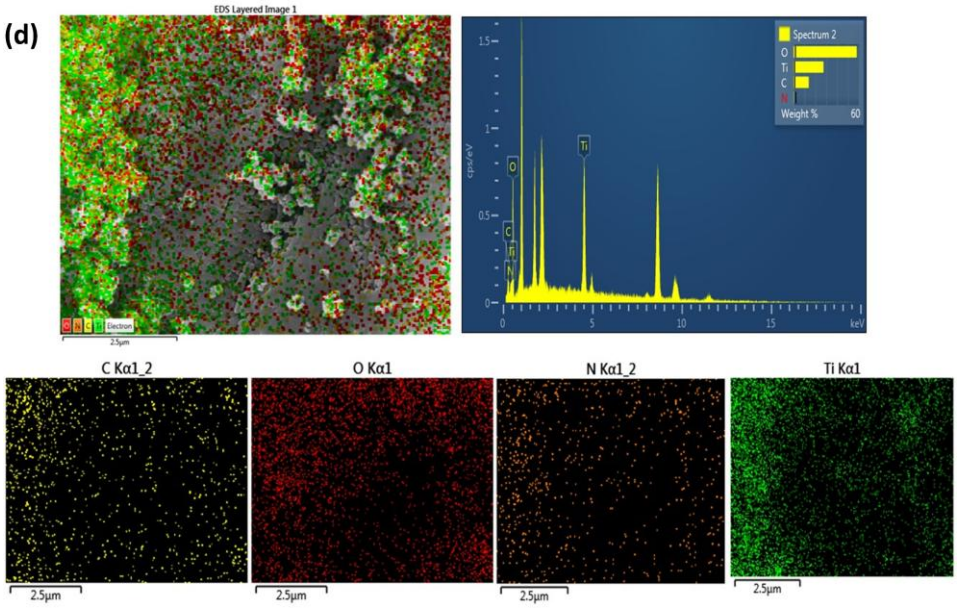


Figure 4.26 EDS mapping of (a) CCAC (b) CT13 (c) CT11 and (d) CT31 composite.

Table 4.8 Content of elements in atomic% and weight % of CCAC, CT13, CT11 and CT31.

Composite →	**CCAC**		**CT13**		**CT11**		**CT31**	
Elements ↓	Atomic %	Weight %	Atomic %	Weight %	Atomic %	Weight %	Atomic %	Weight %
C	91.93	89.53	8.03	3.30	4.57	2.17	21.66	14.04
O	8.07	10.47	49.51	27.10	65.75	41.60	67.38	58.17
N	-	-	0.00	0.00	0.00	0.00	0.29	0.22
Ti	-	-	42.47	69.60	29.68	56.23	10.67	27.58
Total	100.00	100.00	100.00	100.00	100.00	100.00	100.00	100.00

4.2.1.2 Functional group Analysis

The FT-IR study was done to identify characteristic functional groups on the synthesized materials. **Figure 4.27** displays the FTIR spectra of CCAC, N-TiO_2, and the structural changes brought about by the interaction of CCAC and N-TiO_2 in composites CT13, CT11, and CT31 with varying weight ratios. For FTIR spectrum of CCAC, the stretching vibration peak of the CCAC particle hydroxyl (-OH) is visible at 3663 cm^{-1}. The asymmetric stretching of $–CH_2$ groups at 2978 cm^{-1} and symmetric stretching of $–CH_3$ groups at 2869 cm^{-1} of the organic aliphatic chains are visible. The vibrations at 1761 cm^{-1} and 1018 cm^{-1} are corresponding to C-O-C pyramid ring skeleton, whereas a sharp band located at 1728 cm^{-1} are assigned to carbonyl (C=O)

functionalities. Medium intensity band at 1559 cm^{-1} could be accredited to C=C in aromatics. 1601 cm^{-1} and 1567 cm^{-1} are tiny absorption peaks next to the carbonyl vibration peak as lignin distinctive peaks. On the aromatic ring of lignin, 1280 cm^{-1} corresponds to the stretching vibrations of C=C and C-O, which reveals that cellulose, along with lignin and hemicellulose, is the significant structural component of the sample. Several other bands positioned at 1398 cm^{-1} were due to the bending vibrations of C-H groups, while those at 1136 cm^{-1}, 773 cm^{-1} and 604 cm^{-1} were caused by O-C, C-H and O-H groups, respectively. The three next peaks, which occurred at 1136, 1060 and 1009 cm^{-1}, illustrated the presence of C-O groups. These results revealed that CCAC contains different oxygen containing functionalities over the surface [*He et al., 2023*].

FTIR study effectively detected the changes of the surface functional group of CT13, CT11 and CT31 composites as shown in **Figure 4.27**. The peaks at 2978 cm^{-1} and 2911 cm^{-1} can be assigned to the stretching vibration of C-H on the aliphatic molecular chain. Signals at 1572 cm^{-1} corresponded to Ti–OH bending vibrations while the signal at 1069 cm^{-1} was Ti–O-C stretching vibrations. This suggests that chemical bonds were generated between N-TiO_2 and CCAC. The signals at 480–660 cm^{-1} corresponding to Ti–O-Ti stretching vibrations belong to characteristic peaks of N-TiO_2 [*Fazal et al., 2020*]. The peak at 759 cm^{-1} and the narrow peak at 553 cm^{-1} indicated the formation of activated carbon-loaded titanium dioxide nanoparticles and established the oxygen–metal–oxygen bonding. The CCAC loading modified the adsorption capability of N-TiO_2 nanoparticles. The peak of 2984 cm^{-1} decreased their intensity due to the doping of CCAC and derived the OH-stretching on the surface. The peak at 1218 cm^{-1} denotes the stretching vibrations of the C-O bond. The peaks at 824 cm^{-1} and 567 cm^{-1} characterized the C-O-Ti-O bonding, which recognized the formation of CCAC-loaded N-TiO_2 nanoparticles. Therefore, based on reported literature, the respective absorption band for CT13, CT11 and CT31 samples indicates the formation of Ti-O-C bond in the hybrid composite samples which can modify the optical and charge transfer properties [*Parvathiraja et al., 2022*]. Hence, FTIR spectra provides a clear clue about the presence of N-TiO_2, and formation of Ti-O-C in CT13, CT11 and CT31 samples. It can be speculated that the surface structure of CCAC was changed by N-TiO_2 after reaction.

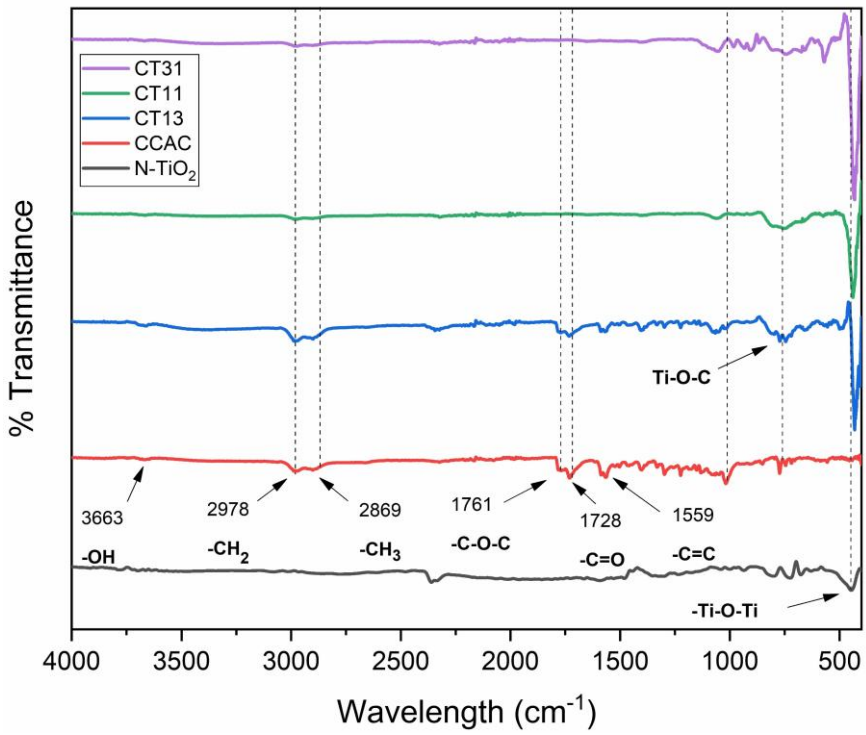


Figure 4.27 FTIR spectra of N-TiO_2, CCAC, CT13, CT11, and CT31.

4.2.1.3 X-ray Diffraction Analysis

The crystallinity of pure N-TiO_2, CCAC, and CCAC/N-TiO_2 (CT13, CT11, and CT31) samples was investigated by X-ray diffraction (XRD) analysis shown in **Figure 4.28**. The XRD pattern of N-TiO_2 shows a homogeneous pure crystalline structure with the peaks recorded at 2θ values of 25.3°, 36.9°,37.8°, 38.5°, 48.0°, 53.9°, and 55.0° indicating the presence of orientation planes of (101), (103), (004), (112), (200), (105), and (211), respectively, that confirmed the presence of tetragonal anatase phase. The XRD peaks of CCAC were shown at 25.7°, 28.2°, 31.8°, 34.6°, 36.2°, 42.8°, 47.5°, 56.5°, 63.1°, 69.3° indicating the presence of orientation planes of (020), (200), (201), (112), (101), (212), (102), (110), (114), (340). In XRD patterns of CT13, CT11 and CT31 composites, typical peaks of CCAC as well as the characteristic peaks of N-TiO_2 corresponding to anatase phase still existed with high intensity. This means that the preparation process of CCAC/N-TiO_2 composites did not change N-TiO_2 crystal phase. TiO_2 is known to have three different crystal structures: rutile, brookite, and anatase. Since anatase crystal has more oxygen vacancies than rutile and brookite crystals, it has the highest catalytic activity of any of them. Additionally, TiO_2 in anatase crystal form

has a high electron mobility, a low dielectric constant, and a low mass density [*Lu et al., 2019*].

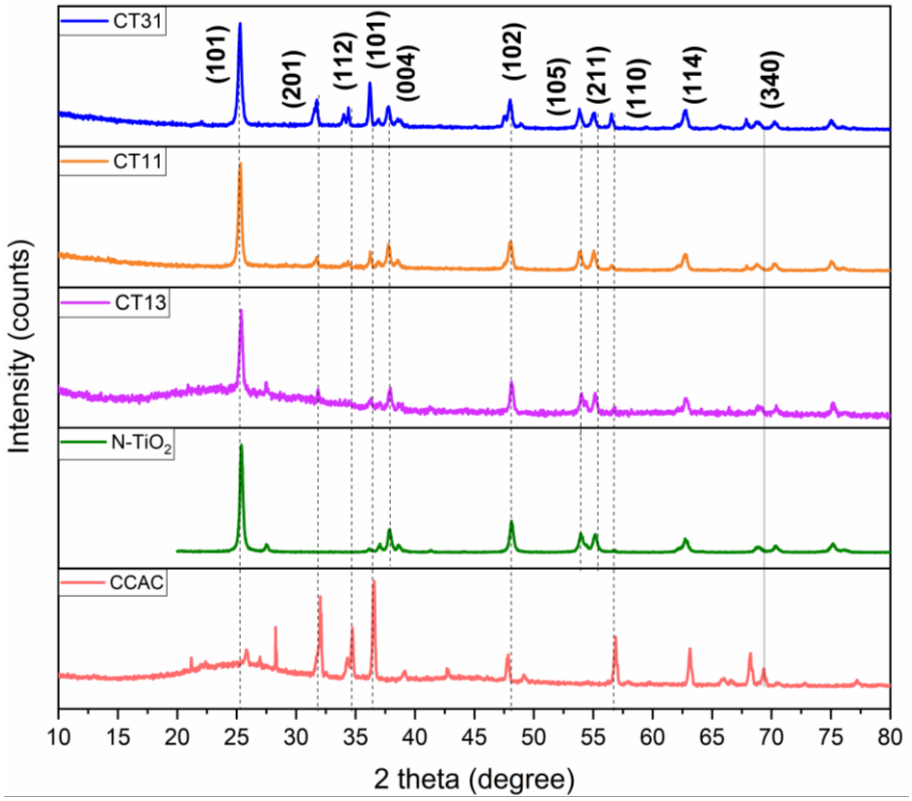


Figure 4.28 XRD analysis of N-TiO_2, CCAC, CT13, CT11, and CT31.

Average crystalline size of CCAC, N- TiO_2, CT13, CT11 and CT31 were also calculated using XRD analysis through Debye Scherer formula as shown in **Table 4.9**. Crystallite sizes of CCAC/N-TiO_2 composites are found to be greater than N-TiO_2. Crystallite sizes of CCAC/N-TiO_2 composites decrease as the amount of CCAC decreases from CT31 to CT11 to CT13. A decrease in crystallite size results in increased surface areas, which enhance reactant adsorption and, in turn, photo-reactivity [*Xie et al., 2010*, *Xu et al., 1999*, *Wang et al., 2014*]. Greater surface area from smaller crystallites results in more surface-active sites, which raises photonic efficiency. Furthermore, the charge carriers' diffusion path length from the photogenerated site to the surface site of reaction is shortened by the sample's lower crystallite size. Photocatalytic efficiency is increased when this diffusion path length is decreased because it lowers the rate at which photogenerated charge carriers recombine [*Devi et al., 2010*].

Table 4.9 The average crystallite sizes of CCAC, N-TiO_2, CT13, CT11, and CT31.

S. No.	Material	Average crystallite sizes (in nm)
1.	CCAC	40.39
2.	N-TiO_2	13.69
3.	CT13	28.15
4.	CT11	28.76
5.	CT31	33.86

4.2.1.4 Optical Bandgap Analysis

Band gap energy (E_g) deduced by extrapolation from Tauc plot shown in **Figure 4.29**.

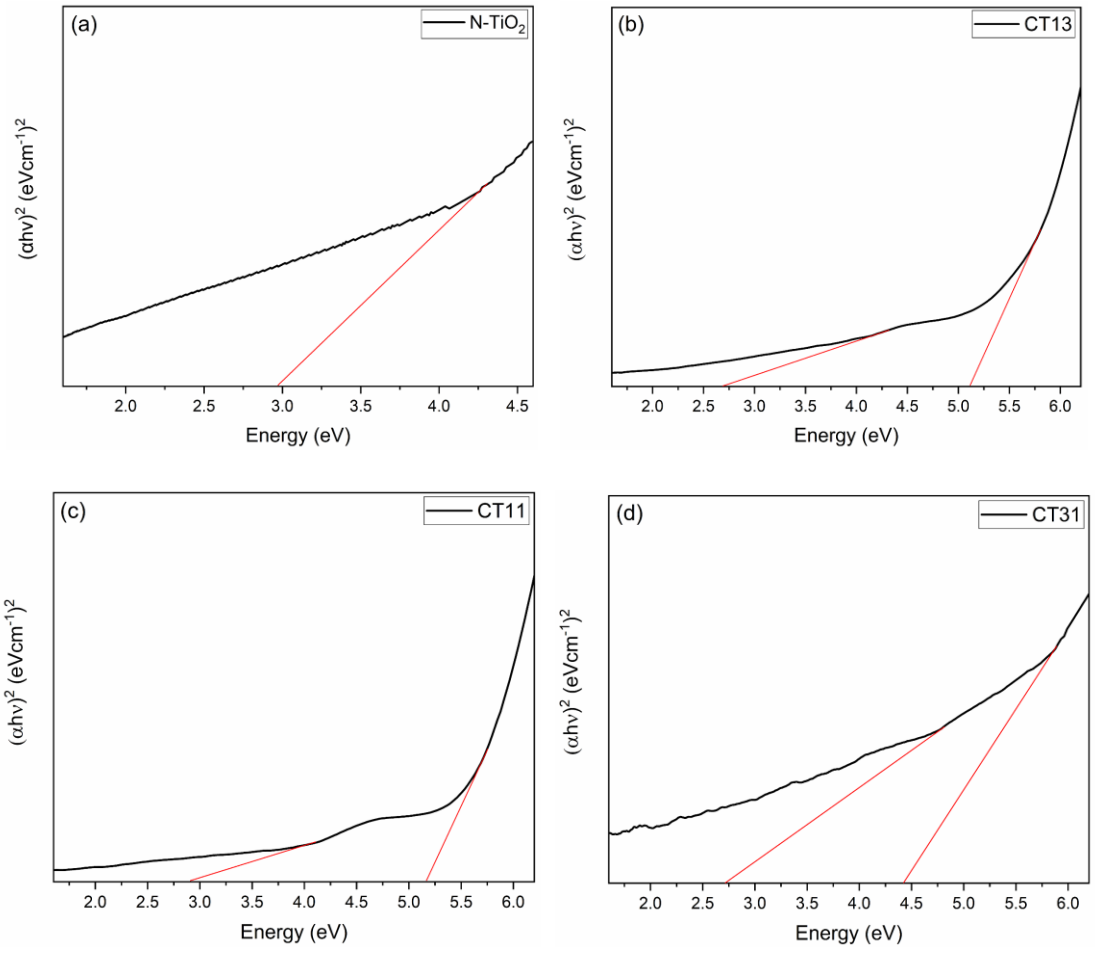


Figure 4.29 Optical bandgap of (a) N-TiO_2 (b) CT13 (c) CT11 and (d) CT31.

Optical band gap values of CCAC and N-TiO_2, CT13, CT11, and CT31 are given in **Table 4.10**.

Table 4.10 Optical band gap values of N-TiO_2, CT13, CT11 and CT31.

S. No.	Material	Optical band gap (E_g) (eV)
1.	N-TiO_2	2.9
2.	CT13	2.66–5.1
3.	CT11	2.98–5.1
4.	CT31	2.80-4.4

The band gap of N-TiO_2 was found out to be about 2.95 eV which is less than that of pure TiO_2. The presence of nitrogen doping reduces the band gap of TiO_2 by mixing N2p and O2p states on top of the valence band or by introducing a new mid-gap state produced by nitrogen incorporation, it extends the optical absorption of TiO_2 to the visible light region and improves the visible light response [*Wang et al., 2014*]. It is interesting to note that the CCAC/N-TiO_2 composites CT13, CT11, and CT31 exhibit the band gaps within range as shown in **Table 4.10**. It has been proposed that this behaviour, which has previously been observed in intercalated composites [*Megat Nabil Mohsin et al., 2018*], arises from a generation of composites with new energy states brought about by the formation of chemical bonds between the constituents, in this case Ti-O-C bonds [*Fazal et al., 2020*]. These results suggest that Ti-O-C bonds are generated due to the N-TiO_2 interaction with the CCAC, which might correspond to the development of new heterojunction structures or defects during the synthesis of CT13 [*Abdullah el at., 2023*, *Wang et al., 2016*], which is further confirmed by FT-IR and XPS analysis. According to reports, carbonaceous compounds can reduce the band gap by acting as impurities through this type of bond [*Woan et al., 2009*].

4.2.1.5 Photoluminescence Analysis

Electron-hole pair separation efficiency is commonly measured using photoluminescence (PL) analysis. Since photogenerated electrons and holes recombine to produce photoluminescence emission, a higher signal intensity often indicates a higher rate of recombination of these charges and, thus, a lower level of overall photocatalytic activity [*Eskandarloo et al., 2016*, *Huang et al., 2019*, *Wang et al., 2014*]. All the catalysts displayed comparable emission spectra when excited by ultraviolet light at 266 nm, as seen in **Figure 4.30**. It was observed that adding CCAC

considerably reduced the intensity of emission band. The significant reduction in PL peak intensity suggested that CCAC had the potential to prevent the recombination of photoelectrons and holes. According to reports, there were three primary causes of the decline in PL intensity. (1) Photogenerated electrons could be effectively transported from N-TiO_2 to CCAC in the presence of a CCAC/N-TiO_2 heterojunction, increasing the electron-hole pair separation efficiency [*Kim et al., 2016*]. (2) The quenching effect was brought about by the CCAC's absorption of photoluminescence [*Liu et al., 2014*]. (3) Low charge recombination could result from low electron photoexcitation [*Zhang et al., 2017*].

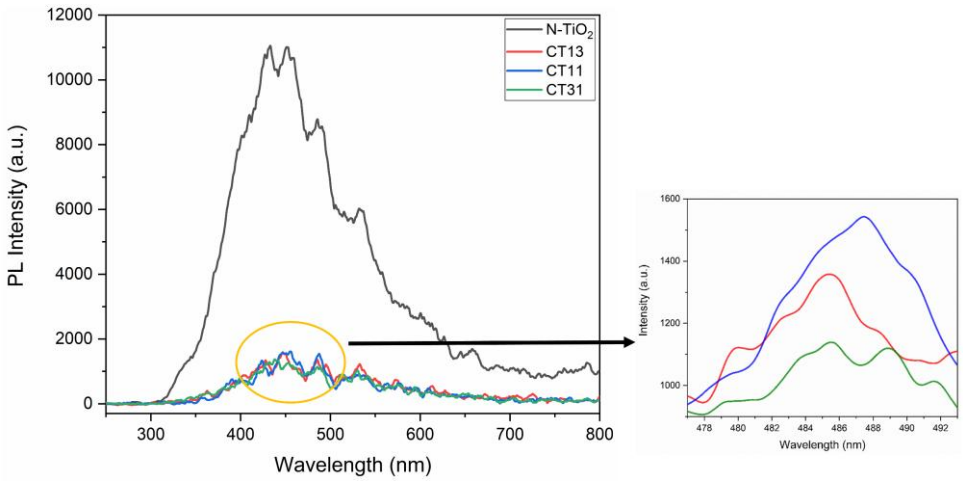


Figure 4.30 Photoluminescence emission spectra of N-TiO_2, CT13, CT11 and CT31.

According to reports, biochar, activated carbon and other carbonaceous materials can facilitate the transport of photogenerated electrons on the TiO_2 surface, promote the separation of electron-hole pairs, and, in accordance with the aforementioned, lower the photoluminescence signal by functioning as an acceptor and conductor of electrons [*Ao et al., 2022*, *Djellabi et al., 2019*, *Kim et al., 2016*]. Activated carbons are made up of complex aromatic-aliphatic organic compounds in addition to pores and minerals. Among these aromatic components are compounds with conjugated bonds that are resonant, like graphene, and are what give activated carbons their conductive capacity (electron storage/transport), which makes them appealing for photocatalysis [*Klüpfel et al., 2014*]. The lignin, cellulose, and hemicellulose molecules that make up the biomass break down through dehydrogenation, hydrogen transfer, and isomerization reactions to the point of producing these locally bonded aromatic rings as the temperature of pyrolysis and carbonization increases. The aromatic ring sheets stack in a turbostratic

pattern as the temperature is raised higher [*Lehmann, et al., 2012*]. Electrons photogenerated on the TiO_2 surface can be transferred to these conjugated structures, lowering the rate of electron-hole pair recombination that limits photocatalytic efficiency. This is made possible by the condensed aromatic substructures of activated carbon, which permit electronic transfer through the π-conjugated systems [*Klüpfel et al., 2014*].

4.2.1.6 Thermogravimetric Analysis

Thermogravimetric analysis (TGA) was used to assess the composites' thermal stability in an N_2 environment at a heating rate of 10 °C/min. **Figure 4.31** displays the TGA curves for the composite materials CT13, CT11, and CT31, as well as bare N-TiO_2 and CCAC (inset), which include three weight loss stages up to 600 °C. The weight loss of CCAC was approximately 78.55 % at 600°C.

Cellulose, hemicellulose, and lignin have different chemical structures and thermal stability, therefore they breakdown at different temperatures. The three steps of the pyrolysis process-drying, decomposition, and carbonization are determined by the TGA curve of corncob. A mass loss of around 19.04% occurred during the first step, or drying stage, between 30 and 75 °C, confirming that the corncob sample had lost moisture and some volatile materials. The primary mass loss stage was the second stage, often known as the disintegration stage. At about 210°C, mass loss began, and it ended at about 600°C. Inside the reactor, hemicelluloses, cellulose, and a portion of lignin underwent pyrolytic breakdown within this temperature range. The breakdown of cellulose and hemicellulose starts about 220–340°C and 340–400°C, respectively. Lignin is relatively more thermostable and most difficult to break and covers a large temperature range of up to 800-900°C. The first range of carbonization is 400°C since the minute degradation that occurs before it due to some non-combustible biomaterial can be disregarded. [*Yang et al., 2007*, *Gupta et al., 2018*, *Minz et al., 2023*]. On the other hand, bare N-TiO_2 sample exhibits stability up to 600°C, with a total weight loss of 1.46 weight %. Its remarkable thermal stability is most likely the result of calcining it for six hours at 500°C. The loss of residual carbon from the gum matrix may have contributed to the slight linear reductions in weight that were seen in the 100–600°C range [*Saranya et al., 2018*]. The weight loss curve for the CCAC/N-TiO_2 composite was composed of three steps. The first phase was the loss of physisorbed water, and some organic

solvents adsorbed on the surface of the composites that caused the first thermal event of CCAC/N-TiO_2 weight loss, which occurred between 30 and 220°C [*Lee et al., 2017*]. Then the subsequent decrease in weight was linked to the breakdown of cellulose and hemicellulose as well as the loss of hydroxyl groups on N-TiO_2, this weight loss became more noticeable at temperatures between 220 and 340°C [*Boujibar et al., 2018*]. Finally, the third drop in weight was likely due to the exothermic process - which involves the burning of carbon - was the cause of yet another notable weight loss at temperatures higher than 340°C [*Wang et al., 2016*, *Pang et al., 2020*]. The incorporation of N-TiO_2 placed on the CCAC substrate surface reduced the weight loss of CCAC/N-TiO_2 composites. Briefly, it is suggested that the thermal stability of the composite might be improved by adding N-TiO_2 nanoparticles to CCAC. The weight loss of CCAC/N-TiO_2 composites decreased with the increasing loading of N-TiO_2 deposited on the surface of CCAC substrate. This is because the main weight loss in the TGA curves of these composites is attributed to the decomposition of the activated carbon (AC) phase, and as the N-TiO_2 concentration increases, the amount of CCAC decreases, leading to a lower overall weight loss.

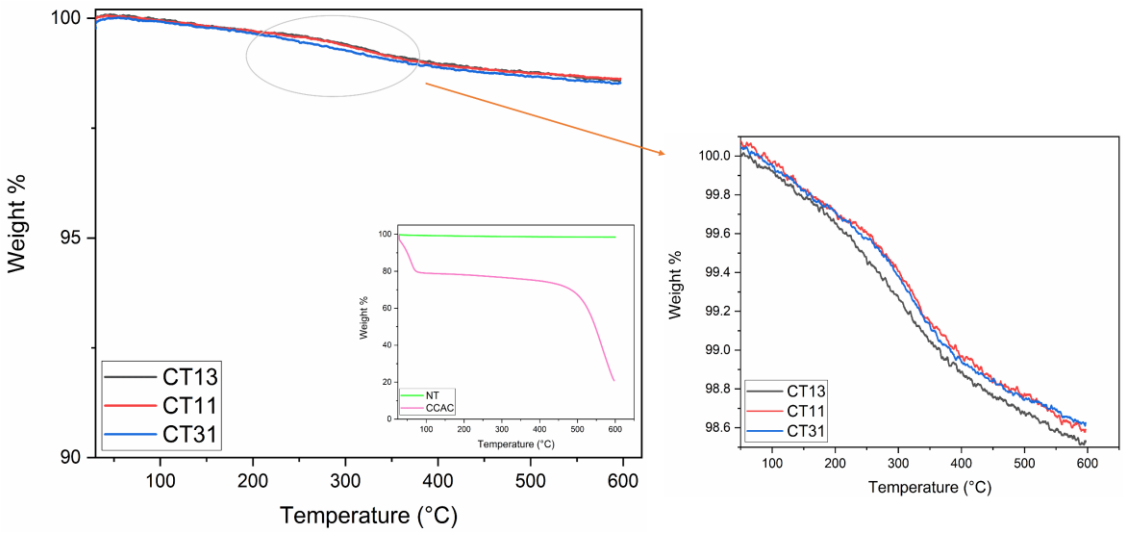


Figure 4.31 TGA of CT13, CT11, and CT31 composites. Inset TGA of bare N-TiO_2 and CCAC.

4.2.1.7 X-Ray Photoelectron Spectroscopy Analysis

X-ray photoelectron spectroscopy was used to assess the chemical composition and valency of the synthesized CCAC/N-TiO_2 composites. **Figure 4.32** displays a detailed X-ray photoelectron spectra (XPS) of the CCAC/N-TiO_2 composites CT13, CT11, and

CT31 that were collected in order to further support the successful deposition of N-TiO_2 onto the CCAC surface. X-ray photoelectron spectra investigation (**Figure 4.32a**) revealed that all three CCAC/N-TiO_2 composites CT13, CT11, and CT31 were made up of carbon, nitrogen, titanium, and oxygen. The binding energies of Ti2p, O1s, N1s, and C1s are 458.6, 531, 400, and 283.7 eV, respectively.

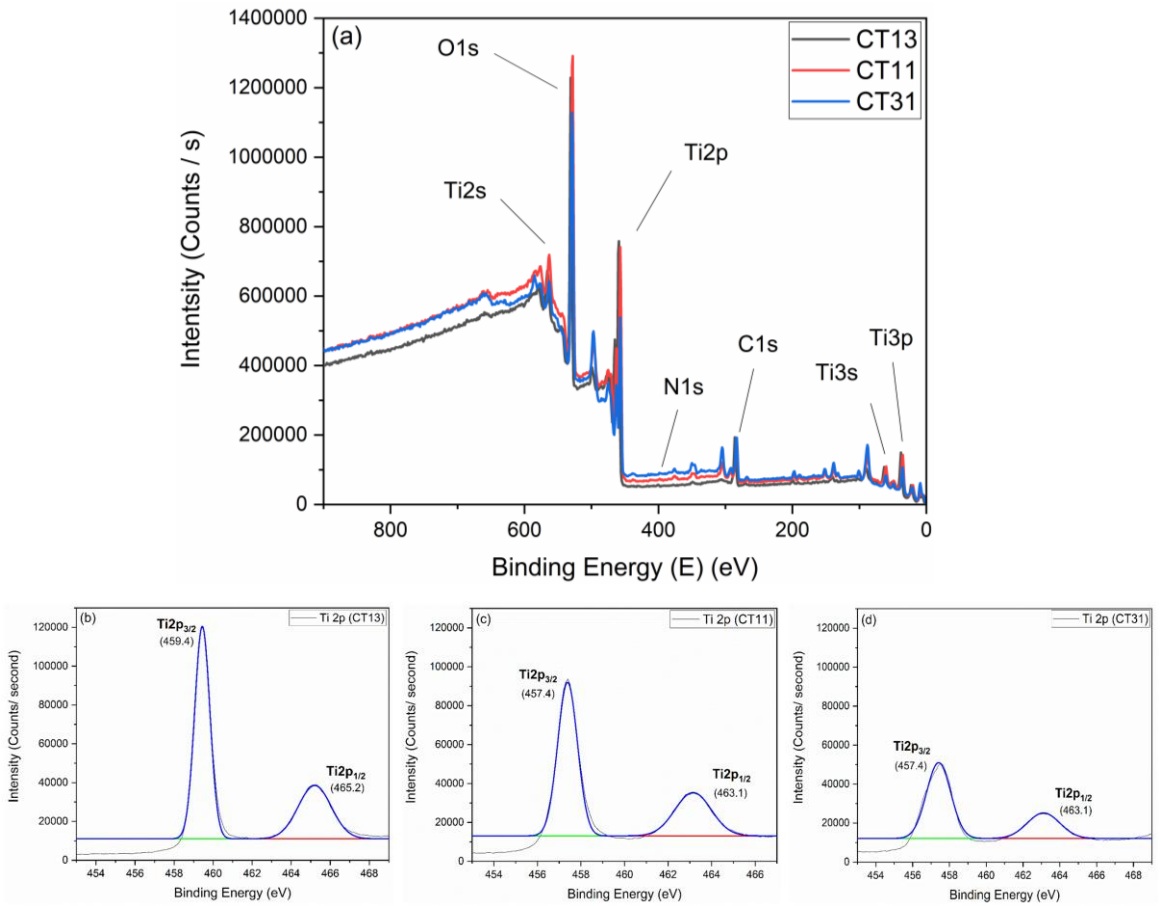
Two peaks in the Ti 2p spectra, at 459.4 eV and 465.4 eV, were associated with Ti $2p_{3/2}$ and Ti $2p_{1/2}$, respectively [*Xing et al., 2009*]. The Ti 2p peaks were in good agreement with pure N-TiO_2. The results show that the titanium signal in the samples increases as the N-TiO_2 ratio in the impregnation increases in CT13.

The O 1s core level spectra were fitted to two Gaussian curves centered at 530.9 eV and 532.8 eV, which corresponded to -OH on the surface of activated carbon and Ti-O-Ti bonds and were consistent with FTIR data. Combined with the aforementioned study, it could be determined that there was a significant contact between N-TiO_2, consequently the CCAC could transmit photo-induced electrons from N-TiO_2 [*Lu et al., 2019*]. A peak in the O 1s spectrum in **Figure 4.32 (e-g)**, located at about 239 eV, suggested the presence of metal oxides, specifically Ti=O. Furthermore, O 1s have a lattice oxygen spectrum at 530 and 531 eV, and their association with O-C=O and C=O, respectively is due to activated carbon.

A Gaussian deconvolution of the spectrum in the 282 and 298 eV range was used to monitor and examine the C1s orbital signals in order to confirm if the impregnation of N-TiO_2 on CCAC resulted in the formation of chemical bonds. The deconvoluted C1s spectrum of the CT13, CT11, and CT31 composites is shown in **Figure 4.32(i)**, **4.32(j)**, and **4.32(k)**, respectively, where the signals for Ti-C, C-C, C=C, C-O, Ti-O-C and, π-π are located at ~ 284.7, ~285.5, ~286.1, ~ 287, ~ 289.4, and ~ 293.9 eV, respectively [*Smith et al., 2016*]. The relative strength of the C–C peak indicated that the CCAC in the CCAC/N-TiO_2 composites had a carbon structure similar to graphite [*Yue et al., 2024*]. The structural composition of the CCAC/N-TiO_2 composites was further supported by the XPS measurements, which validated the previously described FTIR results. **Figure 4.32 (i-k)** shows that the CT13 sample had a larger ratio of C-C (hydrophobic) bonds to hydrophilic bonds (C-O, C = O, -COO) compared to the other two samples. In CT13, the peak area of C=C declines while the peak area of C-C increases. This suggests that C=C sp^2 hybridization (graphite state) is transformed into

C-C sp^3 hybridization. Instead of just intermolecular binding, it is demonstrated that the heteroatoms (such as O, Ti, etc.) are linked on CCAC by chemical bonds [*Chen et al., 2022*]. This indicates that the material's surface is more hydrophobic than other samples, resulting in decreased interaction with air moisture. The presence of hydrophilic groups in CCAC/N-TiO_2 material is important for photocatalytic applications as it interacts with moisture to form hydroxyl radicals, a highly oxidizing species that degrade organic matter. Modifying the synthesis conditions of CCAC/N-TiO_2 composites can enhance their hydrophobic/hydrophilic nature, resulting in stronger interactions with pollutants of different chemical nature (e.g., hydrophobic or hydrophilic), which may be beneficial in their removal [*Castilla-Caballero et al., 2023, Lim et al., 2011*].

The presence of nitrogen and its efficient doping into Ti (TiO_2), as shown by the peak at 399.8 eV in **Figure 4.32(k-m)**. By replacing oxygen atoms in the TiO_2 lattice, the peak verifies the formation of an O-Ti-N bond [*Shi et al., 2012*].



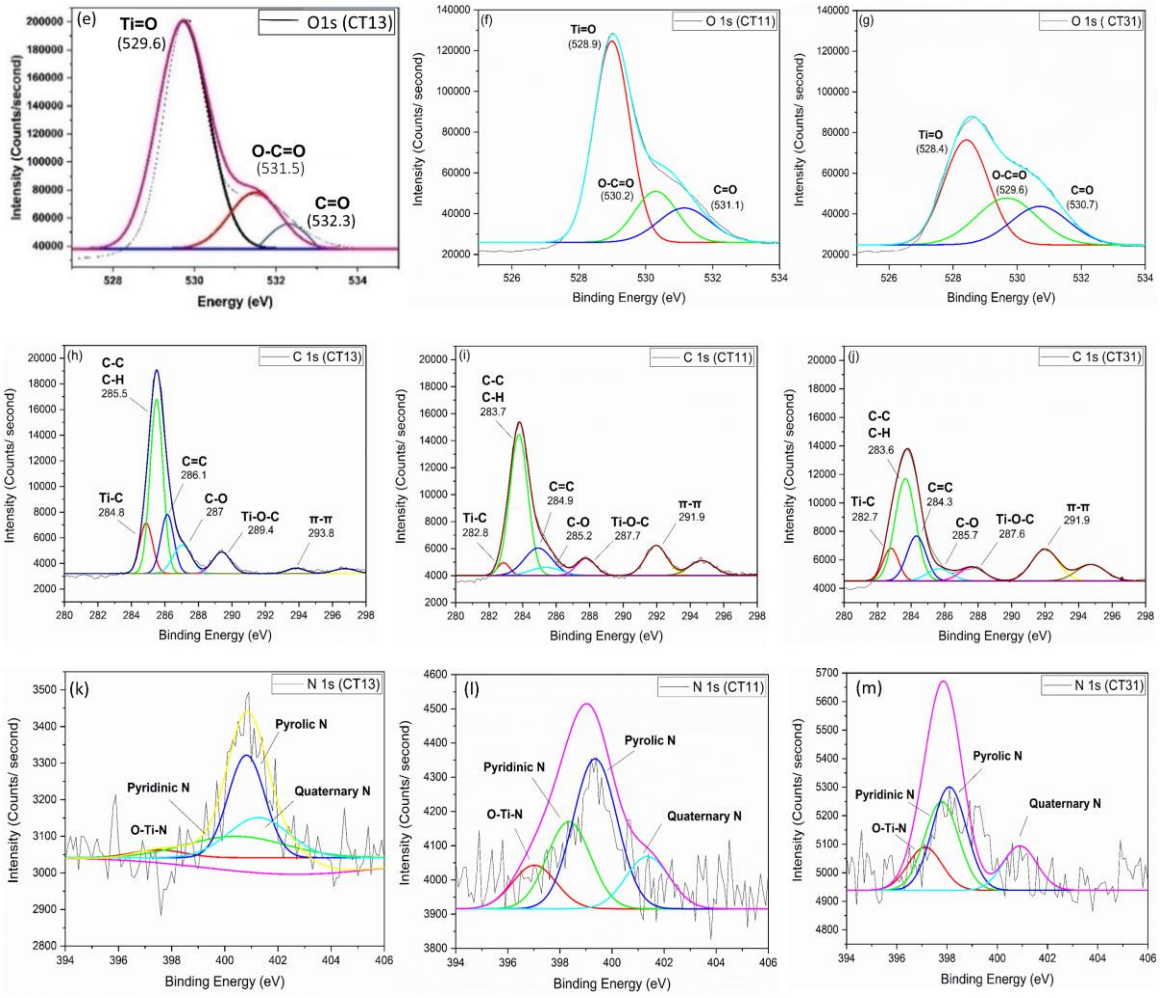


Figure 4.32 (a) Fully scanned XPS of CT13, CT11 and CT31; Ti 2p states the composites (b) CT13, (c) CT11 and (d) CT31; O 1s states the composites (e) CT13, (f) CT11 and (g) CT31; C 1s states the composites (h) CT13, (i) CT11 and (j) CT31; N 1s states the composites (h) CT13, (i) CT11 and (j) CT31.

4.2.2 Removal of PVC-NPs by using Synthesized Composites under different Conditions

A series of experiments were conducted to determine the removal efficiency of the composite material (Figure 10) under dark, tungsten light and room light conditions. CCAC and pure N-TiO_2 achieved the highest PVC-NPs removal of 33.58% and 24.98% followed by the CCAC/TiO_2 composites (48.6%, 35.6% and 31.7% for CT13, CT11 and CT31 respectively) as shown in **Figure 4.33(a)**.

The efficiency of composites in removing PVC-NPs was subsequently examined in both tungsten light (**Figure 4.33(c)**), and room light (**Figure 4.33(b)**). Under these

conditions, CT13, CT11, and CT31 demonstrated greater removal of PVC-NPs than under dark conditions; CT13 reached the highest percentage removal of 94% in tungsten light. It could be said that photocatalytic degradation would also concurrently occur with adsorption as light interacts with the material. Additionally, the percentage removal of PVC-NPs by pure N-TiO_2 under light conditions improved from 35.7% (dark) to 47.5% (room light) and 59.9% (tungsten-light), demonstrating the photocatalytic effects of N-TiO_2.

The composite materials exhibited higher PVC-NPs removal efficiencies after 180 min with that of the CCAC alone due to the synergistic effect of both the adsorption properties of CCAC and the photocatalytic properties of N-TiO_2. The CCAC/TiO_2 composites exhibited higher removal efficiencies of PVC-NPs than N-TiO_2 alone after 180 min, most likely due to the synergistic effect of CCAC and N-TiO_2. The CCAC provided a porous structure that allowed the efficient adsorption of PVC-NPs, while the N-TiO_2 facilitated photocatalytic degradation of the PVC-NPs. This combination resulted in contact between the composite material and PVC-NPs, leading to relatively efficient removal.

Figure 4.33 shows the PVC-NPs degradation rates for three composites. The highest removal rate was observed in CT13 composite having CCAC: N-TiO_2 as 1:3. The photocatalytic activity sequence of the CCAC/N-TiO_2 samples is CT13 > CT11 > CT31. These findings suggest that maximum photocatalytic efficiency can be achieved at a specific N-TiO_2 loading amount. However, as the CCAC loading increased beyond this point, the removal rate began to decrease instead. **Figure 4.34(b)** presents a real-life image of PVC-NPs degradation by CT13 composite material at pH 4. A clear and transparent liquid is observed with CT13 composite material. The photoactivity of N-TiO_2 was suppressed by the catalyst with the highest CCAC concentration. The effective photocatalytic activity of N-TiO_2 is decreased by the catalyst with the highest CCAC concentration because it hinders photon uptake by the N-TiO_2 surface [*Mao et al., 2009*]. The well-dispersed N-TiO_2 particles on the surface of CCAC, as shown by the XRD pattern in **Figure 4.28**, may be responsible for the improvement of the photocatalytic rates for the CCAC/TiO_2 composites up to a ratio of 1: 3 (in CT13) as

compared to neat N-TiO_2, because the PVC-NPs that are adsorbed on the CCAC surface can be readily transferred to the N-TiO_2 surface.

4.2.2.1 Effect of pH on the Removal of PVC-NPs

For the removal of PVC-NPs using prepared CT13, CT11 and CT31 nanocomposite at pH 4, pH 7 and pH 10 have been studied. The photodegradation process can be optimized by evaluating the catalyst's surface charge properties in relation to the pH of the water. Point of zero charge (PZC) is essential for researching the surface chemistry of the material and helps in the development of efficient wastewater treatment techniques for particular pollutants. The PZC of the N-TiO_2 is 5, indicating that at pH values lower than this, the surface charge of N-TiO_2 is positive (pH < PZC) on the other hand, the surface charge turns negative as the pH rises above 5 [*Nguyen et al., 2020*]. However, introducing CCAC changed the PZC value, moving it from acidic to neutral pH [*Abdu et al., 2025*]. The PZC values for CT13, CT11, and CT31 were 6, 6.15, and 6.37, respectively. The pH value increased with an increasing percentage of CCAC in CCAC/N-TiO_2 composites. According to the results, CCAC/N-TiO_2 composites showed the maximum removal capacity of 94%, 92.7%, and 51.4% under tungsten bulb light for CT13, CT11, and CT31 composites, respectively, for PVC-NPs (having a negative surface charge, as discussed in **Section 4.1.2.4**) in an acidic medium at pH 4, as shown in **Table 4.11**, because the surface of CCAC/N-TiO_2 composites was positively charged (pH < PZC) and attracts negatively charged pollutants when the pH is below point zero charge (PZC) [*Jedynak et al., 2024*]. This indicates that adsorption is dependent on electrostatic interactions [*Chakhtouna et al., 2021*]. By increasing the pH from 4 to 7, CCAC/N-TiO_2 gradually lost its positive charge until it reached the PZC of composites, i.e., ~6, and the adsorption capacity of PVC-NPs decreased. At higher pH levels (7 and 10), both PVC-NPs molecules and CCAC/N-TiO_2 composites (pH > PZC) were negatively charged, resulting in a significant decrease in adsorption capacity due to increased electrostatic repulsions and, ultimately, photocatalytic activity [*Varela et al., 2024*].

4.2.2.2 Effect of Light Source on the Removal of PVC-NPs

Furthermore, it was observed that the removal efficiency was greatly influenced by changing the light sources and at different pH as shown in **Table 4.11**. Tungsten bulb and room light have been used in a number of experiments. Room light was a light source with the visible light spectrum range from approximately 400 nm to 780 nm [Duncan et al., 2012], while tungsten bulb light was within a wavelength range of 350-1000 nm [Thoms et al., 2013], the experimental results demonstrated that the degradation rate under room light conditions was lower than that under tungsten bulb light. This is because, the wavelength of the light source significantly impacts a photocatalyst's ability to absorb light and subsequently drive a reaction. Shorter wavelengths (higher energy) range are generally more effective for exciting electrons across the band gap of photocatalysts, leading to higher photocatalytic activity. UV-A radiation, which usually has a wavelength range of 315–400 nm, is included in tungsten bulb light. In theory, higher light intensity enhances the excitation of electrons from the valence band to the conduction band and increase the rate at which electron–hole pairs are generated by increasing the number of incident photons on the photocatalyst surface per unit time [Paiu et al., 2025].

4.2.2.3 Effect of scavengers

The common substances involved in photocatalytic reactions that contribute to the degradation of organic matter are holes, hydroxyl radicals, and superoxide anion radicals [*Dorraj et al., 2017*]. To investigate the degradation mechanism of CCAC/N-TiO_2 composites on PVC-NPs, active species trapping experiments were conducted. Isopropyl alcohol, sodium oxalate, and parabenzoquinone were used to quench hydroxyl radicals, holes, and superoxide anion radicals, respectively. The addition of isopropyl alcohol, sodium oxalate, and parabenzoquinone decreased the removal efficiency of PVC-NPs to 6.8%, 22.1% and 20.6%, respectively, as illustrated in **Figure 4.33(d)**, suggesting that the breakdown of PVC-NPs was inhibited to different extents. As a result, it could be concluded that all three active species were engaged in the oxidation of PVC-NPs, with hydroxyl radicals playing a significant role. Zhao et al. reported the similar results [*Zhao et al., 2018*].

Table 4.11 Comparison of % removal of N-TiO_2, CCAC, CT13, CT11 and CT31 with light and without light.

	% Removal with CCAC			% Removal with N-TiO_2			% Removal with CT13				% Removal with CT11			% Removal with CT31		
	TL	RL	Dark	TL	RL	Dark	TL	RL	CFL	Dark	TL	RL	Dark	TL	RL	Dark
pH 4	38.7	39.8	33.6	59.9	47.5	35.7	94	69.0	58.8	48.6	92.7	50.9	35.8	51.4	24.5	31.7
pH 7	36.9	31.6	29.7	13.3	10.3	20.1	15.9	14.9	11.6	14.8	26.2	14.9	15.3	24.6	13.9	11.2
pH 10	35.2	36.2	28.5	1.8	4.9	13.6	9.9	9.7	7.2	14.1	16.7	9.8	8.6	19.3	17.7	7.4

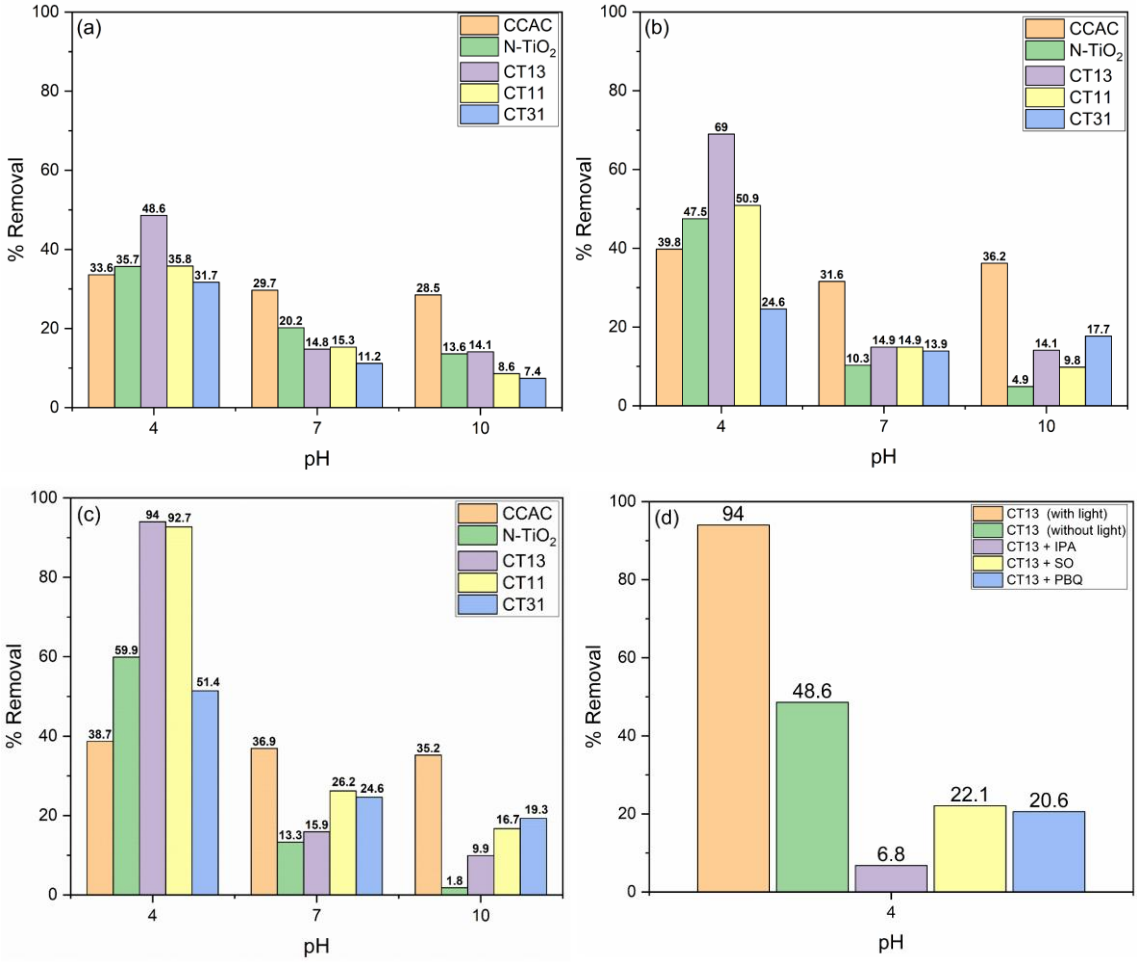
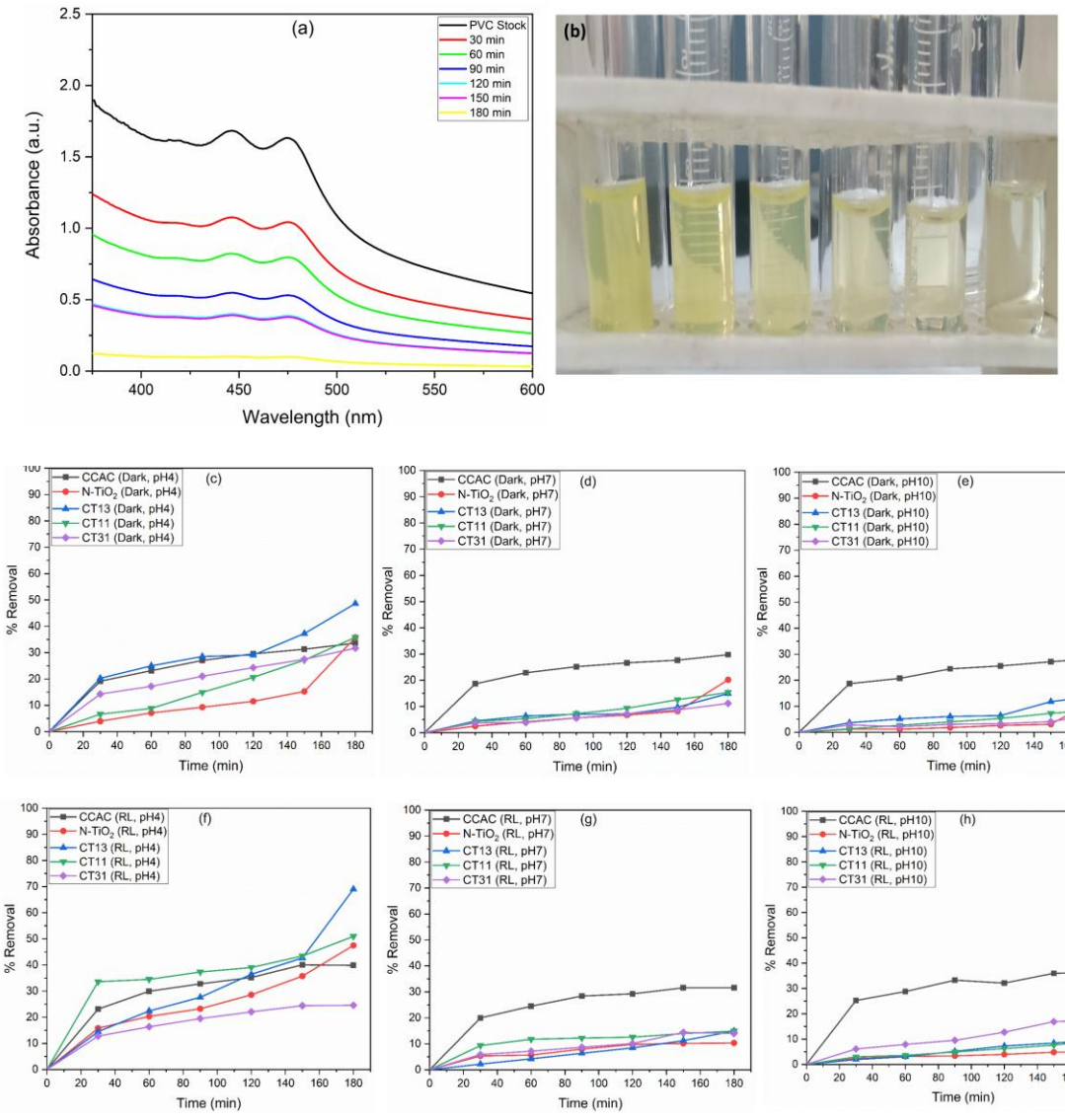


Figure 4.33 Comparison of % removal PVC-NPs with CCAV, N-TiO_2, CT13, CT11, and CT31 under (a) without light (b) room light (c) tungsten bulb light (d) comparison of % removal PVC-NPs under tungsten bulb light using CT13 +quenchers isopropyl alcohol, sodium oxalate, and parabenzoquinone at pH 4.

4.2.2.4 Effect of Time on the Removal of PVC-NPs

Another important aspect to look at was how removal time affected the synthetic composites' capacity to extract PVC-NPs from water. PVC solutions were agitated with composites at intervals of 30 to 180 minutes in order to examine their removal efficacy. The elimination rate of PVC-NPs was assessed using an optimal quantity of the generated composites (80 mg). As the duration increased from 30 to 180 minutes, the removal rate (%) of PVC particles for CCAC, N-TiO_2, CT13, CT11, and CT31 at pH4 under tungsten bulb light increased from 18.4% to 38.7%, 17.8% to 59.9%, 36% to 94%, 24.6 %to 92.7%, 21.3% to 51.4%, respectively (**Figures 4.34b**, **4.34c**, and **4.34d**). The catalyst's surface receives more light energy over time, which causes photoexcited species to develop and increases photocatalytic activity. Real-life image of PVC-NP solution in the time interval of 30–180min at pH 4 is shown in **Figure 4.34(b)**.



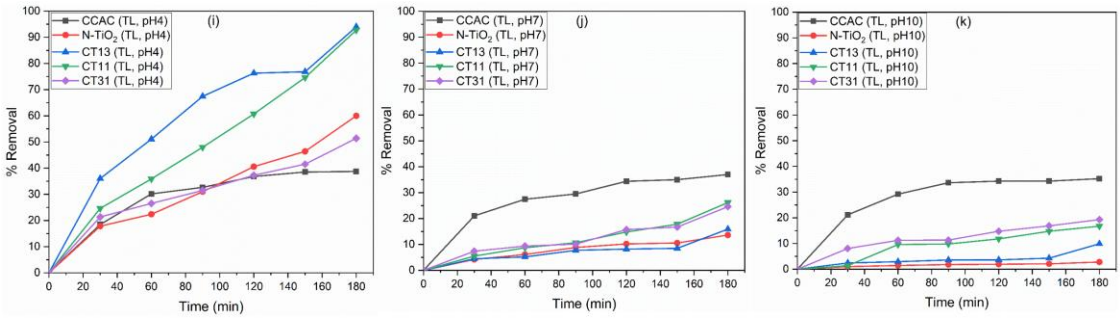


Figure 4.34 (a) UV absorption spectra of PVC-NP removal with CT13 at pH4 (b) real-life image of PVC-NP solution in the time interval of 30–180min at pH 4; PVC-NP removal from water treated with CCAC, N-TiO_2, CT13, CT11, and CT31 over a 30- to 180-minute time period under (c) dark at pH 4 (d) dark at pH 7 (e) dark at pH 10 (f) room light at pH 4 (g) room light at pH 7 (h) room light at pH 10 (i) tungsten bulb light at pH 4 (j) tungsten bulb light at pH 7, and (k) tungsten bulb light at pH 10.

4.2.2.5 Analysis of Composite Material and PVC-NP Solution after Removal Experiment

To understand the mechanism involved in the remediation process, further SEM, EDS, fluorescence microscopy, zeta potential, FTIR spectroscopy, and GCMS studies were conducted on CT13 and the solution left behind after the remediation experiment.

To understand the mechanism involved in the remediation process, more research was conducted on CT13 and the solution left behind after the removal experiment. After the process, a real-life image of PVC-NPs adsorbed on CT13 composite at pH 4 was clearly visible and decreases at pH 7 and pH 10. A visible colour changes as well as swelling of CT13 at pH 4 was observed after the reaction, as shown in **Figure 4.35**.

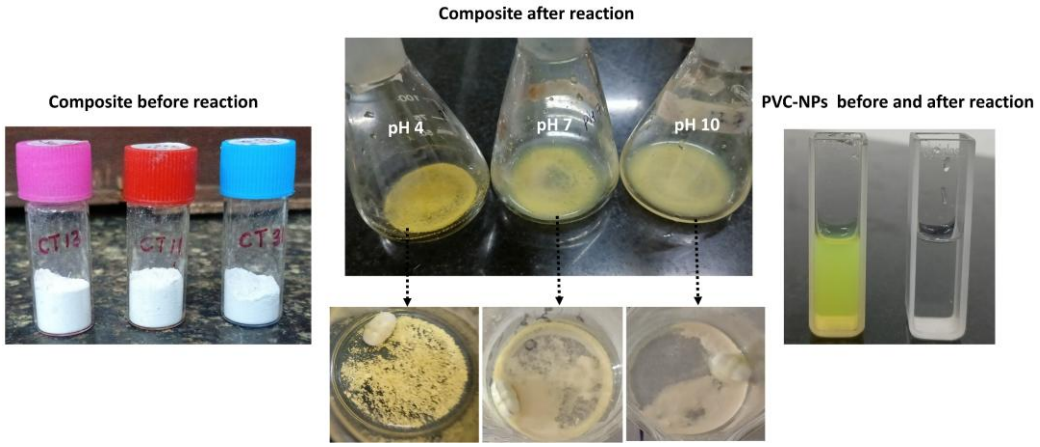
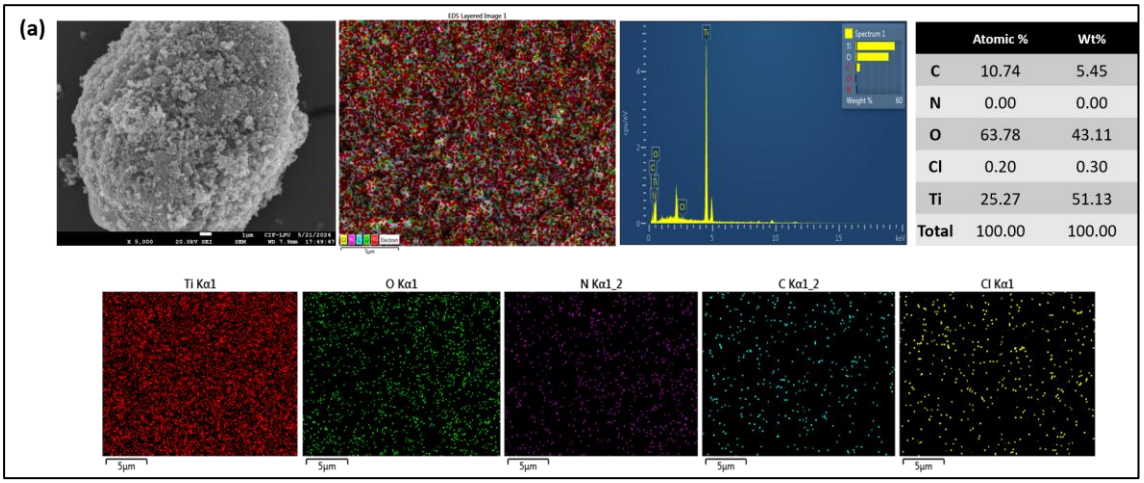
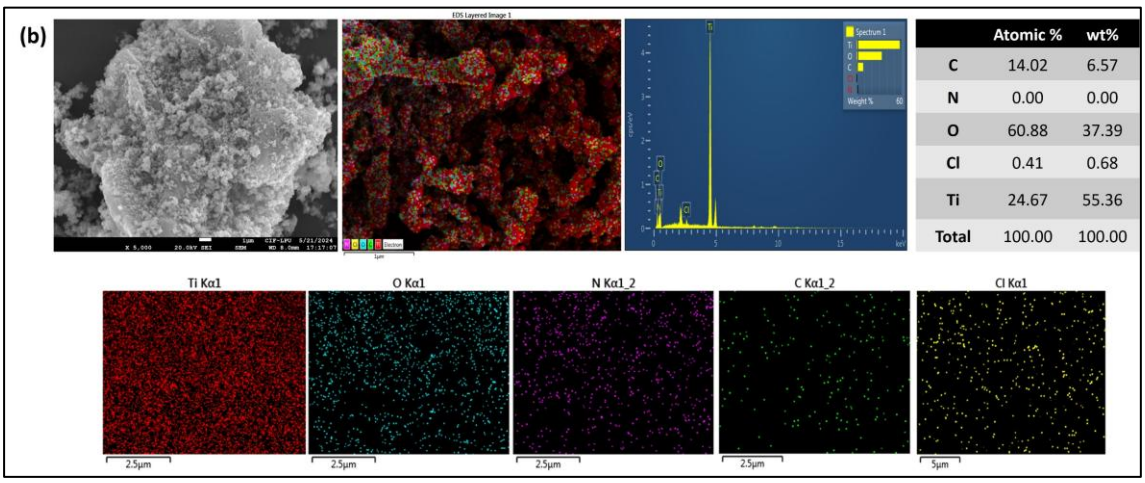


Figure 4.35 Real-life image of CT13 composite before and after reaction showing PVC-NPs adsorbed on composite at pH 4, pH 7 and pH 10, and PVC-NPs solution before and after reaction.

The swelling of CT13 composite could be attributed to adsorption-induced swelling, which refers to the expansion or deformation of a porous material when it adsorbs a pollutant [Bakhshian et al., 2017].

SEM micrographs of the surface morphology of CT13 composite and N-TiO_2 after the removal of PVC-NPs are shown in **Figure 4.36(a)**, **4.36(b)**, and **4.36(c)**, with and without light, respectively. It was discovered that there are some distinct spherical particles of PVC-NPs on the surface of CT13, but the distinction is difficult to distinguish because both N-TiO_2 and PVC-NPs exhibit spherical surface morphology. EDS analysis and elemental mapping confirmed the presence of chlorine, as depicted in **Figure 4.36(a)**, **4.36(b)** and **4.36(b)**, demonstrating the interaction between PVC-NPs, CT13 composite and N-TiO_2, respectively, after the removal reaction.





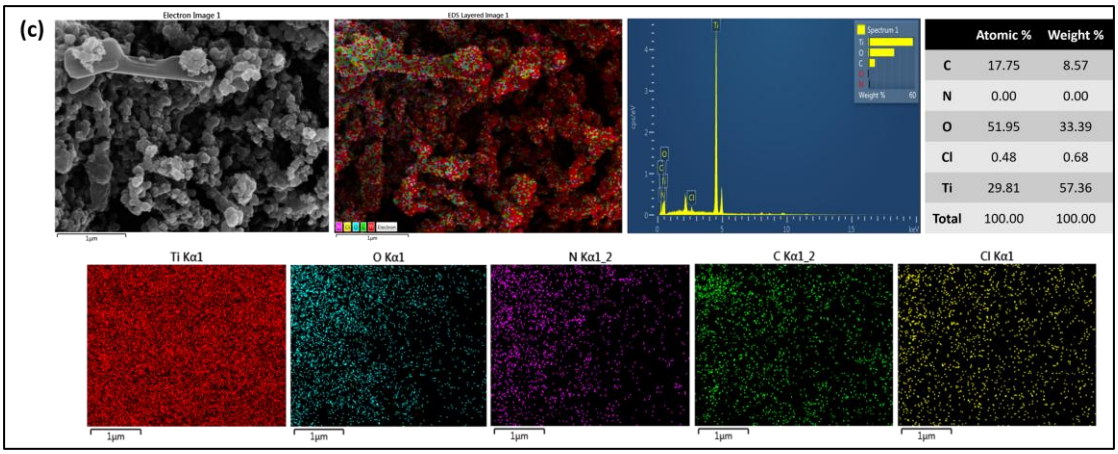


Figure 4.36 SEM, EDS and elemental mapping images after reaction using (a) CT13 with light (b) CT13 without light (c) N-TiO_2 with light.

Furthermore, a **fluorescence microscope** was used to investigate the presence of yellow dyed PVC nanoparticles on CT13 composite following the removal experiment. **Figure 4.37** shows fluorescence microscopic images of pure PVC-NPs, CT13, and CT11 composites following remediation. The photos showed that the CT13 and CT11 surfaces had been covered with green, fluorescent PVC-NPs following their interaction with PVC-NPs. This suggested the existence of significant interactions between composite surface functionalities and those of PVC-NPs.

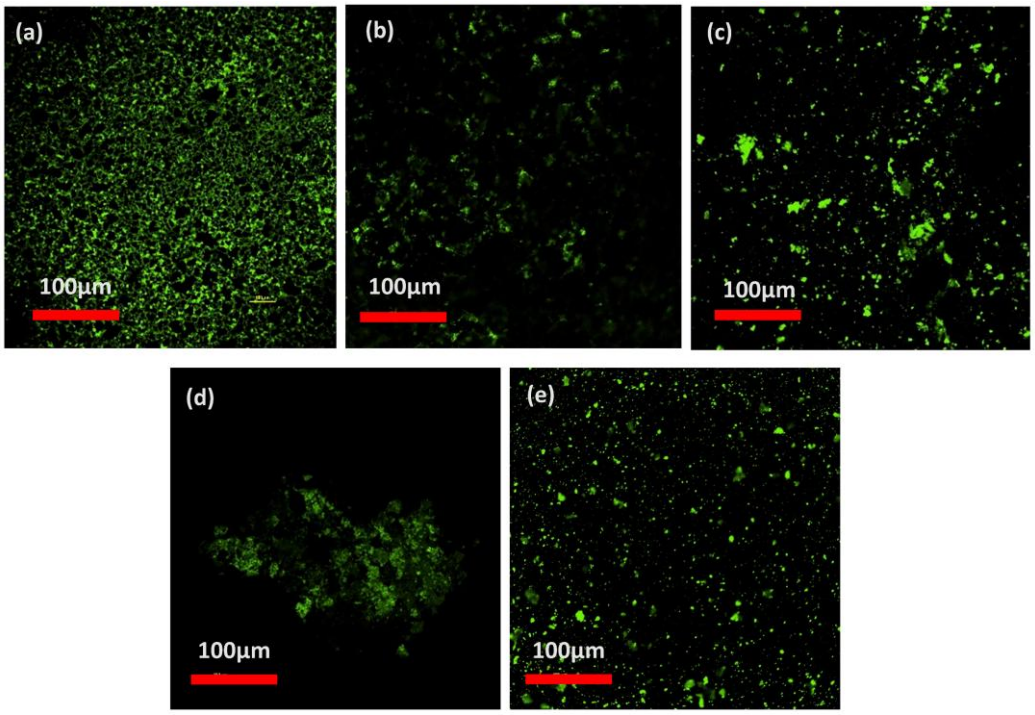


Figure 4.37 Optical micrographs of (a) PVC-NPs; CT13 after the remediation experiment (b) with light (c) without light; CT11 composite after the remediation experiment (d) with light (e) without light.

In order to evaluate changes in particle zeta potential, **DLS measurements** were performed on solution obtained right after the removal experiment. The observed zeta potential of the solution after removing PVC nanoparticles was -13.9 mV. The values are lower than those of pure PVC-NPs, which may be due to charge neutralization by the CT13 composite [*Batool et al., 2020*].

FTIR spectroscopy was used to analyze the composition of CT13 composite and pure PVC solution before and after the removal of PVC nanoparticles as shown in **Figure 4.38(a)**.

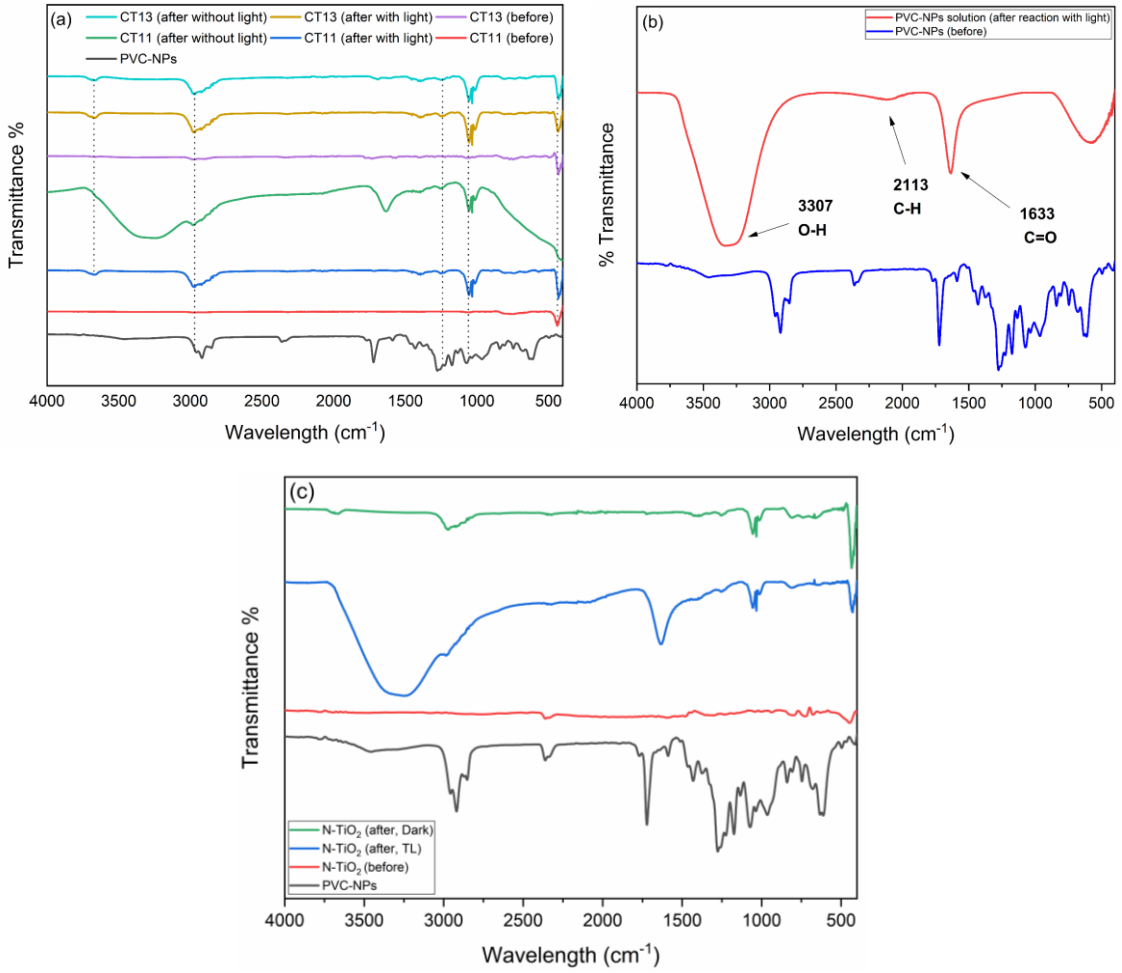
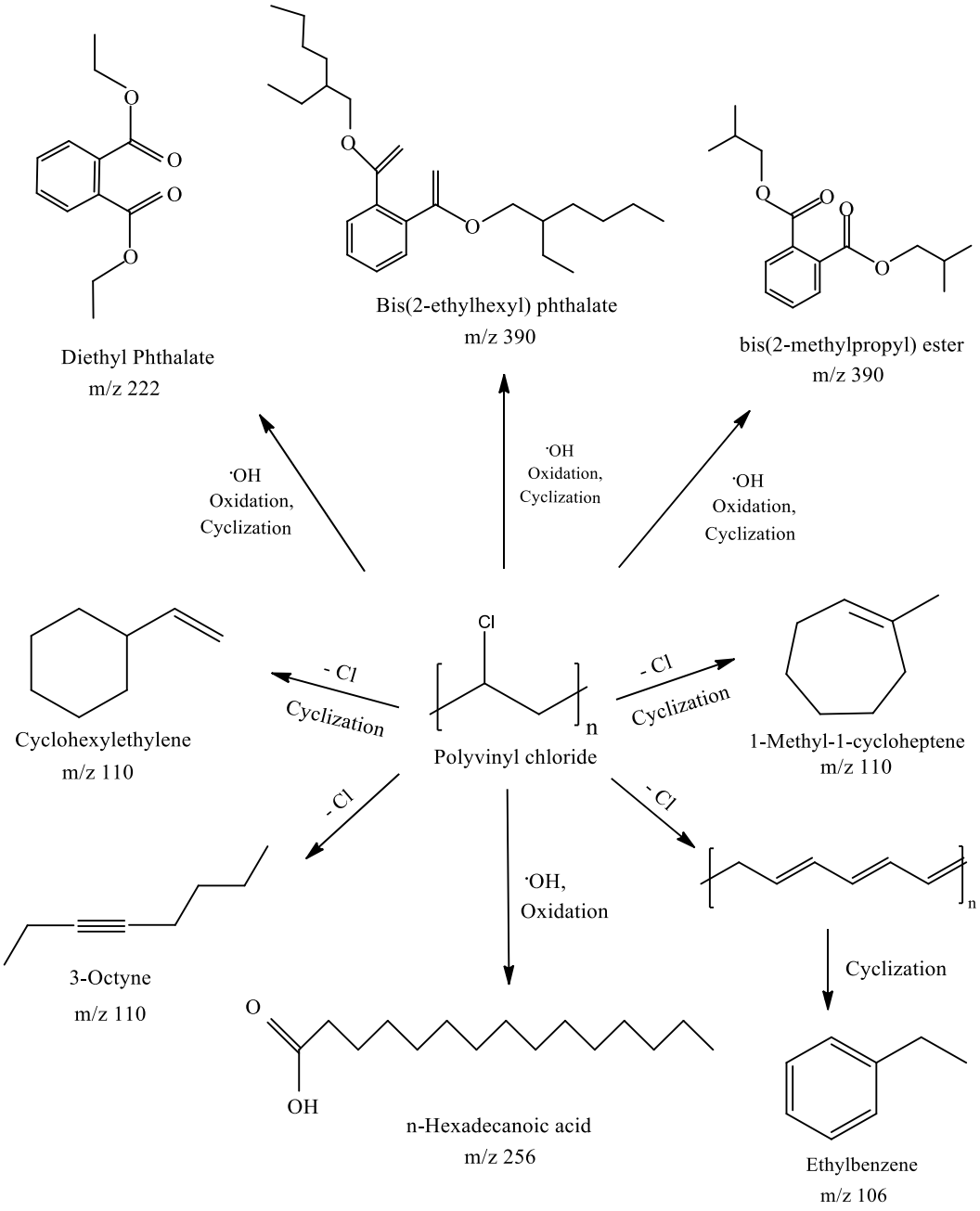


Figure 4.38 FTIR spectra of (a) CT13 and CT11 before and after reaction with and without light (b) pure PVC-NPs solution and PVC solution after the remediation experiment (c) N-TiO_2 before and after reaction with and without light.

The spectra of CT13 before and after don't look same because the PVC-NPs adsorbed on the surface of CT13. The FTIR spectrum of PVC shows peaks at 2965 cm^{-1} and 2924 cm^{-1} consisting of the CH_2 asymmetric stretching vibration mode. The peak at higher wavenumber shows the asymmetric stretching bond of C − H and the lower peak is for the symmetrical stretching bond of C − H. The peaks around 1438cm^{-1} are assigned to the C − H aliphatic bending bond. The peak at 1282 cm^{-1} is attributed to the bending bond of C − H near Cl. The C − C stretching bond of the PVC backbone chain occurs in the range 1000-1100 cm^{-1}. Finally, peaks in the range of 600-650cm^{-1} correspond to the C-Cl bond. After adsorption, FTIR spectra of CT13 displays the addition peaks corresponding to PVC NPs, which point to the existence of PVC NPs adsorbed on CT13 surface. After photocatalytic activity, FTIR spectra of CT11, displays the addition peaks in 850–515 cm^{-1} region, which corresponds to presence of C-Cl bond [*DE LORENZI et al., 1999*]. **Figure 4.38(b)** represents the FTIR spectra of PVC solution before and after treatment.

Degradation products of PVC-NPs must be identified in order to understand the mineralization process and its effects on the environment. The intermediates during the oxidation of PVC-NPs were assessed using **gas chromatography-mass spectrometry (GC-MS)**. A potential degradation mechanism of PVC-NPs was suggested in Scheme 4.3 based on the GC-MS analysis of short-chain organics.

In addition to releasing organic intermediates into solution, PVC-NPs were oxidized by $^{\bullet}OH$ to produce oxyorganics with oxygen groups like C=O and O-H. The exfoliating hydrocarbon species were then subjected to further oxidation by $^{\bullet}OH$ to break down into lower molecular weight components like alcohols, carboxylic acids, and esters. These materials eventually partially mineralized into CO_2 and H_2O. The structures of degraded products were elucidated by their mass fragmentation pattern after correlation with the reported literature [*Miao et al., 2020*].



Scheme 4.3. GC–MS analysis of PVC degradation using CT13.

4.2.2.6 *Mechanism of Removal of PVC-NPs*

As seen in **Scheme 4.4**, the composite's decontamination mechanism was ascribed to the synergistic interaction of CCAC adsorption and N-TiO_2 photocatalysis. Firstly, PVC-NPs are adsorbed by CCAC by hydrophobic interactions, π-π interaction, electrostatic attractions, halogen bonding, and hydrogen bonding between CCAC and PVC-NPs (**Scheme 4.4**) [*Varela et al., 2024*, *Bashir et al., 2024*, *Tilton et al., 1991*,

Nosratabad et al., 2024, *Weidner et al., 2022*, *Zheng et al., 2024*, *Valiyaveettil Salimkumar et al., 2024*, *Das et al., 2025*, *Mulindwa et al., 2024*, *Alom et al., 2024*, *Wu et al., 2019*]. The π-electrons from the benzene rings of CCAC and the halogen atoms of PVC form halogen bonding. While the benzene rings and hydroxyl groups (-OH) can be thought of as electron-donating groups, the -Cl on the PVC branch may operate as an electron acceptor. This could result in the formation of a particular halogen bond between the -Cl groups and electron donor arenes [*Wu et al., 2019*]. Aromatic rings of CCAC and polyene structures in PVC-NPs show π-π interactions, enhanced sorption [*Liang et al., 2021*]. PVC-NPs occupy active adsorption sites on the hydrophobic surface of CCAC/N-TiO_2. The experimental results indicate the presence of hydrophobic interactions between PVC plastic surfaces and the hydrophobic surface of CT13, as confirmed by XPS (**Section 4.5.7**). This is consistent with current study findings, which show that synthetically generated hydrophobic adsorbents are highly effective at adsorbing PVC-NPs from aqueous bodies using hydrophobic interactions as the primary sorption mechanism [*Bhagwat et al., 2023*].

The concentration of pollutants near N-TiO_2 increases as a result of the pollutants being fixed on the composite material's surface by the high adsorption of CCAC. By acting as an electron acceptor during the photocatalytic degradation process, CCAC can lower the rate at which electrons and holes recombine, increasing the quantity of electrons accessible for photocatalytic processes. Additionally, by dispersing N-TiO_2 particles more widely, CCAC can reveal additional photocatalytic reaction active sites [*Yue et al., 2024*].

The presence of CCAC improves the generation of positive holes in N-TiO_2 and the production of $^{\bullet}OH$ radicals. This is due to electron transfer from the conduction band of N-TiO_2 particles to the graphitic structure of CCAC, which reduces electron recombination. This is in good agreement with a recent study by Mao's group on the use of TiO_2/carbon black composite catalysts for the degradation of organic contaminants in the liquid phase. Additionally, they noted a comparable improvement in the photocatalytic activity of TiO_2 combined with carbon black [*Castilla-Caballero et al., 2023*, *Cui et al., 2020*].

It is anticipated that PVC-NPs degradation using CCAC/N-TiO_2 samples will proceed as follows, according to a well-established photocatalysis procedure. (i) Light radiation creates electron-hole pairs in N-TiO_2 nanoparticles in CCAC/N-TiO_2 composite (Eq. 4.1). Photo-excited electrons in the N-TiO_2 conduction band combine with adsorbed and/or dissolved oxygen to generate superoxide free radicals ($^{\bullet}O_2^{-}$) (Eq. 4.3), and (ii) passage from the N-TiO_2 conduction band to the CCAC domains (Eq. 4.2), where it accumulates and reacts with adsorbed or dissolved oxygen to form superoxide free radicals ($^{\bullet}O_2^{-}$) (Eq. 4.4) [*Yang et al., 2019*]. (iii) N-TiO_2 valence band holes react with hydroxyl ions in aqueous PVC-NP solution, forming hydroxyl free radicals ($^{\bullet}OH$) (Eq. 4.6). (iv) These radicals are highly reactive with PVC-NP molecules, breaking them down to less toxic molecules such as CO_2, water and other degraded products [*Zarrin et al., 2018*, *Liu et al., 2015*]. The use of CCAC as a PVC-NP adsorbent improves the interaction between N-TiO_2 nanoparticles and PVC-NPs throughout the process. The CCAC substrates in the CCAC/N-TiO_2 provide an effective electron channel via Ti-O-C bonds for photo-excited electrons in the N-TiO_2 conduction band to flow towards the CCAC surface, where they react with adsorbed/dissolved O_2 to generate PVC-NPs reactive superoxide free radicals ($^{\bullet}O_2^{-}$) [*Chakhtouna et al., 2021, Hirakawa et al., 2005*].

$$CCAC/N\text{-}TiO_2 + h\nu \text{ (light irradiation)} \rightarrow (e^-_{CB}) - CCAC + N\text{-}TiO_2\,(h^+_{VB}) \quad (4.1)$$

$$N\text{-}TiO_2\,(e^-_{CB}) - CCAC \rightarrow CCAC/N\text{-}TiO_2\,(e^-) \quad (4.2)$$

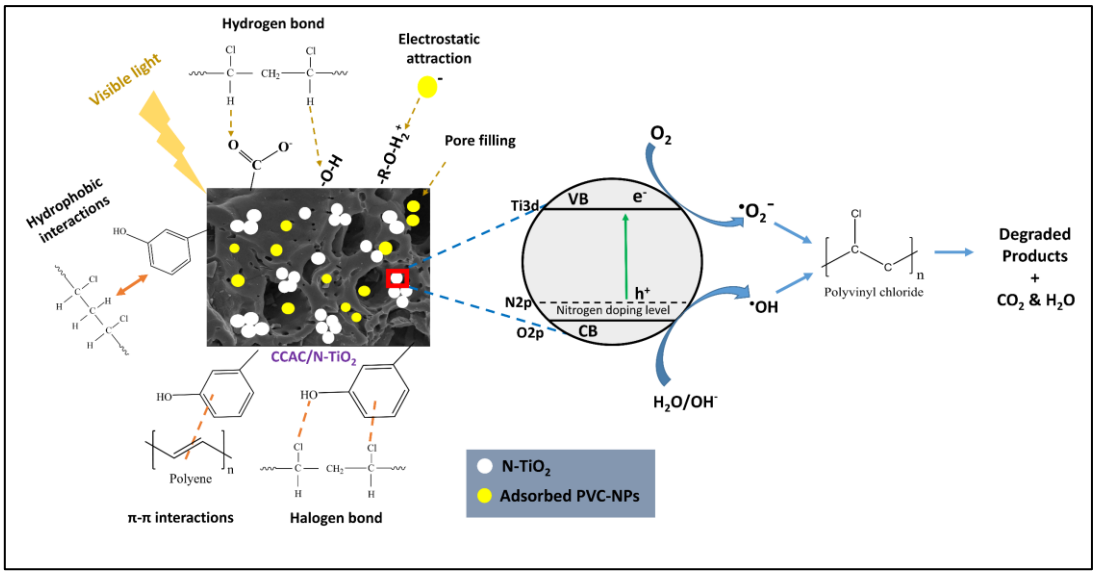
$$N\text{-}TiO_2\,(e^-_{CB}) - CCAC + O_2 \rightarrow {}^{\bullet}O_2^- \quad (4.3)$$

$$CCAC/N\text{-}TiO_2\,(e^-) + O_2 \rightarrow {}^{\bullet}O_2^- \quad (4.4)$$

$$N\text{-}TiO_2\,(h^+_{VB}) + OH^- \rightarrow {}^{\bullet}OH \quad (4.5)$$

$$PVC\text{-}NPs + {}^{\bullet}OH \rightarrow CO_2 + H_2O + \text{Degradation products} \quad (4.6)$$

$$PVC\text{-}NPs + {}^{\bullet}O_2^- \rightarrow CO_2 + H_2O + \text{Degradation products} \quad (4.7)$$



Scheme 4.4 Proposed mechanism of PVC degradation under visible light illumination using CT13 photocatalyst.

4.2.3 Removal Study of PS-NPs using CCAC/N-TiO_2 Nanocomposites

A series of experiments were conducted to determine the removal efficiency of CCAC, N-TiO_2 and CCAC/N-TiO_2 composite materials under tungsten light and dark conditions at pH values of 4, 7, and 10, within 3 hours.

It was observed that in dark, Pure CCAC achieved the highest PS-NPs removal of 26.3% followed by the CCAC/N-TiO_2 composites (15.9%, 14.2% and 17.2% for CT13, CT11 and CT31 respectively) as shown in **Figure 4.39(b)**.

The efficiency of composites in removing PS-NPs was also examined in tungsten light (**Figure 4.39(a)**). Under these conditions, CT13, CT11, and CT31 demonstrated increased % removal of PS-NPs than under dark conditions; CT31 reached the highest percentage removal of 30.8% in tungsten light at pH 4. It could be said that photocatalytic degradation would also concurrently occur with adsorption as light interacts with the material.

4.2.3.1 Effect of pH on the Removal of PS-NPs

The effects of pH on PS-NPs removal using CCAC, and CCAC/N-TiO_2 composite materials were investigated at pH levels 4, 7, and 10 as shown in **Figures 4.39(a)** and **4.39(b)** showing that as pH increases from 4 to 10, the removal percentage of PS-NPs

decreases. A maximum of 30.8% PS-NP removal was achieved at pH 4 by CT31 under TL. The PZC values for CT13, CT11, and CT31 were 6, 6.15, and 6.37, respectively. For PS-NPs (having a negative surface charge, as discussed in **Section 4.1.2.4**) in an acidic medium at pH 4 and the surface of CCAC/N-TiO_2 composites was positively charged (pH < PZC) and attracts negatively charged pollutants when the pH is below point zero charge (PZC) indicates that adsorption is dependent on electrostatic interactions [*Chakhtouna et al., 2021*]. By increasing the pH from 4 to 7, CCAC/N-TiO_2 gradually lost its positive charge until it reached the PZC of composites, i.e., ~6, and the adsorption capacity of PS-NPs decreased. At higher pH levels (7 and 10), both PS-NPs molecules and CCAC/N-TiO_2 composites (pH > PZC) were negatively charged, resulting in a significant decrease in adsorption capacity due to increased electrostatic repulsions and, ultimately, photocatalytic activity [*Varela et al., 2024*].

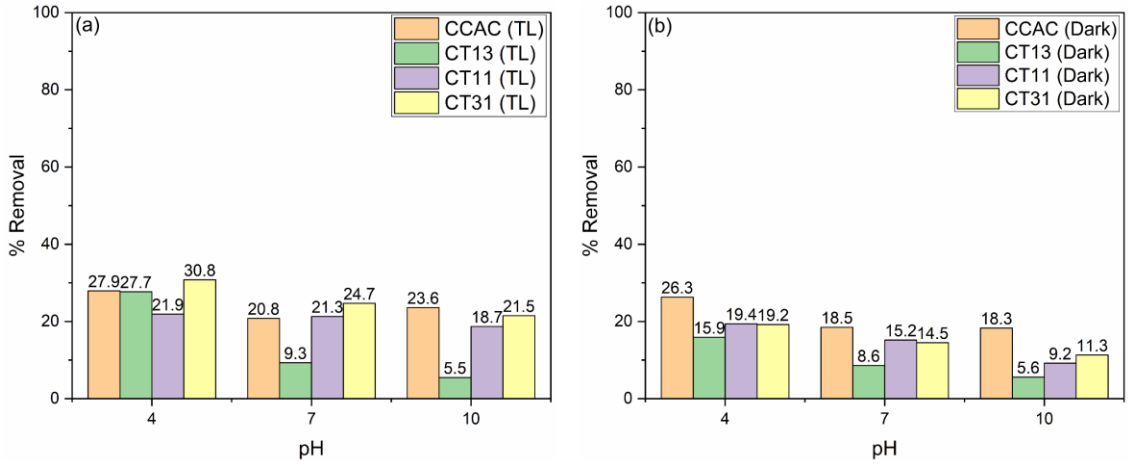


Figure 4.39 Comparison of % removal PS-NPs at pH 4, pH 7 and pH 10 with CCAC, CT13, CT11, and CT31 under (a) tungsten bulb light (b) dark.

4.2.3.2 Effect of Time on the Removal of PS-NPs

The effect of removal time on removal efficacy of PS-NPs was evaluated by agitating them with composites at time interval of 30-180 minutes. To assess the PS-NP removal rate, an optimal quantity of the synthesized bare CCAC and CCAC/N-TiO_2 composites (80 mg) was used. As the time span increased from 30 to 180 minutes, the % removal of PS-NPs for CCAC, CT13, CT11, and GT31 at pH 4, pH 7, pH 10 under tungsten bulb light are shown in **Figure 4.40(c)**, **4.40(d)**, and **4.40(e)** and under dark are shown in **Figure 4.40(f)**, **4.40(g)**, and **4.40(h)** showing that % removal increases with increase

in reaction time. The catalyst's surface receives more contact time, which increases removal activity.

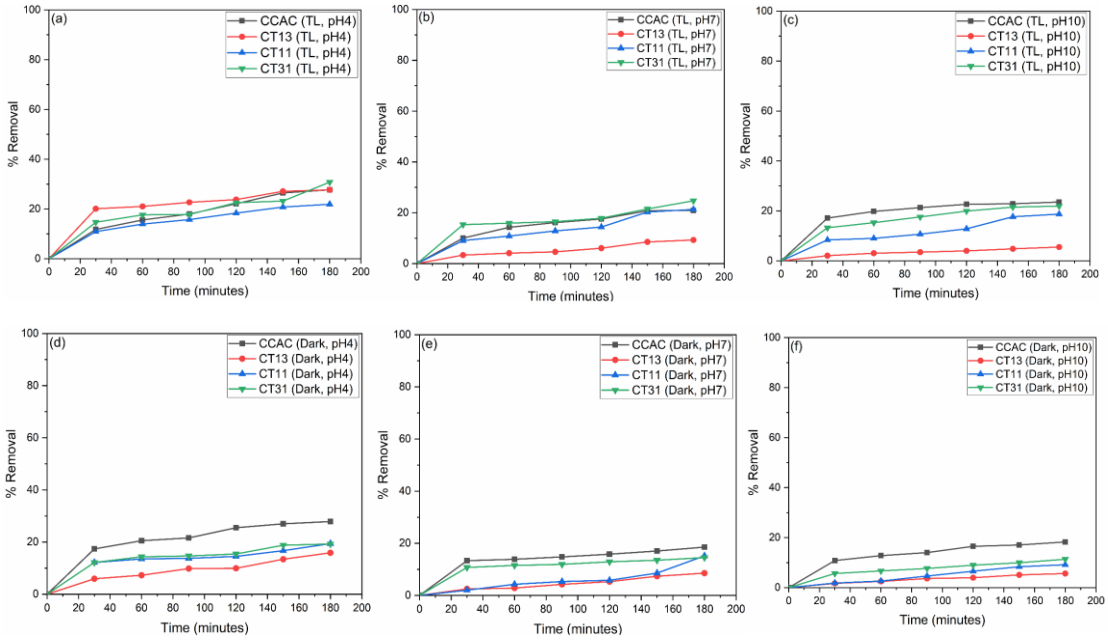


Figure 4.40 PS-NPs removal from water treated with CCAC, N-TiO_2, CT13, CT11, and CT31 over a 30- to 180-minute time period under (a) tungsten bulb light at pH 4 (b) tungsten bulb light at pH 7 (c) tungsten bulb light at pH 10 (d) dark at pH 4 (e) dark at pH 7, and (f) dark at pH 10.

4.3 NITROGEN-DOPED SnO_2 AND GO/N-SnO_2 NANOCOMPOSITES FOR REMOVAL OF POLYVINYL CHLORIDE (PVC) AND POLYSTYRENE (PS) FROM WATER

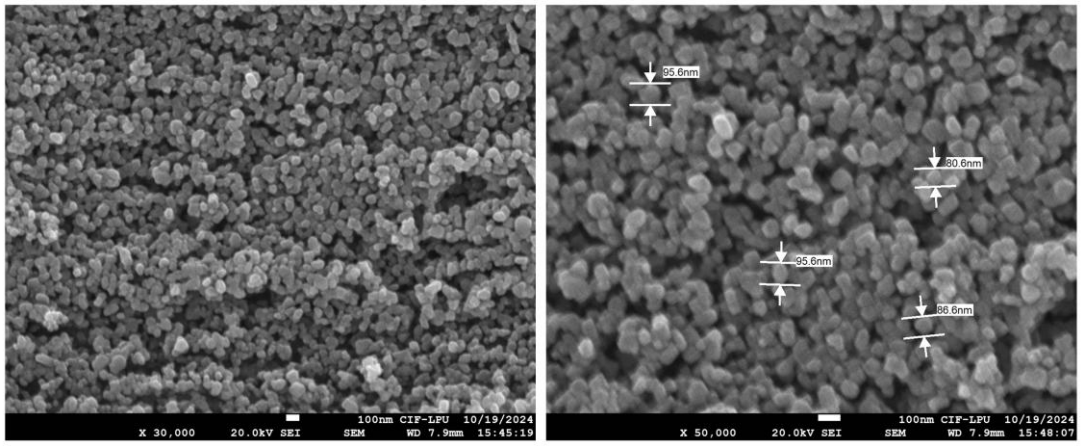
In this section, characterization of bare N-SnO_2 and GO/N-SnO_2 composites and the removal study of PVC-NPs and PS-NPs using the synthesized materials are explained. Furthermore, analysis of material after the PVC-NPs and PS-NPs removal experiment is discussed.

4.3.1 Characterization of N-SnO_2, N-ZrO_2 and GO/N-SnO_2

4.3.1.1 Scanning Electron Microscope Analysis of nanocomposite

The morphology of prepared materials N-SnO_2 nanoparticles GNSO13 (composite of GO and N-SnO_2) and was examined using field emission scanning electron microscope (FESEM). The surface morphology of N-SnO_2 nanoparticles is shown in **Figure 4.41(a)**. N-SnO_2 NPs show a spherical crystalline shape with a size in the range of ~80–95 nm. Based on this, it allows the verification of nanocomposites synthesis. The characteristic surface morphology of GNSO13 is shown in **Figure 4.41(b)**. The SEM image of GO confirms the layered structure as discussed in **Section 4.1.3**. N-SnO_2 nanoparticles are embedded in GO sheets, and these particles are uniformly distributed.

(a)



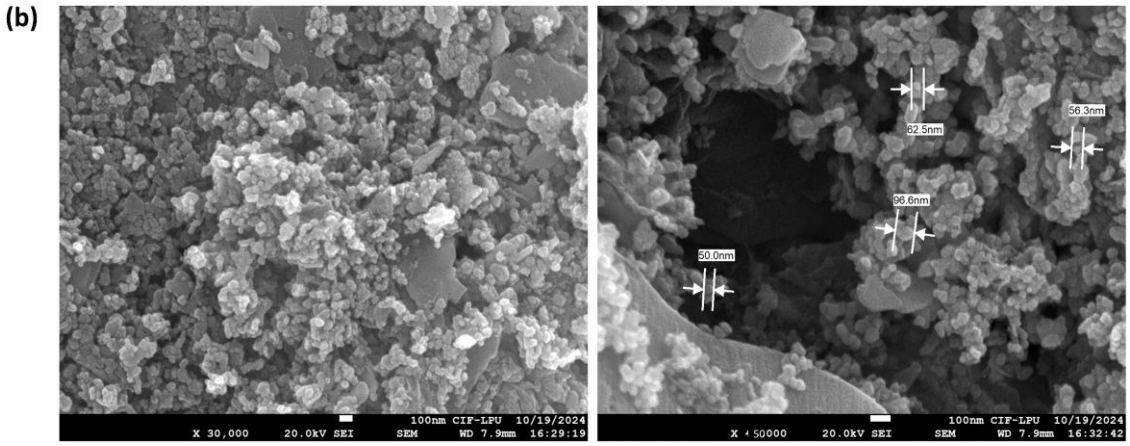
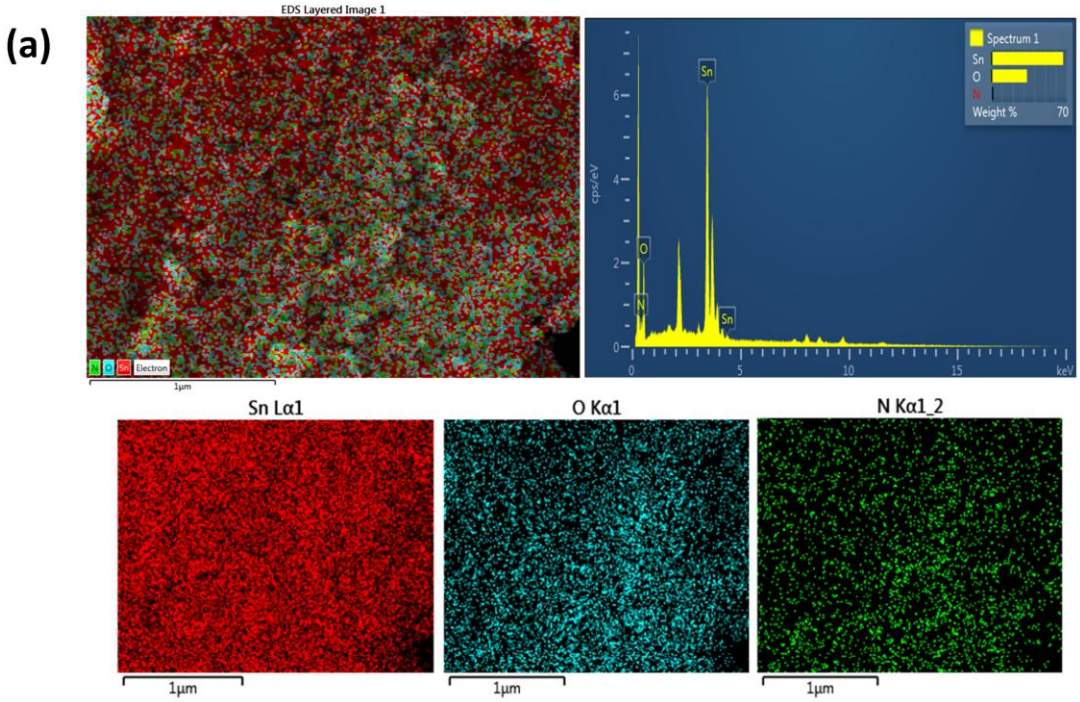


Figure 4.41 Scanning electron microscope (SEM) images of (a) N-SnO_2 and (b) GNSO13 composite.

4.3.1.2 Energy-Dispersive X-ray Spectroscopy Analysis

The elemental composition of all produced composites was determined by energy dispersive X-ray analysis (EDX). The EDX spectrum is shown in **Figure 4.42**, while the quantitative elemental composition is shown in **Table 4.12**. The maps indicate a distinct distribution of each element, indicating that N-SnO_2 nanoparticles were well spread or embedded between the GO layers. The emergence of C, O, Sn and N peaks indicated that the GNSO13 composites had been successfully formed without impurities.



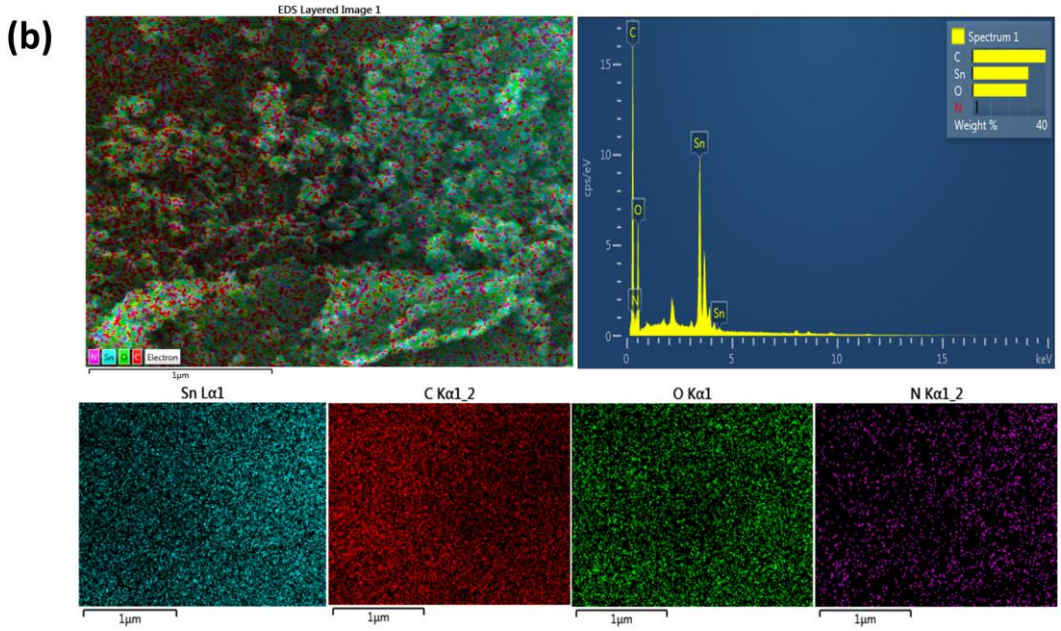


Figure 4.42 EDS mapping of (a) N-SnO_2 (b) GNSO13 composite.

Table 4.12 Content of elements in atomic% and weight % of N-SnO_2 and GNSO13.

Composite →	**N-SnO_2**		**GNSO13**	
Elements ↓	Atomic %	Weight %	Atomic %	Weight %
C	-	-	61.34	39.97
O	78.74	33.31	0.00	0.00
N	0.00	0.00	33.90	29.42
Sn	21.26	66.69	4.75	30.61
Total	100.00	100.00	100.00	100.00

4.3.1.3 Functional group Analysis

The FT-IR study was done to identify characteristic functional groups on the materials. **Figure 4.43** presents spectra of nitrogen doped SnO_2 and GO/N-SnO_2-based nanocomposites (GNSO13, GNSO11 and GNSO31). The characteristic bands from 400 to 700 cm^{-1} in nitrogen doped SnO_2, and their composite with GO corresponded to Sn-O and Sn–O-Sn vibrations [*Dobrucka et al., 2018*]. The bands at 1255 cm^{-1}, and 1417 cm^{-1} have been attributed due to the vibration of Sn-N bonds. N doping occupies the oxide positions into SnO_2 lattice resulting in oxygen vacancies. Thus, FTIR spectra confirm that the Sn-N bond has been formed [*Bhawna et al., 2020*]. Remarkably, the

vibrational bands due to C-containing groups in the spectra of GO-based composites confirm the successful anchoring of particles on the GO sheet. In the spectrum of N-SnO_2/GO based composites, a broad peak approximately 3400–3500 cm^{-1} region was designated due to OH groups (stretching vibration) by the water molecule adsorbed on catalyst surface [*Vidhu et al., 2015*].

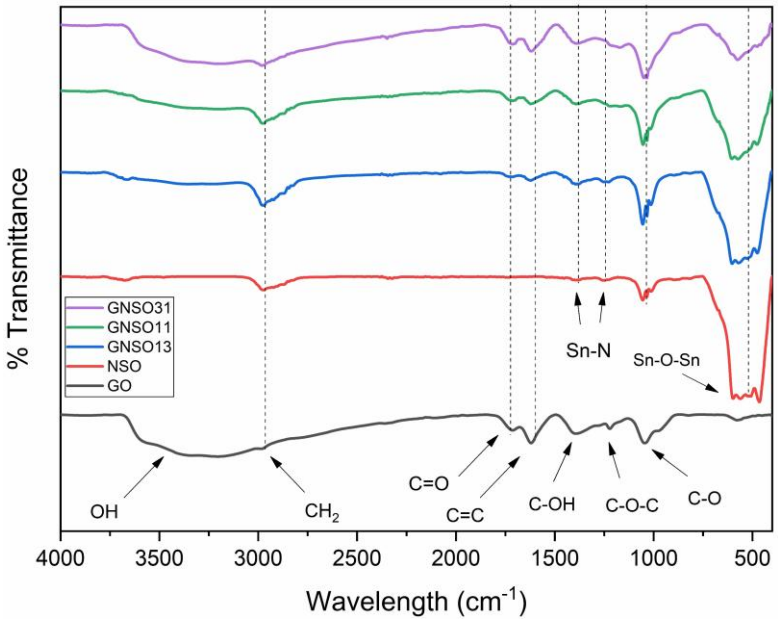


Figure 4.43 FTIR spectra of GO, N-SnO_2, GNSO13, GNSO11, and GNSO31.

4.3.1.4 X-ray diffraction Analysis

The crystallinity of N-SnO_2, GNSO13, GNSO11, and GNSO31 samples was investigated by X-ray diffraction (XRD) analysis. The samples were scanned within range of 2θ = 10°-80°. The XRD pattern for all samples is shown in **Figure 4.44**. The XRD pattern of N-SnO_2 shows a homogeneous pure crystalline structure. The XRD pattern of bare GO exhibits a significant diffraction peak at 11.14° and a smaller peak at 42.27°, indicating reflections from the (001) and (100) planes of GO, respectively [*Siburian et al., 2018*]. The characteristic peaks of N-SnO_2 were observed at 2θ values of 26.5° (110), 33.7° (101), 36.9° (200), 37.8° (111), 51.7° (211), 54.6° (220), 57.7° (002), 61.8° (310), 64.6° (112) 65.8° (301) 71.2° (202), and 78.6° (321) are all the diffraction peaks patterns can be indexed to a rutile tetragonal structure [*Divya et al., 2020, Zulfiqar et al., 2017*]. The XRD patterns of GNSO13, GNSO11, and GNSO31 nanocomposite show a two-phase composition of GO and N-SnO_2. The presence of

diffraction peaks at 11.14° and 42.27° of GO in GNSO13, GNSO11, GNSO31 composite could be attributed to formation of the composites.

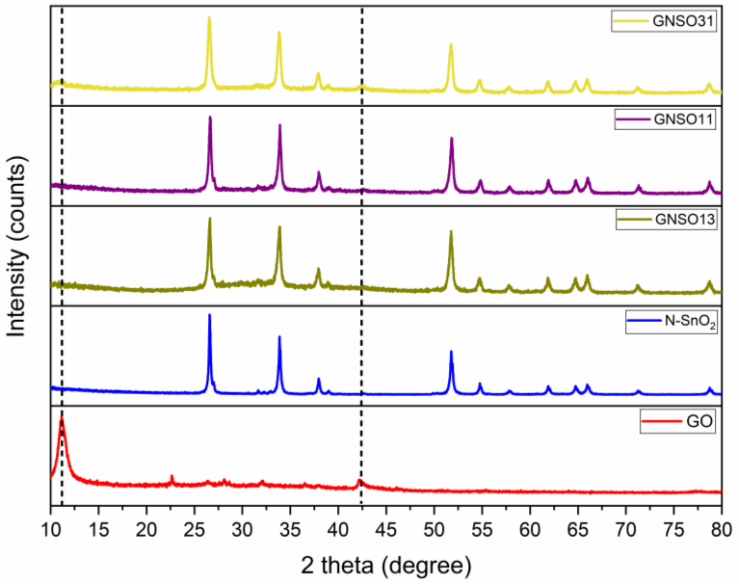
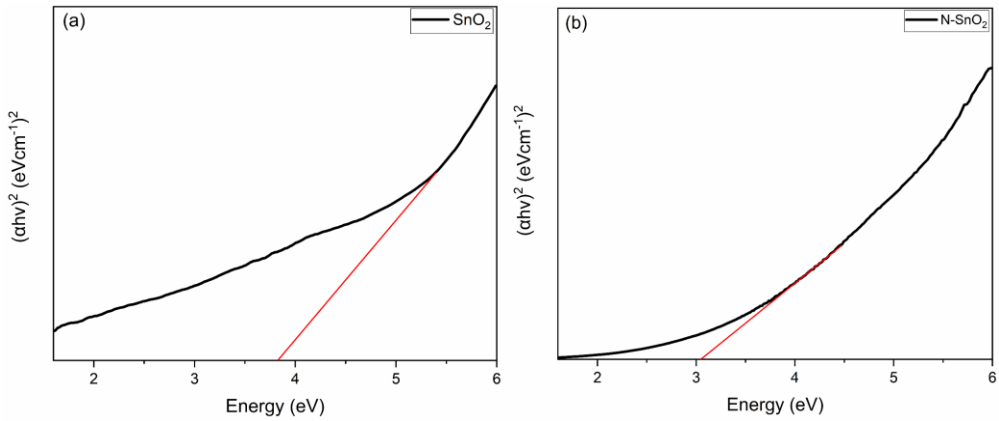


Figure 4.44 XRD of N-SnO_2, GO, GNSO13, GNSO11, and GNSO31.

4.3.1.5 Optical Bandgap Analysis

Tauc's plot for energy bandgap (E_g) of SnO_2, N-SnO_2, GNSO13, GNSO11, and GNSO31 have been displayed in **Figure 4.45**. The band gap of SnO_2 and N- SnO_2 was found out to be about 3.8 eV and 3.04 eV, respectively, whereas the linear line of GNSO13, GNSO11, GNSO31 spectra intercepts on the x-axis in a range of 2.8-3.2 eV, 2.8-3.6 eV and 2.5-3.04 eV respectively. These results suggest that Sn–O–C bonds are generated due to the N-SnO_2 interaction with the GO, which might correspond to the development of new heterojunction structures or defects during the synthesis of composites [*Abdullah et al., 2023*].



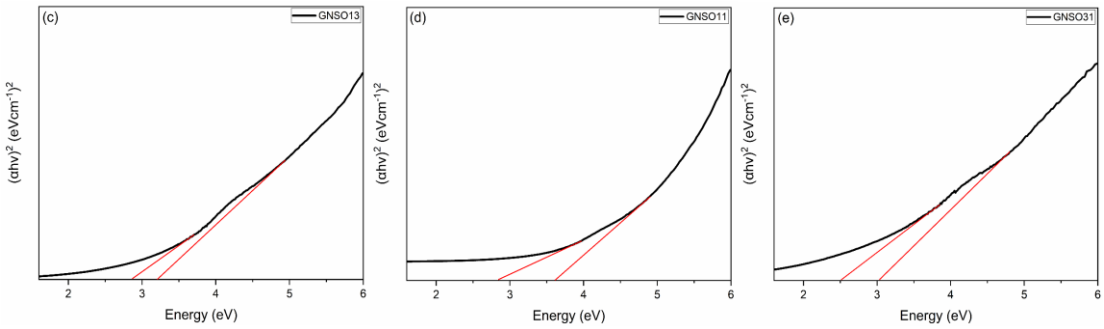


Figure 4.45 Optical bandgap of (a) SnO_2, (b) N-SnO_2, (c) GNSO13 (d) GNSO11, and (e) GNSO31.

4.3.1.6 Photoluminescence Analysis

PL spectra of SnO_2, N-SnO_2, and GNSO13 are shown in **Figure 4.46**. SnO_2 has the highest PL intensity, which decreases with nitrogen doping. When N-SnO_2 combines with GO, its PL intensity decreases. This is because the integrated GO in GNSO13 improves charge transfer, which increases the rate of photogenerated electron and hole separation. Furthermore, GO can act as an effect electron conductor and electron acceptor, accelerating the interfacial electron transfer process from N-SnO_2, and strongly inhibiting charge carrier recombination [*Ramki et al., 2023*].

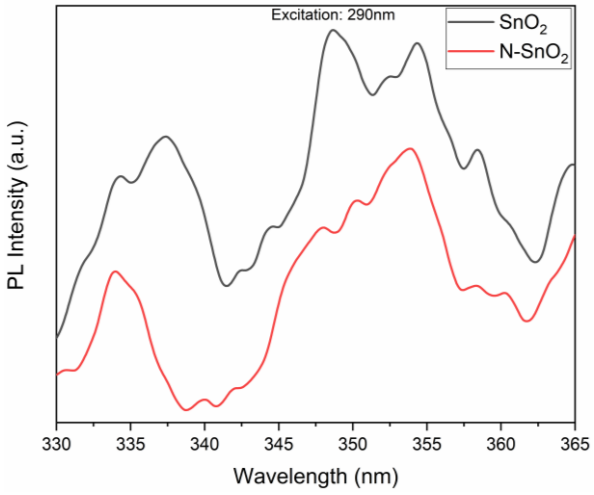


Figure 4.46 Photoluminescence emission spectrum of SnO_2 and N-SnO_2.

4.3.1.7 Thermogravimetric Analysis

Thermogravimetric curves of GO, SnO_2, N-SnO_2, and GNSO13 are shown in **Figure 4.47.** The N-SnO_2 curve displays two areas of weight loss. One below 200°C and another between 200°C to 600°C. First, temperatures below 200 °C resulted in a 0.7% weight loss. First, temperatures below 200 °C clearly resulted in a 0.7% weight loss.

Adsorbed water and gases were removed from the surface of photocatalyst, resulting in the observed weight change. Additionally, a 0.6% weight loss was observed between 200°C and 600°C, which could be attributed to the decomposition of organic molecules or other volatile species or contained in the sample or residual surfactant form the material [*Aslam et al., 2021*]. This suggests that the photocatalyst remained stable at high temperatures due to its inorganic composition of SnO_2 [*Bhawna et al., 2023*]. Furthermore, containing GO and SnO_2 shown the total weight loss of 33.2%. The increased weight loss is due to the presence of GO. The rapid weight reduction from 250°C to 600°C is caused by the destruction of graphene oxide (GO). The variation in total weight loss of N-SnO_2 (1.7%) and GNSO13 composite (33.2%) may be explained by the interaction between graphene oxide (GO) and N-SnO_2 in the nanocomposite, which determines the impact of GO on the thermal degradation of N-SnO_2 [*Azim et al., 2021*].

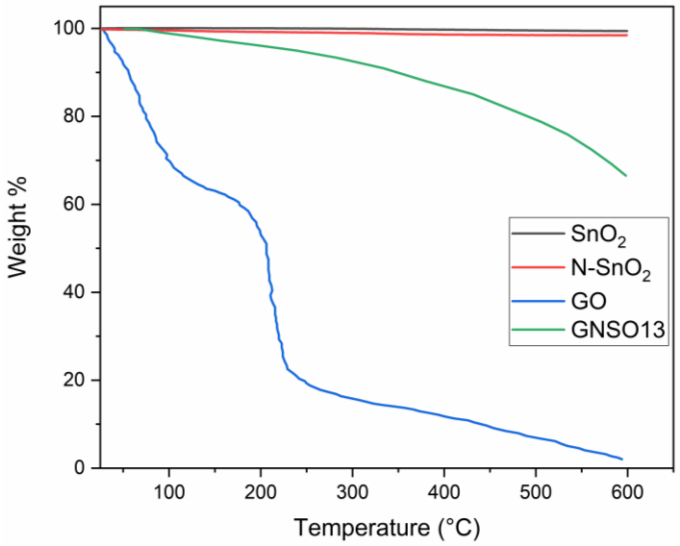


Figure 4.47 TGA of GO, SnO_2, N-SnO_2, and GNSO13.

4.3.2 Removal of PVC-NPs by using Synthesized Materials under different Conditions

To evaluate the removal efficiency of prepared composites, a series of experiments were performed with light (under tungsten bulb and room light) and without light (in dark). For the removal of PVC-NPs using prepared materials at pH 4, pH 7 and pH 10 have been studied. Furthermore, effect of pH, light source and effect of time is also discussed.

To evaluate the role of adsorption on removal of PVC-NPs, an adsorption experiment was conducted using N-SnO_2 and GO/N-SnO_2 composites under dark. Under these experimental conditions, pure N-SnO_2 achieved the highest PVC-NPs removal of 99.6% showing excellent adsorption performance. Whereas GNSO13 achieved 14.7% of percentage removal shown in **Figure 4.48(c)**. The decreased adsorption of GNSO13 is due excessive doping of GO which can reduce the specific active surface area of N-SnO_2. This reduction can result from the formation of larger aggregates due to increased van der Waals forces between the GO sheets and the N-SnO_2 nanoparticles, hindering the material's ability to efficiently interact with light and reactants. The resulting smaller surface area and increased agglomeration can reduce the number of active sites available for photocatalysis, ultimately leading to poorer photocatalytic efficacy. [*Mohtar et al., 2021, Liao et al., 2022*].

Moreover, similar experimental conditions were used for photocatalytic study of removal of PVC-NPs under tungsten bulb light and room light (**Figure 4.48(a) and (b)**). Under these conditions, N-SnO_2 shown almost similar percentage removal of PVC-NPs as that under dark conditions, suggests that the material is likely acting as an adsorbent rather than a photocatalyst in this specific scenario. Photocatalysis relies on light to drive chemical reactions, while adsorption is a process that can occur both in the presence and absence of light. On the other hand, GNSO11 reached the highest percentage removal of 25.6% in tungsten light at pH 10. It could be said that photocatalytic degradation would also concurrently occur with adsorption as light interacts with the material.

4.3.2.1 Effect of pH on the Removal of PVC-NPs

The effects of pH on PVC-NPs removal were investigated at pH levels 4, 7, and 10 as shown in **Figures 4.48(a)**, **4.48(b)**, and **4.48(c)** showing that as pH increases from 4 to 10, the removal percentage of PVC-NPs for N-SnO_2 decreases. A maximum of 99.6% PVC-NP removal was achieved at pH 4 by N-SnO_2 under dark.

The PZC of SnO_2 was found to be 5.6, which is consistent with previously reported values for SnO_2 [*Khairnar et al., 2020*]. The surface would, therefore, have a net-zero charge at PZC and will be charged either positively or negatively at pH < PZC or

pH > PZC, respectively. The surface of N-SnO_2 is positively charged at initial pH values of 4.0 and 7.0, whereas the PVC-NPs solution is negatively charged (**Section 4.1.5.3*)***. Electrostatic attraction forces are therefore expected at pH 4. The removal rates of N-SnO_2 decreased with higher pH 7 and pH 10 due to the electrostatic repulsion of negatively charged surfaces of N-SnO_2 and PVC-NPs.

Similarly, the surface of GNSO13 is positively charged at pH values of 4.0, which show maximum % removal for negatively charged PVC-NPs at pH4 shown in **Figure 4.48(c)**.

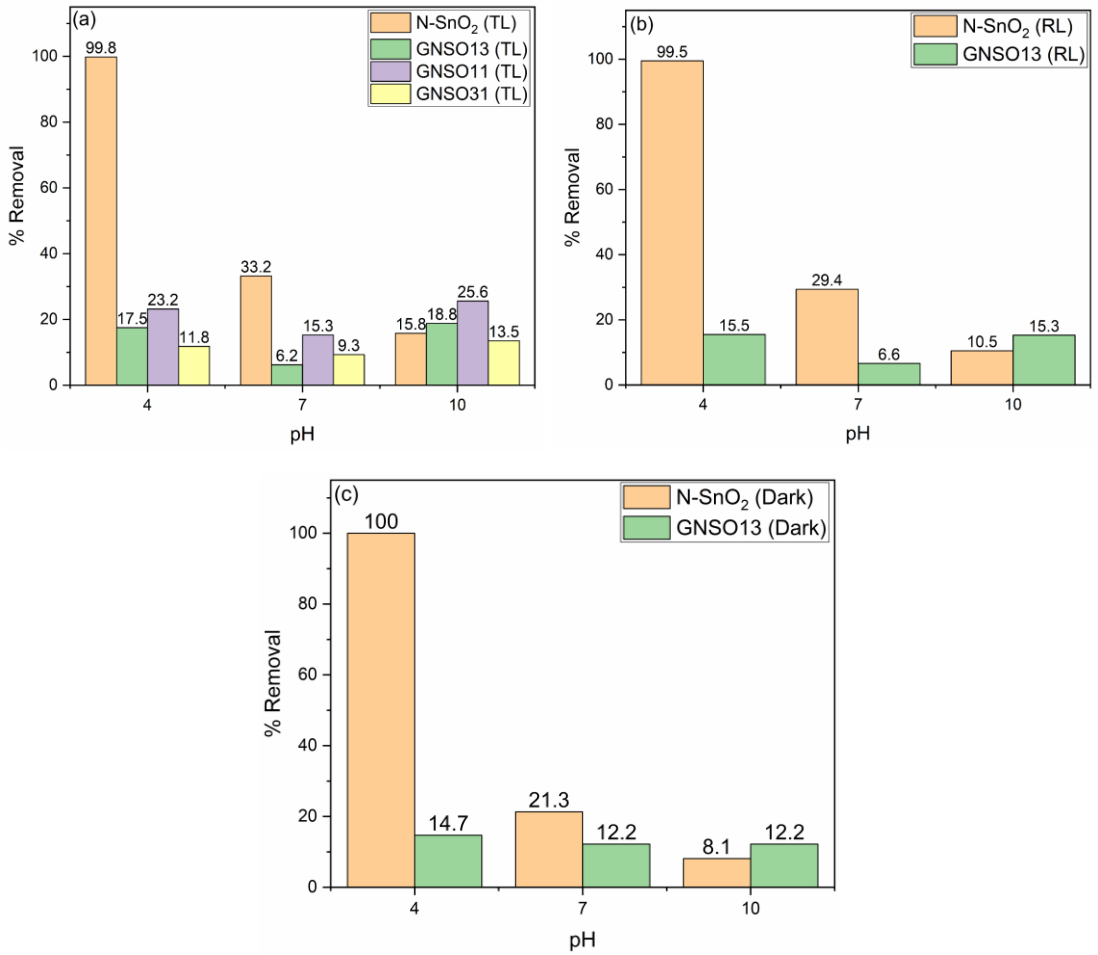


Figure 4.48 Comparison of % removal PVC-NPs at pH 4, pH 7 and pH 10 with N-SnO_2, GNSO13, GNSO11, and GNSO31 under (a) tungsten bulb light (b) room light (c) dark.

4.3.2.2 Effect of Time on the Removal of PVC-NPs

The effect of removal time on removal efficacy of PVC-NPs was evaluated by agitating them with composites at time interval of 30-180 minutes. To assess the PVC-NP

removal rate, an optimal quantity of the synthesized N-SnO_2 and GO/N-SnO_2 composites (80 mg) was used. As the time span increased from 30 to 180 minutes, the % removal of PVC-NPs for N-SnO_2, GNSO13, GNSO11, and GO/N-SnO_2 at different pH under tungsten bulb light, room light and dark are shown in **Figure 4.49(b)**, **4.49(c)**, **4.49(d)** respectively, showing that % removal increases with increase in reaction time. The catalyst's surface receives more contact time, which increases removal activity.

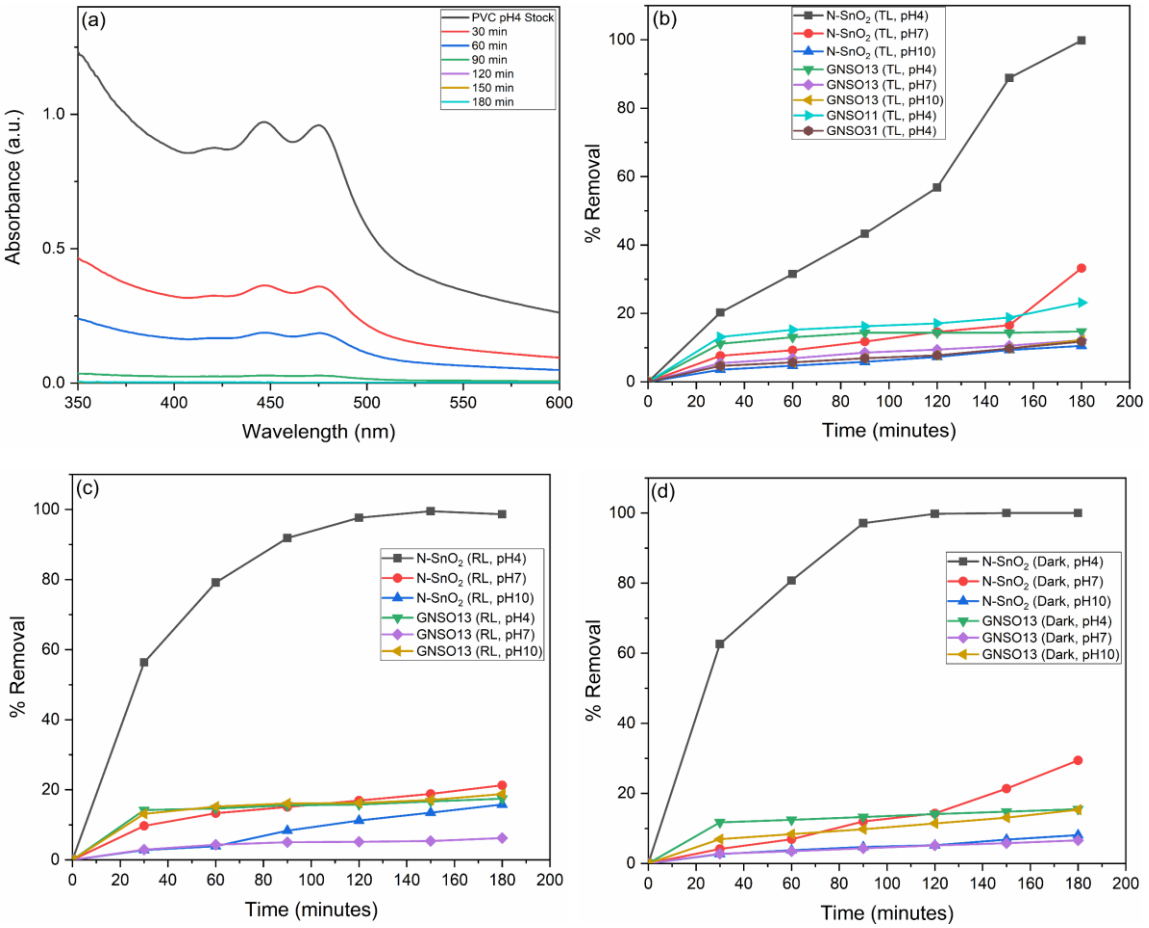


Figure 4.49 (a) UV absorption spectra of PVC-NP removal with N-SnO_2 at pH4; PVC-NP removal from water treated with N-SnO_2, GNSO13, GNSO11, and GNSO31 over a 30- to 180-minute time interval at pH 4, pH7, and pH 10under (b) tungsten bulb light (c) room light (d) dark

4.3.2.3 Analysis of N-SnO_2 after PVC-NPs Removal Experiment

To understand the mechanism involved in the remediation process, more studies were conducted on N-SnO_2 and the solution left behind after the remediation experiment. After the process, a real-life image of PVC-NPs adsorbed on N-SnO_2 at pH 4 was clearly visible and decreases at pH 7 and pH 10. A visible colour changes as well as

swelling of N-SnO_2 at pH 4 was observed after the reaction, as shown in **Figure 4.50**. The swelling of N-SnO_2 nanoparticles could be attributed to adsorption-induced swelling, which refers to the expansion or deformation of a porous material when it adsorbs a pollutant [Bakhshian et al., 2017].

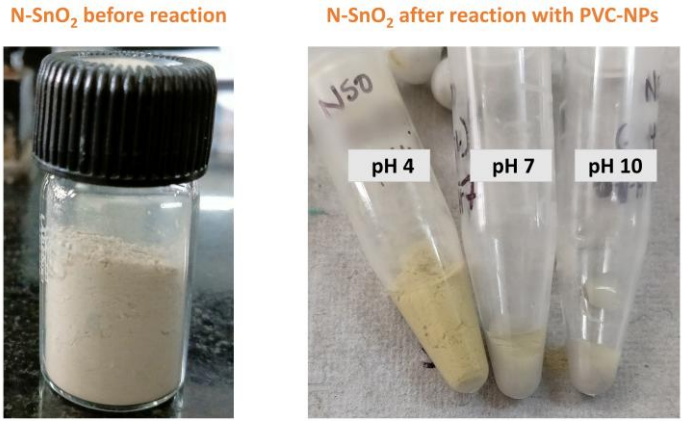


Figure 4.50 Real-life image of N-SnO_2 before and after reaction showing PVC-NPs adsorbed on N-SnO_2 at pH 4, pH 7 and pH 10.

SEM micrographs of the surface morphology of N-SnO_2 after the removal of PVC-NPs under light are shown in **Figure 4.51**. It was discovered that there are some distinct spherical particles of PVC-NPs on the surface of N-SnO_2, but the distinction is difficult because both N-SnO_2 and PVC-NPs exhibit spherical surface morphology. EDS analysis and elemental mapping confirmed the presence of carbon and chlorine, as depicted in **Figure 4.51**, demonstrating the interaction between PVC-NPs and N-SnO_2 after the removal reaction

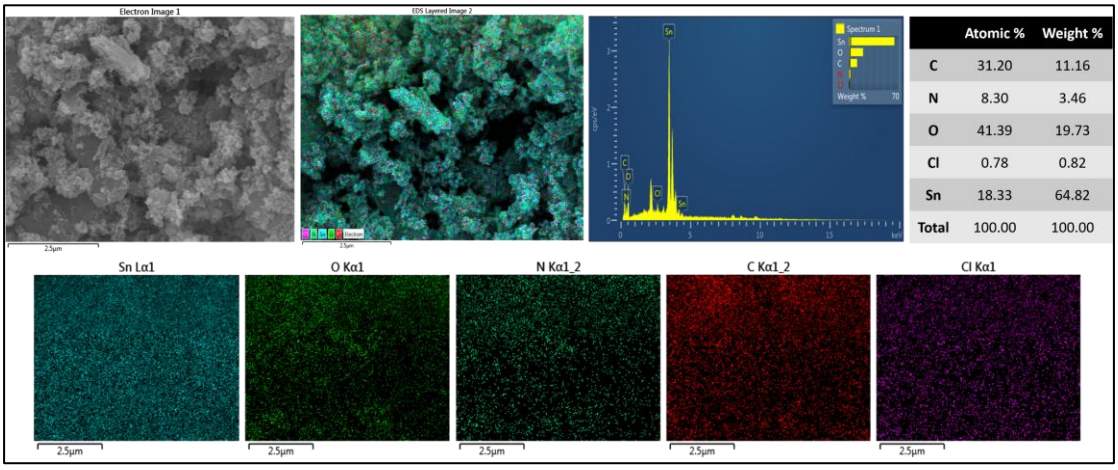


Figure 4.51 SEM, EDS and elemental mapping images after reaction with PVC-NPs using N-SnO_2 with light.

FTIR spectroscopy was used to analyse the N-SnO_2 as shown in **Figure 4.52(a)**. The spectra of N-SnO_2 before and after look relatively same because the small amounts of PVC-NPs adsorbed on the surface of N-SnO_2. FTIR peaks at 400cm^{-1}-700 cm^{-1} are associated with Sn-O-N and Sn-O vibrations, respectively. These peaks showed a significant decrease in intensity, which might be due to the electrostatic attraction of PVC-NPs with Sn-O-N and Sn-O, which shows the interactions of PVC-NPs with N-SnO_2 composite. Furthermore, after the removal of PVC-NPs and some additional peaks are visible which verifies the interaction between PVC and N-SnO_2. **Figure 4.52(b)** represents the FTIR spectra of PVC solution before and after treatment showing the disappearance of characteristic peaks of PVC-NPs.

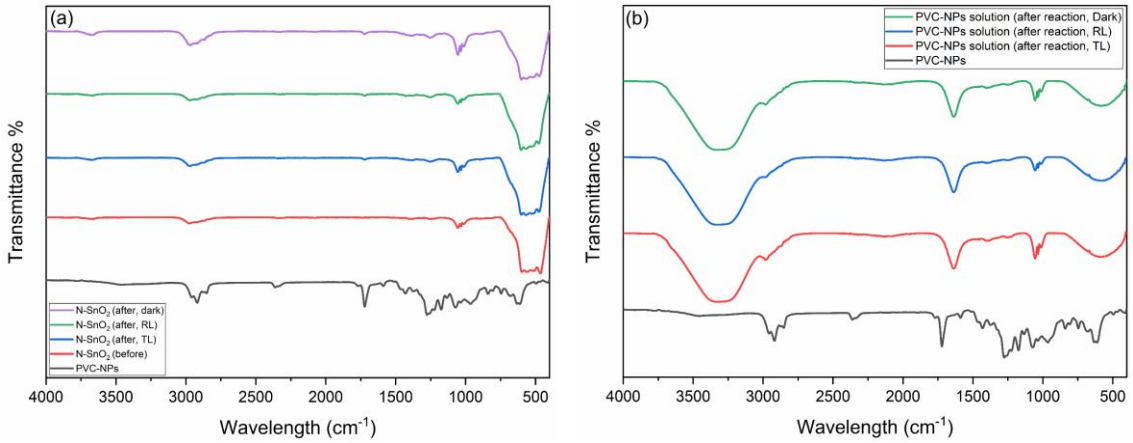


Figure 4.52 FTIR spectra of (a) N-SnO_2 composite before and after removal of PVC-NPs under tungsten bulb light, room light and dark (b) pure PVC-NPs solution and PVC solution after the remediation experiment under tungsten bulb light, room light and dark.

4.3.3 Removal study of PS-NPs using Synthesized Materials under different Conditions

To evaluate the removal efficiency of prepared composites, a series of experiments were performed with light (under tungsten bulb and room light) and without light (in dark). For the removal of PS-NPs using prepared materials at pH 4, pH 7 and pH 10 have been studied. Furthermore, effect of pH, light source and effect of time is also discussed

To evaluate the role of adsorption on removal of PS-NPs, an adsorption experiment was conducted using N-SnO_2 and GO/N-SnO_2 composites under dark. Under these

experimental conditions, pure N-SnO_2 achieved the highest PS-NPs removal of 99.6% showing excellent adsorption performance. Whereas GNSO13 achieved 12.5% of percentage removal shown in **Figure 4.53**. The decreased adsorption of GNSO13 is due to excessive doping of GO which can reduce the specific active surface area of N-SnO_2. This reduction can result from the formation of larger aggregates due to increased van der Waals forces between the GO sheets and the N-SnO_2 nanoparticles, hindering the material's ability to efficiently interact with light and reactants. The resulting smaller surface area and increased agglomeration can reduce the number of active sites available for photocatalysis, ultimately leading to poorer photocatalytic efficacy. [*Mohtar et al., 2021, Liao et al., 2022*].

Moreover, similar experimental conditions were used for photocatalytic study of removal of PS-NPs under light (**Figure 4.53**). Under these conditions, N-SnO_2 shown almost similar percentage removal of PS-NPs as that under dark conditions, suggests that the material is likely acting as an adsorbent rather than a photocatalyst in this specific scenario. Photocatalysis relies on light to drive chemical reactions, while adsorption is a process that can occur both in the presence and absence of light. On the other hand, GNSO31 reached the highest percentage removal of 37.3% in tungsten light at pH 4. It could be said that photocatalytic degradation would also concurrently occur with adsorption as light interacts with the material.

4.3.3.1 Effect of pH on the Removal of PS-NPs

The effects of pH on PVC-NPs removal were investigated at pH levels 4, 7, and 10 as shown in **Figure 4.53** showing that as pH increases from 4 to 10, the removal percentage of PS-NPs for N-SnO_2 decreases. A maximum of 99.6% PS-NP removal was achieved at pH 4 by N-SnO_2 under dark. The PZC of SnO_2 was found to be 5.6, which is consistent with previously reported values for SnO_2 [*Khairnar et al., 2020*]. The surface would, therefore, have a net-zero charge at PZC and will be charged either positively or negatively at pH < PZC or pH > PZC, respectively. The surface of N-SnO_2 is positively charged at initial pH values of 4.0 and 7.0, whereas the PS-NPs solution is negatively charged. Electrostatic attraction forces are therefore expected at pH 4. The removal rates of N-SnO_2 decreased with higher pH 7 and pH 10 due to the electrostatic repulsion of negatively charged surfaces of N-SnO_2 and PS-NPs. Similarly, the surface

of GNSO13 is positively charged at pH values of 4.0, which show maximum % removal for negatively charged PS-NPs at pH4 shown in **Figure 4.53**.

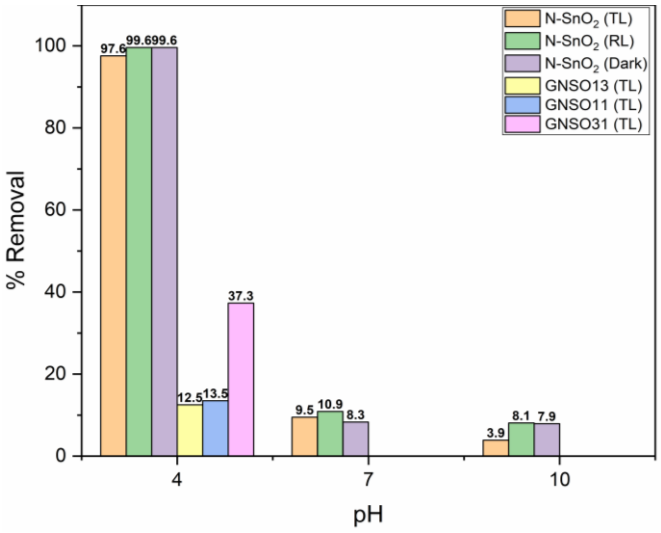
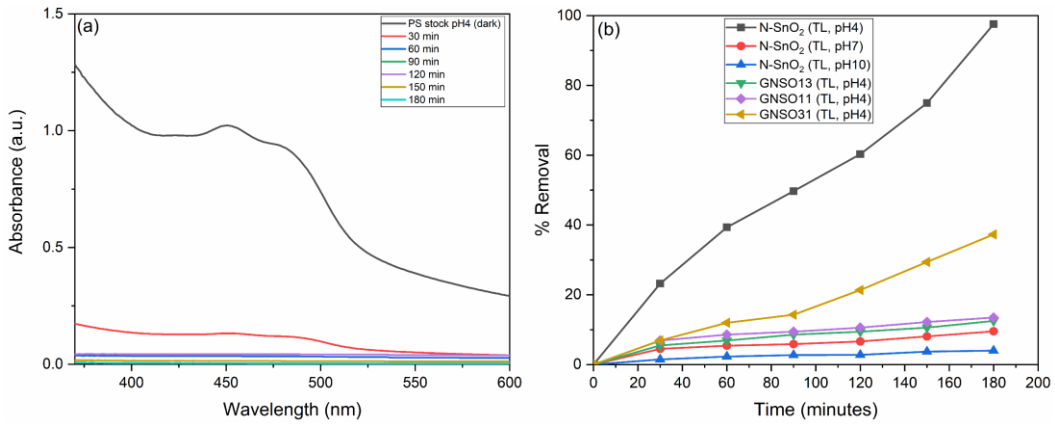


Figure 4.53 Comparison of % removal PS-NPs at pH 4, pH 7 and pH 10 with N-SnO_2, GNSO13, GNSO11, and GNSO31 under tungsten bulb light, room light, and dark.

4.3.3.2 Effect of Time on the Removal of PS-NPs

The effect of removal time on removal efficacy of PS-NPs was evaluated by agitating them with composites at time interval of 30-180 minutes. To assess the PS-NP removal rate, an optimal quantity of the synthesized N-SnO_2 and GO/N-SnO_2 composites (80 mg) was used. As the time span increased from 30 to 180 minutes, the % removal of PS-NPs for N-SnO_2, GNSO13, GNSO11, and GO/N-SnO_2 at different pH under tungsten bulb light, room light and dark are shown in **Figure 4.54(b)**, **4.54(c)**, **4.54(d)** respectively, showing that % removal increases with increase in reaction time. The catalyst's surface receives more contact time, which increases removal activity.



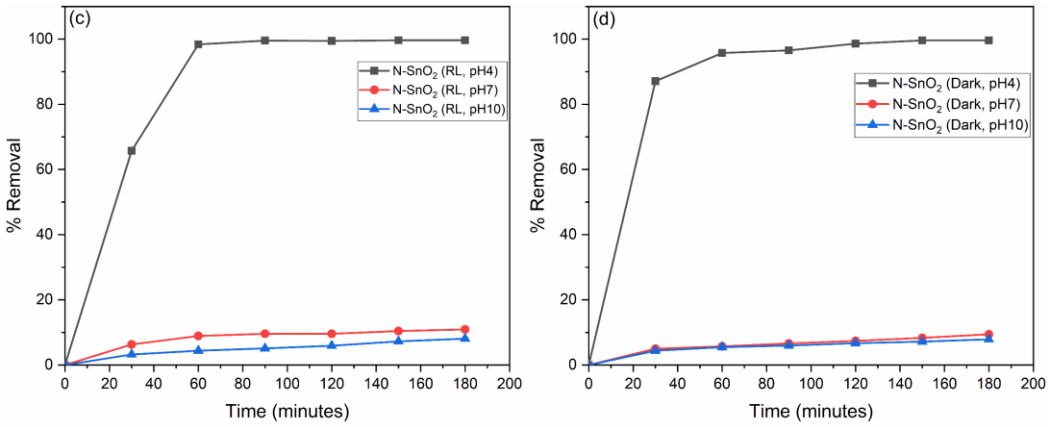


Figure 4.54 (a) UV absorption spectra of PS-NP removal with N-SnO_2 at pH4; PVC-NP removal from water treated with N-SnO_2, GNSO13, GNSO11, and GNSO31 over a 30- to 180-minute time interval at pH 4, pH 7, and pH 10 under (b) tungsten bulb light (c) room light (d) dark.

4.3.3.3 Analysis of N-SnO_2 after PS-NPs Removal Experiment

To understand the mechanism involved in the remediation process, more studies were conducted on N-SnO_2 and the solution left behind after the remediation experiment. After the process, a real-life image of PS-NPs adsorbed on N-SnO_2 at pH 4 was clearly visible and decreases at pH 7 and pH 10. A visible colour changes as well as swelling of N-SnO_2 at pH 4 was observed after the reaction, as shown in **Figure 4.55**. The swelling of N-SnO_2 nanoparticles could be attributed to adsorption-induced swelling, which refers to the expansion or deformation of a porous material when it adsorbs a pollutant [Bakhshian et al., 2017].

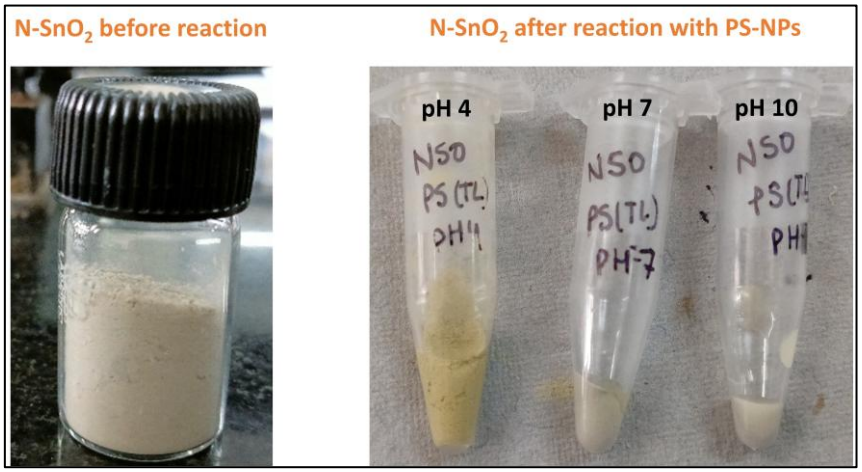


Figure 4.55 Real-life image of N-SnO_2 before and after reaction showing PS-NPs adsorbed on N-SnO_2 at pH 4, pH 7 and pH 10.

SEM micrographs of the surface morphology of N-SnO_2 nanoparticles after the removal of PS-NPs are shown in **Figure 4.56**, under dark at pH 4. It was discovered that there are some distinct spherical particles of PS-NPs on the surface of N-SnO_2 nanoparticles, but the distinction is difficult because both N-SnO_2 and PVC-NPs exhibit spherical surface morphology. EDS analysis and elemental mapping confirmed the presence of carbon of PS-NPs, as depicted in **Figure 4.56**, demonstrating the interaction between PS-NPs and N-SnO_2 nanoparticles after the removal reaction.

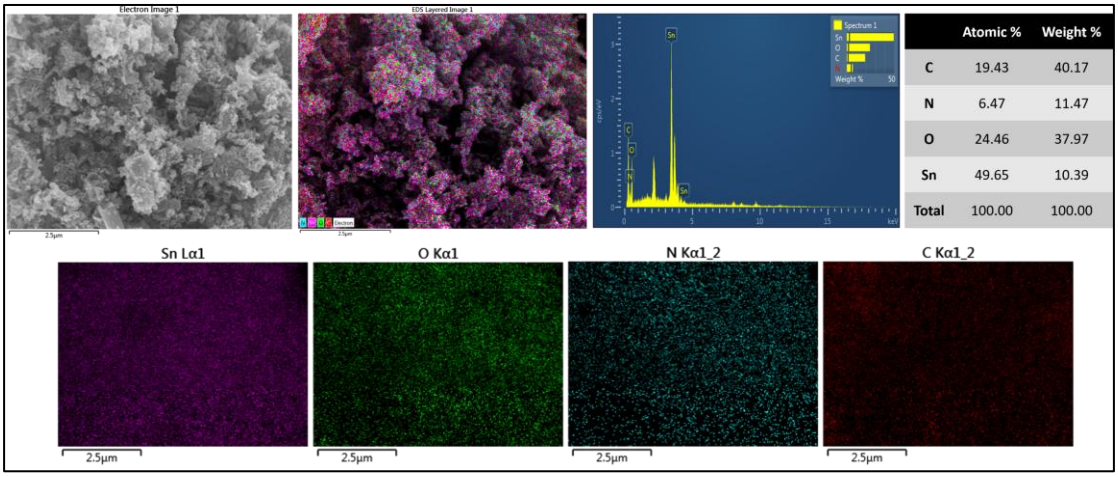


Figure 4.56 SEM, EDS and elemental mapping images after reaction with PS-NPs using N-SnO_2 under dark at pH4.

FTIR spectroscopy was used to analyze the composition of N-SnO_2 nanoparticles and pure PS-NPs before and after the removal of PS nanoparticles as shown in **Figure 4.57**. After removal experiment, FTIR spectra of N-SnO_2 displays the additional peaks corresponding to polystyrene, which point towards the existence of PS-NPs adsorbed on N-SnO_2 surface. The absorption peak at the wave numbers of 3060.8 cm^{-1} corresponds to aromatic C-H stretching vibration absorption. The peak at 2919 cm^{-1} represents the vibration of the CH_2 group. Additionally, the transmission bands at 1600.8, 1492.7, and 1452.2 cm^{-1} were attributed to the aromatic C=C stretching vibration of the benzene ring, as expected in the PS structure. Strong vibrational modes at 744 and 698.2 cm^{-1} indicate out-of-plane bending vibration of C-H, which is characteristic for polystyrene [*Fang et al., 2010*]. In addition, the absorption peak at the wave number of 3446.5 cm^{-1} is for the stretching vibration absorption of O-H.

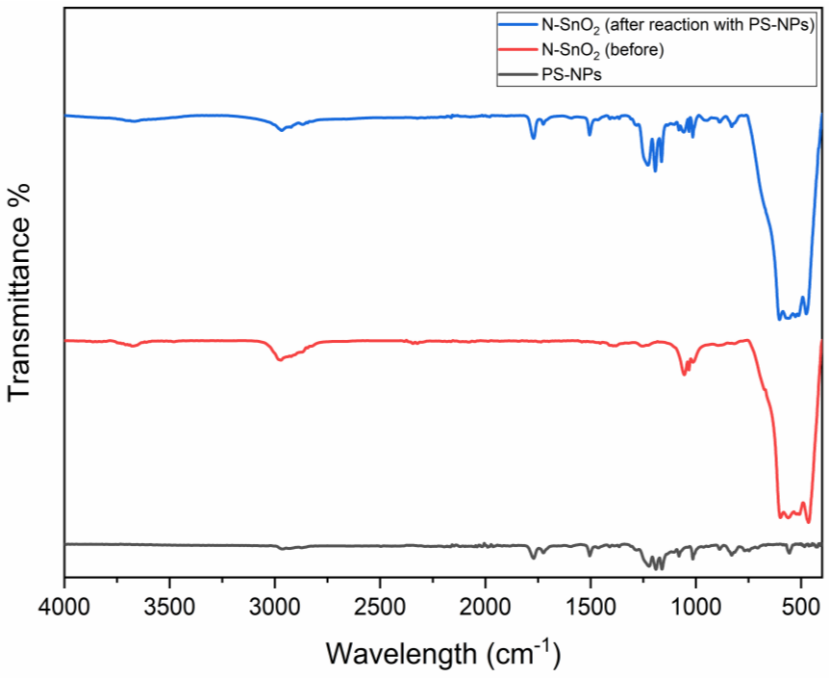


Figure 4.57 FTIR spectra of N-SnO_2 before and after removal of PS-NPs.

4.4 NITROGEN-DOPED ZrO_2 NANOPARTICLES FOR REMOVAL OF POLYVINYL CHLORIDE (PVC) AND POLYSTYRENE (PS) FROM WATER

In this section, characterization of bare N-ZrO_2 and the removal study of PVC-NPs and PS-NPs using the synthesized materials are explained. Furthermore, analysis of material after the PVC-NPs and PS-NPs removal experiment is discussed.

4.4.1 Characterization of N-ZrO_2

4.4.1.1 Scanning Electron Microscope Analysis

The SEM micrograph shows the different agglomerate structures of N-ZrO_2 particles shown in **Figure 4.58**. The diameter of primary particles is in the range of 73-93 nm. It is found that the particles are in almost irregular shape and highly agglomerated.

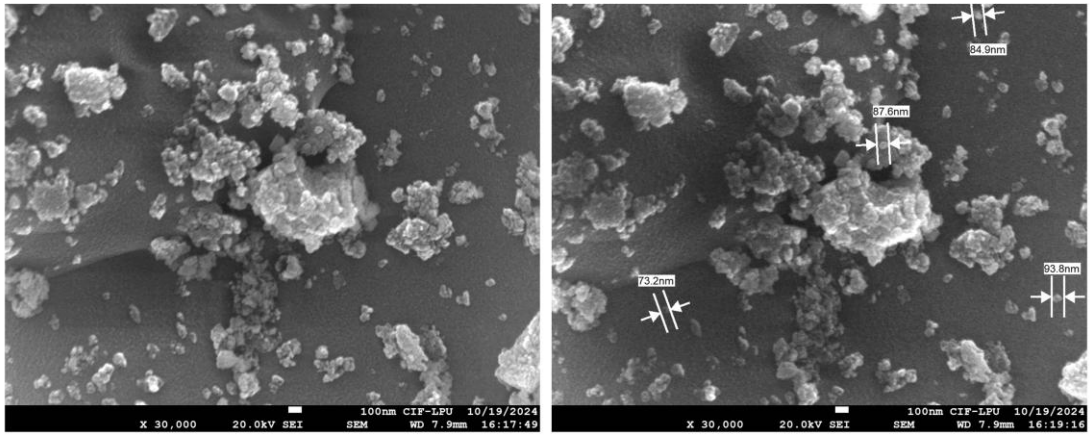


Figure 4.58 Scanning electron microscope (SEM) images of N-ZrO_2.

4.4.1.2 Energy-Dispersive X-ray Spectroscopy Analysis

Figure 4.59 depicts the element distribution of N-ZrO_2 obtained using energy-dispersive spectroscopy (EDS). The EDS findings showed that the sample included Zr, O, and N elements (**Table 4.13**). The elemental composition of N-ZrO_2 nanoparticles was determined by elemental mapping, as evidenced by the various colours in **Figure 4.59**. This investigation validated the fabrication of nitrogen-doped nanoparticles without any impurities.

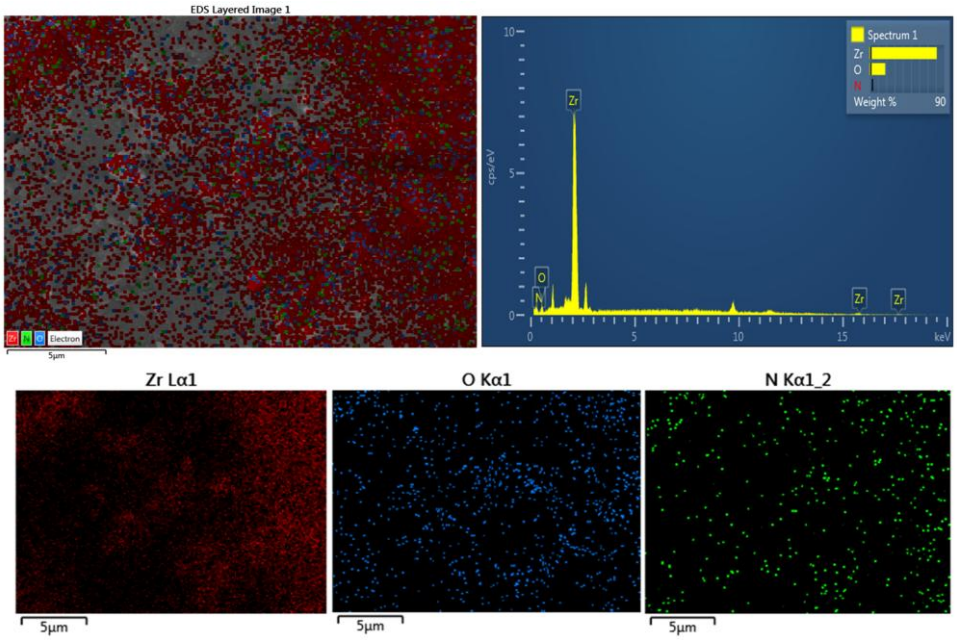


Figure 4.59 EDS mapping of N-ZrO_2.

Table 4.13 Content of elements in atomic% and weight % of N-ZrO_2.

Material →	**N-SnO_2**	
Elements ↓	Atomic %	Weight %
Zr	81.13	42.98
O	18.87	57.02
N	0.00	0.00
Total	100.00	100.00

4.4.1.3 Functional group Analysis

Figure 4.60 shows the FTIR spectra of the nitrogen doped ZrO_2. The peaks at 584 cm^{-1} and 497 cm^{-1} are attributed to the metal and oxygen bond (Zr-O) and metal, oxygen, and metal bond (Zr-O-Zr), respectively. The peaks at around 1240-1380 cm^{-1} correspond to the metal and hydroxide bond (Zr-OH). The peak centered at 1612 cm^{-1} is assigned to the -OH bending vibrations of water molecules. Further, the peaks at around 2368-2370 cm^{-1} are due to the presence of adsorbed CO_2. As can be seen, additional peaks are observed after doping with N. The peaks noticed at around 700-850 cm^{-1} are associated with the wagging vibration of N-H bonds, while those at 1450-1550 cm^{-1} are associated with their bending mode [*Sudrajat el al., 2016*].

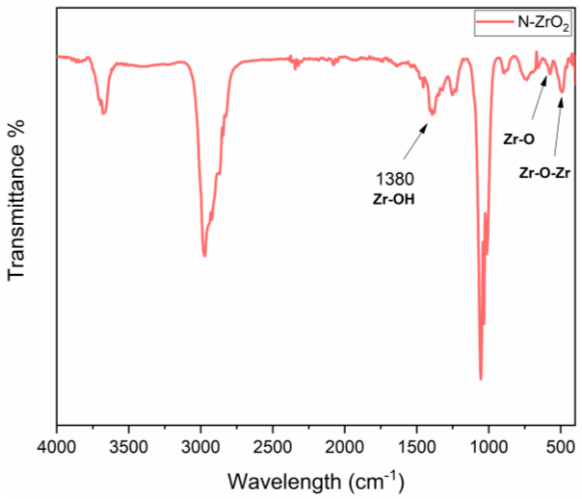


Figure 4.60 FTIR spectra of N-ZrO_2.

4.4.1.4 X-ray diffraction Analysis

The distinguishing characteristic peaks for tetragonal ZrO_2 occur at 2θ = 30.2, 34.5, 50.2, and 60.2 corresponding to the (101), (110), (200), and (211) reflections. After doping with N, the crystalline size decreases, resulting in peak broadening. The crystallinity also slightly decreases due to crystal defects, crystal growth inhibition by the urea, or due to the substitution of O by N. As a result, the peak intensities are reduced [*Farhadi et al., 2009*].

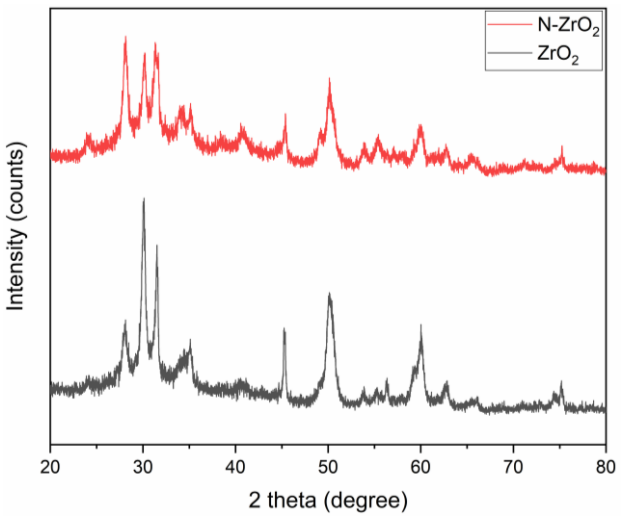


Figure 4.61 XRD of ZrO_2 and N-ZrO_2.

4.4.1.5 Optical Bandgap Analysis

The band gap of ZrO_2 and N-ZrO_2 was found out to be about 5.4 eV and 3.7-5.5 eV, respectively. According to theoretical bandgap studies of N-doped ZrO_2 NPs, doping

ZrO_2 with N can change its electronic band structure and result in a lower band-gap energy. This is because the p states of the N atom hybridize with the two p states of the oxygen atoms in ZrO_2 [Cao et al., 2022].

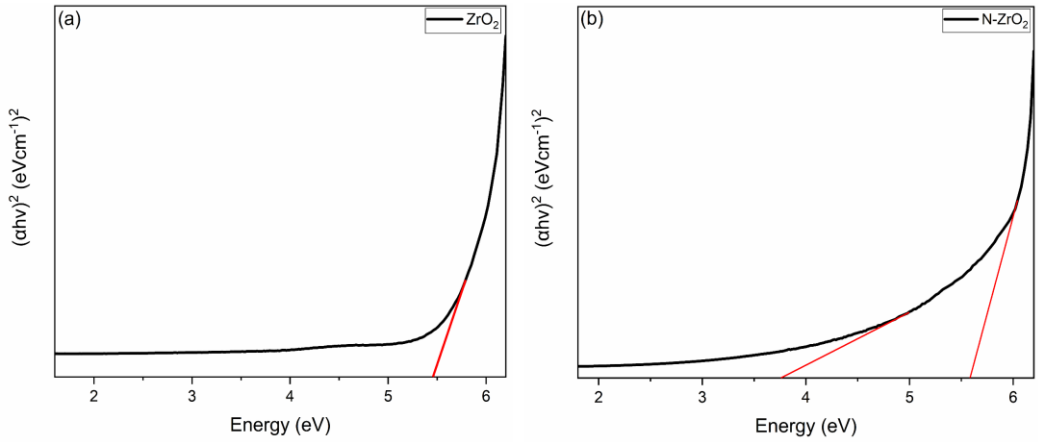


Figure 4.62 Optical bandgap of ZrO_2 and N-ZrO_2.

4.4.1.6 Photoluminescence Analysis

PL spectra of ZrO_2 and N-ZrO_2 are shown in **Figure 4.63**. ZrO_2 has the highest PL intensity, which decreases with nitrogen doping. Doping with N results in the development of a mid-band state with N 2p orbitals within the band gap. In N-ZrO_2, the N mid-gap state may operate as an electron trap. As a result, recombination of electron-hole pairs can be prevented [*Sudrajat et al., 2016*].

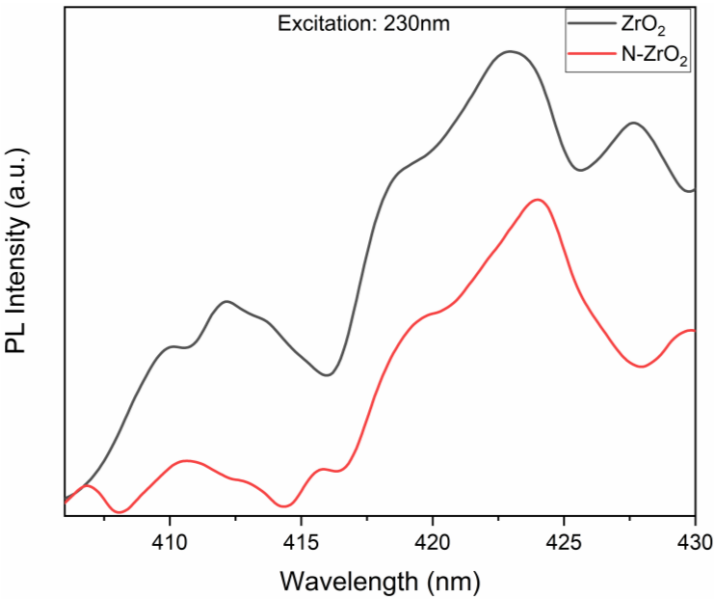


Figure 4.63 Photoluminescence emission spectra of ZrO_2 and N-ZrO_2.

4.4.1.7 Thermogravimetric Analysis

The thermogram of the ZrO_2 and N- ZrO_2 is displayed in **Figure 4.64**, showing total weight loss of 6.54% and 0.9%, respectively. The weight loss below 150°C is caused by the removal of water adsorbed on the catalyst surface, whereas the weight loss between 150 and 600°C is caused by the removal of water adsorbed in catalyst pores. N-ZrO_2 has minor weight loss from 350 to 600°C due to surface hydroxyl group breakdown [*Aimable et al., 2010*]. Overall, less weight losses are observed for N-ZrO_2, suggesting its high thermal stability. Nitrogen doping involves replacing some oxygen atoms in the ZrO_2 lattice with nitrogen atoms. These nitrogen atoms can form strong bonds with zirconium atoms, creating a more stable and robust Zr-N-O network. This modified structure is less prone to decomposition at higher temperatures, leading to increased thermal stability [*Peng et al., 2025]*.

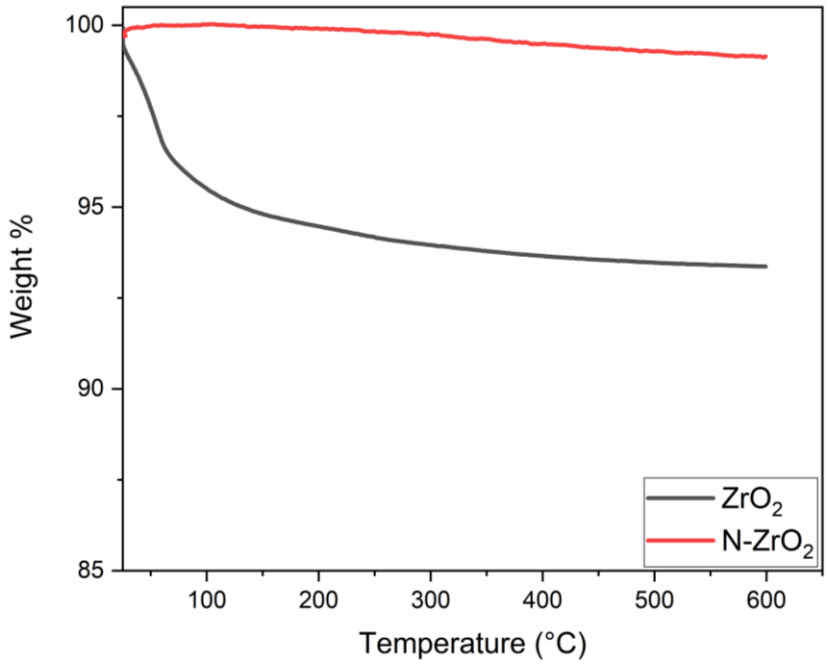


Figure 4.64 TGA of ZrO_2 and N-ZrO_2.

4.4.2 Removal study of PVC-NPs using Synthesized Materials under different Conditions

To evaluate the removal efficiency of N-ZrO_2, a series of experiments were performed with light (under tungsten bulb and room light) and without light (in dark). For the

removal of PVC-NPs using prepared materials at pH 4, pH 7 and pH 10 have been studied. Furthermore, effect of pH, light source and effect of time is also discussed.

To evaluate the role of adsorption on removal of PVC-NPs, an adsorption experiment was conducted using N-ZrO_2 under dark. Under these experimental conditions, N-ZrO_2 achieved the highest PVC-NPs removal of 35.2% showing adsorption performance (**Figure 4.65**).

Moreover, similar experimental conditions were used for photocatalytic study of removal of PVC-NPs under tungsten bulb light and room light (**Figure 4.65**). Under these conditions, N-ZrO_2 shown percentage removal of 31.2% and 27.3%.

4.4.2.1 Effect of pH on the Removal of PVC-NPs

The effects of pH on PVC-NPs removal were investigated at pH levels 4, 7, and 10 as shown in **Figure 4.65** showing that as pH increases from 4 to 10, the removal percentage of PVC-NPs for N-ZrO_2 decreases. The PZC of N-ZrO_2 was found to be 7 [*Sudrajat et al., 2016*]. Below this pH, the catalyst surface is positively charged. Thus, in this pH region, the negatively charged PVC-NPs effectively adsorbed on the catalyst surface and ultimately removal is will be higher due to electrostatic attraction forces at pH 4 and pH 7. The removal rates of N-ZrO_2 decreased at pH 10 due to the electrostatic repulsion of negatively charged surfaces of N-ZrO_2 and PVC-NPs.

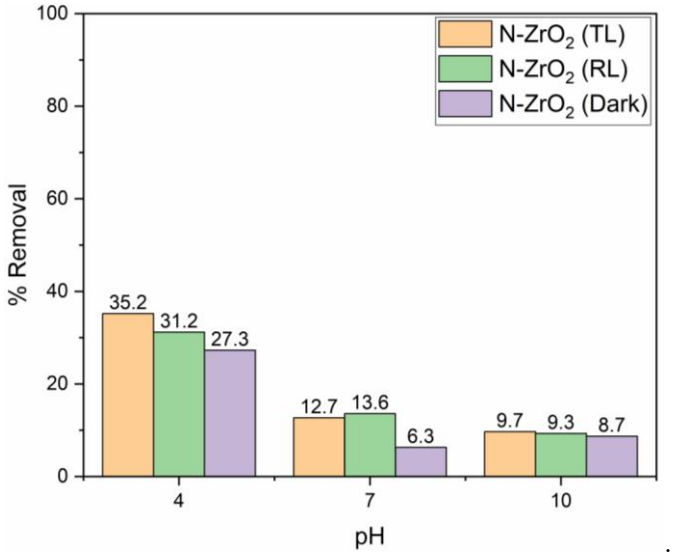


Figure 4.65 % Removal PVC-NPs with N-ZrO_2, under tungsten bulb light, room light, and dark at pH 4, pH 7 and, pH 10.

4.4.2.2 Effect of Time on the Removal of PVC-NPs

The effect of removal time on removal efficacy of PVC-NPs was evaluated by agitating them with composites at time interval of 30-180 minutes. To assess the PVC-NP removal rate, an optimal quantity of the synthesized N-ZrO_2 (80 mg) was used. As the time span increased from 30 to 180 minutes, the % removal of PVC-NPs for N-ZrO_2, at different pH under tungsten bulb light, room light and dark are shown in **Figure 4.66(b)**, **4.66(c)**, **4.66(d)** respectively, showing that % removal increases with increase in reaction time. The catalyst's surface receives more contact time, which increases removal activity.

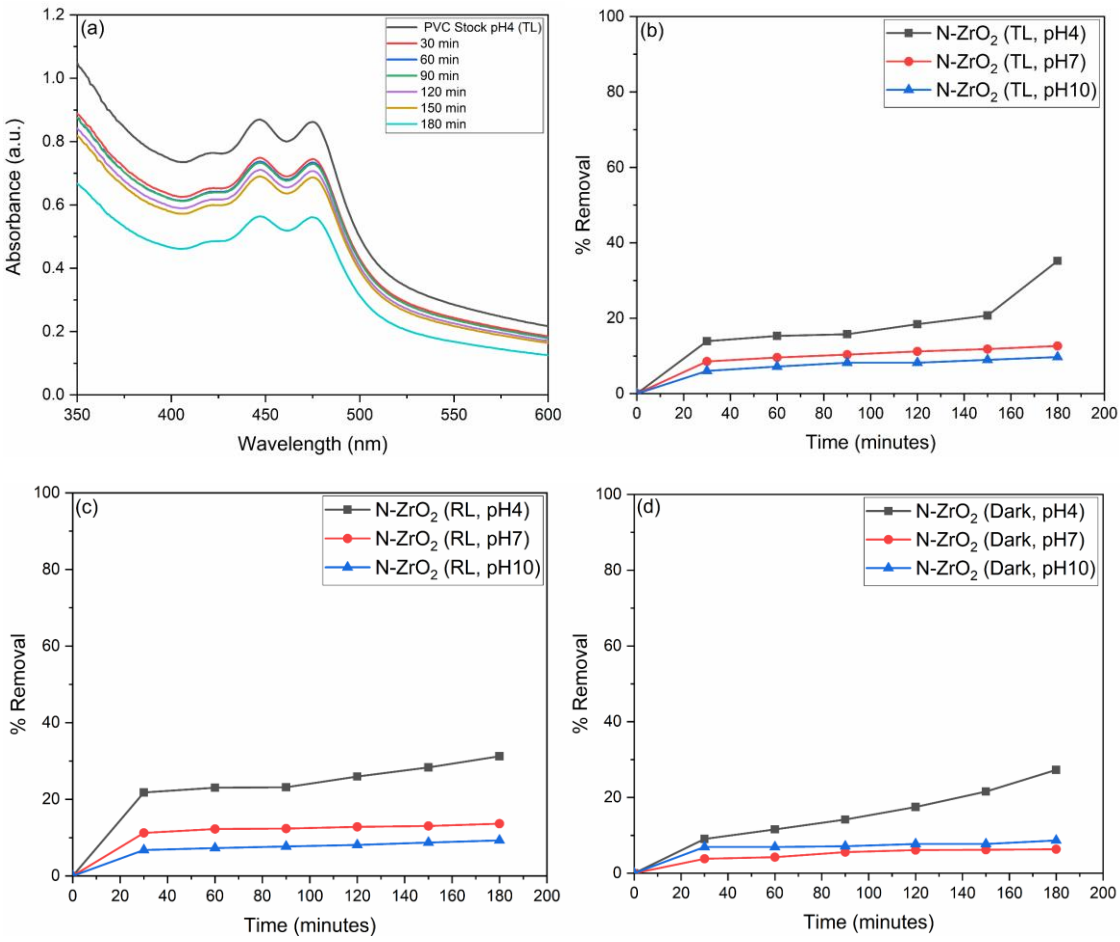


Figure 4.66 (a) UV absorption spectra of PVC-NP removal with N-ZrO_2 at pH4; PVC-NP removal from water treated with N-ZrO_2 over a 30- to 180-minute time period under (b) dark at pH 4, pH 7, and pH 10 (c) room light at pH 4, pH 7, and pH 10 (d) tungsten bulb light at pH 4, pH 7, and pH 10.

4.4.2.3 Analysis of N-ZrO_2 and PVC Solution after Removal Experiment

SEM micrographs of the surface morphology of N-ZrO_2 after the removal of PVC-NPs under light are shown in **Figure 4.67**. It was discovered that there are some distinct spherical particles of PVC-NPs on the surface of N-ZrO_2. Furthermore, EDS analysis and elemental mapping confirmed the presence of carbon and chlorine, as depicted in **Figure 4.67**, demonstrating the interaction between PVC-NPs and N-ZrO_2 after the removal reaction.

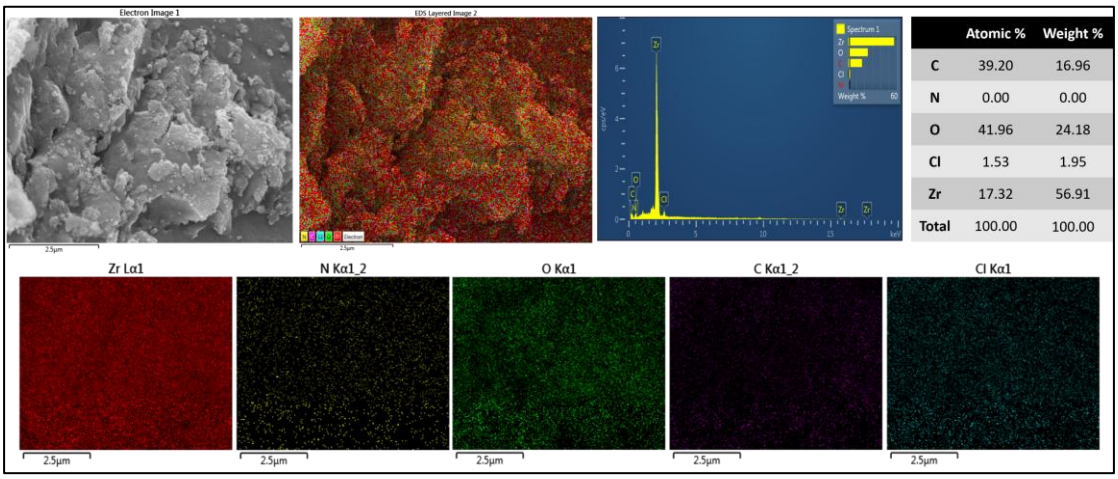


Figure 4.67 SEM, EDS and elemental mapping images after reaction with PVC-NPs using N-ZrO_2 with light.

FTIR spectroscopy was used to analyze the composition of N-ZrO_2 and pure PVC solution before and after the removal of PVC-NPs as shown in **Figure 4.68**. The FTIR spectrum of PVC shows peaks at 2965 cm^{-1} and 2924 cm^{-1} consisting of the CH_2 asymmetric stretching vibration mode. The peak at higher wavenumber shows the asymmetric stretching bond of C − H and the lower peak is for the symmetrical stretching bond of C − H. The peaks around 1438cm^{-1} are assigned to the C − H aliphatic bending bond. The peak at 1282 cm^{-1} is attributed to the bending bond of C − H near Cl. The C − C stretching bond of the PVC backbone chain occurs in the range 1000-1100 cm^{-1}. Finally, peaks in the range of 600-650 cm^{-1} correspond to the C-Cl bond. After adsorption, FTIR spectra of N-ZrO_2 displays the addition peaks corresponding to PVC-NPs, which point to the existence of PVC-NPs adsorbed on N-ZrO_2 surface. After photocatalytic activity, FTIR spectra of N-ZrO_2, displays the addition peaks in 850–515 cm^{-1} region, which corresponds to presence of C-Cl bond [*DE LORENZI et al., 1999*].

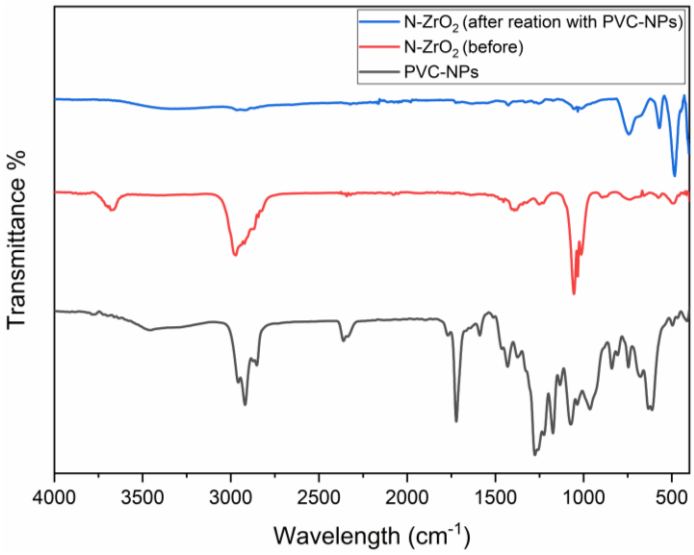


Figure 4.68 FTIR spectra of N-ZrO_2 before and after reaction with PVC-NPs.

4.4.3 Removal Study of PS-NPs using Synthesized Materials under different Conditions

To evaluate the removal efficiency of N-ZrO_2, a series of experiments were performed with light (under tungsten bulb and room light) and without light (in dark). For the removal of PS-NPs using prepared materials at pH 4, pH 7 and pH 10 have been studied. Furthermore, effect of pH, light source and effect of time is also discussed.

To evaluate the role of adsorption on removal of PS-NPs, an adsorption experiment was conducted using N-ZrO_2 under dark. Under these experimental conditions, N-ZrO_2 achieved the highest PS-NPs removal of 44.5% showing adsorption performance (**Figure 4.69**).

Moreover, similar experimental conditions were used for photocatalytic study of removal of PS-NPs under tungsten bulb light and room light (**Figure 4.69**). Under these conditions, N-ZrO_2 shown percentage removal of 16.9% and 14.4%.

4.4.3.1 Effect of pH on the Removal of PS-NPs

The effects of pH on PS-NPs removal were investigated at pH levels 4, 7, and 10 as shown in **Figure 4.69** showing that as pH increases from 4 to 10, the removal percentage of PS-NPs for N-ZrO_2 decreases. The PZC of N-ZrO_2 was found to be 7 [*Sudrajat et al., 2016*]. Below this pH, the catalyst surface is positively charged. Thus, in this pH region, the negatively charged PS-NPs effectively adsorbed on the catalyst

surface and ultimately removal is will be higher due to electrostatic attraction forces at pH 4 and pH 7. The removal rates of N-ZrO_2 decreased at pH 10 due to the electrostatic repulsion of negatively charged surfaces of N-ZrO_2 and PS-NPs.

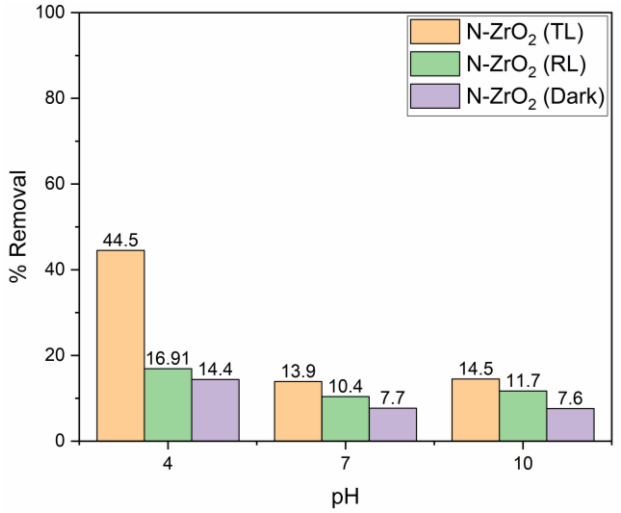
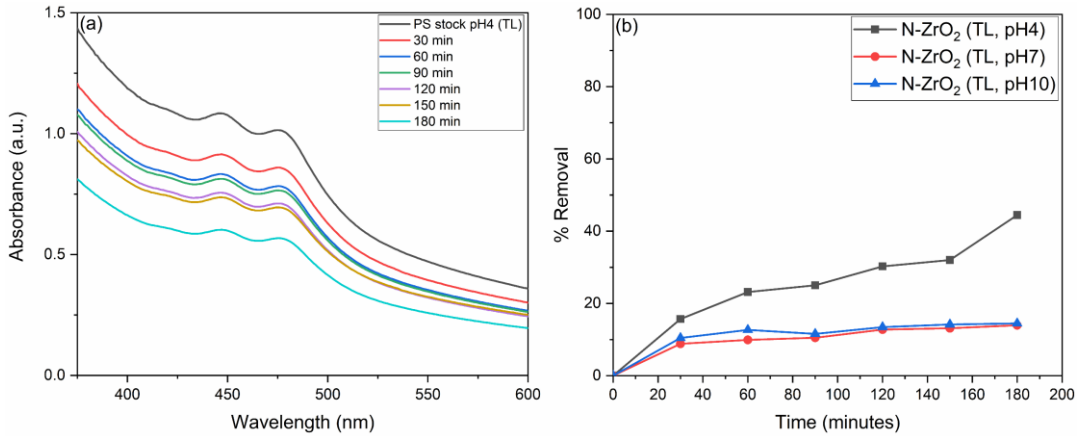


Figure 4.69 % Removal PVC-NPs with N-ZrO_2, under tungsten bulb light, room light, and dark at pH 4, pH 7 and, pH 10.

4.4.3.2 Effect of Time on the Removal of PS-NPs

The effect of removal time on removal efficacy of PS-NPs was evaluated by agitating them with composites at time interval of 30-180 minutes. To assess the PS-NP removal rate, an optimal quantity of the synthesized N-ZrO_2 (80 mg) was used. As the time span increased from 30 to 180 minutes, the % removal of PS-NPs for N-ZrO_2, at different pH under tungsten bulb light, room light and dark are shown in **Figure 4.70(b)**, **4.70(c)**, **4.70(d)** respectively, showing that % removal increases with increase in reaction time. The catalyst's surface receives more contact time, which increases removal activity.



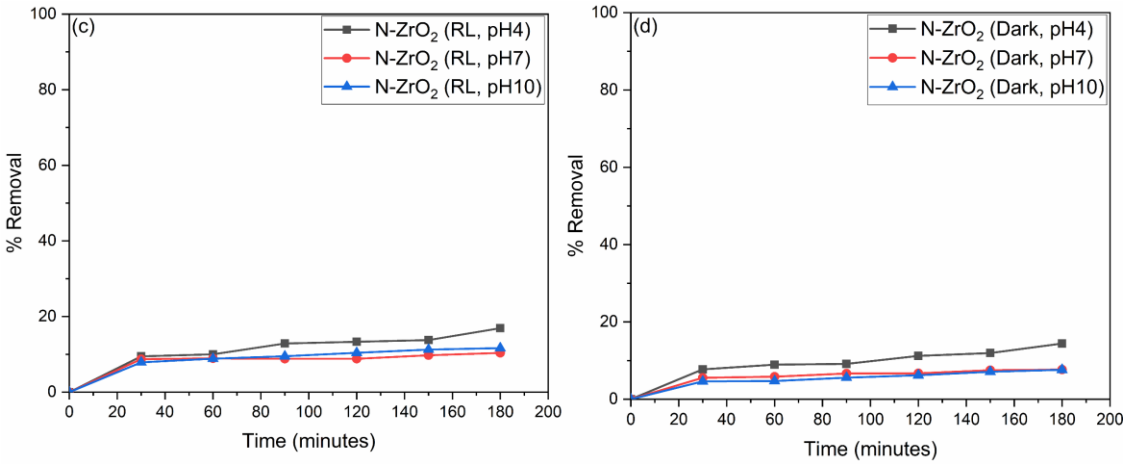


Figure 4.70 (a) UV absorption spectra of PS-NP removal with N-ZrO_2 at pH4; PS-NP removal from water treated with N-ZrO_2 over a 30- to 180-minute time period under (b) dark at pH 4, pH 7, and pH 10 (c) room light at pH 4, pH 7, and pH 10 (d) tungsten bulb light at pH 4, pH 7, and pH 10.

4.4.3.3 Analysis of N-ZrO_2 and PS Solution after Removal Experiment

SEM micrographs of the surface morphology of N-ZrO_2 nanoparticles after the removal of PS-NPs are shown in **Figure 4.71**, under dark at pH 4. It was discovered that there are some distinct spherical particles of PS-NPs on the surface of N-ZrO_2 nanoparticles. Furthermore, EDS analysis and elemental mapping confirmed the presence of carbon of PS-NPs, as depicted in **Figure 4.71**, demonstrating the interaction between PS-NPs and N-TiO_2 nanoparticles after the removal reaction.

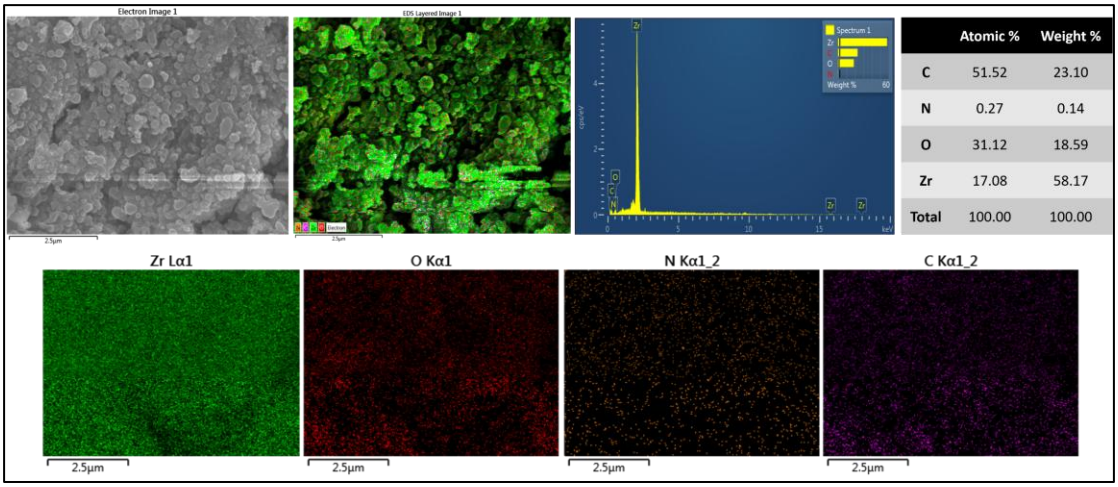


Figure 4.71 SEM, EDS and elemental mapping images after reaction with PS-NPs using N-ZrO_2 with light.

FTIR spectroscopy was used to analyze the composition of N-ZrO_2 nanoparticles and pure PS-NPs before and after the removal of PS nanoparticles as shown in **Figure 4.72**. After removal experiment, FTIR spectra of N-ZrO_2 displays the additional peaks corresponding to polystyrene, which point towards the existence of PS-NPs adsorbed on N-ZrO_2 surface. The absorption peak at the wave numbers of 3060.8 cm^{-1} corresponds to aromatic C-H stretching vibration absorption. The peak at 2919 cm^{-1} represents the vibration of the CH_2 group. Additionally, the transmission bands at 1600.8, 1492.7, and 1452.2 cm^{-1} were attributed to the aromatic C=C stretching vibration of the benzene ring, as expected in the PS structure. Strong vibrational modes at 744 and 698.2 cm^{-1} indicate out-of-plane bending vibration of C-H, which is characteristic for polystyrene [*Fang et al., 2010*]. In addition, the absorption peak at the wave number of 3446.5 cm^{-1} is for the stretching vibration absorption of O-H.

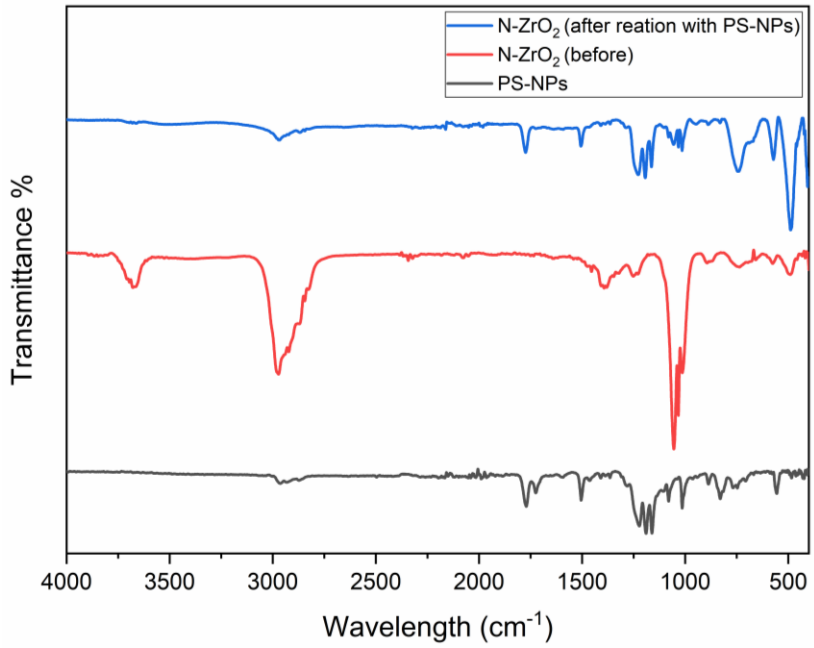


Figure 4.72 FTIR spectra of N-ZrO_2 before and after reaction with PS-NPs.

The comparison of various synthesised materials is shown in **Table 4.14**. The table demonstrates that in previous work photocatalytic remediation of plastics required long irradiation times under UV and solar light to achieve moderate to high degradation efficiencies. Solar-driven systems improved sustainability but still required extended exposure times. The table also shows that most previously reported studies focus on solid-phase microplastic degradation**.** In contrast, the materials developed in this work

achieved high percentage removal of PVC and PS in aqueous medium in 3 h of light irradiation under tungsten bulb light or even in dark conditions.

Table 4.14 A comparison of the efficiency of synthesized materials with other catalysts for plastic remediation:

Photocatalytic Material	Target Microplastic	Light Source	Time	Efficiency	Reference
TiO_2 powder	PVC	UV	300 h	27% weight loss	Cho et al., 2001
PVC-ZnO composite film	PVC	UV	7200 seconds	20% weight loss	Chakrabarti et al., 2008
PVC-$AgNbO_3$ film	PVC	Xenon lamp	120 min	33.83%	Dandan et al., 2014
Ceria-PVC film	PVC	Solar light	312 h	75% weight loss	Gupta et al., 2017
Pomegranate peel extract-based iron nanoparticles	PVC	Solar light	30 days	95%	Al-Munayzil et al., 2025
TiO_2 nanoparticle film	PS	UV	12 h	98.40%	Nabi et al., 2020
FeB/TiO_2	PS	Xe lamp	12 h	92.3%	He et al., 2023
$(BiO)_2CO_3$ nanoparticles	PS	UV-light	100 h	40%	Pino-Ramos et al., 2025
Nitrogen-doped titanium oxide (N-TiO_2)	PVC PS	Tungsten bulb Dark	3h 3h	59.9% 99.6%	This work
Graphene oxide/N-TiO_2	PVC PS	Tungsten bulb Tungsten bulb	3h 3h	99.2% 32.2%	This work
Corncob activated carbon	PVC PS	Room light Tungsten bulb	3h 3h	39.8% 27.9%	This work
Corncob activated carbon/N-TiO_2	PVC PS	Tungsten bulb Tungsten bulb	3h 3h	94% 30.8%	This work
Nitrogen-doped tin oxide (N-SnO_2)	PVC PS	Dark Dark	3h 3h	100% 99.6%	This work
Graphene oxide/N-SnO_2	PVC PS	Tungsten bulb Tungsten bulb	3h 3h	33.2 37.3%	This work
Nitrogen-doped zirconium oxide (N-ZrO_2)	PVC PS	Tungsten bulb Tungsten bulb	3h 3h	44.5% 35.2%	This work

4.5 POLYETHYLENE BASED NANOCOMPOSITES FOR REMOVAL OF METHYLENE BLUE AND RHODAMINE B FROM WATER

In this section, characterization of PE/GO (PEGO), PE/ N-TiO_2 (PENT) and PE/GO/N-TiO_2 (PEGNT) and the removal study of MB and RB using the synthesized materials are explained. Furthermore, analysis of material after the MB and RB removal experiment is discussed.

4.5.1 Characterization of PE/GO (PEGO), PE/N-TiO_2 (PENT) and PE/GO/N-TiO_2 (PEGNT)

4.5.1.1 X-Ray Diffraction Analysis

X-Ray diffraction pattern of the as-obtained polyethylene-based nanocomposites are shown in **Figure 4.73**. The inter-sheet spacing of GO sheets is related to the diffraction peak (001) at around 11.2°. LDPE showed two peaks at 2θ =21.6° (110 plane) and 23.8° (200 plane) [*Carotenuto et al., 2014*]. PEGO nanocomposites and LDPE only differed in their XRD patterns by a broad, marginally strong diffraction peak at 11.2° indicates presence of the GO particles. The XRD peak for LDPE showed a modest change towards a higher 2-theta value from 21.65° to 21.77° and 23.8° to 24.2° in the PEGO, which is indicative of LDPE chains penetrating inside nanoplatelets of GO and the subsequent exfoliation of the GO layers.

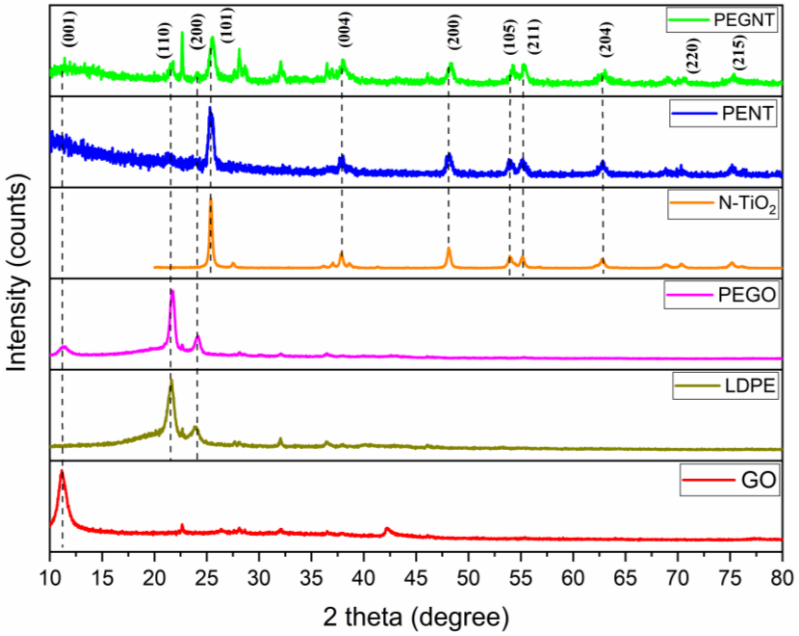


Figure 4.73 X-ray diffraction pattern of GO, LDPE, PEGO, N-TiO_2, PENT and PEGNT.

The pure tetragonal anatase phase of N-TiO_2 nanoparticles was validated by diffraction peaks for these particles at 2θ =25.3°, 37.8°, 48.0°, 53.9°, 55.0°, 62.7°, 70.2°, and 75.2°, which may be indexed to the (101), (004), (200), (105), (211), (204), (220), and (215), orientation planes, respectively. Nearly all diffraction peaks in the PENT and PEGNT nanocomposite correspond to anatase N-TiO_2 nanoparticles. However, the reduced GO intensity in PEGNT nanocomposite at 11.41° denotes the disruption of the usual GO stack by the intercalation of N-TiO_2 nanoparticles.

4.5.1.2 Functional group Analysis

The FTIR spectrum of GO presented in **Figure 4.74** shows the presence of various peaks corresponding to oxygen-containing functional groups. It is seen that the broad absorption band at 2900-3500 cm^{-1} could be assigned to the O-H group stretching vibrations of carboxylic group. The absorption peak at 1730 cm^{-1} and 1633 cm^{-1} can be assigned to C=O stretching of carboxylic and/or carbonyl moiety functional groups. The absorption peak at about 1229 cm^{-1} corresponds to stretching of epoxy skeletal vibrations and 1054 cm^{-1} is assigned to the C–O stretching vibrations [*Le et al., 2020*]. The sharp absorption at 1720 cm^{-1} for GO does not appear in the FTIR spectra of PEGO and PEGNT indicating the reduction of C-O in GO. These results showed the reduction of GO, which will result in the better electron mobility by reconstructing a part of conjugated structure inside graphene oxide with the decrease of oxygen-containing functional groups, such as epoxide, carboxyl and hydroxyl groups [*Spilarewicz-Stanek et al., 2016*]. The N-TiO_2 containing samples showed the broad absorption below 1000 cm^{-1} is attributed to the vibration of Ti-O-Ti. Moreover, peak at 719 cm^{-1} in PEGNT confirms the presence of a peak due to Ti-O-C bond. The existence of Ti-O-C bonds indicates that the chemical bonds were firmly built between GO and N-TiO_2 nanoparticles [*Ida et al., 2020, Nguyen-Phan et al., 2011*]. Peaks at 2916 and 2848cm^{-1} in PEGO, PENT, and PEGNT correspond to CH_2 asymmetric and symmetric stretching band respectively.

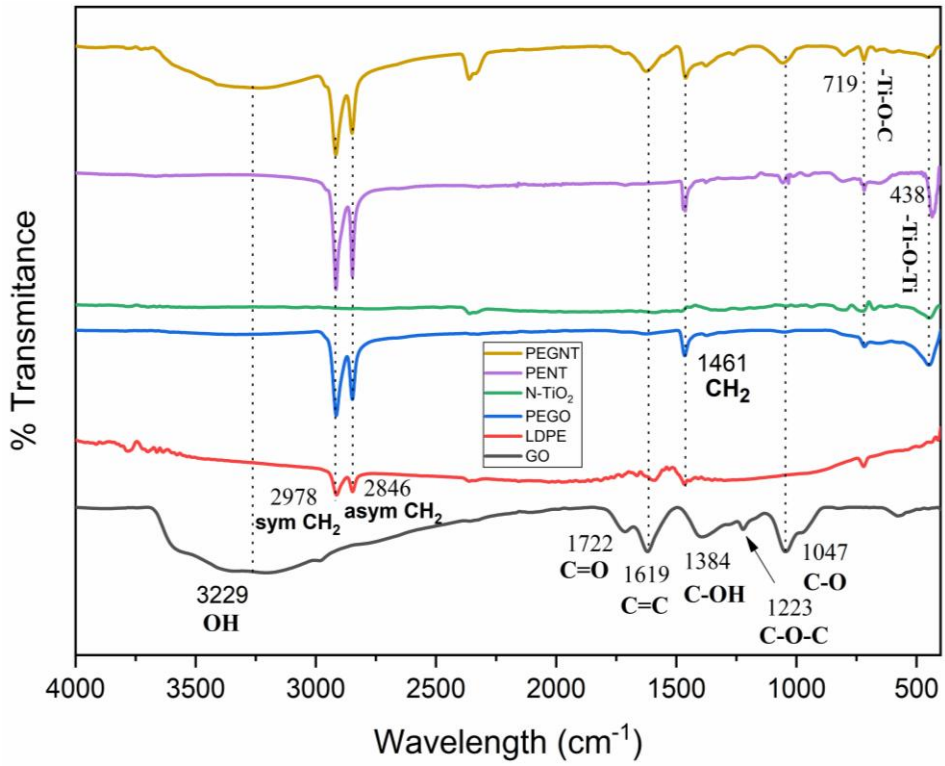


Figure 4.74 FTIR spectra of GO, LDPE, PEGO, N-TiO_2, PENT and PEGNT.

4.5.1.3 Scanning Electron Microscope Analysis

Graphene oxide has a layered structure. These sheets can be folded or continuous at times, and the edges of separate sheets, including kinked and wrinkled sections, can be seen in **Figure 4.3(a)**. In PEGO, GO is covered with LDPE as globules that flare out randomly. According to the collected images, GO exhibit good dispersion in the LDPE matrix [**Figure 4.75(a)]**. The incorporation of N-TiO_2 with PE for PENT nanocomposite is shown in **Figure 4.75(b).** As shown in the magnified image, there were several small, agglomerated particles on the surface of nanocomposites. Furthermore, numerous studies have demonstrated that adding GO to N-TiO_2 produced a rough and porous surface because of the peculiar 2D structure of GO, likewise the introduction of N doped TiO_2 gives rise to coarse and porous surface [*Padmanabhan et al., 2021*] as shown in **Figure 4.75(c)**. The kinked and wrinkled surface of GO has been made porous with incorporation of N-TiO_2. N-TiO_2 particles are decorated on the surface of PEGO, thereby resulting in a proper surface for photocatalytic activity.

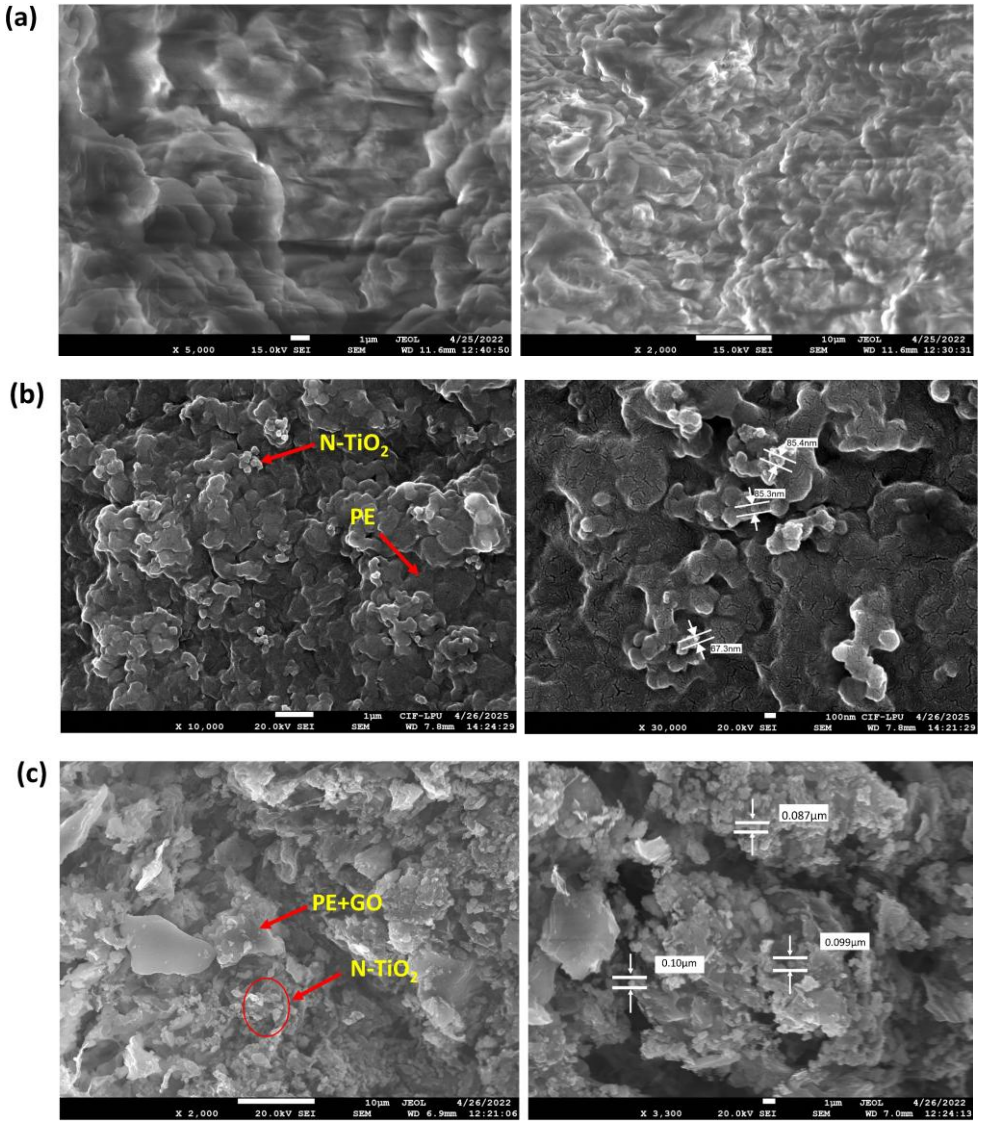


Figure 4.75 FESEM images of (a) PEGO (b) PENT and (c) PEGNT.

4.5.1.4 Energy Dispersive X-ray Spectroscopy Analysis

The elemental composition of PEGO, PENT and PEGNT nanocomposites is represented by the EDX spectrum as shown in **Figures 4.76 (a), 4.76 (b) and 4.76 (c)**, respectively and the quantitative elemental composition is shown in **Table 4.15**. The map of PEGO indicated the presence of C and O. Furthermore, the map of PENT and PEGNT showing the presence of C, O, Ti, and N peaks indicated that plastic-based nanocomposites were successfully formed without impurities. A distinct distribution of each element in nanocomposites, indicating that GO and N-TiO_2 nanoparticles were well spread or embedded between the PE layers.

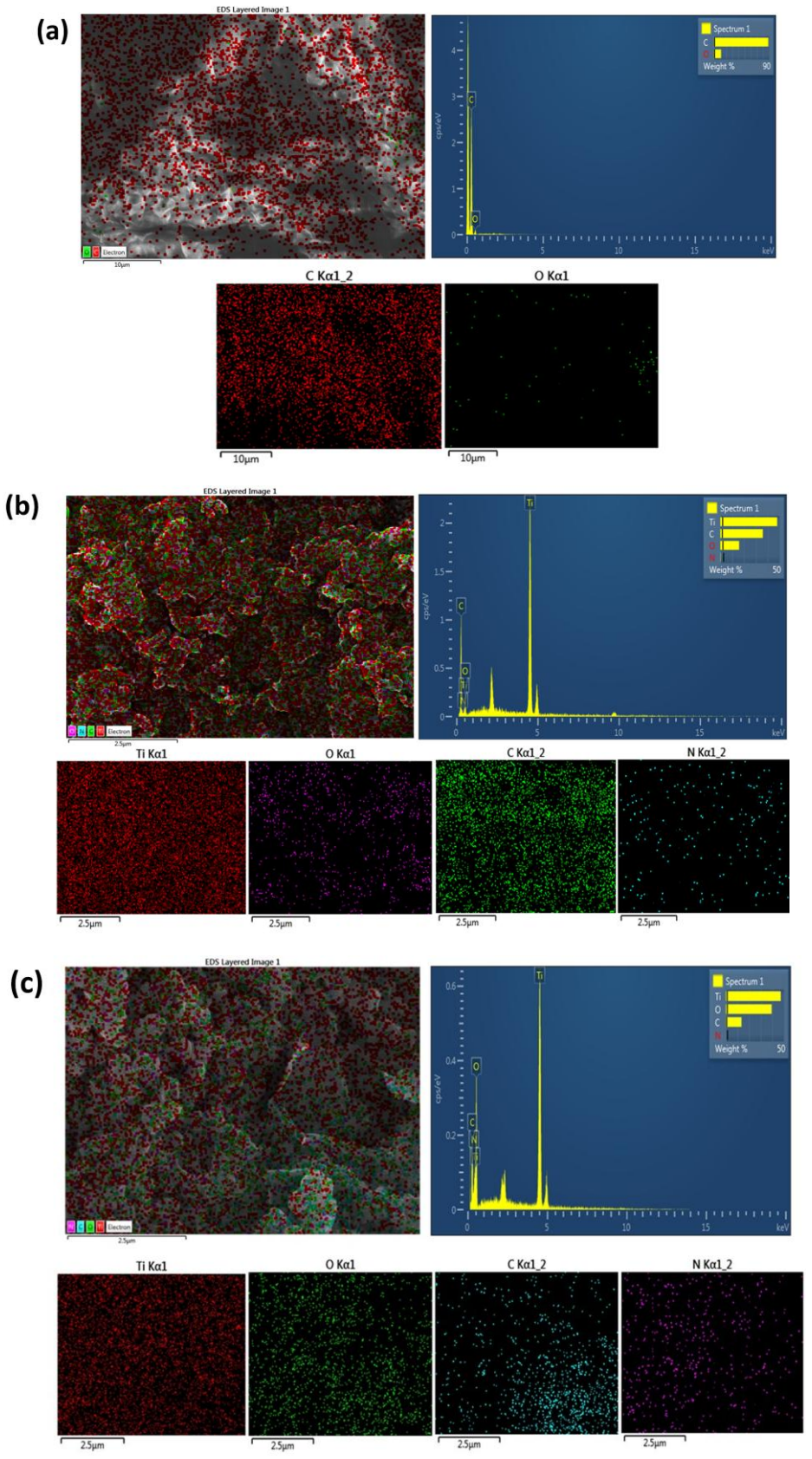


Figure 4.76 EDS mapping of (a) PEGO (b) PENT (c) PEGNT

Table 4.15 Content of elements in atomic% and weight % of PVGO, PVNT, and PVGNT.

Composite →	PEGO		PENT		PEGNT	
Elements ↓	Atomic %	Weight %	Atomic %	Weight %	Atomic %	Weight %
C	90.88	88.21	35.83	59.66	27.83	44.71
O	9.12	11.79	15.90	19.88	26.53	36.21
N	-	-	0.31	0.44	0.00	0.00
Ti	-	-	47.96	20.02	45.64	19.08
Total	100.00	100.00	100.00	100.00	100.00	100.00

4.5.1.5 Brunauer-Emmett-Teller Analysis

The nitrogen adsorption/desorption isotherms were used to investigate the porosity and surface area of the resulting GO/N-TiO_2 composite materials. The specific surface area and pore size distribution of PEGO and PEGNT was investigated by N_2 adsorption/desorption analysis. The BET surface area, pore volume and pore diameter of all materials are shown in **Table 4.16**.

Table 4.16 BET surface area, pore volume and pore diameter of all materials.

Material	**Surface Area (m^2/g)**	**Pore Volume (cm^3/g)**	**Pore Diameter (nm)**
GO	4.104	0.022	3.648
N-TiO_2	92.463	0.218	8.893
PENT	54.752	0.343	1.804
PEGO	267.906	0.342	1.797
PEGNT	88.858	0.111	1.806

4.5.1.6 Thermogravimetric Analysis

The TGA curve for PEGO, PENT and PEGNT nanocomposites involves three steps of weight loss shown in **Figure 4.77**. Adsorbed water and solvent molecules evaporated at the first stage between 27°C to 220°C. At the second stage, which is between 200°C and 400°C, the loss of oxygen atoms from the labile functional groups (hydroxyl and carboxyl) in the GO structure. At temperatures around 400 °C, the GO loses more stable

oxygenated groups like carbonyls on the edge of GO sheets. Finally, in last stage the destruction of the GO carbon skeleton occurs above 400°C. The incorporation of N-TiO_2 on PE and PEGO for the formation of PENT and PEGNT respectively reduced the weight loss of these nanocomposites and suggested that the thermal stability of the composite might be improved by adding N-TiO_2 nanoparticles. This is because the main weight loss in the TGA curves of these nanocomposites is attributed to the decomposition of the PE and GO, and the addition of N-TiO_2 leading to a lower overall weight loss. Total weight loss of GO, PE, PEGO, PENT, and PEGNT is 96.86%, 98.04%, 92.48%, 46.13%, and 42.74% respectively showing that PEGNT is more thermally stable as shown in TGA graph. This enhancement in thermal stability results from strong interactions between N-TiO_2 particles and the polymer matrix [*Khatuaa et al., 2015*].

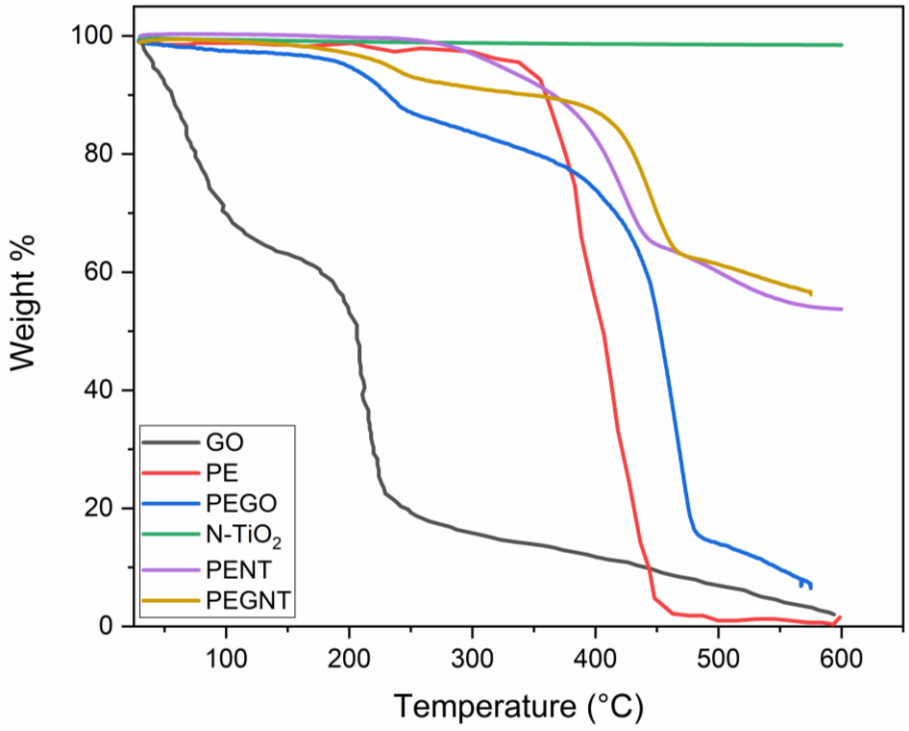


Figure 4.77 TGA of GO, PE, PEGO, N-TiO_2, PENT, and PEGNT.

4.5.1.7 Photoluminescence Analysis

The emission spectra of pure N-TiO_2, PEGO, PENT, and PEGNT are presented in **Figure 4.78.** This study demonstrates that adding C of PE matrix to N-TiO_2 causes the creation of an acceptor impurity energy level above the valence band. The presence of C 2p bands in N-TiO_2 reduces the energy gap between the valence and conduction

bands. This decrease in the energy gap broadens the absorption spectrum to the visible light area [*Romero Saez et al., 2017*].

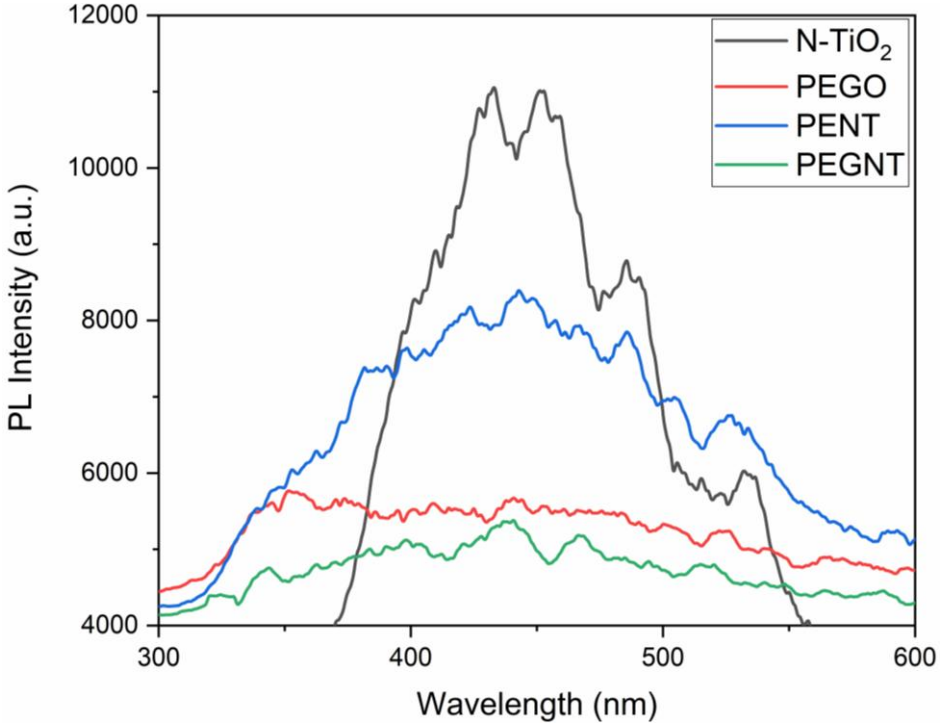


Figure 4.78 Photoluminescence emission spectra of N-TiO_2, PEGO, PENT, and PEGNT.

4.5.1.8 Optical Bandgap Analysis

There are various ways in the literature for calculating the band gap from absorbance spectra. Here, band gap (E_g) is directly calculated from emission spectra obtained from photoluminescence measurements [*Gilic et al., 2018, Ramprasath et al., 2023*]. The band gap energy E_g is related to the wavelength (λ) of the emitted light using the equation:

$$E_g = h\nu = hc/\lambda \quad \textbf{(4.1)}$$

Where, E_g is the band gap energy, h is Planck's constant (6.626 x 10^{-34} Js), c is the speed of light 3.0 x 10^8 m/s, and λ is the wavelength of the emitted light.

The calculated band gap values of PEGO, PENT, and PEGNT are given in **Table 4.17**. The band gap value for PENT is somewhat less than that of pure N-TiO_2. The variation in band gap indicates a synergistic impact between N-TiO_2 and polyethylene due to intermolecular interaction [*Romero Saez et al., 2017*]. Furthermore, the inclusion of GO into nanocomposites can result in the production of localized electronic states, mostly

due to disruptions in the material's electrical structure produced by the presence of GO and functional groups that reduce the band gap of PEGO and PEGNT [*Hurayra–Lizu et al., 2021*].

Table 4.17 Optical band gap values of GO, N-TiO_2, PEGO, PENT, and PGNT.

S. No.	Material	Optical band gap (E_g) (eV)
1.	GO	2.2
2.	N-TiO_2	2.9
3.	PEGO	2.81
4.	PENT	2.86
5.	PEGNT	2.80

4.5.2 Removal Study of MB using Synthesized Materials under different Conditions

To evaluate the removal efficiency of PEGO, PENT and PEGNT nanocomposites, a series of experiments were performed under tungsten bulb light and without light under dark. For the removal of MB using prepared nanocomposites at pH 4, pH 7 and pH 10 have been studied. Furthermore, effect of pH, light source and effect of time is also discussed. The concentration change in MB and RB were measured at λ_{max} 664nm and 554nm, respectively.

To evaluate the role of adsorption on removal of MB, an adsorption experiment was conducted using synthesized nanocomposites under dark. Under these experimental conditions, PEGO, PENT and PEGNT nanocomposites achieved the highest MB removal of 39.5%, 7.5%, and 95.8% at pH 10 as shown in **Figure 4.79(b)**. PEGNT achieved the highest removal showing excellent adsorption performance. The PEGNT nanocomposite exhibit a higher adsorption capacity for MB compared to PEGO because of synergistic effect of the three components. N-TiO_2 nanoparticles offer enhanced adsorption sites [*Scrimieri et al., 2020*] and potentially photocatalytic activity, while GO provides a large surface area and π-π interaction sites for MB. The combination maximizes the interactions with MB molecules, leading to increased adsorption [*Kocijan et al., 2021, Kusiak-Nejman et al., 2020*]. The removal of MB

decreased with PENT nanocomposite, which may be due to a decrease in the accessibility of N-TiO_2 due to the PE layer [*Panchenko et al., 2023*].

Moreover, similar experimental conditions were used for photocatalytic study of removal of MB under tungsten bulb light (**Figure 4.79(a)**). Under these conditions, PEGO, PENT and PEGNT nanocomposites shown greater removal of MB than under dark conditions; PEGNT reached the highest percentage removal of 98.8% under tungsten light at pH 10. Whereas PEGO and PENT shown percentage removal 96.9% and 20.6% under similar conditions. It could be said that photocatalytic degradation would also concurrently occur with adsorption as light interacts with the material. It is clear from the results that the decomposition of MB increased significantly under TL irradiation for PEGO and PENT nanocomposites. The mechanism is discussed in **Section *4.5.3.5.***

4.5.2.1 Effect of pH on the Removal of MB

The effects of pH on MB removal were investigated at pH levels 4, 7, and 10 as shown in **Figure 4.76(b)** showing that as pH increases from 4 to 10, the removal percentage of MB for PEGO and PEGNT increases. The PZC for PEGO, PENT, and PEGNT is approximately pH 3.2, 6.2, and 4.2 respectively, indicating that at pH values lower than this, the surface charge of nanocomposite is positive (pH < PZC) and, the surface charge turns negative as the pH rises above PZC [*Nguyen et al., 2020*]. According to the results, removal efficiency of PEGO and PEGNT for the removal of positively charged MB increases as pH increases (from 4 to 10) from their corresponding PZC because surfaces of these nanocomposites become negatively charged above PZC. This indicates that adsorption is dependent on electrostatic interactions [*Chakhtouna et al., 2021*]. For PEGO and PEGNT the adsorption is slightly increased at higher pH values may be due to the deprotonation of carboxylic groups of graphene oxide that can participate in MB removal [*El-Sharkaway et al., 2020*]. The reduced removal of MB when using PENT nanocomposite is likely due to the PE layer hindering the accessibility of the N-TiO_2 to the MB molecules. This could be due to the PE layer physically blocking the active sites on the N-TiO_2 or affecting the nanocomposite's overall interactions with MB in solution [*Cazan et al., 2021*]. This means the PE layer is acting as a barrier, preventing

the MB from reaching the active sites on the N-TiO_2 surface where degradation occurs [*Charitha et al., 2021*].

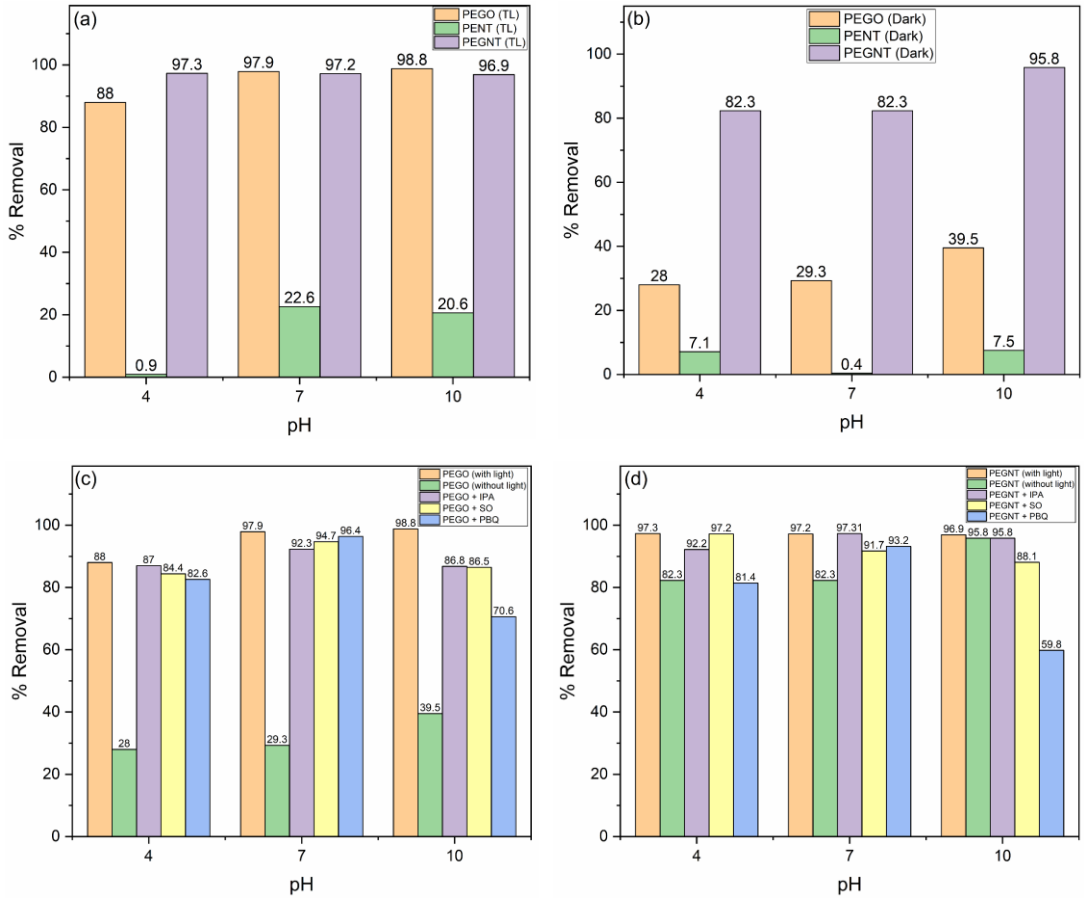


Figure 4.79 Comparison of % removal MB with PEGO, PENT, and PEGNT under (a) tungsten bulb light (b) dark; comparison of % removal MB under tungsten bulb light at pH 4 using (c) PEGO + quenchers isopropyl alcohol, sodium oxalate, and parabenzoquinone (d) PEGNT + quenchers isopropyl alcohol, sodium oxalate, and parabenzoquinone.

4.5.2.2 Effect of Time on the Removal of MB

Finding the optimum time for complete dye removal is an essential aspect for subsequent removal processes. **Figure 4.80 (c-e)** illustrates the effect of contact time on percentage removal of MB for PEGO, PENT and PEGNT. As is apparent from the figures approximately 98.8% of MB was removed within 180 min using PEGNT at pH 10 under tungsten bulb light, but for PEGO and PENT after 180 min, the percentage under removal of MB similar was 96.9% and 20.6%, respectively. After the removal of MB, the solution turns colourless and real-life image of MB solution in the time interval of 30–180 min with PEGNT at pH 10 is shown in **Figure 4.80(b)** and **Figure 4.80(a)**

is showing its UV absorption spectra, showing that % removal increases with increase in reaction time. This is because the catalyst's surface receives more contact time, which increases removal activity.

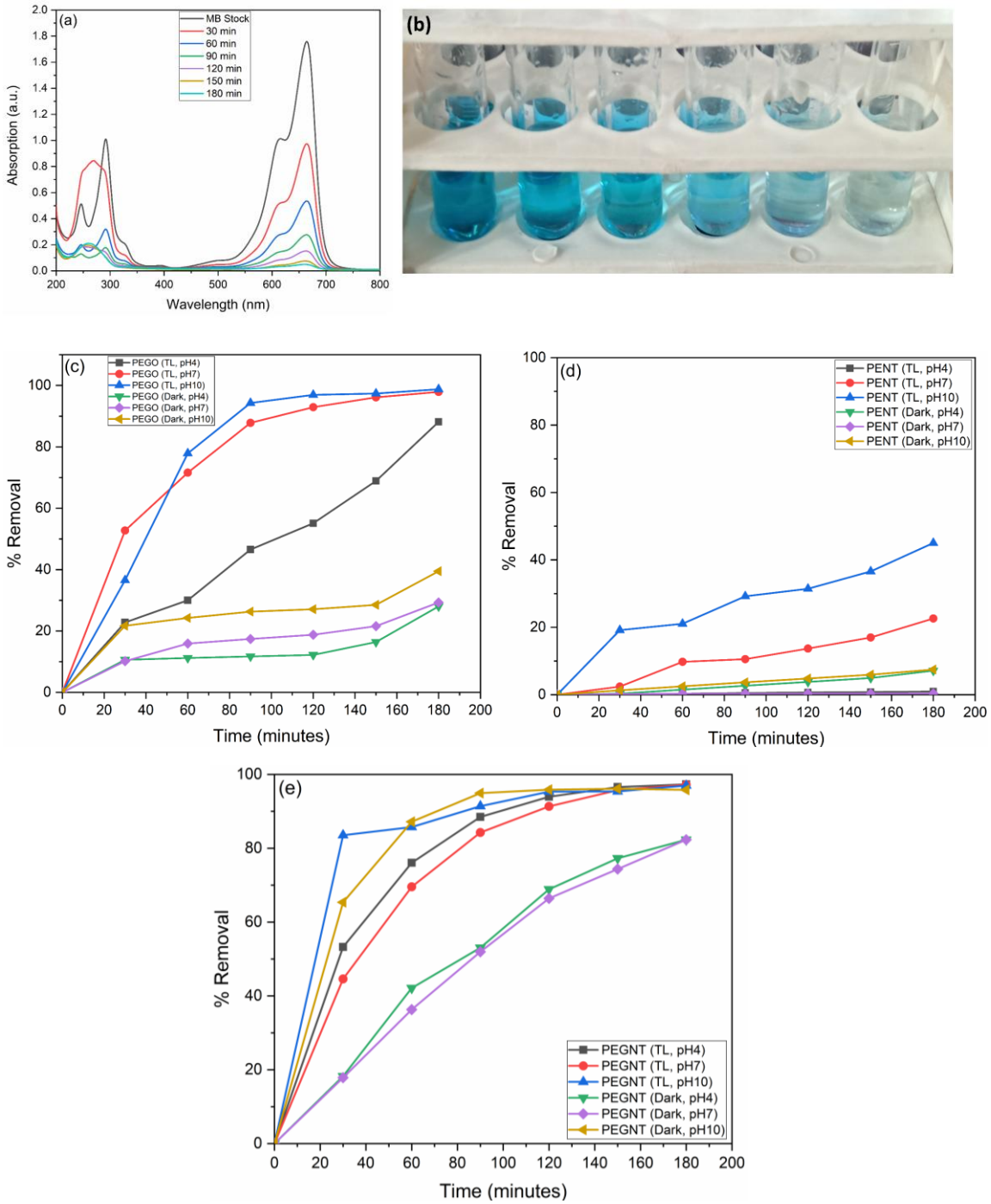


Figure 4.80 (a) UV absorption spectra of MB removal with PEGNT at pH 10 (b) real-life image of MB solution in the time interval of 30–180min at pH 10; MB removal from water treated over a 30- to 180-minute time period under TL and dark with (c) PEGO (d) PENT (e) PEGNT.

4.5.2.3 Effect of Scavengers

To study the mechanism of the photocatalytic reaction, isopropyl alcohol (IPA), sodium oxalate (SO), and parabenzoquinone (PBQ) were chosen as scavengers of $^{\bullet}OH$, h^{+}, and $^{\bullet}O_2^{-}$, respectively. **Figure 4.79 (c-d)** illustrates that the degradation rates of MB using PEGO and PEGNT decrease upon the addition of IPA, PBQ, and SO, and the results indicate that all three reactive radical species (RRS) $^{\bullet}OH$, h^{+}, and $^{\bullet}O_2^{-}$, play important roles in the photocatalytic reaction of MB.

4.5.2.4 Analysis of PE-based Nanocomposites after Removal of MB

The **FTIR spectra** before and after removal of MB using PEGO and PEGNT are shown in **Figure 4.81 (a) and Figure 4.81 (b)**, respectively showing the remarkable change of the intensities of infrared bands with some additional peaks but with no change in the positions. The changes in the intensities of FTIR spectra confirmed that the process involved inclusion of methylene blue with functional groups of PEGO and PEGNT [*Ainane et al., 2014*]

The spectral analysis before and after MB adsorption revealed that –OH groups and C=O stretching was involved in MB adsorption. Carboxyl and hydroxyl groups could induce a negative charge on the surface of the sorbent which could attract positively charged MB. The wavenumber in the range of 3780–3510 cm^{-1} is the –NH/–OH overlapped stretching vibration associated with MB seen is both PEGO and PEGNT. The absorption bands at 2914 and 2845 cm^{-1} in the PEGO spectra have intensified after MB adsorption. This could be associated with the C–H stretching vibration involved in MB adsorption [*Zazouli et al., 2016*]. After the removal of MB photocatalyst showed most of the characteristic absorption peaks associated with MB such as side ring stretching of C=C at 1500 cm^{-1} to 1400 cm^{-1}, CH=N at 1600 cm^{-1}, the $–CH_2$ or $–CH_3$ stretching at 1400 cm^{-1} to 1300 cm^{-1}, the –C–N and N–N stretching absorption peaks at 1252 cm^{-1} and 1224 cm^{-1}, C-H at 1176 cm^{-1}, C–N at 1146 cm^{-1}, C–S–C at 1064 cm^{-1} and C–H out of plane bending vibrations of ring at 881 cm^{-1} and 824 cm^{-1} are visible in FTIR spectra of PEGO and PEGNT [*Alshehri et al., 2019*].

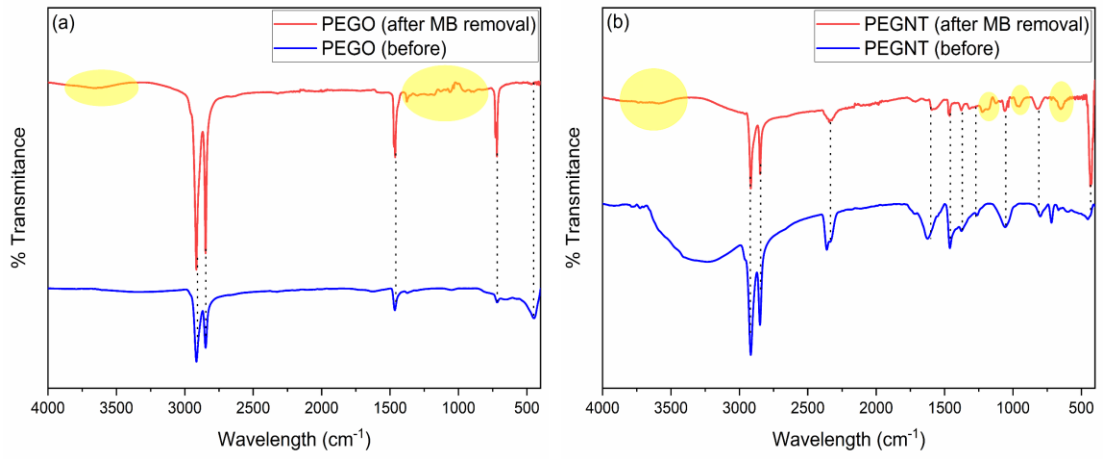


Figure 4.81 FTIR spectra of removal of MB before and after reaction (a) PEGO (b) PEGNT.

4.5.3 Removal Study of RB using Synthesized Materials under different Conditions

To evaluate the removal efficiency of PEGO, PENT and PEGNT nanocomposites, a series of experiments were performed under tungsten bulb light and without light under dark. For the removal of RB using prepared nanocomposites at pH 4, pH 7 and pH 10 have been studied. Furthermore, effect of pH, light source and effect of time is also discussed. The concentration change in MB and RB were measured at λ_{max} 664nm and 554nm, respectively.

To evaluate the role of adsorption on removal of RB, an adsorption experiment was conducted using synthesized nanocomposites under dark. Under these experimental conditions, PEGO, PENT and PEGNT nanocomposites achieved the highest RB removal of 28.5%, 0.5%, and 74.2% as shown in **Figure 4.82(b)**. PEGNT achieved the highest RB removal showing excellent adsorption performance. The PEGNT nanocomposite exhibit a higher adsorption capacity for RB compared to PEGO because of synergistic effect of the three components. The addition of N-TiO_2 to the PEGO composite provides more active sites for RB molecules to attach [*Scrimieri et al., 2020*] and potentially photocatalytic activity, while GO provides a large surface area and π-π interaction sites for RB. The combination maximizes the interactions with RB molecules, leading to increased adsorption [*Kocijan et al., 2021, Kusiak-Nejman et al., 2020*]. The removal of RB is almost negligible with PENT nanocomposite, which may

be due to a decrease in the accessibility of N-TiO_2 due to the PE matrix [*Panchenko et al., 2023*].

Moreover, similar experimental conditions were used for photocatalytic study of removal of RB under tungsten bulb light (**Figure 4.82(a)**). Under these conditions, PEGO, PENT and PEGNT nanocomposites shown greater removal of RB than under dark conditions; PEGNT reached the highest percentage removal of 84.9% under tungsten light at pH 4. Whereas PEGO and PENT shown percentage removal 75.4% and 1.1% under similar conditions. It could be said that photocatalytic degradation would also concurrently occur with adsorption as light interacts with the material. It is clear from the results that the decomposition of RB increased significantly under TL irradiation for PEGO and PENT nanocomposites. The mechanism is discussed in **Section 4.5.3.5**

4.5.3.1 Effect of pH on the Removal of RB

The effects of pH on RB removal were investigated at pH levels 4, 7, and 10 as shown in **Figures 4.86(b)** showing the variation in removal percentage of RB for as pH increases from 4 to 10 for PEGO, PENT and PEGNT. The PZC for PEGO, PENT, and PEGNT is approximately pH 3.2, 6.2, and 4.2 respectively, indicating that at pH values lower than this, the surface charge of nanocomposite is positive (pH < PZC) and, the surface charge turns negative as the pH rises above PZC [*Nguyen et al., 2020*]. The removal efficiency of PEGO, PENT and PEGNT for the removal of positively charged RB is expected to be increased as pH increases (from 4 to 10) from their corresponding PZC because surfaces of these nanocomposites become negatively charged above PZC and indicates that adsorption is dependent on electrostatic interactions [*Chakhtouna et al., 2021*]. But according to the results, an increase in pH of solution from 4 to 10 does not change much in the percentage removal of RB using the PEGO. A small decrease in the percentage removal was observed from 4 to 10 using PEGNT. The electrostatic interaction between the RB molecules and PEGNT is responsible for the high removal efficiency and low pH. On the one hand, the acidic oxygen groups on the PEGNT surface deprotonate and become negatively charged as the pH of the solution rises above PZC. In contrast, RB is found as cations and zwitterions in polar solvents. The carboxyl group of the RB undergoes deprotonation when the pH of the solution rises

beyond 3.7 (the pK_a of RB), causing the cationic form to change into a zwitterionic form. This resulted in electrostatic repulsion between RB and negatively charged PEGNT. However, the overall variation in removal efficiency is lower. It is believed that the electrostatic effect does not dominate the adsorption process [*Xiao et al., 2020*]. The reduced removal of RB when using PENT nanocomposite is likely due to the PE layer hindering the accessibility of the N-TiO_2 to the RB molecules. This could be due to the PE layer physically blocking the active sites on the N-TiO_2 or affecting the nanocomposite's overall interactions with RB in solution [*Cazan et al., 2021*]. This means the PE layer is acting as a barrier, preventing the RB from reaching the active sites on the N-TiO_2 surface where degradation occurs [*Charitha et al., 2021*].

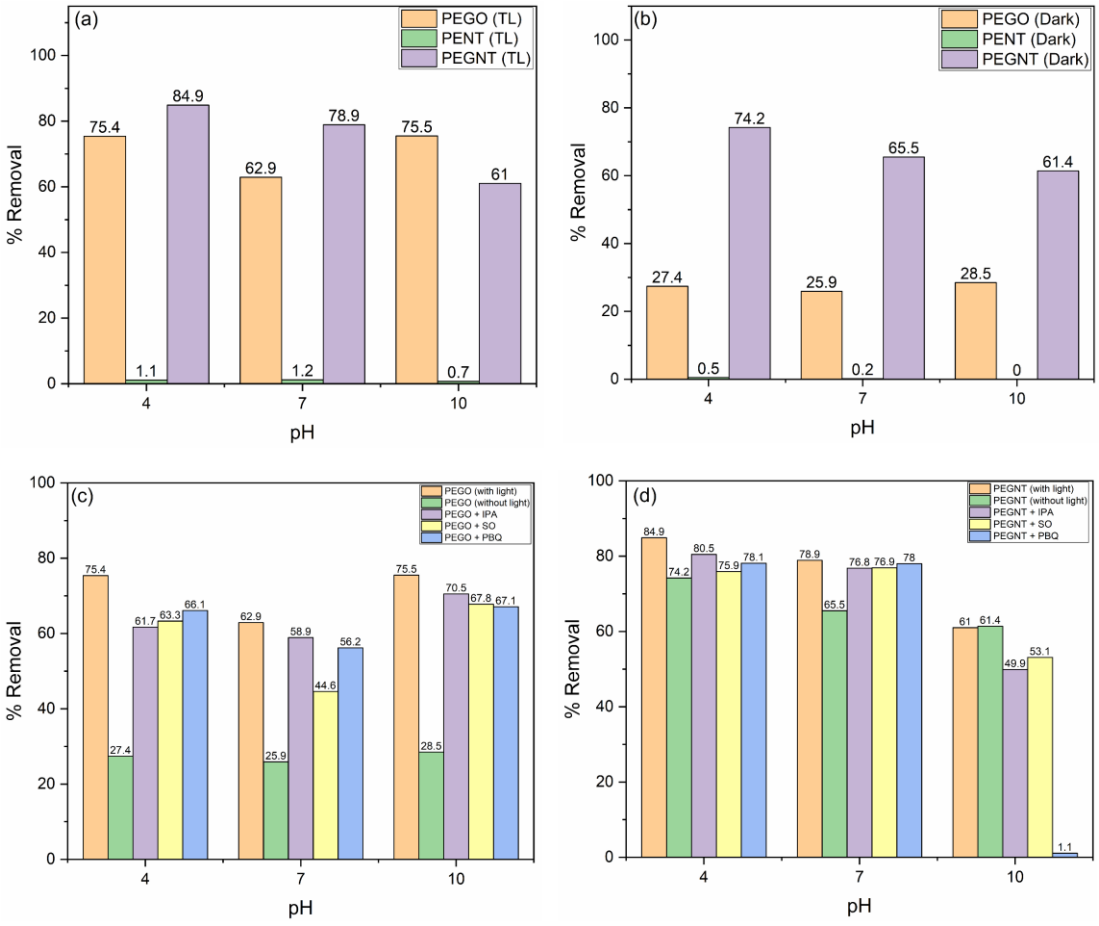
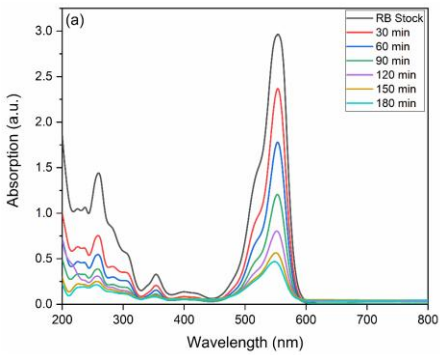
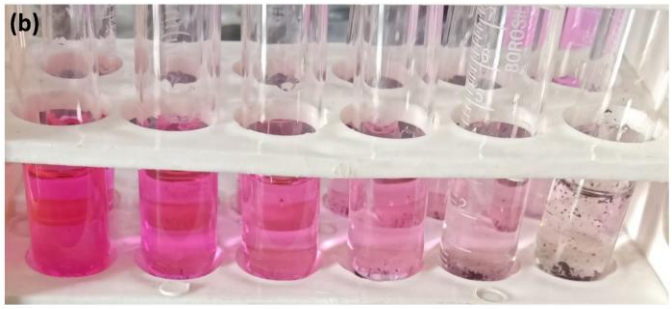


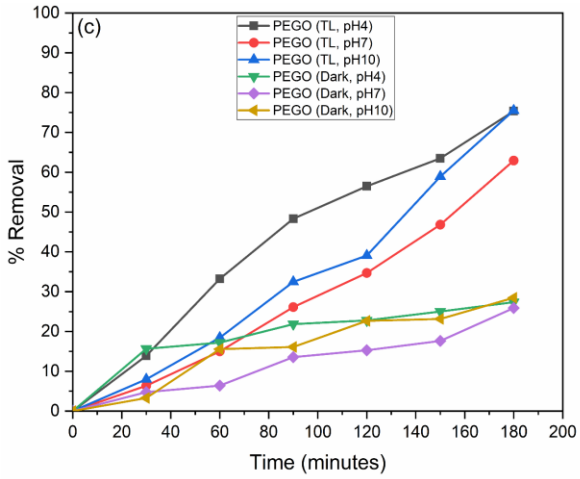
Figure 4.82 Comparison of % removal RB with PEGO, PENT, and PEGNT under (a) tungsten bulb light (b) dark; comparison of % removal RB under tungsten bulb light at pH 4 using (c) PEGO + quenchers isopropyl alcohol, sodium oxalate, and parabenzoquinone (d) PEGNT + quenchers isopropyl alcohol, sodium oxalate, and parabenzoquinone.

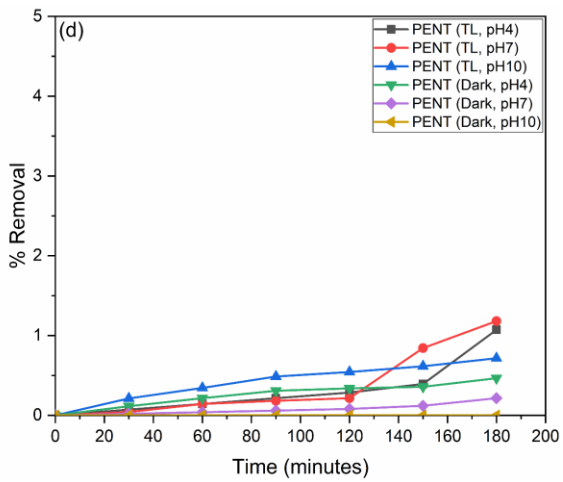
4.5.3.2 Effect of Time on the Removal of RB

Figure 4.83 (c-e) illustrates the effect of contact time on percentage removal of RB for PEGO, PENT and PEGNT. As is apparent from the figures approximately 84.9% of RB was removed within 180 min using PEGNT at pH 4 under tungsten bulb light, but for PEGO and PENT after 180 min, the percentage under removal of RB similar was 75.4% and 1.1%, respectively. After the removal of RB, the solution turns colourless and real-life image of RB solution in the time interval of 30–180 min with PEGNT at pH 4 is shown in **Figure 4.83(b)** and **Figure 4.83(a)** is showing its UV absorption spectra, showing that % removal increases with increase in reaction time. This is because the catalyst's surface receives more contact time, which increases removal activity.









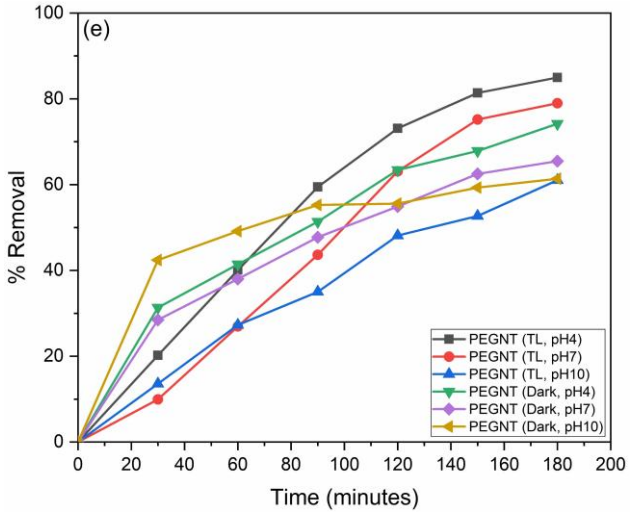


Figure 4.83 (a) UV absorption spectra of RB removal with PEGNT at pH 4 (b) real-life image of RB solution in the time interval of 30–180 min at pH 4; RB removal from water treated over a 30- to 180-minute time period under TL and dark with (c) PEGO (d) PENT (e) PEGNT.

4.5.3.3 Effect of Scavengers

To study the mechanism of the photocatalytic reaction, isopropyl alcohol (IPA), sodium oxalate (SO), and parabenzoquinone (PBQ) were chosen as scavengers of $^{\bullet}OH$, h^{+}, and $^{\bullet}O_2^{-}$, respectively. **Figure 4.82 (c-d)** illustrates that the degradation rates of RB using PEGO and PEGNT decrease upon the addition of IPA, PBQ, and SO, and the results indicate that all three reactive radical species (RRS) $^{\bullet}OH$, h^{+}, and $^{\bullet}O_2^{-}$, play important roles in the photocatalytic reaction of RB.

4.5.3.4 Analysis of PE-based Nanocomposites after Removal of RB

The FTIR spectra before and after removal of RB using PEGO and PEGNT are shown in **Figure 4.83 (a) and Figure 4.83 (b)**, respectively showing the remarkable change of the intensities of infrared bands of PEGO. Furthermore, FTIR spectra of both PEGO and PEGNT show some additional peaks, and PEGNT shows a change in the positions of a few peaks. Shifts in these peaks and the appearance of new peaks can indicate interactions of RB with PEGO and PEGNT after adsorption or degradation [*Ainane et al., 2014*].

The spectral analysis before and after RB adsorption revealed that –OH groups and C=O stretching was involved in RB adsorption. The wavenumber in the range of 3780–3510 cm^{-1} is the –NH/–OH overlapped stretching vibration associated with RB seen is

both PEGO and PEGNT. The absorption bands at 2914 and 2845 cm^{-1} in the PEGO spectra have intensified after RB adsorption. This could be associated with the C–H stretching vibration involved in RB adsorption [*Zazouli et al., 2016*]. After the removal of RB photocatalyst most of the characteristic absorption peaks associated with RB such as aromatic C=C stretching (1450-1600 cm^{-1}), aromatic C-H bending (1000-1253 cm^{-1}), and C=O stretching (around 1630 cm^{-1}). Additionally, peaks associated with C-H stretching in CH_2 groups are observed at 2850 and 2935 cm^{-1} and the presence –COO group in RB symmetric and asymmetric stretching vibrations at 1405 and 1580 cm^{-1} [*Pang et al., 2012*].

According to FTIR spectra, the peak of PEGNT at 3281 cm^{-1}, which corresponds to the stretching vibration of O-H for hydroxyl groups, shifted slightly to 3624 cm^{-1} after the RB removal experiment, indicating the presence of hydrogen bonding between PEGNT and RB molecules. Furthermore, the peak at 1624 cm^{-1}, which corresponds to the stretching vibration of C=C groups in the aromatic ring, shifted to 1579 cm^{-1} after removal, possibly due to the π-π interactions.

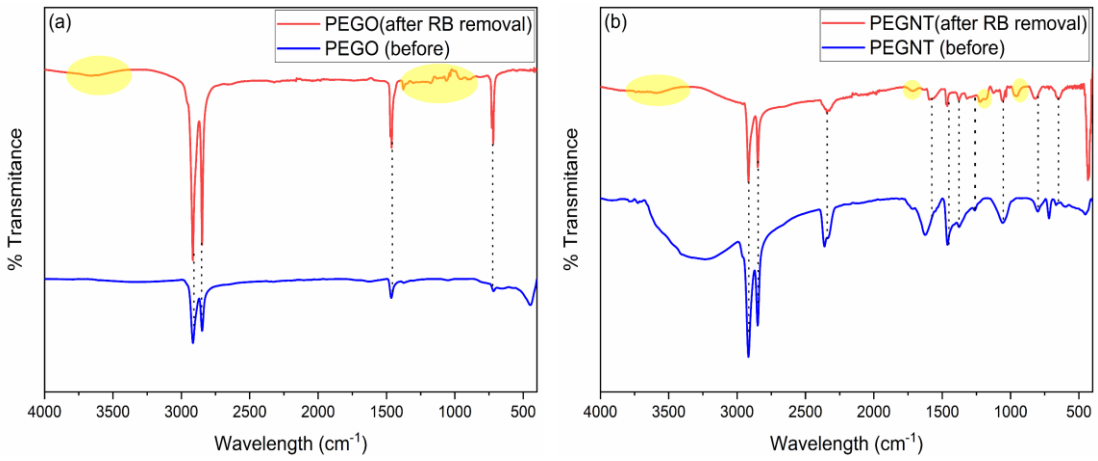


Figure 4.84 FTIR spectra of removal of RB before and after reaction (a) PEGO (b) PEGNT.

4.5.3.5 Mechanism of MB and RB Removal using Synthesized PE based Nanocomposites

For PEGO, the combination of PE and GO can lead to synergistic effects. For instance, the PE matrix can provide a flexible and mechanically robust support for the GO and any other photocatalytic material incorporated in the composite, while GO can enhance the light absorption and charge separation within the composite. Light interacts with a

solution containing MB and RB molecules and PEGO nanocomposite as photocatalysts, producing photoexcited electrons and holes due to a π-π* excitation in the π-conjugated sp^2 domains of GO. These photogenerated electrons and holes combined with oxygen and water molecules to form reactive oxygen species (ROS). ROS eventually degraded MB and RB molecules, producing CO_2 and H_2O. GO behaves as a semiconductor, electrons in the VB are jumped into the CB due to light absorption. The photogenerated electrons and holes in CB and VB produce ROS, which then participate in photochemical degradation of MB as shown in following equations [*Prakash et al., 2022*].

$$GO + h\nu \rightarrow GO\ (h^+) + GO\ (e^-)$$

$$GO\ (e^-) + O_2 \rightarrow GO + {}^{\bullet}O_2^-$$

$$GO\ (h^+) + H_2O/OH^- \rightarrow GO + {}^{\bullet}OH$$

$${}^{\bullet}O_2^- + dye \rightarrow CO_2 + H_2O$$

$${}^{\bullet}OH + dye \rightarrow CO_2 + H_2O$$

In case of PEGNT, photogenerated carriers (electrons and holes) form on the surface of N-TiO_2 photocatalysts when exposed to sufficient light. Photogenerated electrons (e^-) are produced when light energy excites electrons from the valence band to the conduction band and photogenerated holes (h^+) with oxidative properties were created in the valence band. The photogenerated electrons can be moved from N-TiO_2 to GO due to the excellent conduction property of GO [*Si et al., 2017*]. By storing and transmitting electrons, GO can enhance the migration and separation of electrons produced by N-TiO_2, prevent carrier combination, and boost photocatalytic activity. When H_2O and O_2 are adsorbed on N-TiO_2 and GO surfaces during photocatalysis, ${}^{\bullet}OH$ and ${}^{\bullet}O_2^-$ are produced [*Linsebigler et al., 1995, Zan et al., 2006*]. The PVC molecular chain was attacked by ${}^{\bullet}O_2^-$ and ${}^{\bullet}OH$, resulting in degradation of MB. Furthermore, the holes combine with water molecule to produce hydroxyl radicals (·OH), which can degrade the dye into water and CO_2. The following are the reaction equations involved in the process:

$$N\text{-}TiO_2 + h\nu \rightarrow N\text{-}TiO_2\ (e^- + h^+)$$

$$N\text{-}TiO_2\,(e^-) + GO \rightarrow GO\,(e^-) + N\text{-}TiO_2$$

$$GO\,(e^-) + O_2 \rightarrow GO + {}^{\bullet}O_2^-$$

$$N\text{-}TiO_2\,(h^+) + H_2O \rightarrow {}^{\bullet}OH + H^+$$

$${}^{\bullet}O_2^- + \text{dye} \rightarrow CO_2 + H_2O$$

$${}^{\bullet}OH + \text{dye} \rightarrow CO_2 + H_2O$$

Photodegradation scavenger tests in PEGO and PEGNT revealed the superoxide radicals to be the primary reactive species responsible for the efficient degradation of dye. Also, in some cases, the low percentage decreases in photodegradation upon adding scavengers shown in **Figure 4.79 (c-d)** imply that another pathway for MB degradation particular scenario [*Prakash et al., 2023*]. In the absence of significant reactive oxygen species (ROS) involvement in dye degradation, other mechanisms like direct photolysis or reactions with photogenerated species (e.g., electrons) can become dominant. Direct photolysis involves dye molecules directly absorbing light and breaking down [*Pingmuang et al., 2017*].

4.6 POLYVINYL CHLORIDE BASED NANOCOMPOSITES FOR REMOVAL OF METHYLENE BLUE AND RHODAMINE B FROM WATER

In this section, characterization of PVC/GO (PVGO), PVC/ N-TiO_2 (PVNT) and PVC/GO/N-TiO_2 (PVGNT) and the removal study of MB and RB using the synthesized materials are explained. Furthermore, analysis of material after the MB and RB removal experiment is discussed.

4.6.1 Characterization of PVC/GO (PVG), PVC/ N-TiO_2 (PVNT) and PVC/GO/N-TiO_2 (PVGNT)

4.6.1.1 X-Ray Diffraction Analysis

X-Ray diffraction pattern of the as-obtained polyethylene-based nanocomposites are shown in **Figure 4.85**.

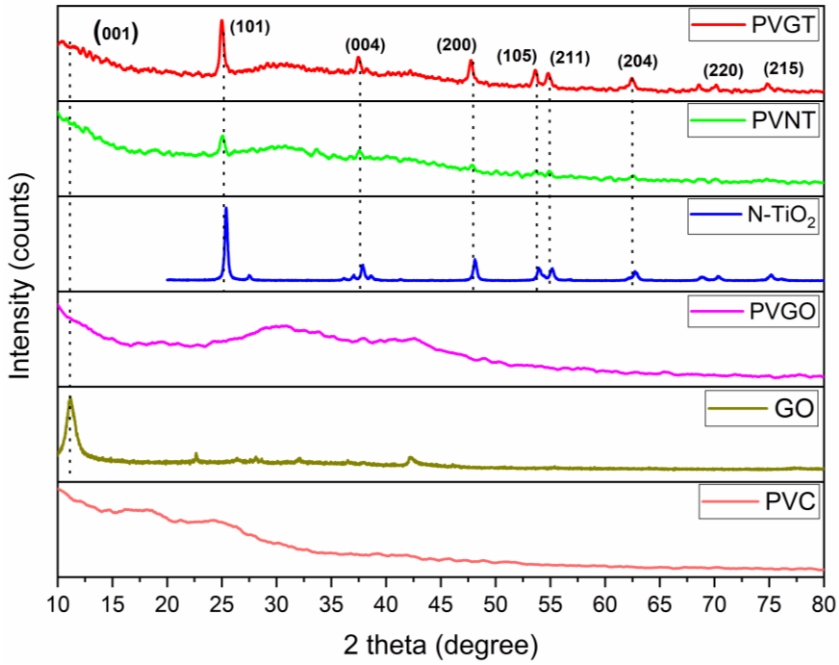


Figure 4.85 X-ray diffraction pattern of PVC, GO, PVGO, N-TiO_2, PVNT and PVGNT.

The inter-sheet spacing of GO sheets is related to the diffraction peak (001) at around 11.2°. Pure PVC is indicated through a broad peak in the region of 15–30° [*Abdel-Baset et al., 2016*]. PVGO nanocomposites and PVC only differed in their XRD patterns by a broad, marginally strong diffraction peak at 11.2° indicates presence of the GO particles. After incorporation of N-TiO_2 anatase into the PVC matrix, the

characteristic X-ray diffraction peaks of PVC and N-TiO_2 anatase appear in the diffractogram of the PVNT anatase nanocomposite.

The pure tetragonal anatase phase of N-TiO_2 nanoparticles was validated by diffraction peaks for these particles at 2θ =25.3°, 37.8°, 48.0°, 53.9°, 55.0°, 62.7°, 70.2°, and 75.2°, which may be indexed to the (101), (004), (200), (105), (211), (204), (220), and (215), orientation planes, respectively. Nearly all diffraction peaks in the PVNT and PVGNT nanocomposite correspond to anatase N-TiO_2 nanoparticles. However, the reduced GO intensity in PVGNT nanocomposite at 11.41° denotes the disruption of the usual GO stack by the intercalation of N-TiO_2 nanoparticles.

4.6.1.2 Functional group Analysis

Figure 4.86 shows the FTIR spectrum of GO, PVC, PVGO, N-TiO_2, PVNT, and PVGNT nanocomposites. For PVC, there are some characteristic peaks: peak at 2971 cm^{-1} of CH_2 stretching vibrations, CH-Cl out of plane angular deformation at 1225 cm^{-1}, C-H out of plane trans deformation at 976 cm^{-1}, and C-Cl bond stretching at 830 cm^{-1} [*Mallakpour et al., 2017*]. The FTIR spectrum of GO shows the presence of various peaks corresponding to oxygen-containing functional groups. It is seen that the broad absorption band at 2900-3500 cm^{-1} could be assigned to the O-H group stretching vibrations of carboxylic group. The absorption peak at 1730 cm^{-1} and 1633 cm^{-1} can be assigned to C=O stretching of carboxylic and/or carbonyl moiety functional groups. The absorption peak at about 1229 cm^{-1} corresponds to stretching of epoxy skeletal vibrations and 1054 cm^{-1} is assigned to the C–O stretching vibrations [*Le et al., 2020*]. The FTIR spectra of PVGO and PVGNT indicating presence of all the characteristic peaks of GO and PVC. The N-TiO_2 containing samples showed the broad absorption below 1000 cm^{-1} is attributed to the vibration of Ti-O-Ti. Moreover, peak at 747 cm^{-1} in PVGNT confirms the presence of a peak due to Ti-O-C bond. The existence of Ti-O-C bonds indicates that the chemical bonds were firmly built between GO and N-TiO_2 nanoparticles [*Ida et al., 2020, Nguyen-Phan et al., 2011*]. Peaks at 2916 cm^{-1} and 2848 cm^{-1} in PVGO, PVNT, and PVGNT correspond to CH_2 asymmetric and symmetric stretching band respectively.

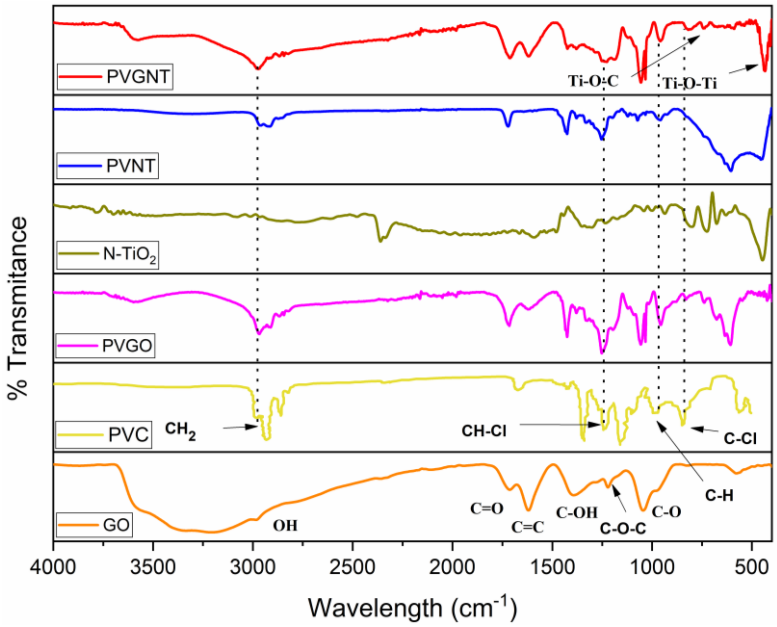
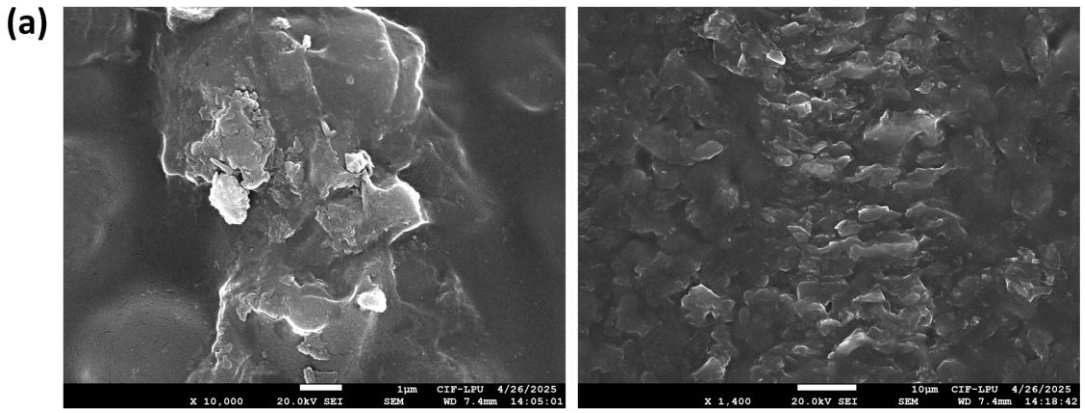


Figure 4.86 FTIR spectra of GO, PVC, PVGO, N-TiO_2, PVNT, and PVGNT.

4.6.1.3 Scanning Electron Microscope Analysis

In PVGO, GO is covered with PVC as globules that flare out randomly. According to the collected images, GO exhibit good dispersion in the PVC matrix [**Figure 4.87(a)]**. The incorporation of N-TiO_2 with PVC for PVNT nanocomposites is shown in **Figure 4.87(b).** As shown in the magnified image, there were several small, agglomerated particles on the surface of nanocomposites. Addition of GO to N-TiO_2 produced a rough and porous surface because of the peculiar 2D structure of GO, likewise the introduction of N-TiO_2 gives rise to coarse and porous surface [*Padmanabhan et al., 2021*] as shown in **Figure 4.75(c)**. The kinked and wrinkled surface of GO has been made porous with incorporation of N-TiO_2. N-TiO_2 particles are decorated on the surface of PVGO, thereby resulting in a proper surface for photocatalytic activity.



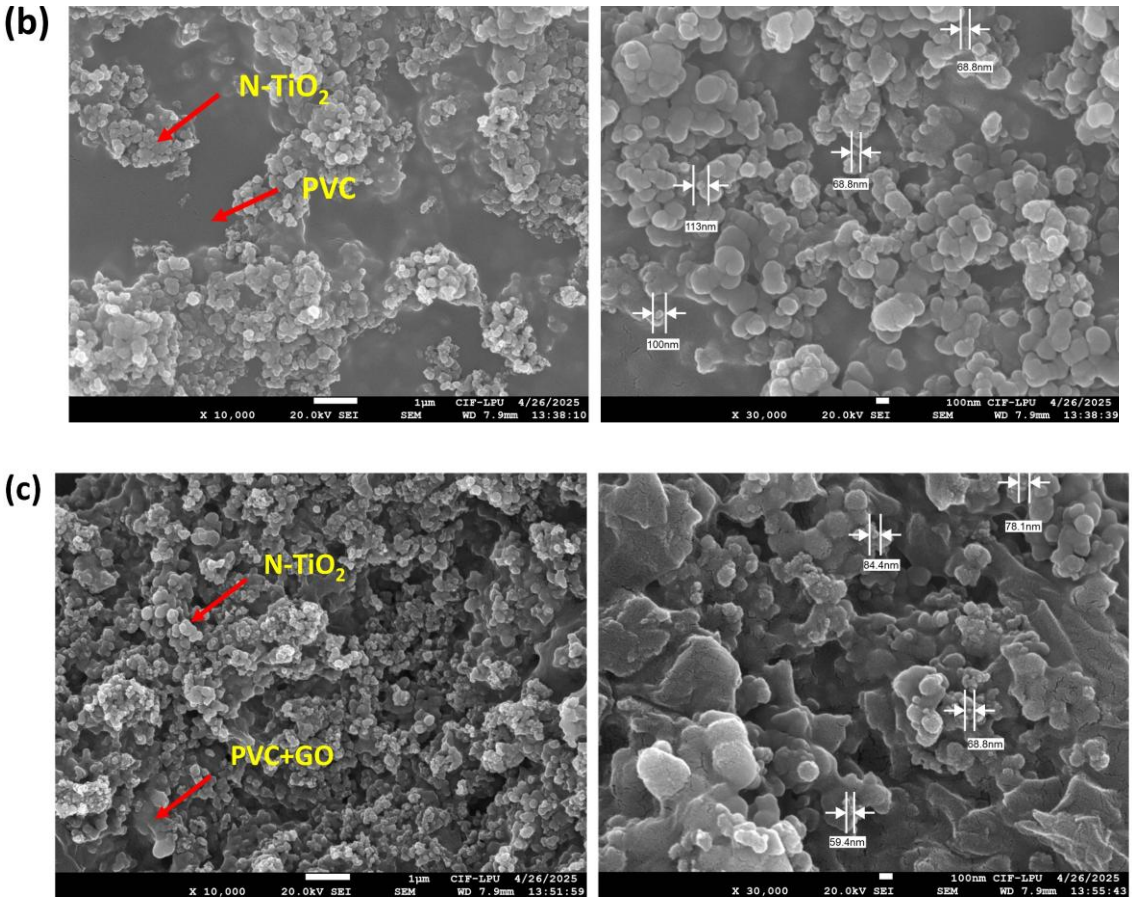
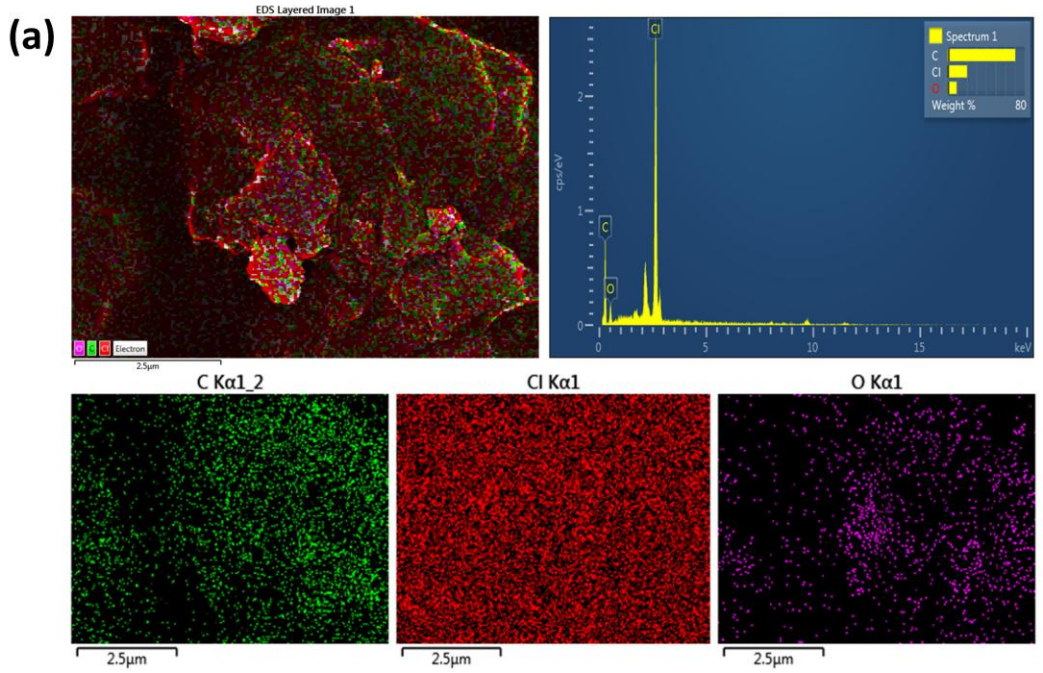
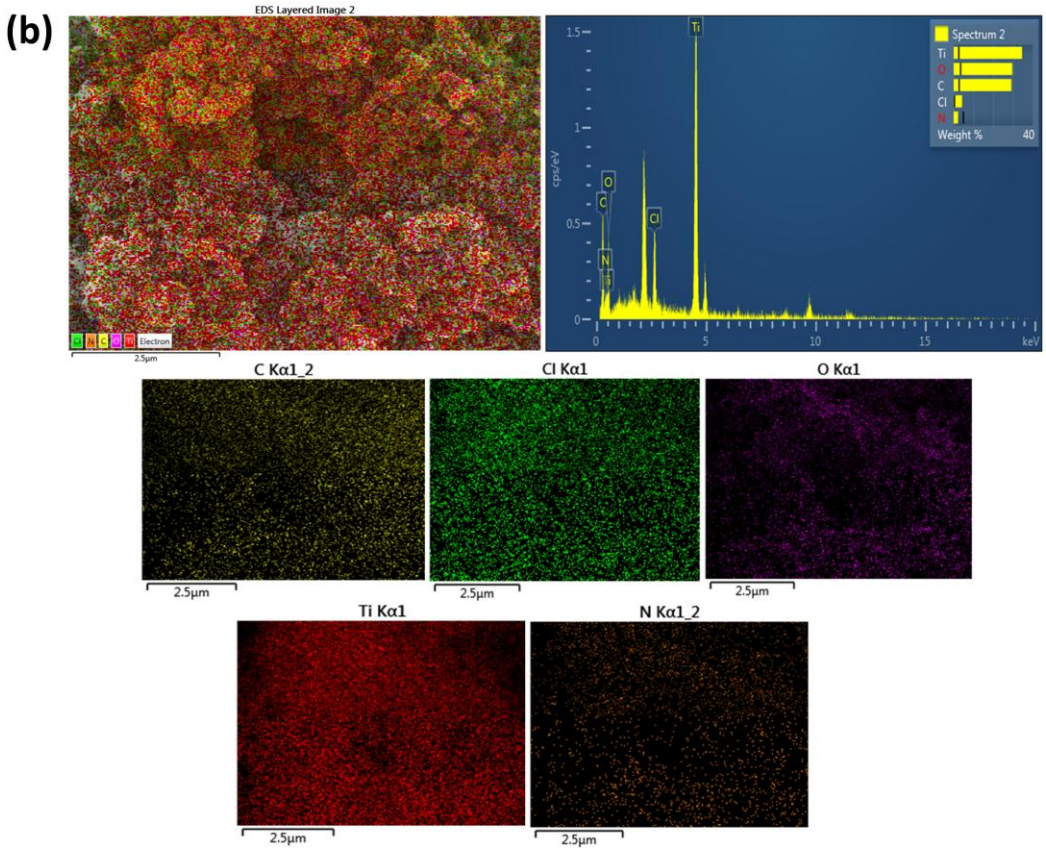


Figure 4.87 FESEM images of (a) PVGO, (b) PVNT, and (c) PVGNT.

4.6.1.4 Energy-Dispersive X-ray Spectroscopy Analysis

The elemental composition of PVGO, PVNT and PVGNT nanocomposites is represented by the EDX spectrum as shown in **Figures 4.88(a), 4.88(b) and 4.88(c)**, respectively and the quantitative elemental composition is shown in **Table 4.18**. The map of PVGO indicated the presence of C, Cl and O. Furthermore, the map of PVNT and PVGNT showing the presence of C, O, Ti, N and Cl peaks indicated that nanocomposites were successfully formed without impurities. A distinct distribution of each element in nanocomposites, indicating that GO and N-TiO_2 nanoparticles were well spread or embedded between the PVC layers.


(a)
EDS Layered Image 1
Spectrum 1
C
Cl
O
Weight %
80
cps/eV
keV
C Kα1_2
Cl Kα1
O Kα1
2.5µm


(b)
EDS Layered Image 2
Spectrum 2
Ti
O
C
Cl
N
Weight %
40
cps/eV
keV
C Kα1_2
Cl Kα1
O Kα1
Ti Kα1
N Kα1_2
2.5µm

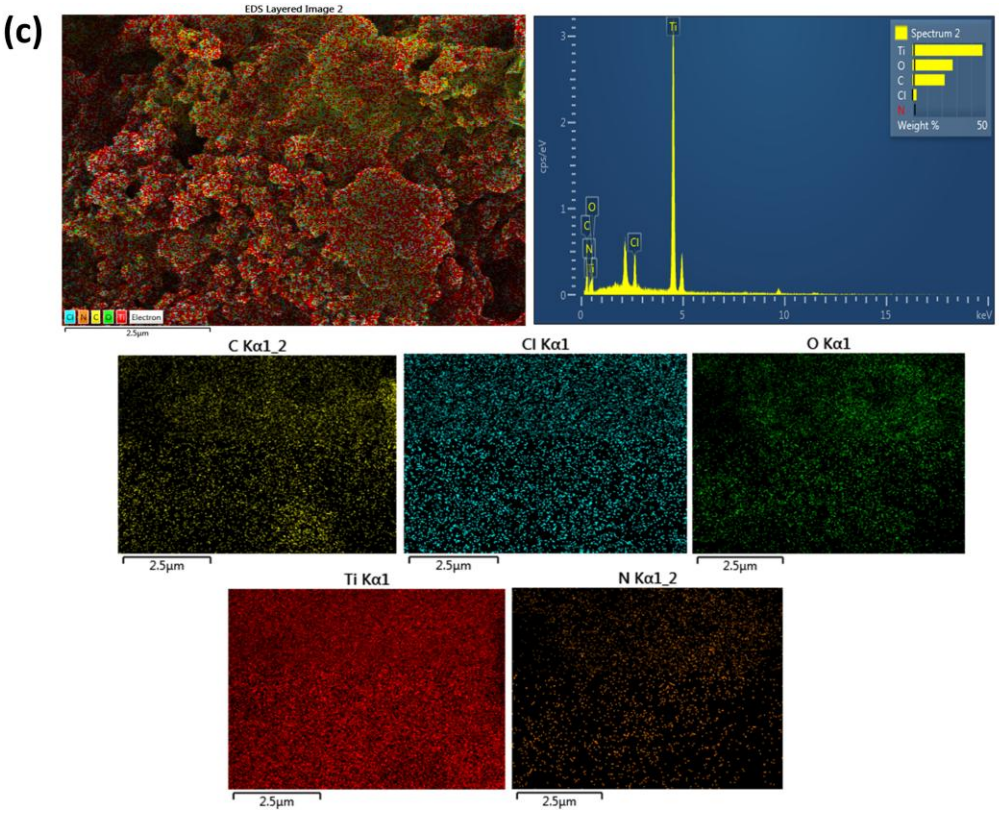


Figure 4.88 EDS mapping of (a) PVGO (b) PVNT (c) PVGT.

Table 4.18 Content of elements in atomic% and weight % of PVGO, PVNT, and PVGT.

Composite →	**PVGO**		**PVNT**		**PVGNT**	
Elements ↓	Atomic %	Weight %	Atomic %	Weight %	Atomic %	Weight %
C	70.27	83.42	29.23	46.00	21.95	39.56
O	9.44	8.41	29.67	35.06	27.42	37.10
N	-	-	2.24	3.03	0.00	0.00
Ti	-	-	34.61	13.66	47.79	21.60
Cl	20.29	8.16	4.24	2.26	2.84	1.74
Total	100.00	100.00	100.00	100.00	100.00	100.00

4.6.1.5 Thermogravimetric Analysis

Weight loss in PVC began at around 220 °C due to moisture and volatile contaminants. The second weight loss began at 240 °C and ended at 370 °C. The second weight loss could be attributed to thermal degradation of PVC. At this point, dehydrochlorination takes place, followed by the formation of conjugated polyenes. The third weight loss started at 400 °C and finished at 520 °C. The third stage involves the scission of polyene

sequences in various types of methods, including cracking, crosslinking, and aromatization, which produced a diverse spectrum of hydrocarbons such as benzene, toluene, and xylene [*Abdel-Baset et al., 2016*]. Furthermore, the TGA curve for PVGO, PVNT and PVGNT nanocomposites involves three steps of weight loss shown in **Figure 4.89**. Adsorbed water and solvent molecules evaporated at the first stage between 27°C to 220°C. At the second stage, which is between 200°C and 400°C, the loss of oxygen atoms from the labile functional groups (hydroxyl and carboxyl) in the GO structure. At temperatures around 400 °C, the GO loses more stable oxygenated groups like carbonyls on the edge of GO sheets. Finally, in last stage the destruction of the GO carbon skeleton occurs above 400°C. The incorporation of N-TiO_2 on PVC and PVGO for the formation of PVNT and PVGNT respectively reduced the weight loss of these nanocomposites and suggested that the thermal stability of the composite might be improved by adding N-TiO_2 nanoparticles. This is because the main weight loss in the TGA curves of these plastic-based nanocomposites is attributed to the decomposition of the PVC and GO, and the addition of N-TiO_2 leading to a lower overall weight loss. Total weight loss of GO, PVC, PVGO, PVNT, and PVGNT is 96.86%, 98.03%, 86.1%, 78.8%, and 31% respectively showing that PVGNT is more thermally stable as shown in TGA graph. This enhancement in thermal stability results from strong interactions between N-TiO_2 particles and the polymer matrix [*Khatuaa et al., 2015*].

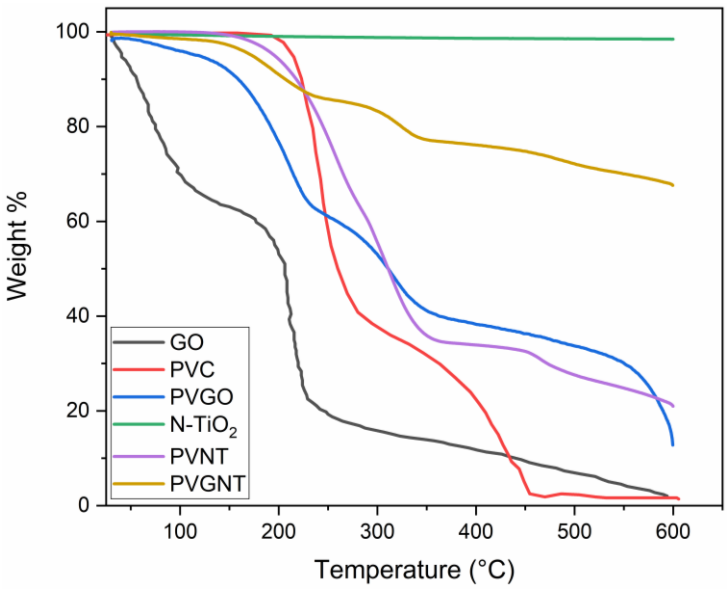


Figure 4.89 TGA of GO, PVC, PVGO, N-TiO_2, PVNT, and PVGNT.

4.6.1.6 Photoluminescence Analysis

The emission spectra of pure N-TiO_2, PVGO, PENT, and PVGNT are presented in **Figure 4.90.** This study demonstrates that adding C of PVC matrix to N-TiO_2 causes the creation of an acceptor impurity energy level above the valence band. The presence of C 2p bands in N-TiO_2 reduces the energy gap between the valence and conduction bands. This decrease in the energy gap broadens the absorption spectrum to the visible light area [*Romero Saez et al., 2017*]. The presence of GO and N-TiO_2 in the PVC matrix can modify the PL spectra due to charge transfer and altered recombination dynamics. Specifically, GO can act as an electron trap, potentially reducing PL intensity and enhancing photocatalytic activity by delaying electron-hole recombination [*Kumar et al., 2023*].

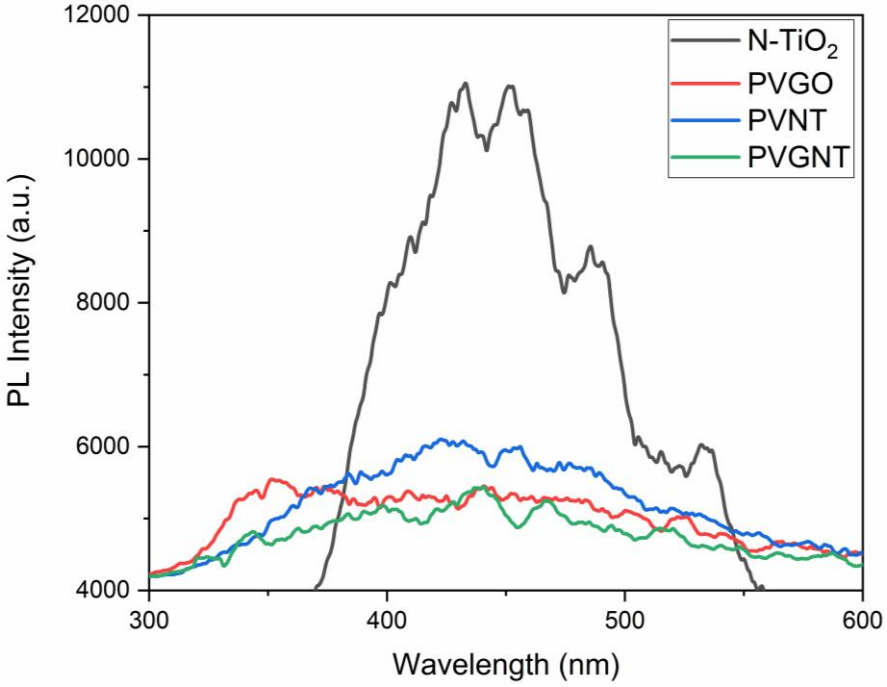


Figure 4.90 Photoluminescence emission spectra of N-TiO_2, PVGO, PVNT, and PVGNT.

4.6.1.7 Optical Bandgap Analysis

There are various ways in the literature for calculating the band gap from absorbance spectra. Here, band gap (E_g) is directly calculated from emission spectra obtained from photoluminescence measurements [*Gilic et al., 2018, Ramprasath et al., 2023*]. The band gap energy E_g is related to the wavelength (λ) of the emitted light using the **Equation 4.1**

The calculated band gap values of PVGO, PVNT, and PVGNT are given in **Table 4.19**. The band gap value for PVNT is somewhat less than that of pure N-TiO_2. The variation in band gap indicates a synergistic impact between N-TiO_2 and PVC due to intermolecular interaction [*Romero Saez et al., 2017*]. Furthermore, the inclusion of GO into nanocomposites can result in the production of localized electronic states, mostly due to disruptions in the material's electrical structure produced by the presence of GO and functional groups that reduce the band gap of PVGO and PVGNT [*Hurayra–Lizu et al., 2021*].

Table 4.19 Optical band gap values of GO, N-TiO_2, PVGO, PVNT, and PVGNT.

S. No.	Material	Optical band gap (E_g) (eV)
1.	GO	2.2
2.	N-TiO_2	2.9
3.	PVGO	2.80
4.	PVNT	2.9
5.	PVGNT	2.82

4.6.2 Removal study of MB using Synthesized Materials under different Conditions

To evaluate the removal efficiency of PVGO, PVNT and PVGNT nanocomposites, a series of experiments were performed under tungsten bulb light and without light under dark. For the removal of MB using prepared nanocomposites at pH 4, pH 7 and pH 10 have been studied. Furthermore, effect of pH, light source and effect of time is also discussed. The concentration change in MB and RB were measured at λ_{max} 664nm and 554nm, respectively.

To evaluate the role of adsorption on removal of MB, an adsorption experiment was conducted using synthesized nanocomposites under dark. Under these experimental conditions, PVGO, PVNT and PVGNT nanocomposites achieved the highest MB removal of 26.1%, 13.8%, and 98.9% as shown in **Figure 4.91(b)**. PVGNT achieved the highest PS-NPs removal showing excellent adsorption performance. The PVGNT nanocomposites exhibit a higher adsorption capacity for MB compared to PVGO

because of synergistic effect of the three components. N-TiO_2 nanoparticles offer enhanced adsorption sites [*Scrimieri et al., 2020*] and potentially photocatalytic activity, while GO provides a large surface area and π-π interaction sites for MB. The combination maximizes the interactions with MB molecules, leading to increased adsorption [*Kocijan et al., 2021, Kusiak-Nejman et al., 2020*]. The removal of MB decreased with PVNT nanocomposites, which may be due to a decrease in the accessibility of N-TiO_2 due to the PVC layer [*Panchenko et al., 2023*].

Moreover, similar experimental conditions were used for photocatalytic study of removal of MB under tungsten bulb light (**Figure 4.91(a)**). Under these conditions, PVGO, PVNT and PVGNT nanocomposites shown greater removal of MB than under dark conditions; PVGNT reached the highest percentage removal of 99.5% under tungsten light at pH 10. Whereas PVGO and PVNT shown percentage removal 97.4% and 30.5% under similar conditions. It could be said that photocatalytic degradation would also concurrently occur with adsorption as light interacts with the material. It is clear from the results that the decomposition of MB increased significantly under TL irradiation for PVGO and PVNT nanocomposites. The mechanism is discussed in **Section 4.5.3.5**

4.6.2.1 Effect of pH on the Removal of MB

The effects of pH on MB removal were investigated at pH levels 4, 7, and 10 as shown in **Figure 4.91(b)** showing that as pH increases from 4 to 10, the removal percentage of MB for PVGO and PVGNT increases. The PZC for PVGO, PVNT, and PVGNT is approximately pH 3.5, 6.1, and 4.1 respectively, indicating that at pH values lower than this, the surface charge of nanocomposite is positive (pH < PZC) and, the surface charge turns negative as the pH rises above PZC [*Nguyen et al., 2020*]. According to the results, removal efficiency of PVGO and PVGNT for the removal of positively charged MB increases as pH increases (from 4 to 10) from their corresponding PZC because surfaces of these nanocomposites become negatively charged above PZC. This indicates that adsorption is dependent on electrostatic interactions [*Chakhtouna et al., 2021*]. For PVGO and PVGNT the adsorption is slightly increased at higher pH values may be due to the deprotonation of carboxylic groups of graphene oxide that can participate in MB removal [*El-Sharkaway et al., 2020*]. The reduced removal of methylene blue MB when

using PVNT nanocomposite is likely due to the PVC layer hindering the accessibility of the N-TiO_2 to the MB molecules. This could be due to the PVC layer physically blocking the active sites on the N-TiO_2 or affecting the nanocomposite's overall interactions with MB in solution [*Cazan et al., 2021*]. This means the PVC layer is acting as a barrier, preventing the MB from reaching the active sites on the N-TiO_2 surface where degradation occurs [*Charitha et al., 2021*].

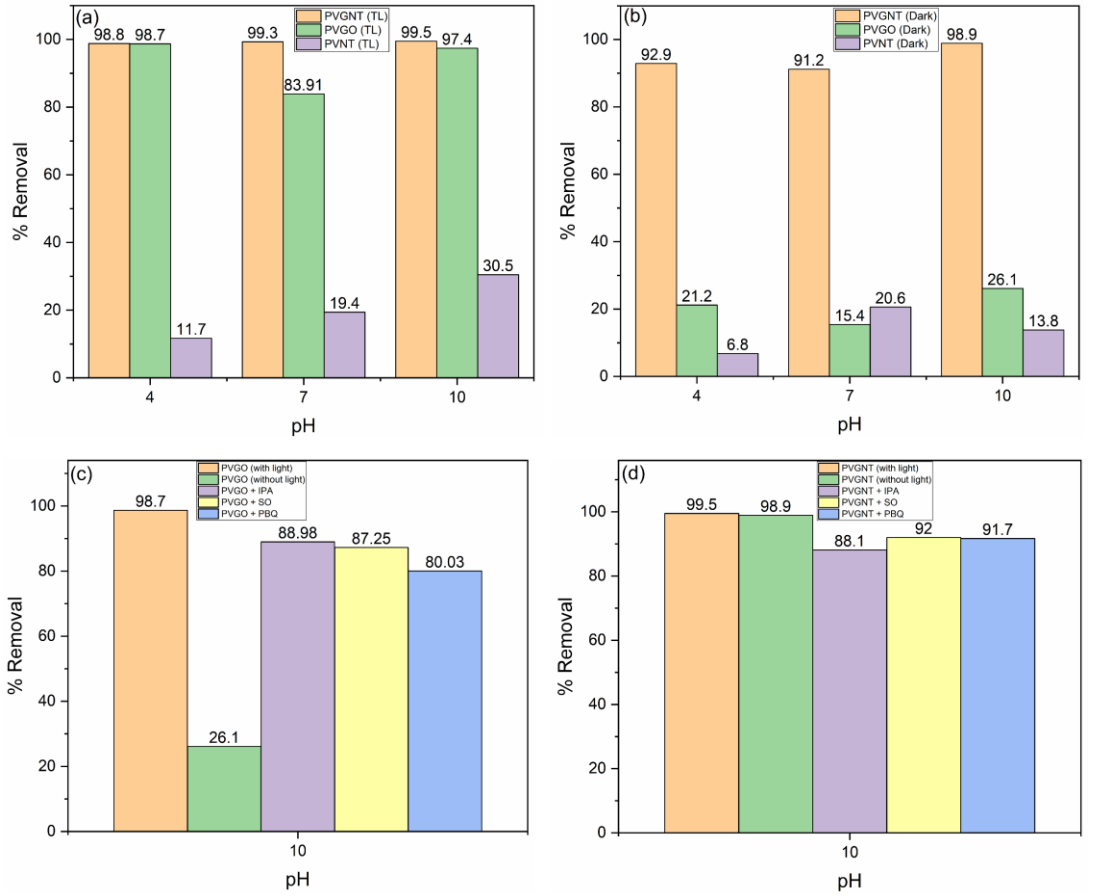
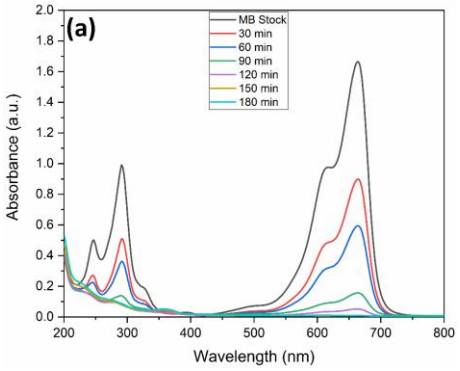


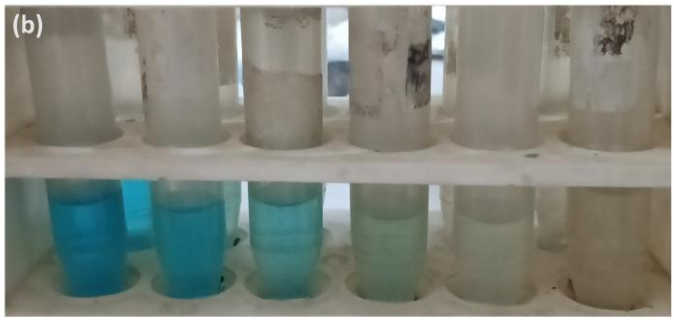
Figure 4.91 Comparison of % removal MB with PVGO, PVNT, and PVGNT under (a) tungsten bulb light (b) dark; comparison of % removal MB under tungsten bulb light at pH 4 using (c) PVGO + quenchers isopropyl alcohol, sodium oxalate, and parabenzoquinone (d) PVGNT + quenchers isopropyl alcohol, sodium oxalate, and parabenzoquinone.

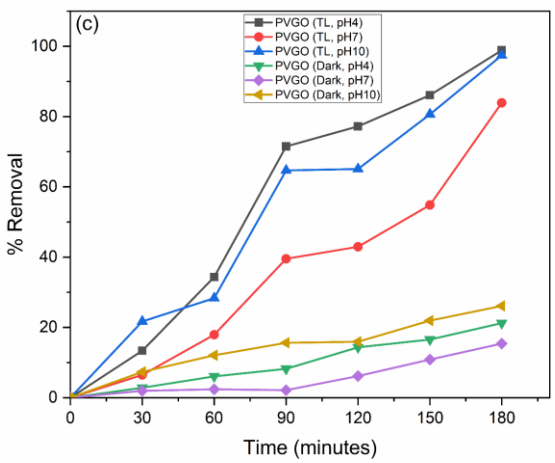
4.6.2.2 Effect of Time on the Removal of MB

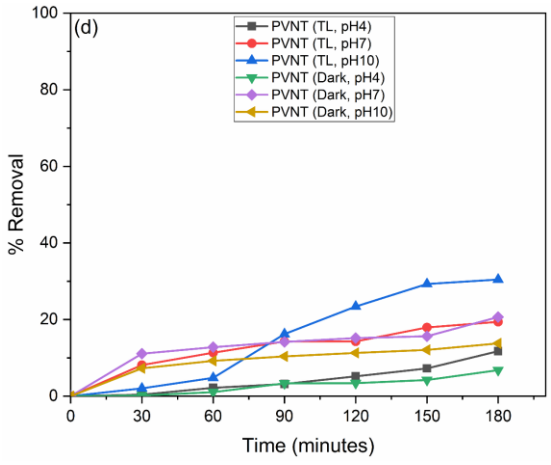
Figures 4.92(c-e) illustrate the effect of contact time on percentage removal of MB for PVGO, PVNT and PVGNT. As is apparent from the figures approximately 99.5% of MB was removed within 180 min using PEGNT at pH 10 under tungsten bulb light, but for PVGO and PVNT after 180 min, the percentage under removal of MB similar was

97.4% and 30.5%, respectively. After the removal of MB, the solution turns colourless and real-life image of MB solution in the time interval of 30–180 min with PVGNT at pH 10 is shown in **Figure 4.92(b)** and **Figure 4.92(a)** is showing its UV absorption spectra, showing that % removal increases with increase in reaction time. This is because the catalyst's surface receives more contact time, which increases removal activity.









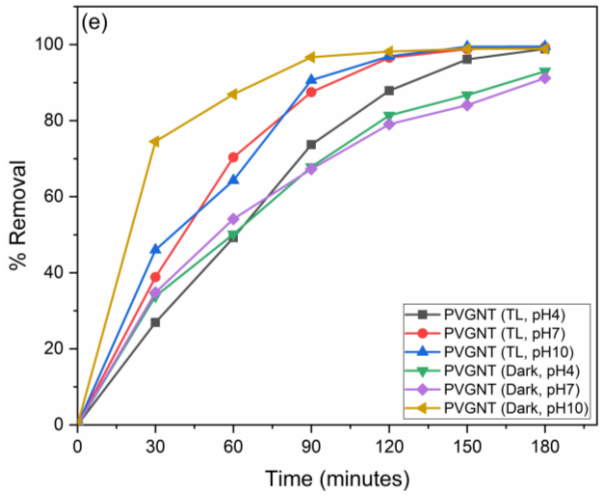


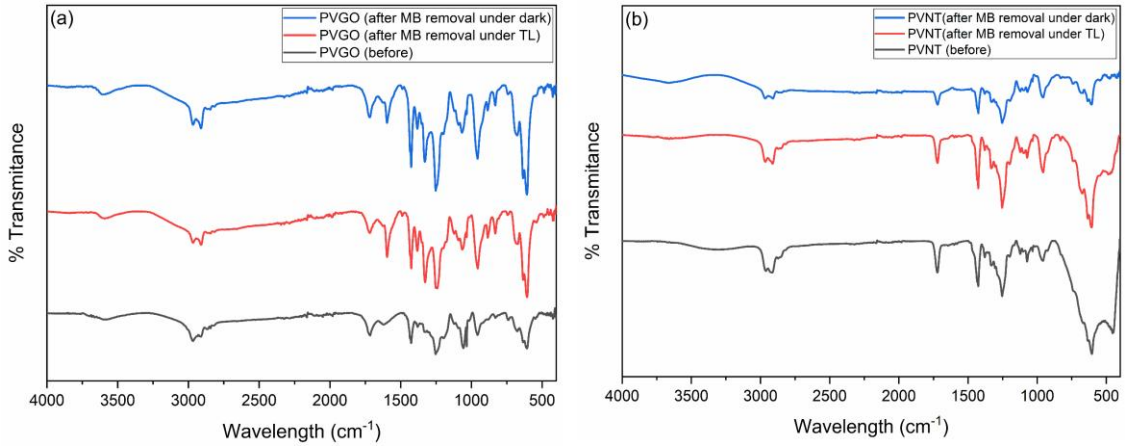
Figure 4.92 (a) UV absorption spectra of MB removal with PVGNT at pH 10 (b) real-life image of MB solution in the time interval of 30–180 min at pH 10; MB removal from water treated over a 30 to 180-minute time period under TL and dark with (c) PVGO (d) PVNT (e) PVGNT.

4.6.2.3 Effect of Scavengers

To study the mechanism of the photocatalytic reaction, isopropyl alcohol (IPA), sodium oxalate (SO), and parabenzoquinone (PBQ) were chosen as scavengers of $^{\bullet}OH$, h^{+}, and $^{\bullet}O_2^{-}$, respectively. **Figure 4.91 (c-d)** illustrates that the degradation rates of MB using PEGO and PVGNT decrease upon the addition of IPA, PBQ, and SO, and the results indicate that all three reactive radical species (RRS) $^{\bullet}OH$, h^{+}, and $^{\bullet}O_2^{-}$, play important roles in the photocatalytic reaction of MB.

4.6.2.4 Analysis of PVC-based Nanocomposites After Removal of MB

The FTIR spectra before and after removal of MB using PVGO, PVNT and PVGNT are shown in **Figure 4.93 (a), Figure 4.93 (b) and Figure 4.93 (c)**, respectively showing the remarkable change of the intensities of infrared bands of PVGO. Furthermore, FTIR spectra of both PVGO and PVGNT show some additional peaks, and PVGNT shows a change in the positions of a few peaks. Shifts in these peaks and the appearance of new peaks can indicate interactions of MB with PVGO and PVGNT after adsorption or degradation [*Ainane et al., 2014*].



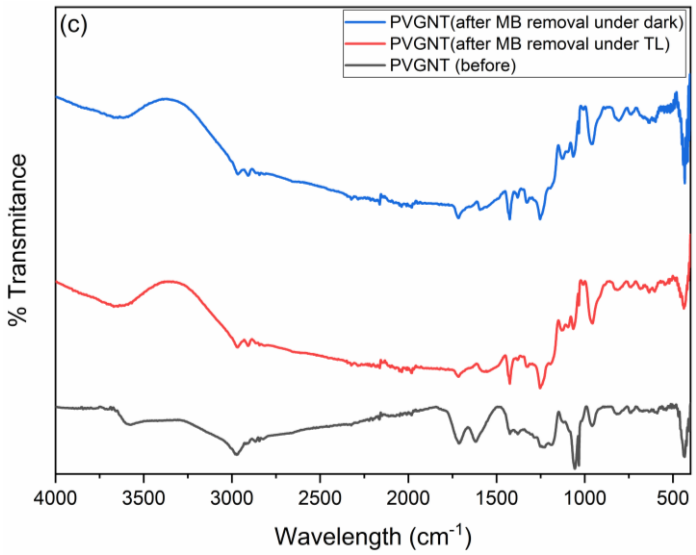


Figure 4.93 FTIR spectra of removal of MB before and after reaction with and without light with (a) PVGO (b) PVNT (c) PVGNT.

4.6.3 Removal Study of RB using Synthesized Materials under different Conditions

To evaluate the removal efficiency of PVGO, PVNT and PVGNT nanocomposites, a series of experiments were performed under tungsten bulb light and without light under dark. For the removal of RB using prepared nanocomposites at pH 4, pH 7 and pH 10 have been studied. Furthermore, effect of pH, light source and effect of time is also discussed. The concentration change in MB and RB were measured at λ_{max} 664nm and 554nm, respectively.

To evaluate the role of adsorption on removal of RB, an adsorption experiment was conducted using synthesized nanocomposites under dark. Under these experimental conditions, PVGO, PVNT and PVGNT nanocomposites achieved the highest RB removal of 1.4%, 0.9%, and 57.3% as shown in **Figure 4.94(b)**. PVGNT achieved the highest RB removal showing excellent adsorption performance. The PVGNT nanocomposite exhibit a higher adsorption capacity for RB compared to PVGO because of synergistic effect of the three components. The addition of N-TiO_2 to the PVGO composite provides more active sites for RB molecules to attach [*Scrimieri et al., 2020*] and potentially photocatalytic activity, while GO provides a large surface area and π-π interaction sites for RB. The combination maximizes the interactions with RB molecules, leading to increased adsorption [*Kocijan et al., 2021, Kusiak-Nejman et al.,*

2020]. The removal of RB is almost negligible with PVNT nanocomposite, which may be due to a decrease in the accessibility of N-TiO_2 due to the PVC matrix [*Panchenko et al., 2023*].

Moreover, similar experimental conditions were used for photocatalytic study of removal of RB under tungsten bulb light (**Figure 4.94a)**). Under these conditions, PVGO, PVNT and PVGNT nanocomposites shown greater removal of MB than under dark conditions; PVGNT reached the highest percentage removal of 95.2% under tungsten light at pH 4. Whereas PVGO and PVNT shown percentage removal 90.9% and 23.2% under similar conditions. It could be said that photocatalytic degradation would also concurrently occur with adsorption as light interacts with the material. It is clear from the results that the decomposition of RB increased significantly under TL irradiation for PVGO and PVNT nanocomposites. The mechanism is discussed in **Section 4.5.3.5**

4.6.3.1 Effect of pH on the Removal of RB

The PZC for PVGO, PVNT, and PVGNT is approximately pH 3.5, 6.1, and 4.1 respectively, indicating that at pH values lower than this, the surface charge of nanocomposite is positive (pH < PZC) and, the surface charge turns negative as the pH rises above PZC [*Nguyen et al., 2020*]. According to the results (**Figures 4.94(a) 4.94(b)**), PVGO composite might show limited adsorption of RB dye at all pH, but its ability to enhance charge separation and transfer result in a significant increase in photocatalytic degradation efficiency [*Prakash et al., 2023*]. Furthermore, removal efficiency of PVGNT for the removal of positively charged RB is more at pH 4 because surfaces of these nanocomposites become negatively charged above PZC. This indicates that adsorption is dependent on electrostatic interactions [*Chakhtouna et al., 2021*]. But a small decrease in the percentage removal was observed from 4 to 10 using PVGNT. The electrostatic interaction between the RB molecules and PEGNT is responsible for the high removal efficiency and low pH. On the one hand, the acidic oxygen groups on the PVGNT surface deprotonate and become negatively charged as the pH of the solution rises above PZC. In contrast, RB is found as cations and zwitterions in polar solvents. The carboxyl group of the RB undergoes deprotonation when the pH of the solution rises beyond 3.7 (the pK_a of RB), causing the cationic form

to change into a zwitterionic form. Moreover, at higher pH, the interaction between zwitterionic forms (electrostatic interaction between carboxyl and xanthene groups of monomers) of RB in water creates larger molecules. Due to this, the entry of aggregated zwitterionic form of RB into the adsorbent pores is impeded; consequently, the adsorption of RB is decreased [*Xiao et al., 2020, Meena et al., 2024*]. The reduced removal of RB when using PVNT nanocomposite is likely due to the PE layer hindering the accessibility of the N-TiO_2 to the RB molecules. This could be due to the PVC layer physically blocking the active sites on the N-TiO_2 or affecting the nanocomposite's overall interactions with RB in solution [*Cazan et al., 2021*]. This means the PVC layer is acting as a barrier, preventing the RB from reaching the active sites on the N-TiO_2 surface where degradation occurs [*Charitha et al., 2021*].

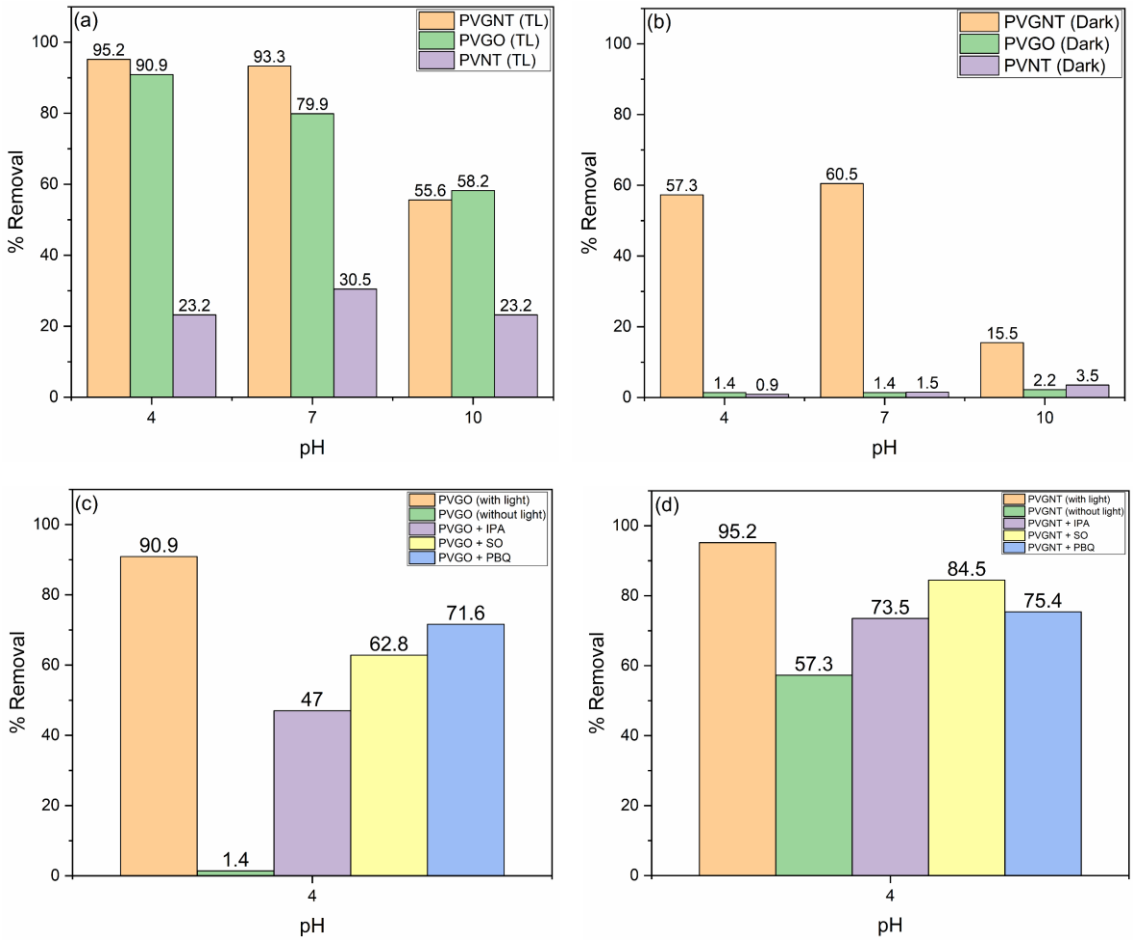
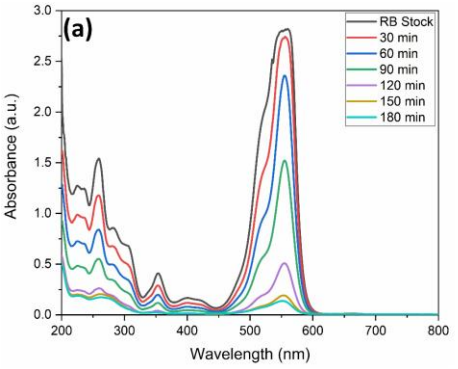
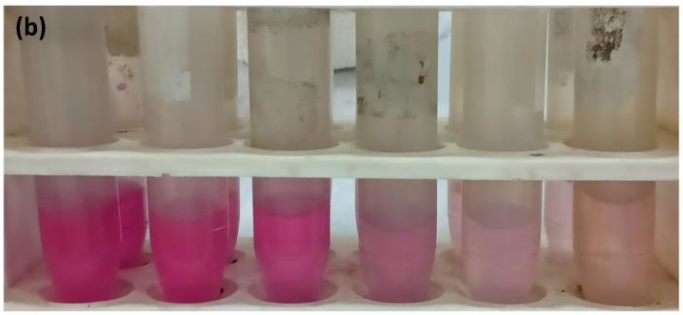


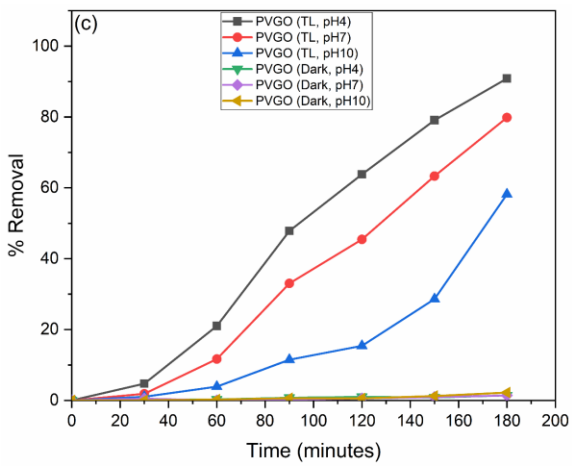
Figure 4.94 Comparison of % removal RB with PVGO, PVNT, and PVGNT under (a) tungsten bulb light (b) dark; comparison of % removal RB under tungsten bulb light at pH 4 using (c) PVGO + quenchers isopropyl alcohol, sodium oxalate, and parabenzoquinone (d) PVGNT + quenchers isopropyl alcohol, sodium oxalate, and parabenzoquinone.

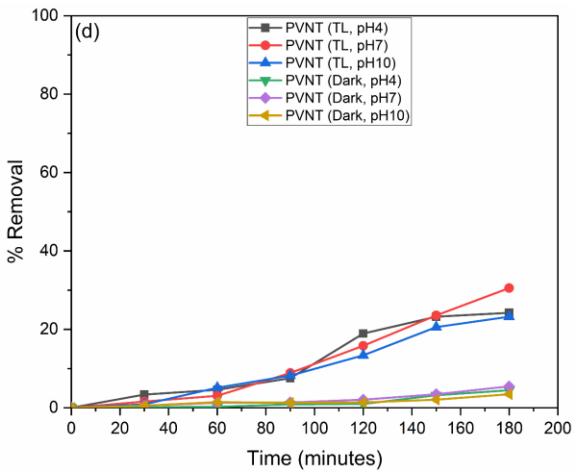
4.6.3.2 Effect of Time on the Removal of RB

Figure 4.95 (c-e) illustrates the effect of contact time on percentage removal of RB for PVGO, PVNT and PVGNT. As is apparent from the figures approximately 95.2% of RB was removed within 180 min using PVGNT at pH 4 under tungsten bulb light, but for PVGO and PVNT after 180 min, the percentage under removal of RB similar was 90.9% and 23.2%, respectively. After the removal of RB, the solution turns colourless and real-life image of RB solution in the time interval of 30–180 min with PVGNT at pH 4 is shown in **Figure 4.95(b)** and **Figure 4.95(a)** is showing its UV absorption spectra, showing that % removal increases with increase in reaction time. This is because the catalyst's surface receives more contact time, which increases removal activity.









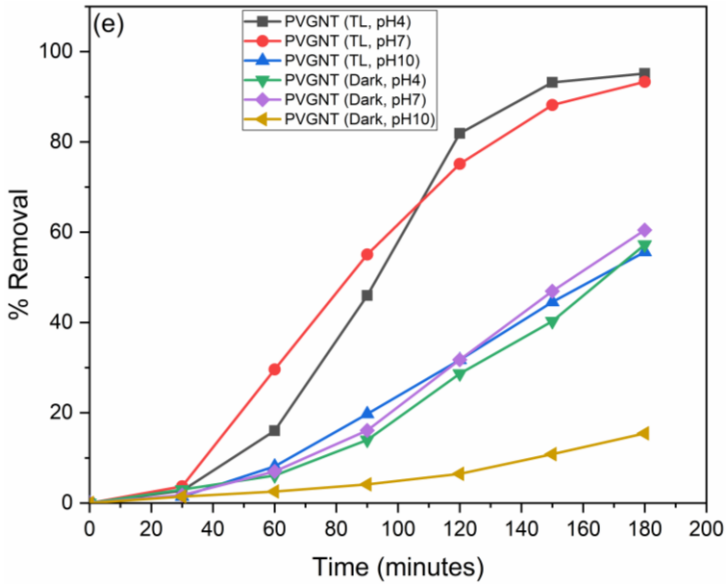


Figure 4.95 (a) UV absorption spectra of RB removal with PVGNT at pH 4 (b) real-life image of RB solution in the time interval of 30–180min at pH 4; RB removal from water treated over a 30- to 180-minute time period under TL and dark with (c) PVGO (d) PVNT (e) PVGNT.

4.6.3.3 Effect of Scavengers

To study the mechanism of the photocatalytic reaction, isopropyl alcohol (IPA), sodium oxalate (SO), and parabenzoquinone (PBQ) were chosen as scavengers of $^{\bullet}OH$, h^{+}, and $^{\bullet}O_2^{-}$, respectively. **Figure 4.94 (c-d)** illustrates that the degradation rates of RB using PVGO and PVGNT decrease upon the addition of IPA, PBQ, and SO, and the results indicate that all three reactive radical species (RRS) $^{\bullet}OH$, h^{+}, and $^{\bullet}O_2^{-}$, play important roles in the photocatalytic reaction of RB.

4.6.3.4 Analysis of PVC-based Nanocomposites After Removal of RB

The FTIR spectra before and after removal of RB using PVGO, PVNT and PVGNT are shown in **Figure 4.96 (a), Figure 4.96 (b) and Figure 4.96 (c)**, respectively showing the remarkable change of the intensities of infrared bands of PVGO. Furthermore, FTIR spectra of both PVGO and PVGNT show some additional peaks, and PVGNT shows a change in the positions of a few peaks. Shifts in these peaks and the appearance of new peaks can indicate interactions of RB with PVGO and PVGNT after adsorption or degradation [*Ainane et al., 2014*].

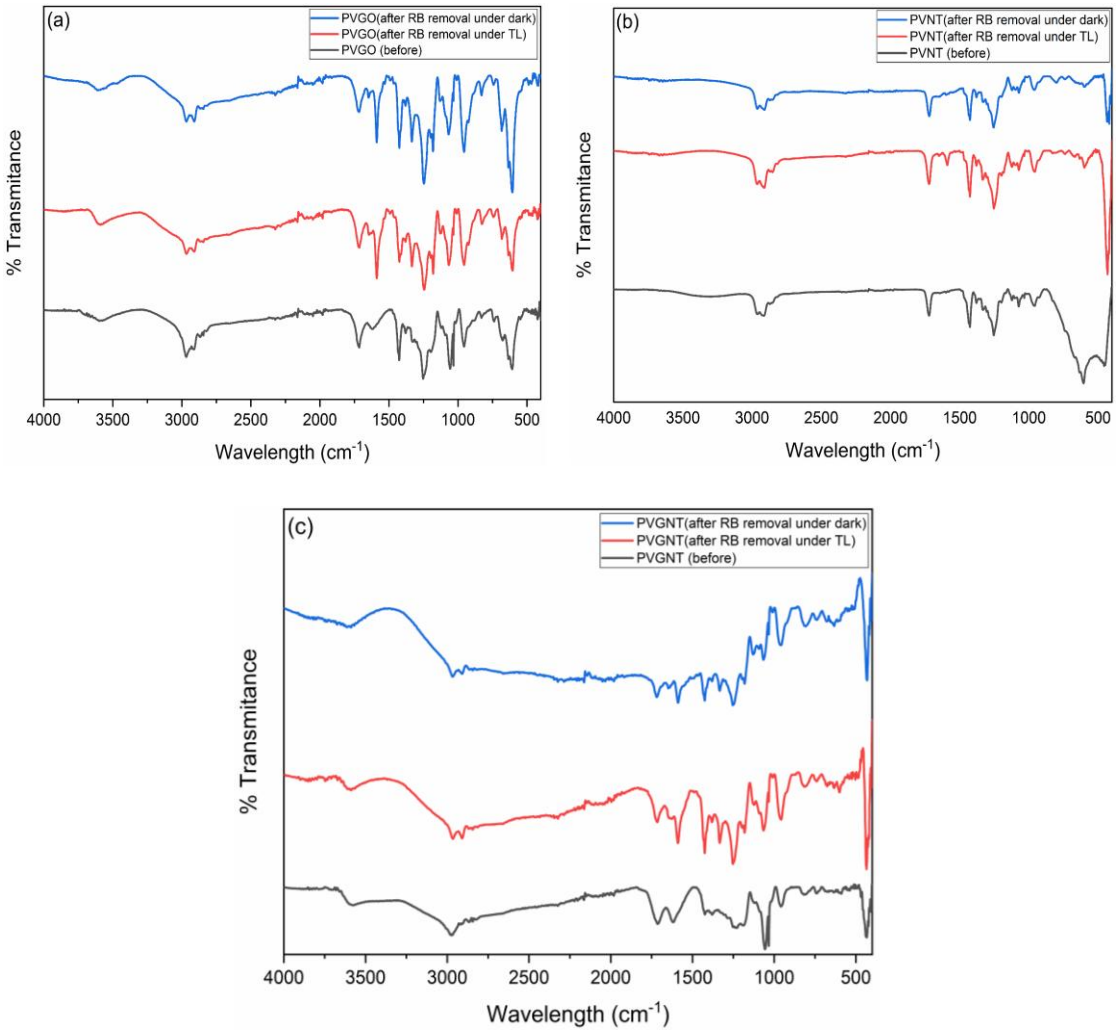


Figure 4.96 FTIR spectra of removal of RB before and after reaction with and without light with (a) PVGO (b) PVNT (c) PVGNT.

4.6.3.5 Mechanism of MB and RB Removal using Synthesized PVC based **Nanocomposites**

The mechanism is discussed in **Section 4.5.3.5**.

Chapter – 5 Conclusion and Future Perspective

5.1 Summary and Conclusion

The research work on preparation of three different nitrogen doped metal oxides were successfully synthesized via sol-gel method and were named as N-TiO_2, N-SnO_2 and N-ZrO_2. Furthermore, carbonaceous materials (graphene oxide and corncob based activated carbon) and nitrogen doped metal oxides-based nanocomposite materials in varying weight ratios of carbonaceous materials: metal oxide (1:3, 1:1, 3:1) such as GO/N-TiO_2 (GT13, GT11, GT31), CCAC/N-TiO_2 (CT13, CT11, CT31), GO/SnO_2 (GNSO13, GNSO11, GNSO31) were synthesized by one-step colloidal blending process and facile wet impregnation methods. The formation, structure, phase, surface morphology, size, shape, thermal stability, optical study and removal studies of synthesized metal oxide nanoparticles and carbonaceous materials/nitrogen doped metal oxide nanocomposites have been characterized by using different characterization techniques such as: XRD, FTIR, FESEM, EDX, XPS, TGA, PL and UV-VIS analytical techniques. The synthesized nanoparticles and nanocomposites were used as adsorbents and photocatalysts for adsorptive removal and photocatalytic degradation of polyvinylchloride (PVC) and polystyrene (PS). Moreover, plastic (polyethylene (PE) and polyvinylchloride (PVC)), graphene oxide (GO) and N-TiO_2 based nanocomposites such as PE/GO, PE/N-TiO_2, PE/GO/N-TiO_2, PVC/GO, PVC/N-TiO_2 and PVC/GO/N-TiO_2 were synthesized, characterized and used for the adsorptive removal and photocatalytic degradation of toxic organic dyes. The cationic dyes having such as methylene blue (MB), and rhodamine B (RB) have been selected as model organic pollutants in this study. The following major conclusions have been drawn from this study.

Major Conclusions

- Among the three nitrogen-doped metal oxide (N-TiO_2, N-SnO_2, and N-ZrO_2) nanoparticles, N-SnO_2 was the most effective adsorbent for the removal of PVC-NPs and PS-NPs, with maximum sorption of 100% and 99.6%, respectively, at pH 4.
- The addition of GO and CCAC to N-TiO_2 improved the surface morphology of N-TiO_2 nanoparticles and produced a C-Ti-O bond by altering the N-TiO_2

lattice system, confirmed by FTIR and XPS data. This alteration aided in lattice distortions and narrowed the bandgap and reduced the electron/hole pair recombination more than the bare N-TiO_2 confirmed by the optical bandgap study and photoluminescence spectra. In addition, the formation of superoxide and hydroxyl radicals on the surfaces of composites allowed the composites to show photocatalytic degradation under visible light.

- Among all the GO/N-TiO_2 nanocomposites (GT13, GT11, and GT31) with varying weight ratios, GT13 showed an excellent removal efficiency for PVC-NPs from water under light and dark conditions. Under tungsten bulb light irradiation, GT13 exhibited more than 95% removal efficiency at pH 4, 7, and 10 with a maximum removal % of 99.2% at pH 4. GT13 also showed higher thermal stability with a total weight loss ratio of 12.8%, confirmed by TGA study.
- Similarly, out of all the CCAC/N-TiO_2 nanocomposites (CT13, CT11 and CT31) with varying weight ratio, CT13 shown an excellent removal efficiency of 94% at pH4, in contrast to the 59.9% efficiency of N-TiO_2 nanoparticles for PVC-NPs under tungsten bulb illumination.
- The reactive species were produced on the surface of GO/N-TiO_2 and CCAC/N-TiO_2 nanocomposites due to the interaction of electrons and holes with H_2O and O_2 under light radiation, confirmed by quenching experiments. These intermediates then react with PVC-NPs to produce various degradative products, which were then examined further using GCMS. After the removal experiment, the left-out nanocomposite revealed the presence of PVC on its surface, as validated by subsequent characterization with SEM, fluorescence microscopy, DLS, and FTIR, confirming the removal of PVC-NPs from water.
- The mechanism of PVC-NP removal using GT13 and CT13 composites is shown to have the synergistic effect of GO/CCAC and N-TiO_2. The GO and CCAC allowed the adsorption, while the N-TiO_2 promoted photocatalytic degradation of the PVC-NPs. This combination resulted in contact between the composite material and PVC-NPs, leading to relatively efficient removal. PVC-NPs were adsorbed over the surface of the composite through various interactions like hydrophobic interactions, π-π interactions, electrostatic

attractions, halogen bonding, and hydrogen bonding. The increased adsorption led to an increase in reaction sites, and the photocatalytic removal of PVC-NPs was increased.

- Maximum percentage removal of PS-NPs was 32.2% and 30.8% using GT13 and CT31 nanocomposites, respectively. Whereas bare N-TiO_2 exhibited 98.7% of PS-NP removal, which was almost similar to removal under dark conditions, suggested that the material is acting as an adsorbent rather than a photocatalyst. PS might be resistant to degradation due to its stable aromatic rings, which did not participate in chemical reactions of photocatalytic degradation.
- Furthermore, among PE- and PVC-supported nanocomposites, PE/GO, PE/GO/N-TiO_2, PVC/GO, and PVC/GO/N-TiO_2 exhibited excellent results for removal of MB and RB dyes under light and dark conditions.
- PE and PVC matrix provided robust support for the GO and N-TiO_2 incorporated in the composite, while GO and N-TiO_2 enhanced the light absorption and charge separation within the composite and produced reactive oxygen species (ROS), which then participate in photochemical degradation of dyes.

5.2 Future perspectives

The majority of photocatalysis research is still exploratory, and there are a number of important areas that need more study:

- This research focused on the adsorption and degradation of common plastics such as PVC and PS. As plastic pollution increases, it's crucial to investigate and explore various plastic categories thoroughly.
- Further research is needed to understand the degradation mechanisms of common plastic types, which will aid in the practical implementation of photocatalytic technology for managing plastic pollution.
- Different photocatalyst categories have unique strengths and limitations. Catalysts can perform well at particular light wavelengths but have lower efficiency under other conditions. Selecting and deploying catalysts requires rigorous evaluation to achieve optimal performance in specific environments and conditions. Currently, only a few photocatalysts have been studied for

plastic degradation, and many semiconductors remain unexplored. Further research into photocatalysts, particularly new semiconductors, is necessary to enhance degrading efficiency.

Bibliography

[1] Abdel-Baset, T., Elzayat, M., & Mahrous, S. (2016). Characterization and optical and dielectric properties of polyvinyl chloride/silica nanocomposites films. *International Journal of Polymer Science*, *2016*(1), 1707018. https://doi.org/10.1155/2016/1707018

[2] Abdu, M., Worku, A., Babaee, S., Diale, P., Msagati, T. A., & Nure, J. F. (2025). The development of TiO_2-biochar composite material for photodegradation of basic blue 41 and erichrome black T azo dyes from water. *Surfaces and Interfaces, 62*, 106156. https://doi.org/10.1016/j.surfin.2025.106156

[3] Abdullah, M., Iqbal, J., Rehman, M. S. U., Khalid, U., Mateen, F., Arshad, S. N., Al-Sehemi, A.G., Algarni, H., Al-Hartomy, O.A. & Fazal, T. (2023). Removal of ceftriaxone sodium antibiotic from pharmaceutical wastewater using an activated carbon based TiO_2 composite: Adsorption and photocatalytic degradation evaluation. *Chemosphere, 317*, 137834. https://doi.org/10.1016/j.chemosphere.2023.137834

[4] Abid, N., Khan, A. M., Shujait, S., Chaudhary, K., Ikram, M., Imran, M., Haider, J., Khan, M., Khan, Q. & Maqbool, M. (2022). Synthesis of nanomaterials using various top-down and bottom-up approaches, influencing factors, advantages, and disadvantages: A review. *Advances in colloid and interface science*, *300*, 102597. https://doi.org/10.1016/j.cis.2021.102597

[5] Adamopoulos, N. D., Tsierkezos, N. G., Ntziouni, A., Zhang, F., Terrones, M., & Kordatos, K. V. (2023). Synthesis, characterization, and electrochemical performance of reduced graphene oxide decorated with Ag, ZnO, and AgZnO nanoparticles. *Carbon*, *213*, 118178. https://doi.org/10.1016/j.carbon.2023.118178

[6] Adán, C., Carbajo, J., Bahamonde, A., & Martínez-Arias, A. (2009). Phenol photodegradation with oxygen and hydrogen peroxide over TiO_2 and Fe-doped TiO_2. *Catalysis Today*, *143*(3-4), 247-252. https://doi.org/10.1016/j.cattod.2008.10.003

[7] Afridi, S. K., & Umar, K. (2025). Comprehensive Exploration of Photocatalytic Degradation: Eradication of Various Dye Classes Using Elemental-Doped and Graphene-Interfaced Semiconductor Nanocomposites in a Sustainable Framework. *Catalysis Letters*, *155*(5), 167. https://doi.org/10.1007/s10562-025-05000-0

[8] Aimable, A., Buscaglia, M. T., Buscaglia, V., & Bowen, P. (2010). Polymer-assisted precipitation of ZnO nanoparticles with narrow particle size distribution. Journal of the *European Ceramic Society, 30*(2), 591-598. https://doi.org/10.1016/j.jeurceramsoc.2009.06.010

[9] Ainane, T., Khammour, F., Talbi, M., & Elkouali, M. H. (2014). A novel bio-adsorbent of mint waste for dyes remediation in aqueous environments: study

and modeling of isotherms for removal of methylene blue. *Oriental Journal of Chemistry*, *30*(3), 1183-1189.
http://dx.doi.org/10.13005/ojc/300332

[10] Aïnouche, L., Hamadou, L., Kadri, A., Benbrahim, N., & Bradai, D. (2016). Ti^{3+} states induced band gap reduction and enhanced visible light absorption of TiO_2 nanotube arrays: Effect of the surface solid fraction factor. *Solar Energy Materials and Solar Cells*, *151*, 179-190.
https://doi.org/10.1016/j.solmat.2016.03.013

[11] Aksoy, E., Demir, N., & Varlikli, C. (2018). White LED light production using dibromoperylene derivatives in down conversion of energy. *Canadian Journal of Physics, 96*(7), 734-739.
https://doi.org/10.1139/cjp-2017-0752

[12] Al-Madanat, O., AlSalka, Y., Ramadan, W., & Bahnemann, D. W. (2021). TiO_2 photocatalysis for the transformation of aromatic water pollutants into fuels. *Catalysts*, *11*(3), 317.
https://doi.org/10.3390/catal11030317

[13] Al-Munayzil, T., Al-Ahmady, K., & Mhemid, R. K. S. (2025). Photocatalytic degradation of micro-polyvinyl chloride using green-synthesized iron nanoparticles. *Journal of Ecological Engineering, 26*(8), 352-366.
https://doi.org/10.12911/22998993/204120

[14] Alkhalifa, R. A., Albadri, A. E., Ali, R., Alluhayb, A. H., Younis, A. M., & Saleh, S. M. (2025). Sustainable Synthesis of Zirconium Dioxide (ZrO2) Nanoparticles Utilizing Asphodelus fistulosus Extract for Congo Red Degradation. Catalysts, 15(2), 123.
https://doi.org/10.3390/catal15020123

[15] Allé, P. H., Garcia-Muñoz, P., Adouby, K., Keller, N., & Robert, D. (2021). Efficient photocatalytic mineralization of polymethylmethacrylate and polystyrene nanoplastics by TiO_2/β-SiC alveolar foams. *Environmental Chemistry Letters, 19*(2), 1803-1808.
https://doi.org/10.1007/s10311-020-01099-2

[16] Alom, N., Roy, T., Sarkar, T., Rasel, M., Hossain, M. S., & Jamal, M. (2024). Removal of microplastics from aqueous media using activated jute stick charcoal. *Heliyon, 10*(18).
https://doi.org/10.1016/j.heliyon.2024.e37380

[17] Alshehri, A. A., & Malik, M. A. (2019). Biogenic fabrication of ZnO nanoparticles using Trigonella foenum-graecum (Fenugreek) for proficient photocatalytic degradation of methylene blue under UV irradiation. *Journal of Materials Science: Materials in Electronics*, *30*(17), 16156-16173.
https://doi.org/10.1007/s10854-019-01985-8

[18] Alshoaibi, A., Hussain, F., Mohsin, F., Alnaim, N., & Almulhem, N. (2023). Different concentrations of Ti^{4+} as a donor and electronic properties of $Bi_{2-x}Ti_xO_3$. *Frontiers in Materials, 10*, 1004889.
https://doi.org/10.3389/fmats.2023.1004889

[19] Ambasta, V. K., Ghosh, S., & Sen, A. (2025). Exploring the electronic properties of doped zirconia for enhanced optoelectronic applications: A quantum chemical approach. *Journal of Physics and Chemistry of Solids*, *197*, 112412. https://doi.org/10.1016/j.jpcs.2024.112412

[20] Ansari, A. S., Azzahra, G., Nugroho, F. G., Mujtaba, M. M., & Ahmed, A. T. A. (2025). Oxides and metal oxide/carbon hybrid materials for efficient photocatalytic organic pollutant removal. *Catalysts*, *15*(2), 134. https://doi.org/10.3390/catal15020134

[21] Ao, W., Qu, J., Yu, H., Liu, Y., Liu, C., Fu, J., Dai, J., Bi, X., Yuan, Y. & Jin, Y. (2022). TiO_2/activated carbon synthesized by microwave-assisted heating for tetracycline photodegradation. *Environmental Research, 214*, 113837. https://doi.org/10.1016/j.envres.2022.113837

[22] Areti, H. A., Jabesa, A., Muleta, M. D., & Emana, A. N. (2024). Adsorptive performances and valorization of green synthesized biochar–based activated carbon from banana peel and corn cob composites for the abatement of Cr (VI) from synthetic solutions: Parameters, isotherms, and remediation studies. *Heliyon, 10*(13). https://doi.org/10.1016/j.heliyon.2024.e33811

[23] Arossa, S., Martin, C., Rossbach, S., & Duarte, C. M. (2019). Microplastic removal by Red Sea giant clam (Tridacna maxima). *Environmental pollution*, *252*, 1257-1266. https://doi.org/10.1016/j.envpol.2019.05.149

[24] Asahi, R., Morikawa, T., Ohwaki, T., Aoki, K., & Taga, Y. (2001). Visible-light photocatalysis in nitrogen-doped titanium oxides. *science*, *293*(5528), 269-271. https://doi.org/10.1126/science.1061051

[25] Asiltürk, M., Sayılkan, F., & Arpaç, E. (2009). Effect of Fe^{3+} ion doping to TiO_2 on the photocatalytic degradation of Malachite Green dye under UV and vis-irradiation. Journal of Photochemistry and Photobiology A: Chemistry, 203(1), 64-71. https://doi.org/10.1016/j.jphotochem.2008.12.021

[26] Aslam, M., Mahmood, T., Naeem, A., & Ali, R. (2021). Investigation of HDTMA mediated sol gel synthesis of N-doped SnO2 nanoparticles: studies of their electrical and optical properties. *Materials Technology*, *36*(3), 169-178. https://doi.org/10.1080/10667857.2020.1736851

[27] Awfa, D., Ateia, M., Fujii, M., Johnson, M. S., & Yoshimura, C. (2018). Photodegradation of pharmaceuticals and personal care products in water treatment using carbonaceous-TiO_2 composites: A critical review of recent literature. *Water research, 142*, 26-45. https://doi.org/10.1016/j.watres.2018.05.036\

[28] Azim, M. B., Jani, M., Qadir, M., Hasanuzzaman, M., Gafur, M., Gulshan, F., & Firoz, S. (2021). GO-SnO_2 nanocomposite for photodegradation of methyl orange under direct sunlight irradiation and mechanism insight. *Department of Materials and Metallurgical Engineering, BUET, Dhaka, Bangladesh*.

[29] Babuji, P., Thirumalaisamy, S., Duraisamy, K., & Periyasamy, G. (2023). Human health risks due to exposure to water pollution: a review. *Water*, *15*(14), 2532. https://doi.org/10.3390/w15142532

[30] Bakhshian, S., & Sahimi, M. (2017). Adsorption-induced swelling of porous media. International *Journal of Greenhouse Gas Control, 57*, 1-13. https://doi.org/10.1016/j.ijggc.2016.12.011

[31] Bansal, A., Kumar, A., Kumar, P., Bojja, S., Chatterjee, A. K., Ray, S. S., & Jain, S. L. (2015). Visible light-induced surface initiated atom transfer radical polymerization of methyl methacrylate on titania/reduced graphene oxide nanocomposite. *RSC Advances, 5*(27), 21189-21196. https://doi.org/10.1039/C4RA15615C

[32] Bartáček, J., Drabina, P., Váňa, J., & Sedlák, M. (2019). Recoverable polystyrene-supported catalysts for Sharpless allylic alcohols epoxidations. *Reactive and Functional Polymers*, *137*, 123-132. https://doi.org/10.1016/j.reactfunctpolym.2019.01.009

[33] Basahel, S. N., Ali, T. T., Mokhtar, M., & Narasimharao, K. (2015). Influence of crystal structure of nanosized ZrO_2 on photocatalytic degradation of methyl orange. Nanoscale research letters, 10(1), 73. https://doi.org/10.1186/s11671-015-0780-z

[34] Bashir, M., Ahanger, M. A., & Gani, K. M. (2024). Investigations on adsorptive removal of PVC microplastics from aqueous solutions using Pinus roxburghii–derived biochar. *Environmental Science and Pollution Research, 31*(49), 59416-59429. https://doi.org/10.1007/s11356-024-35166-w

[35] Batool, A., & Valiyaveettil, S. (2020). Coprecipitation-an efficient method for removal of polymer nanoparticles from water. *ACS Sustainable Chemistry & Engineering, 8*(35), 13481-13487. https://doi.org/10.1021/acssuschemeng.0c04511

[36] Bedia, J., Muelas-Ramos, V., Peñas-Garzón, M., Gómez-Avilés, A., Rodríguez, J. J., & Belver, C. (2019). A review on the synthesis and characterization of metal organic frameworks for photocatalytic water purification. *Catalysts*, *9*(1), 52. https://doi.org/10.3390/catal9010052

[37] Begum, M., Vaishnavi, G., Muralidaran, Y., & Mishra, P. (2025). Chemical, physical, and biological techniques to remove microplastics. In *Microplastics* (pp. 509-530). Elsevier. https://doi.org/10.1016/B978-0-443-29804-2.00022-6

[38] Begum, S., Devi, T. B., & Ahmaruzzaman, M. (2016). L-lysine monohydrate mediated facile and environment friendly synthesis of SnO_2 nanoparticles and their prospective applications as a catalyst for the reduction and photodegradation of aromatic compounds. Journal of environmental chemical engineering, 4(3), 2976-2989.

https://doi.org/10.1016/j.jece.2016.05.024

[39] Bellardita, M., Di Paola, A., Megna, B., & Palmisano, L. (2018). Determination of the crystallinity of TiO_2 photocatalysts. *Journal of Photochemistry and Photobiology A: Chemistry, 367*, 312-320. https://doi.org/10.1016/j.jphotochem.2018.08.042

[40] Bethi, B., Sonawane, S. H., Bhanvase, B. A., & Gumfekar, S. P. (2016). Nanomaterials-based advanced oxidation processes for wastewater treatment: a review. *Chemical Engineering and Processing-Process Intensification*, *109*, 178-189. https://doi.org/10.1016/j.cep.2016.08.016

[41] Bettinelli, M., Dallacasa, V., Falcomer, D., Fornasiero, P., Gombac, V., Montini, T., Romano, L. & Speghini, A. (2007). Photocatalytic activity of TiO_2 doped with boron and vanadium. *Journal of hazardous materials*, *146*(3), 529-534. https://doi.org/10.1016/j.jhazmat.2007.04.053

[42] Bhagwat, K. P., Rodrigue, D., & Romero-Zerón, L. (2024). Effective Removal of Microplastic Particles from Wastewater Using Hydrophobic Bio-Substrates. *Pollutants, 4*(2), 231-250. https://doi.org/10.3390/pollutants4020015

[43] Bhawna, Gupta, A., Kumar, P., Tyagi, A., Kumar, R., Kumar, A., Singh, P., Singh, R.P & Kumar, V. (2020). Facile Synthesis of N-Doped SnO_2 Nanoparticles: A Cocatalyst-Free Promising Photocatalyst for Hydrogen Generation. *ChemistrySelect, 5*(26), 7775-7782. https://doi.org/10.1002/slct.202001301

[44] Bhawna, Sharma, R., Kumar, S., Kumar, R., Sahu, P. K., Kumari, V., Mishra, A. K., & Kumar, V. (2023). Unlocking the Potential of N-Doped SnO_2 for Sustainable Photocatalytic Degradation of Carcinogenic Dyes. *Separations*, *10*(6), 322. https://doi.org/10.3390/separations10060322

[45] Bhunia, S. K., & Jana, N. R. (2014). Reduced graphene oxide-silver nanoparticle composite as visible light photocatalyst for degradation of colorless endocrine disruptors. *ACS applied materials & interfaces, 6*(22), 20085-20092. https://doi.org/10.1021/am505677x

[46] Biswas, S. K., Pathak, A., Pramanik, N. K., Dhak, D., & Pramanik, P. (2008). Codoped Cr and W rutile nanosized powders obtained by pyrolysis of triethanolamine complexes. *Ceramics international*, *34*(8), 1875-1883. https://doi.org/10.1016/j.ceramint.2007.07.014

[47] Biswas, S., & Pal, A. (2023). A brief review on the latest developments on pharmaceutical compound degradation using g-C_3N_4-based composite catalysts. *Catalysts*, *13*(6), 925. https://doi.org/10.3390/catal13060925

[48] Boujibar, O., Souikny, A., Ghamouss, F., Achak, O., Dahbi, M., & Chafik, T. (2018). CO_2 capture using N-containing nanoporous activated carbon obtained

from argan fruit shells. *Journal of Environmental Chemical Engineering, 6*(2), 1995-2002. https://doi.org/10.1016/j.jece.2018.03.005

[49] Bozzola, J. J., & Russell, L. D. (1999). *Electron microscopy: principles and techniques for biologists*. Jones & Bartlett Learning.

[50] Budlayan, M. L. M., Patricio, J. N., Lagare-Oracion, J. P., Arco, S. D., Alguno, A. C., Basilio, A., Basilio, A., Latayada, F.S. & Capangpangan, R. Y. (2021). Improvised centrifugal spinning for the production of polystyrene microfibers from waste expanded polystyrene foam and its potential application for oil adsorption. *Journal of Engineering and Applied Science, 68*, 1-11. https://doi.org/10.1186/s44147-021-00030-y

[51] Cao, X., Zheng, S., Wang, T., Lin, F., Li, J., & Jiao, L. (2022). N-doped ZrO_2 nanoparticles embedded in a N-doped carbon matrix as a highly active and durable electrocatalyst for oxygen reduction. *Fundamental Research*, *2*(4), 604-610. https://doi.org/10.1016/j.fmre.2021.08.014

[52] Carotenuto, G., Nicola, S. D., Ausanio, G., Massarotti, D., Nicolais, L., & Pepe, G. P. (2014). Synthesis and characterization of electrically conductive polyethylene-supported graphene films. *Nanoscale research letters*, *9*, 1-7. https://doi.org/10.1186/1556-276X-9-475

[53] Castilla-Caballero, D., Hernandez-Ramirez, A., Vazquez-Rodriguez, S., Colina-Márquez, J., Machuca-Martínez, F., Barraza-Burgos, J., Roa-Espinosa, A., Medina-Guerrero, A. & Gunasekaran, S. (2023). Effect of pyrolysis, impregnation, and calcination conditions on the physicochemical properties of TiO_2/Biochar composites intended for photocatalytic applications. *Journal of Environmental Chemical Engineering, 11*(3), 110274. https://doi.org/10.1016/j.jece.2023.110274

[54] Cazan, C., Enesca, A., & Andronic, L. (2021). Synergic effect of TiO_2 filler on the mechanical properties of polymer nanocomposites. *Polymers*, *13*(12), 2017. https://doi.org/10.3390/polym13122017

[55] Chakhtouna, H., Benzeid, H., Zari, N., el kacem Qaiss, A., & Bouhfid, R. (2021). Functional $CoFe_2O_4$-modified biochar derived from banana pseudostem as an efficient adsorbent for the removal of amoxicillin from water. *Separation and Purification Technology, 266*, 118592. https://doi.org/10.1016/j.seppur.2021.118592

[56] Chakhtouna, H., Benzeid, H., Zari, N., Qaiss, A. E. K., & Bouhfid, R. (2021). Recent progress on Ag/TiO_2 photocatalysts: photocatalytic and bactericidal behaviors. *Environmental Science and Pollution Research*, *28*(33), 44638-44666. https://doi.org/10.1007/s11356-021-14996-y

[57] Chakrabarti, S., & Dutta, B. K. (2008). Dye-sensitised photocatalytic degradation of PVC-ZnO composite film. *International Journal of Environmental Technology and Management, 9*(1), 34-46.

https://doi.org/10.1504/IJETM.2008.017858

[58] Chakravorty, A., & Roy, S. (2024). A review of photocatalysis, basic principles, processes, and materials. *Sustainable Chemistry for the Environment*, *8*, 100155. https://doi.org/10.1016/j.scenv.2024.100155

[59] Chang, B. Y. S., Huang, N. M., An'amt, M. N., Marlinda, A. R., Norazriena, Y., Muhamad, M. R., Harrison, I., Lim, H.N. & Chia, C. H. (2012). Facile hydrothermal preparation of titanium dioxide decorated reduced graphene oxide nanocomposite. *International journal of nanomedicine, 7,* 3379-3387. https://doi.org/10.2147/IJN.S2818

[60] Chang, S. K., Abbasi, Z., Khushbakht, F., Ullah, I., Rehman, F. U., & Hafeez, M. (2024). Rapid pH-dependent photocatalytic degradation of methylene blue by CdS nanorods synthesized through hydrothermal process. *Arabian Journal of Chemistry*, *17*(1), 105422. https://doi.org/10.1016/j.arabjc.2023.105422

[61] Charanpahari, A., Umare, S. S., & Sasikala, R. (2013). Visible light active N doped GeO_2 for the photodegradation of both anionic and cationic dyes. *Catalysis Communications*, *40*, 9-12. https://doi.org/10.1016/j.catcom.2013.05.015

[62] Charitha, T., Leshan, U., Shanitha, M., Ramanee, W., Buddi, L., & Martin, B. (2021). Efficient photodegradation activity of α-Fe_2O_3/Fe_2TiO_5/TiO_2 and Fe_2TiO_5/TiO_2 nanocomposites synthesized from natural ilmenite. *Results in Materials*, *12*, 100219. https://doi.org/10.1016/j.rinma.2021.100219

[63] Chen, Y., Wang, C., Chen, J., Wang, S., Ju, J., & Kang, W. (2022). Preparing biomass carbon fiber derived from waste rabbit hair as a carrier of TiO_2 for photocatalytic degradation of methylene blue. *Polymers, 14*(8), 1593. https://doi.org/10.3390/polym14081593

[64] Chiesa, M., Livraghi, S., Paganini, M. C., Salvadori, E., & Giamello, E. (2020). Nitrogen-doped semiconducting oxides. Implications on photochemical, photocatalytic and electronic properties derived from EPR spectroscopy. *Chemical Science*, *11*(26), 6623-6641. https://doi.org/10.1039/D0SC02876B

[65] Cho, S., & Choi, W. (2001). Solid-phase photocatalytic degradation of PVC–TiO_2 polymer composites. *Journal of Photochemistry and Photobiology A: Chemistry, 143*(2-3), 221-228. https://doi.org/10.1016/S1010-6030(01)00499-3

[66] Chuang, S. H., Lin, H. C., & Chen, C. H. (2012). Oxygen vacancy relationship to photoluminescence and heat treatment methods in hafnium oxide powders. *Journal of alloys and compounds, 534*, 42-46. https://doi.org/10.1016/j.jallcom.2012.04.046

[67] Coltro, L., Pitta, J. B., & Madaleno, E. (2013). Performance evaluation of new plasticizers for stretch PVC films. *Polymer Testing, 32*(2), 272-278. https://doi.org/10.1016/j.polymertesting.2012.11.009

[68] Cui, J., Zhang, F., Li, H., Cui, J., Ren, Y., & Yu, X. (2020). Recent progress in biochar-based photocatalysts for wastewater treatment: synthesis, mechanisms, and applications. *Applied Sciences, 10*(3), 1019. https://doi.org/10.3390/app10031019

[69] Dandan, W., Junbo, L., Haibo, C., & Shanshan, T. (2014). Visible Photocatalytic Degradation of Polyvinyl Chloride Film by $AgNbO_3$ Photocatalyst. *CHEMICAL JOURNAL OF CHINESE UNIVERSITIES-CHINESE, 35*(9), 1975-1981. https://doi.org/10.7503/cjcu20140185

[70] Das, J., Yadav, E., & Poluri, K. M. (2025). A review on the role of nanotechnological interventions in sequestration, mitigation and value-added product conversion of micro-/nanoplastics. *Environmental Science: Nano, 12*, 189-218. https://doi.org/10.1039/D4EN00267A

[71] Dayal, L., Yadav, K., Dey, U., Das, K., Kumari, P., Raj, D., & Mandal, R. R. (2024). Recent advancement in microplastic removal process from wastewater-a critical review. *Journal of Hazardous Materials Advances*, *16*, 100460. https://doi.org/10.1016/j.hazadv.2024.100460

[72] de Assis, G. C., de Jesus, R. A., da Silva, W. T. A., Ferreira, L. F. R., Figueiredo, R. T., & de Oliveira, R. J. (2021). Conversion of plastic waste into supports for nanostructured heterogeneous catalysts: application in environmental remediation. *Surfaces*, *5*(1), 35-66. https://doi.org/10.3390/surfaces5010002

[73] De Assis, G. C., Skovroinski, E., Leite, V. D., Rodrigues, M. O., Galembeck, A., Alves, M. C., Eastoe, J. & De Oliveira, R. J. (2018). Conversion of "Waste Plastic" into photocatalytic nanofoams for environmental remediation. *ACS applied materials & interfaces, 10*(9), 8077-8085. https://doi.org/10.1021/acsami.7b19834

[74] DE LORENZI, A., Giorgianni, S., & Bini, R. (1999). High-resolution FTIR spectroscopy of the C-Cl stretching mode of vinyl chloride. *Molecular Physics, 96*(1), 101-108. https://doi.org/10.1080/00268979909482942

[75] Deshmukh, K., Kovářík, T., Křenek, T., Docheva, D., Stich, T., & Pola, J. (2020). Recent advances and future perspectives of sol–gel derived porous bioactive glasses: a review. *RSC advances*, *10*(56), 33782-33835. https://doi.org/10.1039/D0RA04287K

[76] Devesa, S. (2025). Comparative Overview of Metal Oxide Nanoparticle Synthesis Methods: Conventional Sol-Gel Versus Green Approaches. *Sol-Gel-A Versatile and Wide Technology*. https://doi.org/10.5772/intechopen.1008457

[77] Devi, L. G., Murthy, B. N., & Kumar, S. G. (2010). Photocatalytic activity of TiO_2 doped with Zn^{2+} and V^{5+} transition metal ions: Influence of crystallite size

and dopant electronic configuration on photocatalytic activity. *Materials Science and Engineering: B, 166*(1), 1-6. https://doi.org/10.1016/j.mseb.2009.09.008

[78] Divya, J., Pramothkumar, A., Gnanamuthu, S. J., & Victoria, D. B. (2020). Structural, optical, electrical and magnetic properties of Cu and Ni doped SnO_2 nanoparticles prepared via Co-precipitation approach. *Physica B: Condensed Matter, 588*, 412169. https://doi.org/10.1016/j.physb.2020.412169

[79] Djellabi, R., Yang, B., Wang, Y., Cui, X., & Zhao, X. (2019). Carbonaceous biomass-titania composites with Ti-O-C bonding bridge for efficient photocatalytic reduction of Cr (VI) under narrow visible light. *Chemical Engineering Journal, 366*, 172-180. https://doi.org/10.1016/j.cej.2019.02.035

[80] Dobrucka, R., Dlugaszewska, J., & Kaczmarek, M. (2018). Cytotoxic and antimicrobial effect of biosynthesized SnO_2 nanoparticles using Pruni spinosae flos extract. *Inorganic and Nano-Metal Chemistry, 48*(7), 367-376. https://doi.org/10.1080/24701556.2019.1569054

[81] Dorraj, M., Alizadeh, M., Sairi, N. A., Basirun, W. J., Goh, B. T., Woi, P. M., & Alias, Y. (2017). Enhanced visible light photocatalytic activity of copper-doped titanium oxide–zinc oxide heterojunction for methyl orange degradation. *Applied Surface Science, 414*, 251-261. https://doi.org/10.1016/j.apsusc.2017.04.045

[82] Duncan, S. E., & Hannah, S. (2012). Light-protective packaging materials for foods and beverages. In *Emerging food packaging technologies* (pp. 303-322). Woodhead publishing. https://doi.org/10.1533/9780857095664.3.303

[83] Ejeta, S. Y., & Imae, T. (2026). Photocatalytic degradation of polyethylene microplastics by copper-doped titanium dioxide nanoparticles. *Chemosphere, 394,* 144819. https://doi.org/10.1016/j.chemosphere.2025.144819

[84] El-Sayed, M. E. (2020). Nanoadsorbents for water and wastewater remediation. *Science of the Total Environment*, *739*, 139903. https://doi.org/10.1016/j.scitotenv.2020.139903

[85] El-Sharkaway, E. A., Kamel, R. M., El-Sherbiny, I. M., & Gharib, S. S. (2020). Removal of methylene blue from aqueous solutions using polyaniline/graphene oxide or polyaniline/reduced graphene oxide composites. *Environmental technology*. https://doi.org/10.1080/09593330.2019.1585481

[86] Eskandarloo, H., Badiei, A., Behnajady, M. A., Tavakoli, A., & Ziarani, G. M. (2016). Ultrasonic-assisted synthesis of Ce doped cubic–hexagonal $ZnTiO_3$ with highly efficient sonocatalytic activity. *Ultrasonics Sonochemistry, 29*, 258-269.

https://doi.org/10.1016/j.ultsonch.2015.10.004

[87] Estrada-Flores, S., Martínez-Luévanos, A., Perez-Berumen, C. M., García-Cerda, L. A., & Flores-Guia, T. E. (2020). Relationship between morphology, porosity, and the photocatalytic activity of TiO_2 obtained by sol–gel method assisted with ionic and nonionic surfactants. *boletín de la sociedad española de cerámica y vidrio*, *59*(5), 209-218. https://doi.org/10.1016/j.bsecv.2019.10.003

[88] Estrellan, C. R., Salim, C., & Hinode, H. (2010). Photocatalytic decomposition of perfluorooctanoic acid by iron and niobium co-doped titanium dioxide. *Journal of hazardous materials*, *179*(1-3), 79-83. https://doi.org/10.1016/j.jhazmat.2010.02.060

[89] Estruga, M., Domingo, C., Domènech, X., & Ayllón, J. A. (2010). Zirconium-doped and silicon-doped TiO_2 photocatalysts synthesis from ionic-liquid-like precursors. *Journal of colloid and interface science*, *344*(2), 327-333. https://doi.org/10.1016/j.jcis.2009.12.063

[90] Fadli, M. H., Ibadurrohman, M., & Slamet, S. (2021). Microplastic pollutant degradation in water using modified TiO_2 photocatalyst under UV-irradiation. In IOP conference series: materials science and engineering (Vol. 1011, No. 1, p. 012055). IOP Publishing. https://doi.org/10.1088/1757-899X/1011/1/012055

[91] Fang, J., Xuan, Y., & Li, Q. (2010). Preparation of polystyrene spheres in different particle sizes and assembly of the PS colloidal crystals. *Science China Technological Sciences*, *53*, 3088-3093. https://doi.org/10.1007/s11431-010-4110-5

[92] Farghaly, A., Maher, E., Gad, A., & El-Bery, H. (2024). Synergistic photocatalytic degradation of methylene blue using TiO_2 composites with activated carbon and reduced graphene oxide: a kinetic and mechanistic study. *Applied Water Science*, *14*(10), 228. https://doi.org/10.1007/s13201-024-02286-0

[93] Farhadi, S., & Zaidi, M. (2009). Polyoxometalate–zirconia (POM/ZrO_2) nanocomposite prepared by sol–gel process: A green and recyclable photocatalyst for efficient and selective aerobic oxidation of alcohols into aldehydes and ketones. Applied Catalysis A: General, *354*(1-2), 119-126. https://doi.org/10.1016/j.apcata.2008.11.024

[94] Fazal, T., Razzaq, A., Javed, F., Hafeez, A., Rashid, N., Amjad, U. S., Rehman, M.S.U., Faisal, A. & Rehman, F. (2020). Integrating adsorption and photocatalysis: A cost effective strategy for textile wastewater treatment using hybrid biochar-TiO_2 composite. *Journal of hazardous materials, 390*, 121623. https://doi.org/10.1016/j.jhazmat.2019.121623

[95] Fiorenza, R., Di Mauro, A., Cantarella, M., Gulino, A., Spitaleri, L., Privitera, V., & Impellizzeri, G. (2020). Molecularly imprinted N-doped TiO_2 photocatalysts for the selective degradation of o-phenylphenol fungicide from water. *Materials Science in Semiconductor Processing, 112*, 105019. https://doi.org/10.1016/j.mssp.2020.105019

[96] Ganie, Z. A., Khandelwal, N., Tiwari, E., Singh, N., & Darbha, G. K. (2021). Biochar-facilitated remediation of nanoplastic contaminated water: Effect of pyrolysis temperature induced surface modifications. Journal of Hazardous Materials, 417, 126096. https://doi.org/10.1016/j.jhazmat.2021.126096

[97] Ganguly, A., Sharma, S., Papakonstantinou, P., & Hamilton, J. (2011). Probing the thermal deoxygenation of graphene oxide using high-resolution in situ X-ray-based spectroscopies. *The Journal of Physical Chemistry C, 115*(34), 17009-17019. https://doi.org/10.1021/jp203741y

[98] Gilic, M., Kostic, R., Stojanovic, D., Romcevic, M., Hadzic, B., Petrovic, M., Ralevic, U., Lazarevic, Z., Trajic, J., Ristić-Djurovic, J. and Cirkovic, J., & Romcevic, N. (2018). Photoluminescence spectroscopy of CdSe nanoparticles embedded in transparent glass. *Optical and Quantum Electronics*, *50*, 1-8. https://doi.org/10.1007/s11082-018-1552-7

[99] Giovannetti, R., Rommozzi, E., Zannotti, M., & D'Amato, C. A. (2017). Recent advances in graphene based TiO_2 nanocomposites ($GTiO_2Ns$) for photocatalytic degradation of synthetic dyes. *Catalysts*, *7*(10), 305. https://doi.org/10.3390/catal7100305

[100] Gupta, A., Lakshmp, Y. N., Manivannan, R., & Victoria, S. N. (2017). Visible range photocatalysts for solid phase photocatalytic degradation of polyethylene and polyvinyl chloride. *Journal of the Chilean Chemical Society, 62*(1), 3393-3398. https://doi.org/10.4067/S0717-97072017000100018

[101] Gupta, G. K., Ram, M., Bala, R., Kapur, M., & Mondal, M. K. (2018). Pyrolysis of chemically treated corncob for biochar production and its application in Cr (VI) removal. *Environmental Progress & Sustainable Energy, 37*(5), 1606-1617. https://doi.org/10.1002/ep.12838

[102] Hamadanian, M., Reisi-Vanani, A., & Majedi, A. (2010). Synthesis, characterization and effect of calcination temperature on phase transformation and photocatalytic activity of Cu, S-codoped TiO_2 nanoparticles. *Applied Surface Science*, *256*(6), 1837-1844. https://doi.org/10.1016/j.apsusc.2009.10.016

[103] Hanafi, M. F., & Sapawe, N. (2019). The potential of ZrO2 catalyst toward degradation of dyes and phenolic compound. Materials Today: Proceedings, 19, 1524-1528. https://doi.org/10.1016/j.matpr.2019.11.177

[104] Hassaan, M. A., El-Nemr, M. A., Elkatory, M. R., Ragab, S., Niculescu, V. C., & El Nemr, A. (2023). Principles of photocatalysts and their different applications: a review. *Topics in Current Chemistry*, *381*(6), 31. https://doi.org/10.1007/s41061-023-00444-7

[105] He, C., Tian, B., & Zhang, J. (2010). Thermally stable SiO_2-doped mesoporous anatase TiO_2 with large surface area and excellent photocatalytic activity. *Journal of Colloid and Interface Science*, *344*(2), 382-389. https://doi.org/10.1016/j.jcis.2010.01.002

[106] He, J., Han, L., Ma, W., Chen, L., Ma, C., Xu, C., & Yang, Z. (2023). Efficient photodegradation of polystyrene microplastics integrated with hydrogen evolution: Uncovering degradation pathways. *Iscience, 26*(6). https://doi.org/10.1016/j.isci.2023.106833

[107] He, X., Chen, X., Wang, X., & Jiang, L. (2023). Optimization of activated carbon production from corn cob using response surface methodology. *Frontiers in Environmental Science, 11*, 1105408. https://doi.org/10.3389/fenvs.2023.1105408

[108] He, Y., Rehman, A. U., Xu, M., Not, C. A., Ng, A. M., & Djurišić, A. B. (2023). Photocatalytic degradation of different types of microplastics by TiOx/ZnO tetrapod photocatalysts. *Heliyon, 9*(11). https://doi.org/10.1016/j.heliyon.2023.e22562

[109] Heo, Y., Lee, E. H., & Lee, S. W. (2022). Adsorptive removal of micron-sized polystyrene particles using magnetic iron oxide nanoparticles. *Chemosphere*, *307*, 135672. https://doi.org/10.1016/j.chemosphere.2022.135672

[110] Hirakawa, T., & Kamat, P. V. (2005). Charge separation and catalytic activity of Ag@ TiO_2 core-shell composite clusters under UV-irradiation. *Journal of the American Chemical Society, 127*(11), 3928-3934. https://doi.org/10.1021/ja042925a

[111] Ho, W., Jimmy, C. Y., & Lee, S. (2006). Low-temperature hydrothermal synthesis of S-doped TiO_2 with visible light photocatalytic activity. *Journal of solid state chemistry*, *179*(4), 1171-1176. https://doi.org/10.1016/j.jssc.2006.01.009

[112] Hodaei, A., Dezfuli, A. S., & Naderi, H. R. (2018). A high-performance supercapacitor based on N-doped TiO_2 nanoparticles. *Journal of Materials Science: Materials in Electronics*, *29*, 14596-14604. https://doi.org/10.1007/s10854-018-9595-x

[113] Hou, Y., Lv, S., Liu, L., & Liu, X. (2020). High-quality preparation of graphene oxide via the Hummers' method: understanding the roles of the intercalator, oxidant, and graphite particle size. *Ceramics International, 46*(2), 2392-2402. https://doi.org/10.1016/j.ceramint.2019.09.231

[114] Hu, Z., Huang, Y., Sun, S., Guan, W., Yao, Y., Tang, P., & Li, C. (2012). Visible light driven photodynamic anticancer activity of graphene oxide/TiO_2 hybrid. *Carbon*, *50*(3), 994-1004. https://doi.org/10.1016/j.carbon.2011.10.002

[115] Huang, J., Veksha, A., Chan, W. P., Giannis, A., & Lisak, G. (2022). Chemical recycling of plastic waste for sustainable material management: A prospective

review on catalysts and processes. *Renewable and Sustainable Energy Reviews*, *154*, 111866. https://doi.org/10.1016/j.rser.2021.111866

[116] Huang, M., Xu, C., Wu, Z., Huang, Y., Lin, J., & Wu, J. (2008). Photocatalytic discolorization of methyl orange solution by Pt modified TiO_2 loaded on natural zeolite. *Dyes and pigments*, *77*(2), 327-334. https://doi.org/10.1016/j.dyepig.2007.01.026

[117] Huang, Y., Qin, J., Fan, Z., Wei, D., & Seo, H. J. (2019). Photoenergy conversion behaviors of photoluminescence and photocatalysis in silver-coated $LiBaPO_4$: Eu^{2+}. *Inorganic Chemistry, 58*(19), 13161-13169. https://doi.org/10.1021/acs.inorgchem.9b02037

[118] Hummers Jr, W. S., & Offeman, R. E. (1958). Preparation of graphitic oxide. *Journal of the american chemical society, 80*(6), 1339-1339. https://doi.org/10.1021/ja01539a017

[119] Hung, W. C., Fu, S. H., Tseng, J. J., Chu, H., & Ko, T. H. (2007). Study on photocatalytic degradation of gaseous dichloromethane using pure and iron ion-doped TiO_2 prepared by the sol–gel method. *Chemosphere*, *66*(11), 2142-2151. https://doi.org/10.1016/j.chemosphere.2006.09.037

[120] Hurayra–Lizu, K. A., Bari, M. W., Gulshan, F., & Islam, M. R. (2021). GO based PVA nanocomposites: tailoring of optical and structural properties of PVA with low percentage of GO nanofillers. *Heliyon*, *7*(5). https://doi.org/10.1016/j.heliyon.2021.e06983

[121] Ida, S., Wilson, P., Neppolian, B., Sathish, M., Shaheer, A. M., & Ravi, P. (2020). Tuning the type of nitrogen on N-RGO supported on N-TiO_2 under ultrasonication/hydrothermal treatment for efficient hydrogen evolution–A mechanistic overview. *Ultrasonics Sonochemistry, 64,* 104866. https://doi.org/10.1016/j.ultsonch.2019.104866

[122] Irie, H., Watanabe, Y., & Hashimoto, K. (2003). Nitrogen-concentration dependence on photocatalytic activity of TiO_{2-x} N_x powders. *The Journal of Physical Chemistry B*, *107*(23), 5483-5486. https://doi.org/10.1021/jp030133h

[123] Ishibai, Y., Sato, J., Nishikawa, T., & Miyagishi, S. (2008). Synthesis of visible-light active TiO_2 photocatalyst with Pt-modification: Role of TiO_2 substrate for high photocatalytic activity. *Applied Catalysis B: Environmental*, *79*(2), 117-121. https://doi.org/10.1016/j.apcatb.2007.09.040

[124] Jaffrezic-Renault, N., Pichat, P., Foissy, A., & Mercier, R. (1986). Study of the effect of deposited platinum particles on the surface charge of titania aqueous suspensions by potentiometry, electrophoresis, and labeled-ion adsorption. *J. Phys. Chem.;(United States), 90*(12). https://doi.org/10.1021/j100403a035

[125] Jayanthi, S., Eswar, N. K., Singh, S. A., Chatterjee, K., Madras, G., & Sood, A. K. (2016). Macroporous three-dimensional graphene oxide foams for dye adsorption and antibacterial applications. *RSC Advances, 6*(2), 1231-1242.

https://doi.org/10.1039/C5RA19925E

[126] Jedynak, K., & Charmas, B. (2024). Adsorption properties of biochars obtained by KOH activation. *Adsorption, 30*(2), 167-183. https://doi.org/10.1007/s10450-023-00399-7

[127] Jiang, G., Lin, Z., Chen, C., Zhu, L., Chang, Q., Wang, N., Wei, W. & Tang, H. (2011). TiO_2 nanoparticles assembled on graphene oxide nanosheets with high photocatalytic activity for removal of pollutants. *Carbon, 49*(8), 2693-2701. https://doi.org/10.1016/j.carbon.2011.02.059

[128] Jin, C., Zheng, R. Y., Guo, Y., Xie, J. L., Zhu, Y. X., & Xie, Y. C. (2009). Hydrothermal synthesis and characterization of phosphorous-doped TiO_2 with high photocatalytic activity for methylene blue degradation. *Journal of Molecular Catalysis A: Chemical*, *313*(1-2), 44-48. https://doi.org/10.1016/j.molcata.2009.07.021

[129] Jin, R., Wu, Z., Liu, Y., Jiang, B., & Wang, H. (2009). Photocatalytic reduction of NO with NH_3 using Si-doped TiO_2 prepared by hydrothermal method. *Journal of Hazardous Materials*, *161*(1), 42-48. https://doi.org/10.1016/j.jhazmat.2008.03.041

[130] John, D., Rajalakshmi, A. S., Lopez, R. M., & Achari, V. S. (2020). TiO_2-reduced graphene oxide nanocomposites for the trace removal of diclofenac. SN Applied Sciences, 2(5), 840. https://doi.org/10.1007/s42452-020-2662-y

[131] Juárez, G. A. S., Barojas, E. G., Quiroga-González, E., Sánchez-Mora, E., & Santamaría-Juárez, J. D. (2019). Preparation and characterization of reduced graphene oxide/titanium dioxide composites by hydrothermal method. *European Journal of Engineering and Technology Research, 4*(9), 165-173. https://doi.org/10.24018/ejeng.2019.4.9.1364

[132] Jung, K. Y., Park, S. B., & Ihm, S. K. (2002). Linear relationship between the crystallite size and the photoactivity of non-porous titania ranging from nanometer to micrometer size. *Applied Catalysis A: General, 224*(1-2), 229-237. https://doi.org/10.1016/S0926-860X(01)00784-0

[133] Kaewkam, P., Kanchanapaetnukul, A., Khamyan, J., Phadmanee, N., Lin, K. Y. A., Kobwittaya, K., & Sirivithayapakorn, S. (2022). UV-assisted TiO_2 photocatalytic degradation of virgin LDPE films: effect of UV-A, UV-C, and TiO_2. Journal of Environmental Chemical Engineering, 10(4), 108131. https://doi.org/10.1016/j.jece.2022.108131

[134] Kamalam, M., Menaka, J., Inbanathan, S. S. R., Sethuraman, K., Shahid, A., Fouad, H., & Hussain, S. (2023). Tin oxide-graphene oxide (SnO_2/GO) nanocomposite: A promising photocatalyst for rhodamine-B dye degradation. *Science of Advanced Materials*, *15*(5), 648-654. https://doi.org/10.1166/sam.2023.4465

[135] Kamble, S. P., Sawant, S. B., Schouten, J. C., & Pangarkar, V. G. (2003). Photocatalytic and photochemical degradation of aniline using concentrated

solar radiation. Journal of Chemical Technology & Biotechnology: *International Research in Process, Environmental & Clean Technology, 78*(8), 865-872.
https://doi.org/10.1002/jctb.867

[136] Kansal, S. K., Singh, M., & Sud, D. (2007). Studies on photodegradation of two commercial dyes in aqueous phase using different photocatalysts. *Journal of hazardous materials, 141*(3), 581-590.
https://doi.org/10.1016/j.jhazmat.2006.07.035

[137] Khairnar, S. D., Shirsath, D. S., Patil, P. S., & Shrivastava, V. S. (2020). Adsorptive and photocatalytic removal of carcinogenic methylene blue dye by SnO_2 nanorods: an equilibrium, kinetic and thermodynamics exploration. *SN Applied Sciences*, *2*, 1-12.
https://doi.org/10.1007/s42452-020-2607-5

[138] Khammar, M., Ynineb, F., Guitouni, S., Bouznit, Y., & Attaf, N. (2020). Crystallite size and intrinsic strain contribution in band gap energy redshift of ultrasonic-sprayed kesterite CZTS nanostructured thin films. *Applied Physics A, 126*(6), 398.
https://doi.org/10.1007/s00339-020-03591-6

[139] Khan, I., Saeed, K., & Khan, I. (2019). Nanoparticles: Properties, applications and toxicities. *Arabian journal of chemistry*, *12*(7), 908-931.
https://doi.org/10.1016/j.arabjc.2017.05.011

[140] Khan, R., Kim, S. W., Kim, T. J., & Nam, C. M. (2008). Comparative study of the photocatalytic performance of boron–iron Co-doped and boron-doped TiO_2 nanoparticles. *Materials Chemistry and Physics*, *112*(1), 167-172.
https://doi.org/10.1016/j.matchemphys.2008

[141] Khan, S. A., Arshad, Z., Shahid, S., Arshad, I., Rizwan, K., Sher, M., & Fatima, U. (2019). Synthesis of TiO_2/Graphene oxide nanocomposites for their enhanced photocatalytic activity against methylene blue dye and ciprofloxacin. *Composites Part B: Engineering*, *175*, 107120.
https://doi.org/10.1016/j.compositesb.2019.107120

[142] Kharisov, B. I. (2008). A review for synthesis of nanoflowers. *Recent patents on nanotechnology*, *2*(3), 190-200.
https://doi.org/10.2174/187221008786369651

[143] Khatuaa, C., Chinyaa, I., Saha, D., Das, S., Sen, R., Dhar, A., & Sahab, D. (2015). Modified clad optical fibre coated with PVA/TiO_2 nano composite for humidity sensing application. *International Journal on Smart Sensing and Intelligent Systems*, *8*(3), 1424.
http://dx.doi.org/10.21307/ijssis-2017-813

[144] Kim, J. R., & Kan, E. (2016). Heterogeneous photocatalytic degradation of sulfamethoxazole in water using a biochar-supported TiO_2 photocatalyst. *Journal of Environmental Management, 180*, 94-101.
https://doi.org/10.1016/j.jenvman.2016.05.016

[145] Klüpfel, L., Keiluweit, M., Kleber, M., & Sander, M. (2014). Redox properties of plant biomass-derived black carbon (biochar). *Environmental science & technology, 48(*10), 5601-5611. https://doi.org/10.1021/es500906d

[146] Kneipp, K., Kneipp, H., Itzkan, I., Dasari, R. R., & Feld, M. S. (1999). Ultrasensitive chemical analysis by Raman spectroscopy. *Chemical reviews*, *99*(10), 2957-2976. https://doi.org/10.1021/cr980133r

[147] Ko, W., Zhao, S., Kim, K., Kim, Y. D., & Seo, H. O. (2023). Template free sol-gel synthesis of mesoporous TiO_2 particles as an efficient photocatalyst for gaseous toluene removal. *Materials Chemistry and Physics*, *299*, 127519. https://doi.org/10.1016/j.matchemphys.2023.127519

[148] Kocijan, M., Ćurković, L., Bdikin, I., Otero-Irurueta, G., Hortigüela, M. J., Gonçalves, G., Radošević, T., Vengust, D. & Podlogar, M. (2021). Immobilised rGO/TiO_2 nanocomposite for multi-cycle removal of methylene blue dye from an aqueous medium. *Applied Sciences*, *12*(1), 385. https://doi.org/10.3390/app12010385

[149] Kozlova, E. A., & Vorontsov, A. V. (2007). Influence of mesoporous and platinum-modified titanium dioxide preparation methods on photocatalytic activity in liquid and gas phase. *Applied Catalysis B: Environmental*, *77*(1-2), 35-45. https://doi.org/10.1016/j.apcatb.2007.07.001

[150] Králik, B., Chang, E. K., & Louie, S. G. (1998). Structural properties and quasiparticle band structure of zirconia. *Physical Review B*, *57*(12), 7027. https://doi.org/10.1103/PhysRevB.57.7027

[151] Krishnan, A., Swarnalal, A., Das, D., Krishnan, M., Saji, V. S., & Shibli, S. M. A. (2024). A review on transition metal oxides based photocatalysts for degradation of synthetic organic pollutants. *Journal of Environmental Sciences*, *139*, 389-417. https://doi.org/10.1016/j.jes.2023.02.051

[152] Kumar, A., Raorane, C. J., Syed, A., Bahkali, A. H., Elgorban, A. M., Raj, V., & Kim, S. C. (2023). Synthesis of TiO_2, TiO2/PAni, TiO_2/PAni/GO nanocomposites and photodegradation of anionic dyes Rose Bengal and thymol blue in visible light. *Environmental research*, *216*, 114741. https://doi.org/10.1016/j.envres.2022.114741

[153] Kumar, M., Chaudhary, V., Kumar, R., Chaudhary, V., & Srivastav, A.L. (2025). Microplastics, their effects on ecosystems, and general strategies for mitigation of microplastics: A review of recent developments, challenges, and future prospects. *Environmental Pollution and Management*, *2*, 87–105, https://doi.org/10.1016/j.epm.2025.03.001

[154] Kumar, R., Verma, A., Shome, A., Sinha, R., Sinha, S., Jha, P. K., Kumar, R., Kumar, P., Shubham, Das, S. and Sharma, P. & Vara Prasad, P. V. (2021). Impacts of plastic pollution on ecosystem services, sustainable development

goals, and need to focus on circular economy and policy interventions. *Sustainability*, *13*(17), 9963. https://doi.org/10.3390/su13179963

[155] Kumari, P., & Kumar, A. (2023). Advanced oxidation process: A remediation technique for organic and non-biodegradable pollutant. Results in Surfaces and Interfaces, 11, 100122. https://doi.org/10.1016/j.rsurfi.2023.100122

[156] Kurniawan, S. B., Said, N. S. M., Imron, M. F., & Abdullah, S. R. S. (2021). Microplastic pollution in the environment: Insights into emerging sources and potential threats. *Environmental Technology & Innovation*, *23*, 101790. https://doi.org/10.1016/j.eti.2021.101790

[157] Kusiak-Nejman, E., Moszyński, D., Kapica-Kozar, J., Wanag, A., & Morawski, A. W. (2018). Assessment of the suitability of the one-step hydrothermal method for preparation of non-covalently/covalently-bonded TiO_2/graphene-based hybrids. *Nanomaterials, 8*(9), 647. https://doi.org/10.3390/nano8090647

[158] Kusiak-Nejman, E., Wanag, A., Kapica-Kozar, J., Kowalczyk, Ł., Zgrzebnicki, M., Tryba, B., Przepiórski, J. & Morawski, A. W. (2020). Methylene blue decomposition on TiO_2/reduced graphene oxide hybrid photocatalysts obtained by a two-step hydrothermal and calcination synthesis. *Catalysis Today*, *357*, 630-637. https://doi.org/10.1016/j.cattod.2019.04.078

[159] Lagarde, F., Olivier, O., Zanella, M., Daniel, P., Hiard, S., & Caruso, A. (2016). Microplastic interactions with freshwater microalgae: hetero-aggregation and changes in plastic density appear strongly dependent on polymer type. *Environmental pollution*, *215*, 331-339. https://doi.org/10.1016/j.envpol.2016.05.006

[160] Lares, M., Ncibi, M. C., Sillanpää, M., & Sillanpää, M. (2018). Occurrence, identification and removal of microplastic particles and fibers in conventional activated sludge process and advanced MBR technology. *Water research*, *133*, 236-246. https://doi.org/10.1016/j.watres.2018.01.049

[161] Le, V. H., Nguyen, T. H., Nguyen, H. H., Huynh, L. T. N., Vo, A. L., Nguyen, T. K. T., Nguyen, D.T. & Lam, V. Q. (2020). Fabrication and Electrochemical Behavior Investigation of a Pt-Loaded Reduced Graphene Oxide Composite (Pt@ rGO) as a High-Performance Cathode for Dye-Sensitized Solar Cells. *International Journal of Photoenergy*, *2020*(1), 8927124. https://doi.org/10.1155/2020/8927124

[162] Lee, H. C., Liu, W. W., Chai, S. P., Mohamed, A. R., Aziz, A., Khe, C. S., Hidayah, N.M. & Hashim, U. (2017). Review of the synthesis, transfer, characterization and growth mechanisms of single and multilayer graphene. *RSC advances*, *7*(26), 15644-15693. https://doi.org/10.1039/C7RA00392G

[163] Lee, Q. Y., & Li, H. (2021). Photocatalytic degradation of plastic waste: a mini review. *Micromachines*, *12*(8), 907. https://doi.org/10.3390/mi12080907

[164] Lee, X. J., Lee, L. Y., Gan, S., Thangalazhy-Gopakumar, S., & Ng, H. K. (2017). Biochar potential evaluation of palm oil wastes through slow pyrolysis: thermochemical characterization and pyrolytic kinetic studies. *Bioresource technology, 236*, 155-163. https://doi.org/10.1016/j.biortech.2017.03.105

[165] Lehmann, J., Czimczik, C., Laird, D., & Sohi, S. (2012). Stability of biochar in soil. In *Biochar for environmental management* (pp. 215-238). Routledge. https://doi.org/10.4324/9781849770552

[166] Letifi, H., Litaiem, Y., Dridi, D., Ammar, S., & Chtourou, R. (2019). Enhanced Photocatalytic Activity of Vanadium-Doped SnO_2 Nanoparticles in Rhodamine B Degradation. *Advances in Condensed Matter Physics*, *2019*(1), 2157428. https://doi.org/10.1155/2019/2157428

[167] Li, D., Haneda, H., Labhsetwar, N. K., Hishita, S., & Ohashi, N. (2005). Visible-light-driven photocatalysis on fluorine-doped TiO_2 powders by the creation of surface oxygen vacancies. *Chemical Physics Letters*, *401*(4-6), 579-584. https://doi.org/10.1016/j.cplett.2004.11.126

[168] Li, G., Dimitrijevic, N. M., Chen, L., Nichols, J. M., Rajh, T., & Gray, K. A. (2008). The important role of tetrahedral Ti^{4+} sites in the phase transformation and photocatalytic activity of TiO_2 nanocomposites. *J. Am. Chem. Soc. Commun., 130*(16), 5402–5403. https://doi.org/10.1021/ja711118u

[169] Li, J., Xu, J., Dai, W. L., Li, H., & Fan, K. (2008). One-pot synthesis of twist-like helix tungsten–nitrogen-codoped titania photocatalysts with highly improved visible light activity in the abatement of phenol. *Applied Catalysis B: Environmental*, *82*(3-4), 233-243. https://doi.org/10.1016/j.apcatb.2008.01.022

[170] Li, L., Xu, Z., Liu, F., Shao, Y., Wang, J., Wan, H., & Zheng, S. (2010). Photocatalytic nitrate reduction over Pt–Cu/TiO_2 catalysts with benzene as hole scavenger. *Journal of Photochemistry and Photobiology A: Chemistry*, *212*(2-3), 113-121. https://doi.org/10.1016/j.jphotochem.2010.04.003

[171] Li, Y., Li, J., Ding, J., Song, Z., Yang, B., Zhang, C., & Guan, B. (2022). Degradation of nano-sized polystyrene plastics by ozonation or chlorination in drinking water disinfection processes. *Chemical Engineering Journal*, *427*, 131690. https://doi.org/10.1016/j.cej.2021.131690

[172] Li, Y., Qu, J., Gao, F., Lv, S., Shi, L., He, C., & Sun, J. (2015). In situ fabrication of Mn_3O_4 decorated graphene oxide as a synergistic catalyst for degradation of methylene blue. *Applied Catalysis B: Environmental, 162,* 268-274. https://doi.org/10.1016/j.apcatb.2014.06.058

[173] Liang, S., Xu, S., Wang, C., Ling, J., Xian, Z., Wu, H., Zhou, S. & Gu, C. (2021). Enhanced alteration of poly (vinyl chloride) microplastics by hydrated electrons derived from indole-3-acetic acid assisted by a common cationic surfactant. *Water Research, 191*, 116797. https://doi.org/10.1016/j.watres.2020.116797

[174] Liao, C., Li, Y., & Tjong, S. C. (2020). Visible-light active titanium dioxide nanomaterials with bactericidal properties. *Nanomaterials*, *10*(1), 124. https://doi.org/10.3390/nano10010124

[175] Liao, R., Han, J., Chen, Z., Wang, J., Wu, H., Huang, S., Yan, C. & Wang, Z. (2022). Facile solvothermal synthesis of nitrogen-doped SnO_2 nanorods towards enhanced photocatalysis. *RSC advances*, *12*(44), 28629-28636. https://doi.org/10.1039/D2RA04900G

[176] Lim, T. T., Yap, P. S., Srinivasan, M., & Fane, A. G. (2011). TiO_2/AC composites for synergistic adsorption-photocatalysis processes: present challenges and further developments for water treatment and reclamation. *Critical Reviews in Environmental Science and Technology, 41*(13), 1173-1230. https://doi.org/10.1080/10643380903488664

[177] Linda, T., Muthupoongodi, S., Shajan, X. S., & Balakumar, S. (2016). Photocatalytic degradation of congo red and crystal violet dyes on cellulose/PVC/ZnO composites under UV light irradiation. *Materials Today: Proceedings*, *3*(6), 2035-2041. https://doi.org/10.1016/j.matpr.2016.04.106

[178] Linsebigler, A. L., Lu, G., & Yates Jr, J. T. (1995). Photocatalysis on TiO_2 surfaces: principles, mechanisms, and selected results. *Chemical reviews, 95*(3), 735-758. https://doi.org/10.1021/cr00035a013

[179] Liqiang, J., Yichun, Q., Baiqi, W., Shudan, L., Baojiang, J., Libin, Y., Wei, F., Honggang, F. & Jiazhong, S. (2006). Review of photoluminescence performance of nano-sized semiconductor materials and its relationships with photocatalytic activity. *Solar Energy Materials and Solar Cells, 90*(12), 1773-1787. https://doi.org/10.1016/j.solmat.2005.11.007

[180] Liu, G., Wang, L., Yang, H. G., Cheng, H. M., & Lu, G. Q. M. (2010). Titania-based photocatalysts-crystal growth, doping and heterostructuring. *Journal of Materials Chemistry*, *20*(5), 831-843. https://doi.org/10.1039/B909930A

[181] Liu, G., Yang, H. G., Pan, J., Yang, Y. Q., Lu, G. Q., & Cheng, H. M. (2014). Titanium dioxide crystals with tailored facets. *Chemical reviews, 114*(19), 9559-9612. https://doi.org/10.1021/cr400621z

[182] Liu, L., & Hao, X. (2008). Study of the effect of low-power pulse laser on arc plasma and magnesium alloy target in hybrid welding by spectral diagnosis technique. *Journal of Physics D: Applied Physics*, *41*(20), 205202. https://doi.org/10.1088/0022-3727/41/20/205202

[183] Liu, W. W., Chai, S. P., Mohamed, A. R., & Hashim, U. (2014). Synthesis and characterization of graphene and carbon nanotubes: A review on the past and recent developments. *Journal of Industrial and Engineering Chemistry*, *20*(4), 1171-1185. https://doi.org/10.1016/j.jiec.2013.08.028

[184] Liu, W., Wang, B., & Zhang, M. (2021). Effect of process parameters on the microstructure and performance of TiO_2-loaded activated carbon. *ACS omega*, *6*(50), 35076-35092. https://doi.org/10.1021/acsomega.1c05833

[185] Liu, X., Yang, Y., Shi, X., & Li, K. (2015). Fast photocatalytic degradation of methylene blue dye using a low-power diode laser. *Journal of hazardous materials, 283*, 267-275. https://doi.org/10.1016/j.jhazmat.2014.09.031

[186] Livraghi, S., Elghniji, K., Czoska, A. M., Paganini, M. C., Giamello, E., & Ksibi, M. (2009). Nitrogen-doped and nitrogen–fluorine-codoped titanium dioxide. Nature and concentration of the photoactive species and their role in determining the photocatalytic activity under visible light. *Journal of Photochemistry and Photobiology A: Chemistry*, *205*(2-3), 93-97. https://doi.org/10.1016/j.jphotochem.2009.04.010

[187] Long, M., Qin, Y., Chen, C., Guo, X., Tan, B., & Cai, W. (2013). Origin of visible light photoactivity of reduced graphene oxide/TiO_2 by in situ hydrothermal growth of undergrown TiO_2 with graphene oxide. *The Journal of Physical Chemistry C, 117*(32), 16734-16741. https://doi.org/10.1021/jp4058109

[188] Lu, L., Shan, R., Shi, Y., Wang, S., & Yuan, H. (2019). A novel TiO_2/biochar composite catalyst for photocatalytic degradation of methyl orange. *Chemosphere, 222*, 391-398. https://doi.org/10.1016/j.chemosphere.2019.01.132

[189] Ma, B., Xue, W., Hu, C., Liu, H., Qu, J., & Li, L. (2019). Characteristics of microplastic removal via coagulation and ultrafiltration during drinking water treatment. *Chemical Engineering Journal*, *359*, 159-167. https://doi.org/10.1016/j.cej.2018.11.155

[190] Ma, Y., Fu, J. W., Tao, X., Li, X., & Chen, J. F. (2011). Low temperature synthesis of iodine-doped TiO_2 nanocrystallites with enhanced visible-induced photocatalytic activity. *Applied Surface Science*, *257*(11), 5046-5051. https://doi.org/10.1016/j.apsusc.2011.01.019

[191] Ma, Y., Zhang, J., Tian, B., Chen, F., & Wang, L. (2010). Synthesis and characterization of thermally stable Sm, N co-doped TiO_2 with highly visible light activity. *Journal of Hazardous Materials*, *182*(1-3), 386-393. https://doi.org/10.1016/j.jhazmat.2010.06.045

[192] Malik, S., Muhammad, K., & Waheed, Y. (2023). Nanotechnology: a revolution in modern industry. *Molecules*, *28*(2), 661. https://doi.org/10.3390/molecules28020661

[193] Mallakpour, S., & Sadeghzadeh, R. (2017). A Benign and Simple Strategy for Surface Modification of Al_2O_3 Nanoparticles with Citric Acid and L (+)-Ascorbic Acid and Its Application for the Preparation of Novel Poly (vinyl chloride) Nanocomposite Films. *Advances in Polymer Technology, 36*(4), 409-417. https://doi.org/10.1002/adv.21622

[194] Mallakpour, S., & Shafiee, E. (2017). The synthesis of poly (vinyl chloride) nanocomposite films containing ZrO_2 nanoparticles modified with vitamin B_1 with the aim of improving the mechanical, thermal and optical properties. *Designed monomers and polymers*, *20*(1), 378-388. https://doi.org/10.1080/15685551.2016.1273436

[195] Manju, Jain, M., Madas, S., Vashishtha, P., Rajput, P., Gupta, G., Kahaly, M.U., Özdoğan, K., Vij, A. & Thakur, A. (2020). Oxygen vacancies induced photoluminescence in $SrZnO_2$ nanophosphors probed by theoretical and experimental analysis. *Scientific Reports, 10*(1), 17364. https://doi.org/10.1038/s41598-020-74436-8

[196] Mao, C. C., & Weng, H. S. (2009). Promoting effect of adding carbon black to TiO_2 for aqueous photocatalytic degradation of methyl orange. *Chemical Engineering Journal, 155*(3), 744-749. https://doi.org/10.1016/j.cej.2009.09.016

[197] Mariano, S., Tacconi, S., Fidaleo, M., Rossi, M., & Dini, L. (2021). Micro and nanoplastics identification: classic methods and innovative detection techniques. *Frontiers in toxicology*, *3*, 636640. https://doi.org/10.3389/ftox.2021.636640

[198] Mazari, S. A., Ali, E., Abro, R., Khan, F. S. A., Ahmed, I., Ahmed, M., Nizamuddin, S., Siddiqui, T.H., Hossain, N., Mubarak, N.M. & Shah, A. (2021). Nanomaterials: Applications, waste-handling, environmental toxicities, and future challenges–A review. *Journal of Environmental Chemical Engineering*, *9*(2), 105028. https://doi.org/10.1016/j.jece.2021.105028

[199] Meena, P. L., Saini, J. K., Surela, A. K., Poswal, K., & Chhachhia, L. K. (2024). Fabrication of polyaniline-coated porous and fibrous nanocomposite with granular morphology using tea waste carbon for effective removal of rhodamine B dye from water samples. *Biomass Conversion and Biorefinery*, *14*(2), 1711-1730. https://doi.org/10.1007/s13399-021-02267-2

[200] Megat Nabil Mohsin, S., Hussein, M. Z., Sarijo, S. H., Fakurazi, S., Arulselvan, P., & Taufiq-Yap, Y. H. (2018). Nanolayered composite with enhanced ultraviolet ray absorption properties from simultaneous intercalation of sunscreen molecules. *International Journal of Nanomedicine*, 6359-6374. https://doi.org/10.2147/IJN.S171390

[201] Miao, F., Liu, Y., Gao, M., Yu, X., Xiao, P., Wang, M., Wang, S & Wang, X. (2020). Degradation of polyvinyl chloride microplastics via an electro-Fenton-

like system with a TiO_2/graphite cathode. *Journal of Hazardous Materials*, *399*, 123023.
https://doi.org/10.1016/j.jhazmat.2020.123023

[202] Miino, M. C., Galafassi, S., Zullo, R., Torretta, V., & Rada, E. C. (2024). Microplastics removal in wastewater treatment plants: A review of the different approaches to limit their release in the environment. *Science of the Total Environment*, *930*, 172675.
https://doi.org/10.1016/j.scitotenv.2024.172675

[203] Min, S., Wang, F., Jin, Z., & Xu, J. (2014). Cu_2O nanoparticles decorated $BiVO_4$ as an effective visible-light-driven pn heterojunction photocatalyst for methylene blue degradation. *Superlattices and Microstructures, 74*, 294-307.
https://doi.org/10.1016/j.spmi.2014.07.003

[204] Minz, P., & Mishra, S. (2023). Jackfruit peel derived $ZnCl_2$-impregnated activated carbon: optimization, characterization, and application in dye removal. *Biomass Conversion and Biorefinery,* 1-18.
https://doi.org/10.1007/s13399-023-04592-0

[205] Mohanta, J., Dey, B., & Dey, S. (2020). Highly porous iron-zirconium binary oxide for efficient removal of Congo red from water. *Desalination and Water Treatment, 189*, 227-242.
https://doi.org/10.5004/dwt.2020.25570

[206] Mohtar, S. S., Aziz, F., Ismail, A. F., Sambudi, N. S., Abdullah, H., Rosli, A. N., & Ohtani, B. (2021). Impact of Doping and Additive Applications on Photocatalyst Textural Properties in Removing Organic Pollutants: A Review. *Catalysts*, *11*(10), 1160.
https://doi.org/10.3390/catal11101160

[207] Molinari, R., Argurio, P., Bellardita, M., Palmisano, L., & Bertoni, C. (2017). Photocatalytic processes in membrane reactors. In *Comprehensive membrane science and engineering 2nd Edition*.
https://doi.org/10.1016/B978-0-12-409547-2.12220-6

[208] Moura, M. M. D. M. S., Lima, V. E., Neto, A. A. D. M., Lucena, A. L. A. D., Napoleão, D. C., & Duarte, M. M. M. (2021). Degradation of the mixture of the ketoprofen, meloxicam and tenoxicam drugs using TiO_2/metal photocatalysers supported in polystyrene packaging waste. *Water Science and Technology*, *83*(4), 863-876.
https://doi.org/10.2166/wst.2021.025

[209] Muhonja, C. N., Makonde, H., Magoma, G., & Imbuga, M. (2018). Biodegradability of polyethylene by bacteria and fungi from Dandora dumpsite Nairobi-Kenya. *PloS one*, *13*(7), e0198446.
https://doi.org/10.1371/journal.pone.0198446

[210] Mulindwa, P., Kasule, J. S., Nantaba, F., Wasswa, J., & Expósito, A. J. (2024). Bioadsorbents for removal of microplastics from water ecosystems: a review. *International Journal of Sustainable Engineering, 17*(1), 582-599.
https://doi.org/10.1080/19397038.2024.2374003

[211] Nabi, I., Li, K., Cheng, H., Wang, T., Liu, Y., Ajmal, S., Yang, Y., Feng, Y. & Zhang, L. (2020). Complete photocatalytic mineralization of microplastic on TiO_2 nanoparticle film. *Iscience*, *23*(7). https://doi.org/10.1016/j.isci.2020.101326

[212] Nagaraja, R., Kottam, N., Girija, C. R., & Nagabhushana, B. M. (2012). Photocatalytic degradation of Rhodamine B dye under UV/solar light using ZnO nanopowder synthesized by solution combustion route. *Powder technology, 215*, 91-97. https://doi.org/10.1016/j.powtec.2011.09.014

[213] Nandiyanto, A. B. D., Zaen, R., & Oktiani, R. (2020). Correlation between crystallite size and photocatalytic performance of micrometer-sized monoclinic WO_3 particles. *Arabian Journal of Chemistry, 13*(1), 1283-1296. https://doi.org/10.1016/j.arabjc.2017.10.010

[214] Natarajan, T. S., Gopi, P. K., Natarajan, K., Bajaj, H. C., & Tayade, R. J. (2021). TiO_2/graphene oxide nanocomposite with enhanced photocatalytic capacity for degradation of 2, 4-dichlorophenoxyacetic acid herbicide. *Water-Energy Nexus, 4*, 103-112. https://doi.org/10.1016/j.wen.2021.07.001

[215] Nazri, S. R. B., Liu, W. W., Khe, C. S., Hidayah, N. M. S., Teoh, Y. P., Voon, C. H., Lee, H.C. & Adelyn, P. Y. P. (2018, December). Synthesis, characterization and study of graphene oxide. In AIP Conference Proceedings (Vol. 2045, No. 1). AIP Publishing. https://doi.org/10.1063/1.5080846

[216] Neme, I., Gonfa, G., & Masi, C. (2022). Activated carbon from biomass precursors using phosphoric acid: A review. *Heliyon*, *8*(12). https://doi.org/10.1016/j.heliyon.2022.e11940

[217] Nguyen, T. P., Tran, Q. B., Ly, Q. V., Hai, L. T., Le, D. T., Tran, M. B., Ho, T.T.T., Nguyen, X.C., Shokouhimehr, M., Vo, D.V.N. & Lam, S.S (2020). Enhanced visible photocatalytic degradation of diclofen over N-doped TiO_2 assisted with H_2O_2: A kinetic and pathway study. *Arabian journal of chemistry, 13*(11), 8361-8371. https://doi.org/10.1016/j.arabjc.2020.05.023

[218] Nguyen-Phan, T. D., Pham, V. H., Shin, E. W., Pham, H. D., Kim, S., Chung, J. S., Kim, E.J. & Hur, S. H. (2011). The role of graphene oxide content on the adsorption-enhanced photocatalysis of titanium dioxide/graphene oxide composites. *Chemical Engineering Journal, 170*(1), 226-232. https://doi.org/10.1016/j.cej.2011.03.060

[219] Ni, Y., Wang, W., Huang, W., Lu, C., & Xu, Z. (2014). Graphene strongly wrapped TiO_2 for high-reactive photocatalyst: A new sight for significant application of graphene. *Journal of colloid and interface science, 428,* 162-169. https://doi.org/10.1016/j.jcis.2014.04.022

[220] Nosratabad, N. A., Yan, Q., Cai, Z., & Wan, C. (2024). Exploring nanomaterial-modified biochar for environmental remediation applications. *Heliyon, 10*, e37123
https://doi.org/10.1016/j.heliyon.2024.e37123

[221] Ozser, M. E., Sarkodie, S. A., Mohiuddin, O., & Ozesme, G. (2017). Novel derivatives of regioisomerically pure 1, 7-disubstituted perylene diimide dyes bearing phenoxy and pyrrolidinyl substituents: Synthesis, photophysical, thermal, and structural properties. *Journal of Luminescence, 192*, 414-423.
https://doi.org/10.1016/j.jlumin.2017.07.019

[222] Padmanabhan, N. T., Thomas, N., Louis, J., Mathew, D. T., Ganguly, P., John, H., & Pillai, S. C. (2021). Graphene coupled TiO_2 photocatalysts for environmental applications: A review. *Chemosphere*, *271*, 129506.
https://doi.org/10.1016/j.chemosphere.2020.129506

[223] Paiu, M., Lutic, D., Favier, L., & Gavrilescu, M. (2025). Heterogeneous Photocatalysis for Advanced Water Treatment: Materials, Mechanisms, Reactor Configurations, and Emerging Applications. Applied Sciences, 15(10), 5681.
https://doi.org/10.3390/app15105681

[224] Pal, D., Prabhakar, R., Barua, V. B., Zekker, I., Burlakovs, J., Krauklis, A., Hogland, W. & Vincevica-Gaile, Z. (2025). Microplastics in aquatic systems: A comprehensive review of its distribution, environmental interactions, and health risks. *Environmental Science and Pollution Research*, *32*(1), 56-88.
https://doi.org/10.1007/s11356-024-35741-1

[225] Pan, S. S., Shen, Y. D., Teng, X. M., Zhang, Y. X., Li, L., Chu, Z. Q., Zhang, J.P., Li, G.H. & Hu, X. (2009). Substitutional nitrogen-doped tin oxide single crystalline submicrorod arrays: Vertical growth, band gap tuning and visible light-driven photocatalysis. Materials Research Bulletin, 44(11), 2092-2098.
https://doi.org/10.1016/j.materresbull.2009.07.011

[226] Pan, Y., Gao, S. H., Ge, C., Gao, Q., Huang, S., Kang, Y., Luo, G., Zhang, Z., Fan, L., Zhu, Y. & Wang, A. J. (2023). Removing microplastics from aquatic environments: A critical review. *Environmental Science and Ecotechnology*, *13*, 100222.
https://doi.org/10.1016/j.ese.2022.100222

[227] Panchenko, V. N., Matsko, M. A., Selishchev, D. S., & Kozlov, D. V. (2023). Polymeric Floating Photocatalysts Based on PE/TiO_2 Composites for the Removal of Organic Pollutants in Water. *Journal of Composites Science*, *7*(8), 318.
https://doi.org/10.3390/jcs7080318

[228] Pandis, P. K., Kalogirou, C., Kanellou, E., Vaitsis, C., Savvidou, M. G., Sourkouni, G., Zorpas, A.A. & Argirusis, C. (2022). Key points of advanced oxidation processes (AOPs) for wastewater, organic pollutants and pharmaceutical waste treatment: A mini review. *ChemEngineering*, *6*(1), 8.
https://doi.org/10.3390/chemengineering6010008

[229] Pang, Y. L., & Abdullah, A. Z. (2012). Comparative study on the process behavior and reaction kinetics in sonocatalytic degradation of organic dyes by powder and nanotubes TiO_2. *Ultrasonics sonochemistry*, *19*(3), 642-651. https://doi.org/10.1016/j.ultsonch.2011.09.007

[230] Pang, Y. L., Lim, S., & Lee, R. K. L. (2020). Enhancement of sonocatalytic degradation of organic dye by using titanium dioxide (TiO_2)/activated carbon (AC) derived from oil palm empty fruit bunch. *Environmental Science and Pollution Research, 27*(28), 34638-34652. https://doi.org/10.1007/s11356-019-05373-x

[231] Parvathiraja, C., Katheria, S., Siddiqui, M. R., Wabaidur, S. M., Islam, M. A., & Lai, W. C. (2022). Activated carbon-loaded titanium dioxide nanoparticles and their photocatalytic and antibacterial investigations. *Catalysts, 12*(8), 834. https://doi.org/10.3390/catal12080834

[232] Pascariu, P., Gherasim, C., & Airinei, A. (2023). Metal oxide nanostructures (MONs) as photocatalysts for ciprofloxacin degradation. *International Journal of Molecular Sciences*, *24*(11), 9564. https://doi.org/10.3390/ijms24119564

[233] Patil, P. O., Nangare, S. N., Patil, P. P., Patil, A. G., Patil, D. R., Tade, R. S., Patil, A.M., Deshmukh, P.K. & Bari, S. B. (2021). Fabrication of N-doped graphene@ TiO_2 nanocomposites for its adsorption and absorbing performance with facile recycling. *Nano Biomed Eng, 13*(2), 179-190. https://doi.org/10.5101/nbe.v13i2.p179-190.

[234] Pattnaik, A., Sahu, J. N., Poonia, A. K., & Ghosh, P. (2023). Current perspective of nano-engineered metal oxide based photocatalysts in advanced oxidation processes for degradation of organic pollutants in wastewater. *Chemical Engineering Research and Design*, *190*, 667-686. https://doi.org/10.1016/j.cherd.2023.01.014

[235] Pei, F., Liu, Y., Xu, S., Lü, J., Wang, C., & Cao, S. (2013). Nanocomposite of graphene oxide with nitrogen-doped TiO_2 exhibiting enhanced photocatalytic efficiency for hydrogen evolution. *International journal of hydrogen energy, 38*(6), 2670-2677. https://doi.org/10.1016/j.ijhydene.2012.12.045

[236] Peng, B. Y., Chen, Z., Chen, J., Zhou, X., Wu, W. M., & Zhang, Y. (2021). Biodegradation of polylactic acid by yellow mealworms (larvae of Tenebrio molitor) via resource recovery: a sustainable approach for waste management. *Journal of Hazardous Materials*, *416*, 125803. https://doi.org/10.1016/j.jhazmat.2021.125803

[237] Peng, F., Cai, L., Huang, L., Yu, H., & Wang, H. (2008). Preparation of nitrogen-doped titanium dioxide with visible-light photocatalytic activity using a facile hydrothermal method. *journal of Physics and Chemistry of Solids*, *69*(7), 1657-1664. https://doi.org/10.1016/j.jpcs.2007.12.003

[238] Peng, W., Li, H., Liu, Y., & Song, S. (2016). Adsorption of methylene blue on graphene oxide prepared from amorphous graphite: Effects of pH and foreign ions. *Journal of Molecular Liquids, 221*, 82-87. https://doi.org/10.1016/j.molliq.2016.05.074

[239] Peng, Z., Cui, Y., Song, J., Chen, S., Ma, Z., & Cao, F. (2025). The effect of nitrogen doping on the ablation resistance of zirconium carbide ceramics. *Journal of Advanced Ceramics*, *14*(5). https://doi.org/10.26599/JAC.2025.9221069

[240] Pérez-Molina, Á., Morales-Torres, S., Maldonado-Hódar, F. J., & Pastrana-Martínez, L. M. (2020). Functionalized graphene derivatives and TiO_2 for high visible light photodegradation of azo dyes. *Nanomaterials*, *10*(6), 1106. https://doi.org/10.3390/nano10061106

[241] Petala, A., Noe, A., Frontistis, Z., Drivas, C., Kennou, S., Mantzavinos, D., & Kondarides, D. I. (2019). Synthesis and characterization of $CoO_x/BiVO_4$ photocatalysts for the degradation of propyl paraben. *Journal of hazardous materials, 372*, 52-60. https://doi.org/10.1016/j.jhazmat.2018.03.008

[242] Pham, T. H., Viet, N. M., Hoai, P. T. T., Jung, S. H., & Kim, T. (2023). Graphitic carbon nitride metal-free photocatalyst for the simultaneous removal of emerging pharmaceutical pollutants in wastewater. *Environmental Research*, *231*, 116246. https://doi.org/10.1016/j.envres.2023.116246

[243] Pilapitiya, P. N. T., & Ratnayake, A. S. (2024). The world of plastic waste: A review. *Cleaner Materials*, *11*, 100220. https://doi.org/10.1016/j.clema.2024.100220

[244] Pingmuang, K., Chen, J., Kangwansupamonkon, W., Wallace, G. G., Phanichphant, S., & Nattestad, A. (2017). Composite photocatalysts containing $BiVO_4$ for degradation of cationic dyes. *Scientific reports*, *7*(1), 8929. https://doi.org/10.1038/s41598-017-09514-5

[245] Pino-Ramos, V. H., Bucio, E., Daza-Gomez, L. C., & Díaz, D. (2025). Photocatalytic degradation of polystyrene under mild conditions by nanostructured bismuth carbonate. *Polymer Degradation and Stability, 235*, 111271. https://doi.org/10.1016/j.polymdegradstab.2025.111271

[246] Posa, V. R., Annavaram, V., Koduru, J. R., Ammireddy, V. R., & Somala, A. R. (2016). Graphene-ZnO nanocomposite for highly efficient photocatalytic degradation of methyl orange dye under solar light irradiation. *Korean Journal of Chemical Engineering*, *33*(2), 456-464. https://doi.org/10.1007/s11814-015-0145-4

[247] Prakash, J. (2022). Mechanistic insights into graphene oxide driven photocatalysis as Co-catalyst and sole catalyst in degradation of organic dye pollutants. *Photochem*, *2*(3), 651-671. https://doi.org/10.3390/photochem2030043

[248] Prakash, O., Tripathy, P., Panchal, D., Sharma, A., & Pal, S. (2023). Advance oxidation processes for remediation of antibiotics from wastewater. In *Degradation of Antibiotics and Antibiotic-Resistant Bacteria from Various Sources* (pp. 369-388). Academic Press. https://doi.org/10.1016/B978-0-323-99866-6.00009-X

[249] Puteri, M. N., Gew, L. T., Ong, H. C., & Ming, L. C. (2025). Technologies to eliminate microplastic from water: Current approaches and future prospects. *Environment International*, 109397. https://doi.org/10.1016/j.envint.2025.109397

[250] Qi, W. J., Nieh, R., Lee, B. H., Kang, L., Jeon, Y., & Lee, J. C. (2000). Electrical and reliability characteristics of ZrO_2 deposited directly on Si for gate dielectric application. *Applied Physics Letters*, *77*(20), 3269-3271. https://doi.org/10.1063/1.1326482

[251] Quevedo, A. C., Guggenheim, E., Briffa, S. M., Adams, J., Lofts, S., Kwak, M., Lee, T.G., Johnston, C., Wagner, S. & Valsami-Jones, E. (2021). UV-Vis spectroscopic characterization of nanomaterials in aqueous media. https://doi.org/10.3791/61764

[252] Raj, K. J. A., Ramaswamy, A. V., & Viswanathan, B. (2009). Surface area, pore size, and particle size engineering of titania with seeding technique and phosphate modification. *The Journal of Physical Chemistry C*, *113*(31), 13750-13757. https://doi.org/10.1021/jp902468v

[253] Rajaitha, P. M., Hajra, S., Sahu, M., Mistewicz, K., Toroń, B., Abolhassani, R., Panda, S., Mishra, Y.K. & Kim, H. J. (2022). Unraveling highly efficient nanomaterial photocatalyst for pollutant removal: a comprehensive review and future progress. *Materials Today Chemistry*, *23*, 100692. https://doi.org/10.1016/j.mtchem.2021.100692

[254] Rajmohan, K. V. S., Ramya, C., Viswanathan, M. R., & Varjani, S. (2019). Plastic pollutants: effective waste management for pollution control and abatement. *Current Opinion in Environmental Science & Health*, *12*, 72-84. https://doi.org/10.1016/j.coesh.2019.08.006

[255] Rajput, R. B., & Kale, R. B. (2021). Hydro/solvothermally synthesized visible light driven modified SnO_2 heterostructure as a photocatalyst for water remediation: A review. *Environmental Advances*, *5*, 100081. https://doi.org/10.1016/j.envadv.2021.100081

[256] Ramesh, K., Gnanavel, B., & Shkir, M. (2021). Enhanced visible light photocatalytic degradation of bisphenol A (BPA) by reduced graphene oxide (RGO)–metal oxide (TiO_2, ZnO and WO_3) based nanocomposites. *Diamond and Related Materials*, *118*, 108514. https://doi.org/10.1016/j.diamond.2021.108514

[257] Ramki, D., Dharmendira Kumar, M., & Siva Karthik, P. (2023). Nanohybrids of 1D tin oxide (SnO_2) nanotubes 2D-reduced graphene oxide (RGO) for improving photodegradation of Cr (VI). *Journal of Materials Science: Materials in Electronics*, *34*(6), 551.

https://doi.org/10.1007/s10854-023-09854-1

[258] Ramprasath, R. H., Kajamuhideen, M. S., Tiwari, B., & Sethuraman, K. (2023). Growth, structural, optical, and thermal behavior of bibenzyl organic single crystal for scintillator applications. *Journal of Materials Science: Materials in Electronics*, *34*(7), 620. https://doi.org/10.1007/s10854-023-10013-9

[259] Rani, N., Khan, Y., Yadav, S., Saini, K., & Maity, D. (2024). Application of Metal Oxide Nanoparticles in Different Carcinomas. *Journal of Nanotheranostics*, *5*(4), 253-272. https://doi.org/10.3390/jnt5040015

[260] Raval, N., Maheshwari, R., Kalyane, D., Youngren-Ortiz, S. R., Chougule, M. B., & Tekade, R. K. (2019). Importance of physicochemical characterization of nanoparticles in pharmaceutical product development. In *Basic fundamentals of drug delivery* (pp. 369-400). Academic Press. https://doi.org/10.1016/B978-0-12-817909-3.00010-8

[261] Romero Saez, M., Jaramillo, L. Y., Saravanan, R., Benito, N., Pabón, E., Mosquera, E., & Gracia Caroca, F. (2017). Notable photocatalytic activity of TiO_2-polyethylene nanocomposites for visible light degradation of organic pollutants. https://doi.org/10.3144/expresspolymlett.2017.86

[262] Ruidíaz-Martínez, M., Álvarez, M. A., López-Ramón, M. V., Cruz-Quesada, G., Rivera-Utrilla, J., & Sánchez-Polo, M. (2020). Hydrothermal synthesis of rGO-TiO_2 composites as high-performance UV photocatalysts for ethylparaben degradation. *Catalysts, 10*(5), 520. https://doi.org/10.3390/catal10050520

[263] Saeed, K., Sadiq, M., Khan, I., Ullah, S., Ali, N., & Khan, A. (2018). Synthesis, characterization, and photocatalytic application of Pd/ZrO_2 and Pt/ZrO_2. Applied Water Science, 8(2), 60. https://doi.org/10.1007/s13201-018-0709-7

[264] Saini, S., Basera, P., Kumar, M., Bhumla, P., & Bhattacharya, S. (2020). Metastability triggered reactivity in clusters at realistic conditions: a case study of N-doped (TiO_2) n for photocatalysis. *Journal of Physics: Materials*, *4*(1), 015001. https://doi.org/10.1088/2515-7639/abc090

[265] Sakthivel, S., Shankar, M. V., Palanichamy, M., Arabindoo, B., Bahnemann, D. W., & Murugesan, V. (2004). Enhancement of photocatalytic activity by metal deposition: characterisation and photonic efficiency of Pt, Au and Pd deposited on TiO_2 catalyst. *Water research*, *38*(13), 3001-3008. https://doi.org/10.1016/j.watres.2004.04.046

[266] Sanad, M. F., Shalan, A. E., Bazid, S. M., & Abdelbasir, S. M. (2018). Pollutant degradation of different organic dyes using the photocatalytic activity of ZnO@ ZnS nanocomposite materials. *Journal of environmental chemical engineering*, *6*(4), 3981-3990. https://doi.org/10.1016/j.jece.2018.05.035

[267] Sandeep, A., Priyadharshini, T., & Ravindra, A. V. (2024). Activated carbon derived from corncob via hydrothermal carbonization as a promising electrode for supercapacitors. *Materials Research Bulletin*, *179*, 112991. https://doi.org/10.1016/j.materresbull.2024.112991

[268] Sandhu, S., Krishnan, S., Karim, A. V., & Shriwastav, A. (2020). Photocatalytic denitrification of water using polystyrene immobilized TiO_2 as floating catalyst. *Journal of Environmental Chemical Engineering*, *8*(6), 104471. https://doi.org/10.1016/j.jece.2020.104471

[269] Sangami, G., & Dharmaraj, N. (2012). UV–visible spectroscopic estimation of photodegradation of rhodamine-B dye using tin (IV) oxide nanoparticles. Spectrochimica Acta Part A: Molecular and Biomolecular Spectroscopy, 97, 847-852. https://doi.org/10.1016/j.saa.2012.07.068

[270] Saranya, K. S., Vellora Thekkae Padil, V., Senan, C., Pilankatta, R., Saranya, K., George, B., Wacławek, S. & Černík, M. (2018). Green synthesis of high temperature stable anatase titanium dioxide nanoparticles using gum kondagogu: characterization and solar driven photocatalytic degradation of organic dye. *Nanomaterials, 8*(12), 1002. https://doi.org/10.3390/nano8121002

[271] Sarno, A., Olafsen, K., Kubowicz, S., Karimov, F., Sait, S. T., Sørensen, L., & Booth, A. M. (2020). Accelerated hydrolysis method for producing partially degraded polyester microplastic fiber reference materials. *Environmental Science & Technology Letters*, *8*(3), 250-255. https://doi.org/10.1021/acs.estlett.0c01002

[272] Sayama, K., & Arakawa, H. (1993). Photocatalytic decomposition of water and photocatalytic reduction of carbon dioxide over zirconia catalyst. *The Journal of Physical Chemistry*, *97*(3), 531-533. https://doi.org/10.1021/j100105a001

[273] Schade, A., Melzer, M., Zimmermann, S., Schwarz, T., Stoewe, K., & Kuhn, H. (2024). Plastic waste recycling-A chemical recycling perspective. *ACS Sustainable Chemistry & Engineering*, *12*(33), 12270-12288. https://doi.org/10.1021/acssuschemeng.4c02551

[274] Scrimieri, L., Velardi, L., Serra, A., Manno, D., Ferrari, F., Cantarella, M., & Calcagnile, L. (2020). Enhanced adsorption capacity of porous titanium dioxide nanoparticles synthetized in alkaline sol. *Applied Physics A*, *126*(12), 926. https://doi.org/10.1007/s00339-020-04103-2

[275] Sen, P., Bhattacharya, P., Mukherjee, G., Ganguly, J., Marik, B., Thapliyal, D., Verma, S., Verros, G.D., Chauhan, M.S. & Arya, R. K. (2023). Advancements in doping strategies for enhanced photocatalysts and adsorbents in environmental remediation. *Technologies*, *11*(5), 144. https://doi.org/10.3390/technologies11050144

[276] Sendão, R. M., da Silva, J. C. E., & da Silva, L. P. (2022). Photocatalytic removal of pharmaceutical water pollutants by TiO_2–Carbon dots nanocomposites: a review. *Chemosphere*, *301*, 134731. https://doi.org/10.1016/j.chemosphere.2022.134731

[277] Senthilnathan, J., & Philip, L. (2010). Photocatalytic degradation of lindane under UV and visible light using N-doped TiO_2. *Chemical engineering journal*, *161*(1-2), 83-92. https://doi.org/10.1016/j.cej.2010.04.034

[278] Shabna, S., Dhas, S. S. J., & Biju, C. S. (2023). Potential progress in SnO_2 nanostructures for enhancing photocatalytic degradation of organic pollutants. Catalysis Communications, 177, 106642. https://doi.org/10.1016/j.catcom.2023.106642

[279] Sheydaei, M., Shiadeh, H. R. K., Ayoubi-Feiz, B., & Ezzati, R. (2018). Preparation of nano N-TiO_2/graphene oxide/titan grid sheets for visible light assisted photocatalytic ozonation of cefixime. *Chemical Engineering Journal, 353,* 138-146. https://doi.org/10.1016/j.cej.2018.07.089

[280] Shi, J. W., Ai, H. Y., Chen, J. W., Cui, H. J., & Fu, M. L. (2014). The composite of nitrogen-doped anatase titania plates with exposed {0 0 1} facets/graphene nanosheets for enhanced visible-light photocatalytic activity. *Journal of colloid and interface science, 430,* 100-107. https://doi.org/10.1016/j.jcis.2014.05.027

[281] Shi, J. W., Cui, H. J., Chen, J. W., Fu, M. L., Xu, B., Luo, H. Y., & Ye, Z. L. (2012). TiO_2/activated carbon fibers photocatalyst: Effects of coating procedures on the microstructure, adhesion property, and photocatalytic ability. *Journal of colloid and interface science, 388*(1), 201-208. https://doi.org/10.1016/j.jcis.2012.08.038

[282] Shi, Y., Liu, P., Wu, X., Shi, H., Huang, H., Wang, H., & Gao, S. (2021). Insight into chain scission and release profiles from photodegradation of polycarbonate microplastics. *Water Research*, *195*, 116980. https://doi.org/10.1016/j.watres.2021.116980

[283] Si, J., Liu, Y., Chang, S., Wu, D., Tian, B., & Zhang, J. (2017). AgBr@ TiO_2/GO ternary composites with enhanced photocatalytic activity for oxidation of benzyl alcohol to benzaldehyde. *Research on Chemical Intermediates*, *43*(4), 2067-2080. https://doi.org/10.1007/s11164-016-2747-9

[284] Siburian, R., Sihotang, H., Raja, S. L., Supeno, M., & Simanjuntak, C. (2018). New route to synthesize of graphene nano sheets. *Oriental journal of chemistry, 34*(1), 182. http://dx.doi.org/10.13005/ojc/340120

[285] Silva, D. B., & Marques, A. C. (2025). TiO_2-based photocatalytic degradation of microplastics in water: Current status, challenges and future perspectives. *Journal of Water Process Engineering*, *72*, 107465. https://doi.org/10.1016/j.jwpe.2025.107465

[286] Smith, M., Scudiero, L., Espinal, J., McEwen, J. S., & Garcia-Perez, M. (2016). Improving the deconvolution and interpretation of XPS spectra from chars by ab initio calculations. *Carbon, 110*, 155-171. https://doi.org/10.1016/j.carbon.2016.09.012

[287] Spilarewicz-Stanek, K., Kisielewska, A., Ginter, J., Bałuszyńska, K., & Piwoński, I. (2016). Elucidation of the function of oxygen moieties on graphene oxide and reduced graphene oxide in the nucleation and growth of silver nanoparticles. *RSC advances*, *6*(65), 60056-60067. https://doi.org/10.1039/C6RA10483E

[288] Sreethawong, T., Laehsalee, S., & Chavadej, S. (2009). Use of Pt/N-doped mesoporous-assembled nanocrystalline TiO_2 for photocatalytic H_2 production under visible light irradiation. *Catalysis Communications*, *10*(5), 538-543. https://doi.org/10.1016/j.catcom.2008.10.029

[289] Sreethawong, T., Ngamsinlapasathian, S., & Yoshikawa, S. (2013). Synthesis of crystalline mesoporous-assembled ZrO_2 nanoparticles via a facile surfactant-aided sol-gel process and their photocatalytic dye degradation activity. *Chemical engineering journal*, *228*, 256-262. https://doi.org/10.1016/j.cej.2013.04.111

[290] Sudrajat, H., Babel, S., Sakai, H., & Takizawa, S. (2016). Rapid enhanced photocatalytic degradation of dyes using novel N-doped ZrO_2. *Journal of environmental management, 165*, 224-234. https://doi.org/10.1016/j.jenvman.2015.09.036

[291] Suhdi, & Wang, S. C. (2021). Fine activated carbon from rubber fruit shell prepared by using $ZnCl_2$ and KOH activation. *Applied Sciences*, *11*(9), 3994. https://doi.org/10.3390/app11093994

[292] Sun, J., Qiao, L., Sun, S., & Wang, G. (2008). Photocatalytic degradation of Orange G on nitrogen-doped TiO_2 catalysts under visible light and sunlight irradiation. *Journal of hazardous materials, 155*(1-2), 312-319. https://doi.org/10.1016/j.jhazmat.2007.11.062

[293] Sun, C., Wang, Z., Chen, L., & Li, F. (2020). Fabrication of robust and compressive chitin and graphene oxide sponges for removal of microplastics with different functional groups. *Chemical Engineering Journal*, *393*, 124796. https://doi.org/10.1016/j.cej.2020.124796

[294] Sun, W., Zhang, S., Liu, Z., Wang, C., & Mao, Z. (2008). Studies on the enhanced photocatalytic hydrogen evolution over Pt/PEG-modified TiO_2 photocatalysts. *International Journal of Hydrogen Energy*, *33*(4), 1112-1117. https://doi.org/10.1016/j.ijhydene.2007.12.059

[295] Tahir, M. B., Rafique, M., Rafique, M. S., Fatima, N., & Israr, Z. (2020). Metal oxide-and metal sulfide-based nanomaterials as photocatalysts. In *Nanotechnology and Photocatalysis for Environmental Applications* (pp. 77-96). Elsevier. https://doi.org/10.1016/B978-0-12-821192-2.00006

[296] Talvitie, J., Mikola, A., Koistinen, A., & Setälä, O. (2017). Solutions to microplastic pollution–Removal of microplastics from wastewater effluent with advanced wastewater treatment technologies. *Water research*, *123*, 401-407. https://doi.org/10.1016/j.watres.2017.07.005

[297] Tayeb, A. M., & Hussein, D. S. (2015). Synthesis of TiO_2 nanoparticles and their photocatalytic activity for methylene blue. *American Journal of Nanomaterials, 3*(2), 57-63. https://doi.org/10.12691/ajn-3-2-2

[298] Tho, N. T., Mai, N. T. T., Van, N. T., Phat, B. D., Hieu, L. V., Thi, C. M., & Viet, P. V. (2019). Direct synthesis of reduced graphene oxide/TiO_2 nanotubes composite from graphite oxide as a high-efficiency visible-light-driven photocatalyst. *Journal of Nanoscience and Nanotechnology, 19*(8), 5195-5204. https://doi.org/10.1166/jnn.2019.16810

[299] Thoms, L. J., Girwidz, R., & Munich, L. M. U. (2013). Experimenting from a distance: Optical spectrometry via the internet. *MPTL18–B. Proc*, 59-63.

[300] Thongkrua, S., & Suriya, P. (2022). Removal of colour and COD in biologically pre-treated leachate using activated carbon from corn cobs. *Pollution, 8*(2), 657-670. https://doi.org/10.22059/poll.2022.328345.1153

[301] Tian, H., Ma, J., Li, K., & Li, J. (2009). Hydrothermal synthesis of S-doped TiO_2 nanoparticles and their photocatalytic ability for degradation of methyl orange. *Ceramics International*, *35*(3), 1289-1292. https://doi.org/10.1016/j.ceramint.2008.05.003

[302] Tilton, R. D., Robertson, C. R., & Gast, A. P. (1991). Manipulation of hydrophobic interactions in protein adsorption. *Langmuir, 7*(11), 2710-2718. https://doi.org/10.1021/la00059a051

[303] Todorova, N., Giannakopoulou, T., Vaimakis, T., & Trapalis, C. (2008). Structure tailoring of fluorine-doped TiO_2 nanostructured powders. *Materials Science and Engineering: B*, *152*(1-3), 50-54. https://doi.org/10.1016/j.mseb.2008.06.019

[304] Tomkiewicz, M. (2000). Scaling properties in photocatalysis. *Catalysis Today, 58*(2-3), 115-123. https://doi.org/10.1016/S0920-5861(00)00246-7

[305] Uheida, A., Mejía, H. G., Abdel-Rehim, M., Hamd, W., & Dutta, J. (2021). Visible light photocatalytic degradation of polypropylene microplastics in a continuous water flow system. *Journal of hazardous materials, 406,* 124299. https://doi.org/10.1016/j.jhazmat.2020.124299

[306] Umar, M., & Aziz, H. A. (2013). Photocatalytic degradation of organic pollutants in water. *Organic pollutants-monitoring, risk and treatment, 8*, 196-197. https://doi.org/10.5772/53699

[307] Umrao, S., Abraham, S., Theil, F., Pandey, S., Ciobota, V., Shukla, P. K. Rupp, C.J., Chakraborty, S., Ahuja, R., Popp, J. and Dietzek, B., & Srivastava, A. (2014). A possible mechanism for the emergence of an additional band gap due to a Ti–O–C bond in the TiO_2–graphene hybrid system for enhanced photodegradation of methylene blue under visible light. *RSC advances, 4*(104), 59890-59901. https://doi.org/10.1039/C4RA10572A

[308] Valadez-Renteria, E., Barrera-Rendon, E., Oliva, J., & Rodriguez-Gonzalez, V. (2021). Flexible CuS/TiO_2 based composites made with recycled bags and polystyrene for the efficient removal of the 4-CP pesticide from drinking water. *Separation and Purification Technology*, *270*, 118821. https://doi.org/10.1016/j.seppur.2021.118821

[309] Valiyaveettil Salimkumar, A., Kurisingal Cleetus, M. C., Ehigie, J. O., Onogbosele, C. O., Nisha, P., Kumar, B. S., Prabhakaran, M.P. & Rejish Kumar, V. J. (2024). Adsorption Behavior and Interaction of Micro-Nanoplastics in Soils and Aquatic Environment. *Management of Micro and Nano-plastics in Soil and Biosolids: Fate, Occurrence, Monitoring, and Remedies*, 283-311. https://doi.org/10.1007/978-3-031-51967-3_11

[310] Varela, C. F., Moreno-Aldana, L. C., & Agámez-Pertuz, Y. Y. (2024). Adsorption of pharmaceutical pollutants on $ZnCl_2$-activated biochar from corn cob: Efficiency, selectivity and mechanism. *Journal of Bioresources and Bioproducts, 9*(1), 58-73. https://doi.org/10.1016/j.jobab.2023.10.003

[311] Vidhu, V. K., & Philip, D. (2015). Biogenic synthesis of SnO_2 nanoparticles: Evaluation of antibacterial and antioxidant activities. *Spectrochimica Acta Part A: Molecular and Biomolecular Spectroscopy*, 134, 372-379. https://doi.org/10.1016/j.saa.2014.06.131

[312] Vital-Grappin, A. D., Ariza-Tarazona, M. C., Luna-Hernandez, V. M., Villarreal-Chiu, J. F., Hernandez-Lopez, J. M., Siligardi, C., & Cedillo-Gonzalez, E. I. (2021). The role of the reactive species involved in the photocatalytic degradation of HDPE microplastics using C, N-TiO_2 powders. *Polymers, 13*(7), 999. https://doi.org/10.3390/polym13070999

[313] Vo, T. S., Vo, T. T. B. C., Suk, J. W., & Kim, K. (2020). Recycling performance of graphene oxide-chitosan hybrid hydrogels for removal of cationic and anionic dyes. *Nano Convergence, 7*(1), 1-11. https://doi.org/10.1186/s40580-019-0215-0

[314] Wagner, C. D. (1979). Handbook of x-ray photoelectron spectroscopy: a reference book of standard data for use in x-ray photoelectron spectroscopy. p. 55344.

[315] Wang, B., Su, D., Park, J., Ahn, H., & Wang, G. (2012). Graphene-supported SnO_2 nanoparticles prepared by a solvothermal approach for an enhanced electrochemical performance in lithium-ion batteries. *Nanoscale research letters*, *7*, 1-7. https://doi.org/10.1186/1556-276X-7-215

[316] Wang, C. L., Hwang, W. S., Chu, H. L., Lin, H. J., Ko, H. H., & Wang, M. C. (2016). Kinetics of anatase transition to rutile TiO_2 from titanium dioxide precursor powders synthesized by a sol-gel process. *Ceramics International, 42*(11), 13136-13143.

https://doi.org/10.1016/j.ceramint.2016.05.101

[317] Wang, C., Ao, Y., Wang, P., Hou, J., Qian, J., & Zhang, S. (2010). Preparation, characterization, photocatalytic properties of titania hollow sphere doped with cerium. *Journal of Hazardous Materials*, *178*(1-3), 517-521. https://doi.org/10.1016/j.jhazmat.2010.01.111

[318] Wang, G., Yang, J., Park, J., Gou, X., Wang, B., Liu, H., & Yao, J. (2008). Facile synthesis and characterization of graphene nanosheets. *The Journal of Physical Chemistry C*, *112*(22), 8192-8195. https://doi.org/10.1021/jp710931h

[319] Wang, J., Liu, B., Wu, J., & Li, H. (2018). Crystallization of $WO_3.H_2O$ nanosheets with high-adsorption capacity for methylene blue. *Journal of Nanoparticle Research, 20*, 1-5. https://doi.org/10.1007/s11051-018-4358-4

[320] Wang, J., Sun, C., Huang, Q. X., Chi, Y., & Yan, J. H. (2021). Adsorption and thermal degradation of microplastics from aqueous solutions by Mg/Zn modified magnetic biochars. *Journal of hazardous materials*, *419*, 126486. https://doi.org/10.1016/j.jhazmat.2021.126486

[321] Wang, S., Cole, I. S., & Li, Q. (2016). Quantum-confined bandgap narrowing of TiO_2 nanoparticles by graphene quantum dots for visible-light-driven applications. *Chemical Communications, 52*(59), 9208-9211. https://doi.org/10.1039/C6CC03302D

[322] Wang, W., Tadé, M. O., & Shao, Z. (2018). Nitrogen-doped simple and complex oxides for photocatalysis: A review. *Progress in Materials Science*, *92*, 33-63. https://doi.org/10.1016/j.pmatsci.2017.09.002

[323] Wang, X., Sø, L., Su, R., Wendt, S., Hald, P., Mamakhel, A., Yang, C., Huang, Y., Iversen, B.B. & Besenbacher, F. (2014). The influence of crystallite size and crystallinity of anatase nanoparticles on the photo-degradation of phenol. *Journal of catalysis, 310*, 100-108. https://doi.org/10.1016/j.jcat.2013.04.022

[324] Wang, X., Teo, S. H., Shamsuddin, M. R., & Wid, N. (2025). Influence of Ag-concentration on TiO_2-supported catalysts for photocatalytic degradation of microplastics PA66 in marine. *Regional Studies in Marine Science, 81,* 103922. https://doi.org/10.1016/j.rsma.2024.103922

[325] Wang, X., Zhang, K., Guo, X., Shen, G., & Xiang, J. (2014). Synthesis and characterization of N-doped TiO_2 loaded onto activated carbon fiber with enhanced visible-light photocatalytic activity. *New Journal of Chemistry, 38*(12), 6139-6146. https://doi.org/10.1039/C4NJ00962B

[326] Wang, Y., Lai, Q., Zhang, F., Shen, X., Fan, M., He, Y., & Ren, S. (2014). High efficiency photocatalytic conversion of CO_2 with H_2O over Pt/TiO_2 nanoparticles. *RSC Advances, 4*(84), 44442-44451. https://doi.org/10.1039/C4RA07457B

[327] Wang, Z., Sun, C., Li, F., & Chen, L. (2021). Fatigue resistance, re-usable and biodegradable sponge materials from plant protein with rapid water adsorption capacity for microplastics removal. *Chemical Engineering Journal*, *415*, 129006. https://doi.org/10.1016/j.cej.2021.129006

[328] Wei, F., Ni, L., & Cui, P. (2008). Preparation and characterization of N–S-codoped TiO_2 photocatalyst and its photocatalytic activity. *Journal of Hazardous Materials*, *156*(1-3), 135-140. https://doi.org/10.1016/j.jhazmat.2007.12.018

[329] Weidner, E., Karbassiyazdi, E., Altaee, A., Jesionowski, T., & Ciesielczyk, F. (2022). Hybrid metal oxide/biochar materials for wastewater treatment technology: a review. *ACS omega, 7*(31), 27062-27078. https://doi.org/10.1021/acsomega.2c02909

[330] Woan, K., Pyrgiotakis, G., & Sigmund, W. (2009). Photocatalytic carbon-nanotube–TiO_2 composites, Adv. Mater. 21(21), 2233–2239. https://doi.org/10.1002/adma.200802738

[331] Wu, P., Cai, Z., Jin, H., & Tang, Y. (2019). Adsorption mechanisms of five bisphenol analogues on PVC microplastics. *Science of the Total Environment, 650*, 671-678. https://doi.org/10.1016/j.scitotenv.2018.09.049

[332] Wu, S., Cao, H., Yin, S., Liu, X., & Zhang, X. (2009). Amino acid-assisted hydrothermal synthesis and photocatalysis of SnO_2 nanocrystals. *The Journal of Physical Chemistry C*, *113*(41), 17893-17898. https://doi.org/10.1021/jp9068762

[333] Wu, Y., Yi, R., Wang, Y., Zhang, C., Zheng, J., Ning, P., Shan, D & Wang, B. (2025). Light-driven degradation of microplastics: Mechanisms, technologies, and future directions. *Journal of Hazardous Materials Advances*, 100628. https://doi.org/10.1016/j.hazadv.2025.100628

[334] Wu, Y., Zhang, J., Xiao, L., & Chen, F. (2010). Properties of carbon and iron modified TiO_2 photocatalyst synthesized at low temperature and photodegradation of acid orange 7 under visible light. *Applied Surface Science*, *256*(13), 4260-4268. https://doi.org/10.1016/j.apsusc.2010.02.012

[335] Xiao, J., Peng, T., Li, R., Peng, Z., & Yan, C. (2006). Preparation, phase transformation and photocatalytic activities of cerium-doped mesoporous titania nanoparticles. *Journal of Solid State Chemistry*, *179*(4), 1161-1170. https://doi.org/10.1016/j.jssc.2006.01.008

[336] Xiao, W., Garba, Z. N., Sun, S., Lawan, I., Wang, L., Lin, M., & Yuan, Z. (2020). Preparation and evaluation of an effective activated carbon from white sugar for the adsorption of rhodamine B dye. *Journal of Cleaner Production*, *253*, 119989. https://doi.org/10.1016/j.jclepro.2020.119989

[337] Xiao, Y., Tian, Y., Xu, W., & Zhu, J. (2024). Photodegradation of microplastics through nanomaterials: Insights into photocatalysts modification and detailed mechanisms. *Materials*, *17*(11), 2755. https://doi.org/10.3390/ma1711275

[338] Xie, M., Jing, L., Zhou, J., Lin, J., & Fu, H. (2010). Synthesis of nanocrystalline anatase TiO_2 by one-pot two-phase separated hydrolysis-solvothermal processes and its high activity for photocatalytic degradation of rhodamine B. *Journal of hazardous materials, 176*(1-3), 139-145. https://doi.org/10.1016/j.jhazmat.2009.11.008

[339] Xie, Y., Zhao, X., Li, Y., Zhao, Q., Zhou, X., & Yuan, Q. (2008). CTAB-assisted synthesis of mesoporous F–N-codoped TiO_2 powders with high visible-light-driven catalytic activity and adsorption capacity. *Journal of Solid State Chemistry*, *181*(8), 1936-1942. https://doi.org/10.1016/j.jssc.2008.04.021

[340] Xing, M., Zhang, J., & Chen, F. (2009). New approaches to prepare nitrogen-doped TiO_2 photocatalysts and study on their photocatalytic activities in visible light. *Applied Catalysis B: Environmental, 89*(3-4), 563-569. https://doi.org/10.1016/j.apcatb.2009.01.016

[341] Xu, J., Ao, Y., Chen, M., & Fu, D. (2009). Low-temperature preparation of Boron-doped titania by hydrothermal method and its photocatalytic activity. *Journal of Alloys and Compounds*, *484*(1-2), 73-79. https://doi.org/10.1016/j.jallcom.2009.04.156

[342] Xu, N., Shi, Z., Fan, Y., Dong, J., Shi, J., & Hu, M. Z. C. (1999). Effects of particle size of TiO_2 on photocatalytic degradation of methylene blue in aqueous suspensions. *Industrial & Engineering Chemistry Research, 38*(2), 373-379. https://doi.org/10.1021/ie980378u

[343] Yadav, A., Yadav, M., Gupta, S., Popat, Y., Gangan, A., Chakraborty, B., Ramaniah, L.M., Fernandes, R., Miotello, A., Press, M.R. & Patel, N. (2019). Effect of graphene oxide loading on TiO_2: Morphological, optical, interfacial charge dynamics-A combined experimental and theoretical study. *Carbon, 143*, 51-62. https://doi.org/10.1016/j.carbon.2018.10.090

[344] Yan, L., Liu, Y., Zhang, Y., Liu, S., Wang, C., Chen, W., Liu, C., Chen, Z. & Zhang, Y. (2020). $ZnCl_2$ modified biochar derived from aerobic granular sludge for developed microporosity and enhanced adsorption to tetracycline. *Bioresource Technology, 297*, 122381. https://doi.org/10.1016/j.biortech.2019.122381

[345] Yang, G., Jiang, Z., Shi, H., Xiao, T., & Yan, Z. (2010). Preparation of highly visible-light active N-doped TiO_2 photocatalyst. Journal of Materials Chemistry, 20(25), 5301-5309. https://doi.org/10.1039/C0JM00376J

[346] Yang, H., Yan, R., Chen, H., Lee, D. H., & Zheng, C. (2007). Characteristics of hemicellulose, cellulose and lignin pyrolysis. *Fuel, 86*(12-13), 1781-1788.

https://doi.org/10.1016/j.fuel.2006.12.013

[347] Yang, L., Luo, Y., Yang, L., Luo, S., Luo, X., Dai, W., Li, T. & Luo, Y. (2019). Enhanced photocatalytic activity of hierarchical titanium dioxide microspheres with combining carbon nanotubes as "e-bridge". *Journal of hazardous materials*, 367, 550-558. https://doi.org/10.1016/j.jhazmat.2019.01.016

[348] Yaqoob, A. A., Parveen, T., Umar, K., & Mohamad Ibrahim, M. N. (2020). Role of nanomaterials in the treatment of wastewater: A review. *Water*, *12*(2), 495. https://doi.org/10.3390/w12020495

[349] Yousif, E., Al-Amiery, A. A., Kadihum, A., Kadhum, A. A. H., & Mohamad, A. B. (2015). Photostabilizing efficiency of PVC in the presence of Schiff bases as photostabilizers. *Molecules, 20*(11), 19886-19899. https://doi.org/10.3390/molecules201119665

[350] Yu, B., Wang, X., Qian, X., Xing, W., Yang, H., Ma, L., Lin, Y., Jiang, S., Song, L., Hu, Y. & Lo, S. (2014). Functionalized graphene oxide/phosphoramide oligomer hybrids flame retardant prepared via in situ polymerization for improving the fire safety of polypropylene. *RSC Advances, 4*(60), 31782-31794. https://doi.org/10.1039/C3RA45945D

[351] Yu, C., Cai, D., Yang, K., Yu, J. C., Zhou, Y., & Fan, C. (2010). Sol–gel derived S, I-codoped mesoporous TiO_2 photocatalyst with high visible-light photocatalytic activity. *Journal of Physics and Chemistry of Solids*, *71*(9), 1337-1343. https://doi.org/10.1016/j.jpcs.2010.06.001

[352] Yu, J., Wang, W., Cheng, B., & Su, B. L. (2009). Enhancement of photocatalytic activity of mesporous TiO_2 powders by hydrothermal surface fluorination treatment. *The Journal of Physical Chemistry C*, *113*(16), 6743-6750. https://doi.org/10.1021/jp900136q

[353] Yu, J., Zhou, M., Cheng, B., & Zhao, X. (2006). Preparation, characterization and photocatalytic activity of in situ N, S-codoped TiO_2 powders. *Journal of Molecular Catalysis A: Chemical*, *246*(1-2), 176-184. https://doi.org/10.1016/j.molcata.2005.10.034

[354] Yuan, F., Yue, L., Zhao, H., & Wu, H. (2020). Study on the adsorption of polystyrene microplastics by three-dimensional reduced graphene oxide. Water Science and Technology, 81(10), 2163-2175. https://doi.org/10.2166/wst.2020.269

[355] Yue, Y., Yue, X., Tang, X., Han, L., Wang, J., Wang, S., & Du, C. (2024). Synergistic adsorption and photocatalysis study of TiO_2 and activated carbon composite. *Heliyon, 10*(10), e30817. https://doi.org/10.1016/j.heliyon.2024.e30817

[356] Zafar, R., Park, S. Y., & Kim, C. G. (2021). Surface modification of polyethylene microplastic particles during the aqueous-phase ozonation process. *Environmental Engineering Research*, *26*(5), 200412.

https://doi.org/10.4491/eer.2020.412

[357] Zaleska, A. (2008). Doped-TiO_2: a review. *Recent patents on engineering*, *2*(3), 157-164. https://doi.org/10.2174/187221208786306289

[358] Zaleska, A., Sobczak, J. W., Grabowska, E., & Hupka, J. (2008). Preparation and photocatalytic activity of boron-modified TiO_2 under UV and visible light. *Applied Catalysis B: Environmental*, *78*(1-2), 92-100. https://doi.org/10.1016/j.apcatb.2007.09.005

[359] Zan, L., Fa, W., & Wang, S. (2006). Novel photodegradable low-density polyethylene− TiO_2 nanocomposite film. *Environmental science & technology, 40*(5), 1681-1685. https://doi.org/10.1021/es051173x

[360] Zarrin, S., & Heshmatpour, F. (2018). Photocatalytic activity of TiO_2/Nb_2O_5/PANI and TiO_2/Nb_2O_5/RGO as new nanocomposites for degradation of organic pollutants. *Journal of hazardous materials, 351*, 147-159. https://doi.org/10.1016/j.jhazmat.2018.02.052

[361] Zazouli, M. A., Azari, A., Dehghan, S., & Salmani Malekkolae, R. (2016). Adsorption of methylene blue from aqueous solution onto activated carbons developed from eucalyptus bark and Crataegus oxyacantha core. *Water science and technology*, *74*(9), 2021-2035. https://doi.org/10.2166/wst.2016.287

[362] Zhang, H., Chen, B., & Banfield, J. F. (2009). The size dependence of the surface free energy of titania nanocrystals. *Physical Chemistry Chemical Physics, 11*(14), 2553-2558. https://doi.org/10.1039/B819623K

[363] Zhang, Q., Li, Y., Ackerman, E. A., Gajdardziska-Josifovska, M., & Li, H. (2011). Visible light responsive iodine-doped TiO_2 for photocatalytic reduction of CO_2 to fuels. *Applied catalysis A: general*, *400*(1-2), 195-202. https://doi.org/10.1016/j.apcata.2011.04.032

[364] Zhang, X., Cao, S., Wu, Z., Zhao, S., & Piao, L. (2017). Enhanced photocatalytic activity towards degradation and H_2 evolution over one dimensional TiO_2@MWCNTs heterojunction. *Applied Surface Science, 402*, 360-368. https://doi.org/10.1016/j.apsusc.2017.01.096

[365] Zhang, X., Qin, J., Hao, R., Wang, L., Shen, X., Yu, R., Limpanart, S., Ma, M. & Liu, R. (2015). Carbon-doped ZnO nanostructures: facile synthesis and visible light photocatalytic applications. *The Journal of Physical Chemistry C*, *119*(35), 20544-20554. https://doi.org/10.1021/acs.jpcc.5b07116

[366] Zhang, Y., Pedersen, J. N., Eser, B. E., & Guo, Z. (2022). Biodegradation of polyethylene and polystyrene: From microbial deterioration to enzyme discovery. *Biotechnology Advances*, *60*, 107991.

https://doi.org/10.1016/j.biotechadv.2022.107991

[367] Zhang, Y., Zhou, G., Yue, J., Xing, X., Yang, Z., Wang, X., Wang, Q. & Zhang, J. (2021). Enhanced removal of polyethylene terephthalate microplastics through polyaluminum chloride coagulation with three typical coagulant aids. *Science of the Total Environment*, *800*, 149589. https://doi.org/10.1016/j.scitotenv.2021.149589

[368] Zhao, D., Sheng, G., Chen, C., & Wang, X. (2012). Enhanced photocatalytic degradation of methylene blue under visible irradiation on graphene@ TiO_2 dyade structure. *Applied Catalysis B: Environmental, 111*, 303-308. https://doi.org/10.1016/j.apcatb.2011.10.012

[369] Zhao, X. X., Liu, D., Li, Y. H., & Cui, G. H. (2018). Two 3D cadmium (II) coordination polymers modulated by flexible bis (benzimidazole) ligands displaying high photocatalytic activities for degradation of methylene blue and methyl orange. *Polyhedron, 156*, 200-207. https://doi.org/10.1016/J.POLY.2018.09.041

[370] Zheng, H., Chen, Q., & Chen, Z. (2024). Carbon-based adsorbents for micro/nano-plastics removal: Current advances and perspectives. *Water Emerging Contaminants & Nanoplastics, 3*(2), N-A. https://doi.org/10.20517/wecn.2023.74

[371] Zheng, H., Liu, K., Cao, H., & Zhang, X. (2009). L-Lysine-assisted synthesis of ZrO_2 nanocrystals and their application in photocatalysis. *The Journal of Physical Chemistry C*, *113*(42), 18259-18263. https://doi.org/10.1021/jp9057324

[372] Zhi, L., Li, R., Li, Z., Su, Z., Chen, F., Qin, Q., Huang, Y., Huang, X. & Wang, J. (2025). Micro/nanoplastics in aquatic ecosystems: Analytical challenges, ecological impacts, and mitigation strategies. Environmental Chemistry and Ecotoxicology. https://doi.org/10.1016/j.enceco.2025.07.009

[373] Zhou, G., Wang, Q., Li, J., Li, Q., Xu, H., Ye, Q., Wang, Y., Shu, S. & Zhang, J. (2021). Removal of polystyrene and polyethylene microplastics using PAC and $FeCl_3$ coagulation: Performance and mechanism. *Science of the Total Environment*, *752*, 141837. https://doi.org/10.1016/j.scitotenv.2020.141837

[374] Zhou, H., Wang, H., Yue, C., He, L., Li, H., Zhang, H., Yang, S. & Ma, T. (2024). Photocatalytic degradation by TiO_2-conjugated/coordination polymer heterojunction: Preparation, mechanisms, and prospects. *Applied Catalysis B: Environment and Energy*, *344*, 123605. https://doi.org/10.1016/j.apcatb.2023.123605

[375] Zhou, Z., & Wu, X. F. (2013). Graphene-beaded carbon nanofibers for use in supercapacitor electrodes: Synthesis and electrochemical characterization. *Journal of Power Sources*, *222*, 410-416. https://doi.org/10.1016/j.jpowsour.2012.09.004

[376] Zhu, J., Zheng, W., He, B., Zhang, J., & Anpo, M. (2004). Characterization of Fe–TiO_2 photocatalysts synthesized by hydrothermal method and their photocatalytic reactivity for photodegradation of XRG dye diluted in water. *Journal of Molecular Catalysis A: Chemical*, *216*(1), 35-43. https://doi.org/10.1016/j.molcata.2004.01.008

[377] Zhu, N., Yan, Q., He, Y., Wang, X., Wei, Z., Liang, D., Yue, H., Yun, Y., Li, G. & Sang, N. (2022). Insights into the removal of polystyrene nanoplastics using the contaminated corncob-derived mesoporous biochar from mining area. Journal of Hazardous Materials, 433, 128756. https://doi.org/10.1016/j.jhazmat.2022.128756

[378] Zulfiqar, Khan, R., Yuan, Y., Iqbal, Z., Yang, J., Wang, W., Ye, Z. & Lu, J. (2017). Variation of structural, optical, dielectric and magnetic properties of SnO_2 nanoparticles. *Journal of Materials Science: Materials in Electronics, 28*, 4625-4636. https://doi.org/10.1007/s10854-016-6101-1

1. List of Publications

[1] Kuljit Kaur, Mankomal Arora & Harpreet Kaur (2023). Synergistic effect of graphene oxide based nitrogen-doped nano-titanium oxide for effective adsorption and photo catalysis of dibutyl phthalate and organic pollutants from water. *Research on Chemical Intermediates*, *49*(10), 4193-4216.

https://doi.org/10.1007/s11164-023-05101-8

[2] Kuljit Kaur, Rajandeep Kaur, Harpreet Kaur (2024). A systematic review of lignocellulosic biomass for remediation of environmental pollutants. *Applied Surface Science Advances*, *19*, 100547.

https://doi.org/10.1016/j.apsadv.2023.100547

[3] Kuljit Kaur, Harpreet Kaur (2025). Visible light induced photocatalytic degradation of polyvinyl chloride from water using graphene oxide/nitrogen-doped TiO_2 nanocomposite. *Journal of Environmental Chemical Engineering*, *13*(2), 115664.

https://doi.org/10.1016/j.jece.2025.115664

[4] Kuljit Kaur, Maha Saleem, and Harpreet Kaur (2025). Biochar and Biopolymer Based Nanomaterials for Microplastic Remediation: A Sustainable Approach for Environment." *Topics in Catalysis*, 1-28.

https://doi.org/10.1007/s11244-025-02185-x

[5] Kuljit Kaur, Harpreet Kaur. Biomass-Derived CCAC/N-TiO_2 Composites for Efficient Photocatalytic Degradation of Polyvinylchloride Nanoplastics in Water. **(Communicated)**

Book Chapters

[1] Kuljit Kaur, Harpreet Kaur (2023). Removal of Microplastic Contaminants from Aquatic Environment. In *Microplastic Pollution: Causes, Effects and Control* (pp. 69-92). Bentham Science Publishers.

https://doi.org/10.2174/9789815165104123010007

[2] Kuljit Kaur, Harpreet Kaur. "Low Carbon Materials: Barriers and Challenges to Implementation". Wiley. **(Accepted)**

2. List of Patents

[1] **Title of the invention:** A METHOD OF RECYCLING OF WASTE PLASTIC INTO BEST MATERIAL FOR REMEDIATION OF WASTE WATER.

Name of Inventor: Dr. Harpreet Kaur, Kuljit Kaur, Dr. Narendra Kumar Pandey

PATENT APPLICATION PUBLICATION INDIA

Date of filing of Application: 15/1 1/2022

Application No.202211065339 A

Publication Date: 25/11/2022

3. List of Conferences Attended

[1] Presented a poster entitled "Lignocellulosic biomass derived activated carbon and its applications in removal of gaseous pollutants: A review" in International Conference of "Recent Advances in Fundamental and Applied Sciences" (RAFAS 2021) at Lovely Professional University, Phagwara on June 25-26, 2021.

[2] Presented a poster entitled "Removal of cationic dyes using waste plastic-based nanocomposite sheets" in International Conference on Molecules and Materials Technology (MMT-2023), Department of Chemistry National Institute of Technology Kurukshetra on April 21-22, 2023.

[3] Presented oral and poster entitled "Waste polyethylene-based nanocomposite sheets as a highly efficient scavenger for the cationic dyes" in Global Indian Young Scientists Research and Innovation Conference 2023, NASC, New Delhi

on May 31- June 2, 2023.

[4] Presented a poster entitled "Cardiovascular Biomarkers: Classification, Characteristics, and Cardiovascular Pathology" in International Conference of "Recent Advances in Fundamental and Applied Sciences" (RAFAS 2021) at Lovely Professional University, Phagwara on April 19-20, 2024.

[5] Presented a poster entitled "Preparation, characterization and removal performance of biochar-based nanocomposite for removal of plastic nanoparticles from water" in International Conference "Goldschmidt Chicago 2024" on August 18-23, 2024.

4. List of Trainings attended

[1] Participated in one-week AICTE and IKCPTU Jalandhar sponsored Faculty Development Programme on "Advancements in the Methodologies for the development of Synthetic Materials" conducted by the Department of Chemical Sciences.

[2] Participated in "Skill development program on sophisticated research instruments from May 12th to 18th, 2023 organized by department of chemistry, H.N.B. Garhwal University, Srinagar (Garhwal), Uttarakhand (A Central University) in association with Banasthali Vidyapith Rajasthan.